

High-energy radiation from spin-down powered pulsars

Contents

1	Introduction	9
1.1	Observational characteristics of pulsars	9
1.2	Outline of this thesis	13
1.2.1	Part I: High-energy emission from normal pulsars at medium γ -ray energies	13
1.2.2	Part II: High-energy emission from recycled pulsars: the case PSR J0218+4232	14
Part I : High-energy radiation from normal pulsars at medium γ -ray energies		
2	Search in the COMPTEL data for MeV emission from Geminga	19
2.1	Introduction	19
2.2	Instrument and analysis techniques	20
2.3	Observations	20
2.4	Timing analysis	20
2.5	Spatial analysis	21
2.5.1	Total spectrum	21
2.5.2	Spectra for different phase components	21
2.6	Summary and Discussion	21
3	Detection of pulsed MeV emission from PSR B1951+32 by COMPTEL	25
3.1	Introduction	25
3.2	Observations	26
3.3	The COMPTEL instrument	26
3.4	Analysis methods	27
3.4.1	Timing analysis	27
3.4.1.1	Procedures and ephemerides	27
3.4.1.2	Detection significance of pulsed emission	27
3.4.2	Spatial and spectral analyses	27
3.5	Timing analysis results	28
3.5.1	COMPTEL Event selections	28
3.5.2	Consistency of COMPTEL and EGRET lightcurves	28
3.5.3	Timing analysis for CGRO Cycles I–VI	29
3.5.4	Lightcurve simulations	30
3.6	Spatial- and spectral analysis	32
3.6.1	Spatial analysis	32
3.6.2	Spectral analysis	33
3.7	Summary and discussion	34
4	COMPTEL detection of pulsed γ-ray emission from PSR B1509-58 up to at least 10 MeV	39
4.1	Introduction	39
4.2	Instrument description and observations	40
4.3	COMPTEL timing analysis	42
4.3.1	Event selections	42
4.3.2	Pulse phase folding	42
4.3.3	Pulse profiles in the 0.75-30 MeV energy range	42
4.3.4	Pulse profiles from soft X-rays to medium energy γ -rays	43
4.3.5	Pulsed 0.75-30 MeV fluxes from the excess counts in the lightcurves	44
4.4	COMPTEL spatial analysis	45
4.4.1	Analysis method	45
4.4.1.1	Imaging results for energies < 10 MeV	45
4.4.1.2	Imaging results for energies > 10 MeV	46
4.5	Analysis of EGRET data	46
4.5.1	Spatial analysis	47
4.5.2	Timing analysis	48

4.6	Spectral analysis	49
4.7	Summary and discussion	49
5	The Crab pulsar in the 0.75-30 MeV range as seen by COMPTEL	55
5.1	Introduction	55
5.2	Instrument description and observations	57
5.3	Timing analysis	58
5.4	Long-term variability	60
5.4.1	Flux variations: total pulsed flux in the 1-10 MeV range	60
5.4.2	Pulse shape variations: P2/P1 ratio in the 1-3 MeV range	60
5.4.3	Variations in arrival time of P1 at energies above 30 MeV	61
5.5	Pulse profiles of PSR B0531+21 from 0.1 keV up to 10 GeV	61
5.5.1	P2/P1 and Bridge/P1 ratios as a function of energy	62
5.6	Spectral analysis	63
5.6.1	Crab nebula spectrum	63
5.6.2	Crab Total Pulse spectrum	65
5.6.3	Spectral behaviour in the narrow pulse phase intervals	67
5.6.4	Parametrization of the emission in the narrow pulse phase intervals	67
5.6.5	Likely hard high-energy γ -ray component in front of P2	69
5.7	P1 arrival time/phase at MeV energies	70
5.8	Summary and discussion	70

Part II : High-energy radiation from recycled pulsars: the case PSR J0218+4232

6	High-energy observations of the millisecond pulsar PSR J0218+4232	77
6.1	Introduction	77
6.2	X-ray observations and data reduction	77
6.3	High-energy γ -ray data and analysis	78
6.4	Discussion	79
7	Detection of pulsed X-ray emission from the binary millisecond pulsar PSR J0218+4232	83
7.1	Introduction	83
7.2	X-ray data and data analysis	83
7.2.1	ROSAT HRI Observation	83
7.2.2	Spatial analysis	83
7.2.3	Timing analyses	84
7.2.3.1	Modulation at the pulsar period	84
7.2.3.2	Modulation at the orbital period	86
7.2.4	Indications for extended emission	86
7.2.5	Flux calculation	87
7.3	Discussion	87
8	The pulse shape and spectrum of the millisecond pulsar PSR J0218+4232 in the energy band 1-10 keV observed with BeppoSAX	93
8.1	Introduction	93
8.2	Observation	94
8.3	Spatial analysis	94
8.4	Timing analysis	95
8.5	Spectral analysis	96
8.6	Discussion	97

9	The likely detection of pulsed high-energy γ-ray emission from millisecond pulsar PSR J0218+4232	101
9.1	Introduction	101
9.2	Instrument description and observations	102
9.3	Spatial analysis	102
9.4	Long-term time variability	104
9.5	Timing analysis	104
9.6	Pulse phase resolved spatial analysis	105
9.7	Multi-wavelengths profile comparisons	106
	9.7.1 Comparison with radio profiles	106
	9.7.2 Comparison with X-ray profiles	107
9.8	Multi-wavelength spectrum	108
9.9	Summary and discussion	109
10	Nederlandse Samenvatting: Hoog-energetische straling van pulsars	113
10.1	Wat is hoog-energetische straling en hoe detecteer je dit?	113
10.2	Hoog-energetische straling vanuit de kosmos	115
10.3	Overzicht van dit proefschrift	116
10.4	Wetenschappelijke bijdrage van dit onderzoek en vooruitzichten	117
	Curriculum vitae	119

High-energy radiation from spin-down powered pulsars

Hoog energetische straling uit het
rotatie-energie verlies van pulsars
met een samenvatting in het Nederlands

Proefschrift ter verkrijging van de graad van Doctor aan de Universiteit
Utrecht op gezag van de Rector Magnificus, Prof. Dr. H.O. Voorma, ingevolge het
besluit van het College voor Promoties in het openbaar te verdedigen
op maandag 8 januari 2001 des middags te 14.30 uur

door

Lucien Marcel Kuiper

geboren op 2 april 1960, te Zaandam

Promotor: **Prof. dr. F. Verbunt**
Sterrenkundig Instituut, Universiteit Utrecht

Co-promotor: **Dr. W. Hermsen**
Stichting Ruimte Onderzoek Nederland, Utrecht

Chapter 1

Introduction

1.1. Observational characteristics of pulsars

The discovery in 1967 by Hewish et al. (1968) of a repetitive radio-signal with a periodicity of ~ 1.3 seconds from a source, nowadays named PSR B1919+21, heralded a new era in astrophysics. The name pulsar was given to the underlying astrophysical object. Interpretation of this short period either in terms of a dynamic instability of a stellar object (pulsation) or in terms of a rapid rotation were then both possible, but pointed in any case to the involvement of a compact object, either a white dwarf with typical core densities of $\lesssim 10^8 \rho_{\odot}$ (ρ_{\odot} is the solar core density) or a neutron star ($\rho/\rho_{\odot} \gtrsim 10^{14}$).

The subsequent detections of periodicities for pulsars within the Crab nebula (Staelin & Reifenstein 1968) and Vela supernova remnant (Large et al. 1968) of 33 and 89 millisecond, respectively, settled the issue and made clear that we were dealing with rapidly rotating neutron stars. The unambiguous pulsar/supernovae association provided crucial information for stellar evolution theory. It is nowadays generally believed that relatively massive stars ($M \gtrsim 8M_{\odot}$) end their nuclear-burning lives in a supernova explosion by blowing away the outer parts of the star into the interstellar medium, while the imploding core forms a rapidly rotating neutron star with a typical mass and radius of about $1.4M_{\odot}$ and 10 km, respectively, or for very massive progenitors a rapidly rotating black hole. Angular momentum conservation during the collapse underlies the rapid rotation, while magnetic flux conservation has been suggested to result in very large magnetic fields of the order of 10^{13} Gauß for the stellar remnants.

The combination of rapid rotation and a strong magnetic field causes strong potential drops in the pulsar's magnetosphere across which charged particles (mainly e^{\pm}) expelled from the neutron star crust or generated in the magnetosphere can be accelerated to very high relativistic energies. These accelerated particles lose energy mainly in the form of curvature radiation (due to the curvature of the dipole field lines), synchrotron radiation (gyration around field lines) or inverse Compton radiation (interaction of a relativistic particle with a low energy photon). The produced electro-magnetic radiation is highly beamed along

the local direction of the magnetic field and for an inclined dipole geometry the line of sight of a distant observer would cross the emission beam once per revolution resembling the emission from a lighthouse.

The system composed of the rotating neutron star and its magnetosphere loses energy in the form of particle outflow (pulsar wind) along field lines in the open-field line zone and in the form of electro-magnetic radiation at the expense of the neutron star's rotational energy $dE/dt = -d/dt(\frac{1}{2}I\Omega^2)$ with I the mass inertia moment and Ω the angular velocity, causing a gradual slow-down of the rotation rate of the neutron star i.e. increasing pulse period as a function of time. The expression "spin-down" powered pulsars is adopted from this underlying energy loss mechanism. In Fig. 1.1 the two-dimensional distribution of measured pulse period and period derivative (P, \dot{P}) is shown for a sample of 706 radio pulsars (Taylor et al. 1995). A striking feature in this figure is the existence of two distinct groups of pulsars: one with periods $\gtrsim 15$ ms and $\dot{P} \gtrsim 10^{-18}$ s/s, the "normal" pulsars having characteristic ages $\tau = P/2\dot{P}$ between 10^3 and 10^8 year; and a second group, the "millisecond" pulsars with $P \lesssim 15$ ms and $\dot{P} \lesssim 10^{-18}$ s/s with characteristic ages larger than $\sim 10^8$ year. Note that lines of constant characteristic age have a slope of 1 in the $\log(P), \log(\dot{P})$ plane with the "youngest" pulsars located in the upper left part of the plane. Similarly, curves corresponding to constant surface magnetic field strengths B , using for B the estimate of $3.2 \times 10^{19} \sqrt{P\dot{P}}$, are given by straight lines with a slope of -1 in the $\log(P), \log(\dot{P})$ plane with the highest fields in the upper right part of the plane. From Fig. 1.1 it is clear that the millisecond pulsars have much lower surface magnetic field strengths than the normal pulsars, typically reduced by a factor of $\sim 10^4$ with respect to the normal pulsars.

Due to the small \dot{P} and large rotation frequency the millisecond pulsars are extremely stable rotators, of which the rotation behaviour can be predicted very accurately. One of them provides even a more stable clock than the best atomic clock on Earth! When such a millisecond pulsar is orbiting another compact object in a tight orbit, subtle general and special relativistic effects can be studied in detail through accurate pulse timing measurements (Taylor et al. 1992).

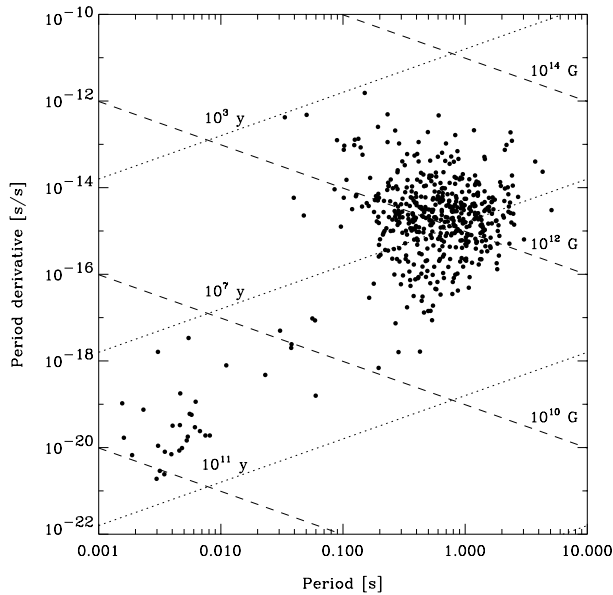


Fig. 1.1. Period and period derivative for a sample of 706 radio pulsars. Notice the existence of 2 distinct clusters: the “normal” pulsars with typical periods and period derivatives of 1 s and 10^{-15} s/s and the millisecond pulsars having typical P, \dot{P} of 5 ms and 10^{-20} s/s. Lines of constant characteristic age (dotted) and constant surface magnetic field strength (dashed) are indicated.

Members belonging to the millisecond pulsar group are preferentially located in binary systems ($\sim 75\%$) commonly with a white dwarf companion, while for the “normal” pulsars just $\sim 1\%$ of the pulsars is member of a binary system. This clear distinction points to a different evolutionary history for both groups. It is commonly accepted that the millisecond pulsars are descendents from an X-ray binary evolutionary phase. The X-ray binaries can be grouped in two different classes: the low-mass X-ray binaries (LMXB) in which a neutron star is accompanied by a low-mass ($\lesssim 2M_{\odot}$) star and the high-mass X-ray binaries (HMXB) having more massive companions. Several dozens of X-ray binaries are nowadays known (van Paradijs 1995). Mass is transferred to the neutron star either through stellar wind or an accretion disk, thereby producing X-rays in the vicinity of the neutron star often modulated at the neutron star’s spin frequency (accretion driven X-ray pulsar). The impulse momentum imported by the mass transfer makes the neutron star spin faster and spin-up periods down to about one millisecond seem possible theoretically (this process is called recycling; see for an overview on the formation of millisecond pulsars e.g. van den Heuvel 1991). This scenario explains naturally the high probability of finding a millisecond radio pulsar in a binary system. The normal (99% single) radio pulsars are the direct evolutionary products of relatively massive single stars ($M \gtrsim 8M_{\odot}$) originating from a supernova explosion.

In the magnetosphere of pulsars not only radio waves are produced in non-thermal radiation processes involving

accelerated charged particles, but from some pulsars also in the optical domain emission has been detected. Soon after the discovery of the Crab pulsar at radio frequencies pulsed optical emission was detected (Cocke et al. 1969). Since then pulsed optical emission has been detected from the Vela pulsar (Wallace et al. 1977; Gouiffes 1998), a young Crab like pulsar PSR B0540-69 located in the Large Magellanic Cloud (Middleitch & Pennypacker 1985), and probably from PSR B0656+14 (Shearer et al. 1997) and the Geminga γ -ray pulsar (Shearer et al. 1998). For some other pulsars like PSR B1055-52 (Mignani et al. 1997), PSR B1509-58 (Wagner & Seifert 2000), PSR B1929-10 and PSR B0950+08 (Pavlov et al. 1996 for the latter 2 pulsars) optical counterparts are proposed based on their spatial coincidence with the radio pulsar, but the emission is too faint (for example; 27.1 magnitude for PSR B0950+08 in Hubble Space Telescope F130LP passband) to reveal the possible underlying pulsations. Moreover, for the older pulsars the pulsed magnetospheric emission could be absent and the optical signal could merely be a manifestation of the Rayleigh-Jeans part of the blackbody spectrum of a cooling neutron star.

At X-ray energies the Crab pulsar was the first showing its pulsed nature (Fritz et al. 1969). The number of spin-down powered pulsars detected at X-rays had steadily grown since then with major contributions from the Einstein observatory (HEAO-2; Nov. 1978 – Apr. 1981), ROSAT (Röntgen Satellite; June 1990 – Feb. 1999) and ASCA (the Advanced Satellite for Cosmology and Astrophysics; Feb. 1993 – present). The current number of spin-down powered pulsars emitting X-rays is $\gtrsim 40$ (e.g. see Becker & Trümper 1997 for an overview). X-rays from such systems are expected to originate from neutron star surface cooling (typical temperatures are of the order of 10^6 K), from non-thermal radiation processes in the magnetosphere and from polar cap heating by inwards directed particle beams, resulting in relatively broad pulses with soft (thermal) spectra. Surprisingly, among the $\gtrsim 40$ spin-down powered X-ray emitting pulsars are 14 milliseconds pulsars of which 6 show definite pulsed emission, while the association of the others is based on positional coincidence. These 6 millisecond pulsars can further be classified in two groups: a low luminosity group (Class-I)¹ showing soft X-ray spectra and emission in (a) fairly broad pulse(s), composed of PSR J0437-4715, PSR J2124-3358 and PSR J0030+451, and a high-luminosity group (Class-II) showing very hard spectra and narrow pulses with members PSR B1821-24, PSR J0218+4232 and PSR B1937+21. The detection of one Class-II member, PSR J0218+4232, as an X-ray (0.1-10 keV) pulsed source and as a likely pulsed high-energy (100-1000 MeV) γ -ray source is presented in detail in the second part of this thesis. Similar physical processes as for the X-ray emitting “normal” radio pulsars are

¹ X-ray emission is merely detected because of the proximity of these pulsars

believed to be responsible for the (pulsed) X-ray emission from millisecond pulsars except neutron star surface cooling does not provide a viable mode in view of the large characteristic age for these systems.

At high-energy (> 30 MeV) γ -ray energies pulsed emission was significantly detected from the Crab and Vela pulsars by the space-borne spark chambers aboard the SAS-2 and COS-B satellites in the seventies (Crab pulsar: Kniffen et al. 1974 and Thompson et al. 1977a for the SAS-2 results, Bennett et al. 1977, Wills et al. 1982 and Clear et al. 1987 for the COS-B results; Vela pulsar: Thompson et al. 1975 and Thompson et al. 1977b for the SAS-2 results, Bennett et al. 1977 and Grenier et al. 1988 for the COS-B results). These findings made clear that the particles accelerated in the magnetosphere must indeed reach extremely relativistic energies in order to account for the release of > 30 MeV photons.

At medium energy (0.5-30 MeV) γ -rays, a window opened later to astronomy due to the difficult detection technique, the only source definitely seen to emit pulsed radiation prior to the nineties was the Crab pulsar (Graser & Schönfelder 1982), although there were indications in measurements from short duration balloon flights that also the Vela pulsar (Tümer et al. 1984) showed its pulsed nature in this energy window at emission levels never confirmed in later more sensitive observations.

The launch of the Compton Gamma-Ray Observatory (CGRO) in April 1991 with the 4 complementary instruments BATSE, OSSE, COMPTEL and EGRET covering the 20 keV - 30 GeV energy window substantially increased the number of pulsar detections at γ -ray energies and most of the results presented in this thesis are based on CGRO data.

The Burst And Transient Source Experiment (BATSE) provides an all-sky monitor in the 20-1000 keV energy window for transient γ -ray events (γ -ray bursts; flaring activity in X-ray transients or in Active Galactic Nuclei). The Oriented Scintillation Spectrometer Experiment (OSSE) is a non-imaging detector system consisting of 4 independent actively shielded NaI(Tl)-Cs(Na) phoswich detectors operating in the 0.05-10 MeV energy range. Each detector has a $3^{\circ}8 \times 11^{\circ}4$ (FWHM) field of view. COMPTEL is the imaging COMPton TELEscope aboard CGRO and operates in the 0.75-30 MeV energy interval. It has an energy resolution of about 5-10% FWHM, a large field of view of about 1 steradian and a location accuracy of $\sim 1^{\circ}$. The Energetic Gamma Ray Experiment Telescope (EGRET), co-aligned with COMPTEL, is sensitive to γ -rays with energies in the range 30 MeV to 30 GeV. Its field of view is 80° in diameter in its normal operation mode, while the energy resolution is about 20% (FWHM). The angular resolution (67% confinement angle) is strongly energy dependent: $10^{\circ}9$ at 35 MeV and $0^{\circ}5$ at 3 GeV. All four CGRO instruments are served by the same on-board clock, the timestamps of which are converted to Coordinated Universal Time (UTC) with an absolute accuracy better than $100\mu s$. The high-energy in-

struments EGRET and COMPTEL have performed the first all-sky survey at medium and high γ -ray energies during the first 1.5 year of the mission.

At the end of the operational phase of CGRO in May 2000 (nine observation Cycles have been performed) the number of γ -ray pulsars has increased from 2 to 7 particularly due to EGRET measurements. The EGRET team discovered pulsed high-energy γ -ray emission of Geminga (Bertsch et al. 1992; Mayer-Hasselwander et al. 1994; Mattox et al. 1998; Fierro et al. 1998), PSR B1706-44 (Thompson et al. 1992; Thompson et al. 1996), PSR B1055-52 (Fierro et al. 1993; Thompson et al. 1999) and PSR B1951+32 (Ramanamurthy et al. 1995) and confirmed high-energy γ -ray emission from the Crab (Nolan et al. 1993; Fierro et al. 1998) and Vela (Kanbach et al. 1994; Fierro et al. 1998) pulsars.

Emission from the latter two pulsars has also been detected at soft and medium γ -ray energies by COMPTEL and OSSE. For Vela this meant the first secure detection at energies smaller than ~ 30 MeV.

Pulsed emission from PSR B1509-58 is only significantly detected up to ~ 10 MeV by BATSE (Wilson et al. 1993), OSSE (Ulmer et al. 1993; Matz et al. 1994) and COMPTEL (Kuiper et al. 1999; see also Chapter 4 of this thesis).

For three other radio pulsars, PSR B0656+14 (Ramanamurthy et al. 1996), PSR B1046-58 (Kaspi et al. 2000) and millisecond pulsar PSR J0218+4232 (Kuiper et al. 2000a) good indications were found. The circumstantial evidence for pulsed 100-1000 MeV emission from PSR J0218+4232 is presented extensively in Chapter 9 of this thesis and this would mean the first detection of pulsed high-energy γ -rays from a millisecond pulsar.

In summary, the number of definite γ -ray pulsar detections at high-energies γ -rays ($\gtrsim 100$ MeV) increased from 2 to 6, while at soft/medium γ -ray energies (0.1-30 MeV) the number of firm detections increased from 1 to 3.

A significant contribution at medium γ -ray energies has been made by COMPTEL, the Compton Telescope aboard CGRO. This thesis work contributed to the search for pulsed signals in the COMPTEL data since launch. Pulsed γ -ray emission (0.75-30 MeV) has been detected from the Crab pulsar (Much et al. 1995, Kuiper et al. 2000b), Vela (Hermsen et al. 1993; Kuiper et al. 1998a) and PSR B1509-58 (Hermsen et al. 1994, Carramiñana et al. 1995; Kuiper et al. 1999), while good indications for pulsed emission have been found for PSR B1951+32 (Carramiñana et al. 1995, Hermsen et al. 1997, Kuiper et al. 1998b) and indications for Geminga (Kuiper et al. 1996), PSR B0656+14 (Hermsen et al. 1997) and PSR B1055-52 (Thompson et al. 1999).

With only ~ 10 detections above 1 MeV listed above the current status of pulsar research at γ -ray energies can be summarized as follows: a wide diversity in both pulse shapes and in spectral distributions is present in the small

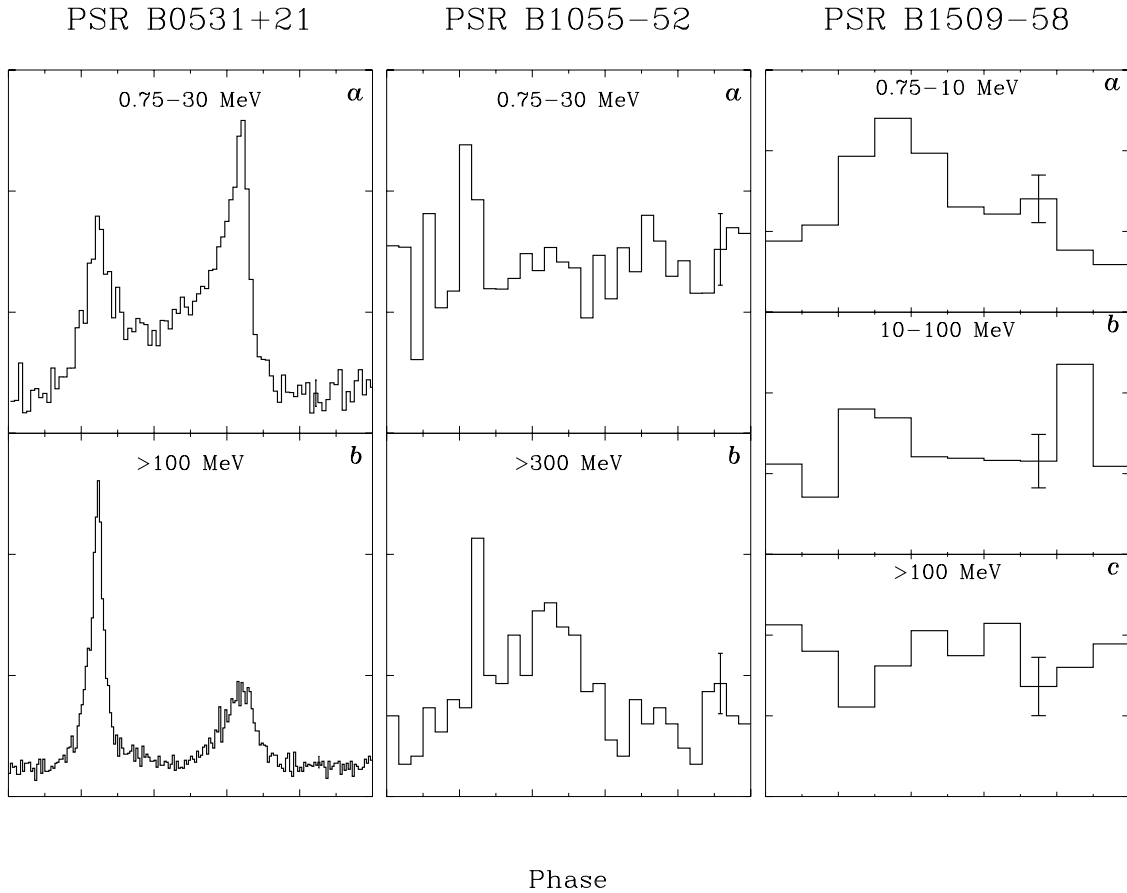


Fig. 1.2. Examples of different morphologies of γ -ray pulse profiles: PSR B0531+21 (Crab pulsar, left panel), a double pulse profile at medium and high-energy γ -rays; PSR B1055-52 (middle panel), a complex profile at high-energy γ -rays, no significant pulsed signal at medium γ -ray energies, possibly a $\sim 3 - 4\sigma$ detection in phase with a narrow high-energy pulse; PSR B1509-58 (right panel), a broad asymmetric profile below 10 MeV (similar to the X-ray/soft γ -ray profiles), no firm detection above 10 MeV. Typical error bars are indicated.

sample of spin-down powered pulsars and a coherent picture can *not* be constructed.

The γ -ray pulses are all out of phase with the radio pulses except for the Crab pulsar where alignment is maintained from radio frequencies up to high-energy γ -rays. Often double pulse phase distributions are observed, like for the Crab, Vela, PSR B1951+32 and Geminga, with phase separations in the range 0.4-0.5 and mostly accompanied with significant interpulse emission. However, the pulse profiles of PSR B1706-44 and PSR B1055-52 are more complex and seem to be composed of 2 or more closely separated pulses forming together a relatively broad complex profile. The pulse profile of PSR B1509-58, detected significantly only below 10 MeV and exhibiting a broad asymmetric shape, can also be described in terms of 2 narrowly separated pulses. The diversity in these pulse profiles is illustrated in the 3 panels of Fig. 1.2.

An impression of the diversity in spectral behaviour can also be obtained from the 3 panels of Fig. 1.2, e.g. PSR B1509-58 (right panel) reaches a maximum luminos-

ity (power per logarithmic energy interval) in the 0.75-10 MeV range (frame a), but is undetected at energies above 100 MeV (frame c; see for details Chapter 4), while PSR B1055-52 (middle panel) reaches a maximum luminosity at high-energy γ -rays (frame b) with no significant emission at medium energy γ -rays (frame a). In the latter case there is an indication ($\sim 3 - 4\sigma$) at medium energy γ -rays for an enhancement coincident in phase with a high-energy γ -ray pulse (see Thompson et al. 1999). The morphology changes in the pulse profiles as a function of energy displayed in the 3 panels of Fig. 1.2 are all manifestations of different spectral behaviour as a function of phase.

Other properties of the small sample of firm γ -ray pulsars are e.g. the existence of a high-energy spectral cutoff in the GeV energy range (except for PSR B1951+32 breaking at higher energies and PSR B1509-58 which has a cutoff energy near $\sim 10 - 30$ MeV) and the stability of the pulsed flux as a function of time. One striking correlation has been revealed in this small sample of γ -ray pulsars: the γ -ray efficiency increases with the pulsar characteristic age.

The older pulsars can emit γ -rays very efficiently at several percentages of the total spin-down power output. For an overview of the characteristics of the γ -ray pulsars see Thompson et al. (1997).

Considering now the energetics of a spin-down powered pulsar it is interesting to note that the energy released in the form of radio waves is just a tiny fraction of the total spin-down energy loss and does not play an important role in the energy house keeping of the system. At soft X-rays the efficiency of converting spin-down energy into soft X-rays is about 0.1% irrespective the nature of the pulsar, normal or millisecond, and this also is not an impressive number. At (high-energy) γ -rays this efficiency, however, is in the range 0.1% - 10% and energy release in the form of γ -rays, especially for the older pulsars, can become an important energy loss channel. In particular, studying the high-energy radiation from spin-down powered pulsars can provide important information on the production sites of the high-energy radiation and on the non-thermal radiative processes in the pulsar magnetosphere. The dominant energy loss mechanism, however, remains the energy loss in the form of relativistic particle outflow (pulsar wind) from the open field line zone in the pulsar magnetosphere.

1.2. Outline of this thesis

This thesis has been divided in two distinct but related parts. In the first part the emission characteristics at medium γ -ray energies based on COMPTEL 0.75-30 MeV data are presented for a number of normal ($p > 15$ ms) spin-down powered pulsars, viz. Geminga, PSR B1951+32 both with characteristic age $> 10^5$ year, and PSR B1509-58 and PSR B0531+21 (the Crab pulsar) both with age $< 10^5$ year. The particular choice of analyzing these pulsars in detail is not fortuitous, but based on a ranking scheme in which the spin-down flux is used as a γ -ray observability measure. The pulsars mentioned above are located at the top in such a ranking scheme and are all firmly detected as γ -ray pulsars at high γ -ray energies (Crab, PSR B1951+32, Geminga) or at soft γ -ray energies (PSR B1509-58) indicating that this simple (conversion efficiency of spin-down power to γ -ray luminosity is put to 1) priority scheme is a useful one. The reported findings are the result of combining many separate COMPTEL observations and are often discussed in a much wider context by including also the results from other high-energy instruments sensitive in other X-ray/ γ -ray windows.

The small intrinsic signal strength in combination with a huge time variable background make source detections by COMPTEL in general very difficult. Moreover, the complex response (four dimensional) and required background modelling complicate the data analysis severely. Only for the Crab pulsar (0.75-10 MeV) and to a lesser extent for the Vela pulsar (10-30 MeV) pulsed emission can be detected in one single observation typically lasting for 2 weeks, adopting the timing parameters obtained contemporaneously from radio timing programs. The simple use

of just one set of timing parameters for a particular pulsar (one trial) avoids a period search in the time domain, which would certainly have made any pulsed signal detection hopeless taking into account the number of trials required for a meaningful search. The intrinsic weakness of the γ -ray pulsar candidates and high background mean that data collected over various observation periods with the source in the field of view ($\sim 60^\circ$ diameter for COMPTEL) should be combined in order to achieve maximal statistics.

Chapters 2 – 5 deal with the COMPTEL results obtained by applying such an approach for the high-energy γ -ray pulsar Geminga combining COMPTEL Cycle 0-III observations, PSR B1951+32 combining Cycle 0-VI observations, PSR B1509-58 combining also Cycle 0-VI observations and finally for the Crab pulsar combining Cycle 0-IX observations. During the COMPTEL mission we improved analysis methods and instrumental response descriptions. At the epoch of data analysis for a particular pulsar the then most recent versions for the response characteristics and software analysis tools were used. This means that the paper presenting the COMPTEL Geminga results (Chapter 2) was based on a limited part of the finally available database and can therefore now be considered as a status report, while the results for the other pulsars, particularly the Crab pulsar, represent final COMPTEL results.

The second part is fully devoted to the presentation of the high-energy properties from soft X-rays up to high-energy γ -rays of the binary millisecond pulsar PSR J0218+4232, a recycled spin-down powered pulsar. This initiative was triggered by our finding of a potential association of the pulsar with a high-energy EGRET source 2EG J0220+4228 (Thompson et al. 1995). For the analysis we benefitted from the developed timing/imaging analysis tools available for the complex COMPTEL data analysis.

1.2.1. Part I: High-energy emission from normal pulsars at medium γ -ray energies

In Chapter 2 the results of a search for MeV emission from Geminga are presented using COMPTEL 0.75-30 MeV data collected over observation Cycles 0-III (time span ~ 4 years). No firm detection of Geminga at MeV energies can be claimed, although some indications are present at energies above 3 MeV.

Chapter 3 deals with an extensive analysis of COMPTEL data for PSR B1951+32 collected over 6 CGRO observation cycles, including the analysis of the simultaneously collected EGRET data. The detection of this pulsar as a firm high-energy γ -ray pulsar was announced by Ramanamurthy et al. (1995) using EGRET high-energy γ -ray data, although Carramiñana et al. (1995) reported somewhat earlier a marginally significant detection of this pulsar at medium γ -ray energies using Cycle 1-2 COMPTEL data. As shown in Chapter 3, an improved analysis increased the evidence for a detection in Cycle 1-2 to an acceptable $\sim 4\sigma$ level, but the addition of more COMPTEL data collected

during Cycles 3-6 did not corroborate the pulsed MeV signal. It is, however, shown through extensive pulsed signal simulations that it is statistically possible to obtain a $\sim 4\sigma$ pulsed signal during Cycles 1-2 followed by a non-detection in the combination of Cycle 3-6 data for a genuine signal close to the detection threshold.

In Chapter 4 the firm detection of PSR B1509-58 as MeV γ -ray pulsar is reported for the first time using Cycle 1-6 COMPTEL data. The COMPTEL findings are put in a broader context by including the analysis results for CGRO EGRET at energies above 30 MeV and other X-ray/soft γ -ray instruments for energies below 0.75 MeV.

Finally, in Chapter 5 the MeV characteristics of the Crab pulsar are presented using almost all available COMPTEL data (Cycle 0-IX). A complete high-energy picture (0.1 keV-10 GeV) of the Crab pulsar and nebula is given predominantly based on data from BeppoSAX (0.1-300 keV), CGRO COMPTEL (0.75-30 MeV) and CGRO EGRET (30 MeV - 10 GeV).

1.2.2. Part II: High-energy emission from recycled pulsars: the case PSR J0218+4232

In Chapter 6 the detection of an X-ray source positionally consistent with the binary millisecond pulsar PSR J0218+4232 is reported in a 20 ks ROSAT HRI (0.1-2.4 keV) observation, while indications were found for pulsed signals at both X-rays and γ -rays using archival EGRET data. The subsequent definite detection of pulsed soft X-ray emission in a 100 ks ROSAT HRI follow-up observation is the topic of Chapter 7. The spectral and timing properties of PSR J0218+4232 at soft/medium X-ray energies (1-10 keV) had been derived from a 83 ks BeppoSAX MECS observation and the findings are presented in detail in Chapter 8. Finally, in Chapter 9 circumstantial evidence is presented for the detection of pulsed high-energy radiation (100-1000 MeV) from PSR J0218+4232 in the combination of several CGRO EGRET observations. A comparison has been made between the radio, X-ray and γ -ray pulse profiles (for the radio and γ -ray profiles this was done in absolute timing). We consider this pulsar as the *first* millisecond pulsar showing its pulsed signature at high-energy γ -rays.

References

Becker W., Trümper J., 1997, A&A 326, 682
 Bennett K., Bignami G.F., Boella G., et al., 1977, A&A 61, 279
 Bertsch D.L., Brazier K.T.S., Fichtel C.E., et al., 1992, Nat 357, 306
 Carramiñana A., Bennett K., Buccheri R., et al., 1995, A&A 304, 258
 Clear J., Bennett K., Buccheri R., et al., 1987, A&A 174, 85
 Cocke W.J., Disney M.J., Taylor D.J., 1969, Nat 221, 525
 Fierro J.M., Bertsch D.L., Brazier K.T., et al., 1993, ApJ 413, L27
 Fierro J.M., Michelson P.F., Nolan P.L., et al., 1998, ApJ 494, 734
 Fritz G., Henry R.C., Meekins J.F., et al., 1969, Sci 164, 709
 Gouiffes C., 1998, In: Neutron Stars and Pulsars, eds. Shibasaki N., Kawai N., Shibata S. and Kifune T., 363

Graser U., Schönfelder V., 1982, ApJ 263, 677
 Grenier I.A., Hermsen W., Clear J., 1988, A&A 204, 117
 Hermsen W., Bloemen H., Kuiper L., et al., 1993, In: Compton Gamma-Ray Observatory, AIP Conf. Proc. 280, eds. Friedlander M., Gehrels N. and Macomb D.J., 204
 Hermsen W., Kuiper L., Diehl R., et al., 1994, ApJS 92, 559
 Hermsen W., Kuiper L., Schönfelder, et al., 1997, In: The Transparent Universe, ESA-SP-382, eds. Winkler et al., 287
 Hewish A., Bell S.J., Pilkington J.D.H., et al., 1968, Nat 217, 709
 Kanbach G., Arzoumanian Z., Bertsch D.L., et al., 1994, A&A 289, 855
 Kaspi V.M., Lackey J.R., Mattox J., et al., 2000, ApJ 528, 445
 Kniffen D.A., Hartman R.C., Thompson D.J., et al., 1974, Nat 251, 397
 Kuiper L., Hermsen W., Bennett K., et al., 1996, A&AS 120, 73
 Kuiper L., Hermsen W., Schönfelder V., et al., 1998a, In: The many face of neutron stars, NATO ASI Series C Vol. 515, eds. Buccheri R., Van Paradijs J. and Alpar M.A., 211
 Kuiper L., Hermsen W., Bennett K., et al., 1998b, A&A 337, 421
 Kuiper L., Hermsen W., Krijger J.M., et al., 1999, A&A 351, 119
 Kuiper L., Hermsen W., Verbunt F., et al., 2000a, A&A 359, 615
 Kuiper L., Hermsen W., Cusumano G., et al., 2000b, A&A submitted
 Large M.I., Vaughan A.E., Mills B.Y., 1968, Nat 220, 340
 Mattox J.R., Halpern J.P., Caraveo P.A., 1998, ApJ 493, 891
 Matz S.M., Ulmer M.P., Grabelsky D.A., et al., 1994, ApJ 434, 288
 Mayer-Hasselwander H.A., Bertsch D.L., Brazier K.T.S., et al., 1994, ApJ 421, 276
 Much R., Bennett K., Buccheri R., et al., 1995, A&A 299, 435
 Middleditch J., Pennypacker C., 1985, Nat 313, 659
 Mignani R., Caraveo P.A., Bignami G.F., 1997, ApJ 474, L51
 Nolan P.L., Arzoumanian Z., Bertsch D.L., et al., 1993, ApJ 409, 697
 Pavlov G.G., Stringfellow G.S., Córdoba F.A., 1996, ApJ 467, 370
 Ramanamurthy P.V., Bertsch D.L., Dingus B.L., et al., 1995, ApJ 447, L109
 Ramanamurthy P.V., Fichtel C.E., Kniffen D.A., et al., 1996, ApJ 458, 755
 Shearer A., Redfern R.M., Gorman G., et al., 1997, ApJ 487, L181
 Shearer A., Golden A., Harfst S., et al., 1998, A&A 335, L2
 Staelin D.H., Reifenstein E.C., 1968, Sci 162, 1481
 Strickman M.S., Grove J.E., Johnson W.N., et al., 1996, ApJ 460, 735
 Taylor J.H., Wolszczan A., Damour T., et al., 1992, Nat 355, 132
 Taylor J.H., Manchester R.N., Lyne A.G., et al., 1995, Unpublished work
 Thompson D.J., Fichtel C.E., Kniffen D.A., et al., 1975, ApJ 200, L79
 Thompson D.J., Fichtel C.E., Hartman R.C., et al., 1977a, ApJ 213, 252
 Thompson D.J., Fichtel C.E., Kniffen D.A., et al., 1977b, ApJ 214, L17
 Thompson D.J., Arzoumanian Z., Bertsch D.L., et al., 1992, Nat 359, 615
 Thompson D.J., Bertsch D.L., Dingus B.L., et al., 1995, ApJS 101, 259
 Thompson D.J., Bailes M., Bertsch D.L., et al., 1996, ApJ 465, 385
 Thompson D.J., Bailes M., Bertsch D.L., et al., 1999, ApJ 516, 297

- Thompson D.J., Harding A.K., Hermsen W., et al., 1997, In: Dermer C.D., Strickman M.S., Kurfess J.D. (eds.), AIP Conf. Proc. 410, 39
- Tümer O.T., Dayton B., Long J., et al., 1984, Nat 310, 214
- Ulmer M.P., Matz S.M., Wilson R.B., et al., 1993, ApJ 417, 738
- Ulmer M.P., Lomatch S., Matz S.M., et al., 1994, ApJ 432, 228
- van den Heuvel, 1991, In: Neutron Stars: Theory and Observation, NATO ASI Series C Vol. 344, eds. Ventura J. and Pines D., 171
- van Paradijs, 1995, In: X-ray binaries, Cambridge Astrophysics Series 26, eds. Lewin W.H.G, van Paradijs J, van den Heuvel E.P.J., 536
- Wagner S.J., Seifert W., 2000, In: Pulsar Astronomy – 2000 and beyond, IAU Coll. 177, ASPC Ser. Vol. 202, eds. Kramer M., Wex N. and Wiełebinski R., 315
- Wallace P.T., Peterson B.A., Murdin P.G., et al., 1977, Nat 266, 692
- Wills R.D., Bennett K., Bignami G.F., et al., 1982, Nat 296, 723
- Wilson R.B., Fishman G.J., Finger M.H., et al., 1993, In: Friedlander M., Gehrels N., Macomb D. (eds.), AIP Conf. Proc. 280, 291

Part I

High-energy radiation from normal pulsars
at medium γ -ray energies

Chapter 2

Search in the COMPTEL data for MeV-emission from Geminga

L. Kuiper², W. Hermsen², K. Bennett⁴, A. Connors³, R. Much⁴, J. Ryan³, V. Schönfelder¹, and A. Strong¹

¹ Max-Planck Institut für Extraterrestrische Physik, D-8046 Garching, Germany

² SRON-Utrecht, Sorbonnelaan 2, 3584 CA Utrecht, The Netherlands

³ Space Science Centre, University of New Hampshire, Durham, NH 03824, U.S.A.

⁴ Astrophysics Division, European Space Research and Technology Centre, 2200 AG Noordwijk, The Netherlands

Astron. Astrophys. Suppl. Ser. 120, 73-76 (1996)

Abstract. Results are presented of a search for MeV-emission from Geminga using all available 0.75-30 MeV data gathered by the imaging Compton telescope COMPTEL between April 1991 and September 1994. Timing analysis yields a negative result in the search for pulsed emission in the 0.75-30 MeV range. A more sensitive method, which produces images for various pulsar-phase selected components and for the total emission yielded in the 3-10 MeV range an indication for emission mainly coming from an interpeak component, called I2. This is the softest component observed by EGRET and COS-B and was therefore the most promising one in the COMPTEL domain. The time-averaged fluxes and 2σ upper-limits estimated for the total emission and for 4 defined phase components do not require a break in the spectra extrapolated from EGRET measurements. Spatial analysis using all available Anti-Centre data for different energy ranges reveals evidence for other sources than the Crab. This is shown for the 10-30 MeV range.

2.1. Introduction

After its detection by SAS-2 (Kniffen et al. 1975; Thompson et al. 1977) and subsequent confirmation by COS-B (Bennett et al. 1977; Masnou et al. 1981) the nature of the high-energy gamma-ray source Geminga remained a mystery for a long time. There were early indications for a rotating neutron star nature (Halpern & Tytler 1988; Grenier et al. 1991), but the true nature of the source was finally revealed by the discovery of soft X-ray pulsations from the X-ray candidate counterpart 1E 0630+178 in the ROSAT 0.1-2 keV data (Halpern & Holt 1992). The 237 ms periodicity found in the X-ray data was also clearly apparent in the high-energy gamma-ray data from EGRET (Bertsch et al. 1992). Using the EGRET data alone it was even possible to determine the period derivative. Extrapolation of the derived ephemeris back to the COS-B and SAS-2 epoch (Bignami & Caraveo 1992;

Hermsen et al. 1992; Mattox et al. 1992) revealed the pulsed signal in the data from both previous experiments, implying that its rotational behaviour is extremely stable.

Its emission characteristics in both the X-ray and gamma-ray energy range make it plausible that we are dealing with an isolated *nearby* rotating neutron star. Recent distance estimates using the Hubble Space Telescope (Caraveo et al. 1996) put Geminga at ~ 160 pc. The lack of counterparts at radio-wavelengths (Seiradakis 1992; Spoelstra & Hermsen 1984) is probably caused by a misalignment of the radio- and gamma-ray emission cones.

Detailed analysis of EGRET data (Mayer-Hasselwander et al. 1994) showed that its phase averaged high-energy gamma-ray emission 30 MeV – 2 GeV can be described by a power law with spectral index of -1.50 ± 0.08 , slightly harder than found in the COS-B data (Grenier et al. 1993) which yielded a 'best' fit single power law with an index of -1.84 ± 0.05 for photon energies between 50 MeV and 5 GeV. The COS-B data, however, indicate that a two-power-law function with a spectral break near 140 MeV significantly improves the fit. Evidence for this spectral break near 140 MeV is not present in the EGRET data. According to Grenier et al. (1994) several components in the lightcurve could be identified - denoted as Peak 1 (P1), Interpeak 1 (I1), Peak 2 (P2) and Interpeak 2 (I2) - each with their own time variability (over time scales of months to years) and spectral shape. In particular the extremely soft I2 component showed strong time variable behaviour. The EGRET data (Mayer-Hasselwander et al. 1994) did not confirm this time variable behaviour in the separate phase components during the first 2 months of the CGRO mission. A recent study on the long-term high-energy gamma-ray emission properties of the Crab, Vela and Geminga pulsars (Ramanamurthy et al. 1995) indicates that Geminga does exhibit long time scale spectral variability for energies above 100 MeV.

In the low- and medium gamma-ray energy range (0.01-10 MeV) no emission had been detected from Geminga by

the space-borne instruments SIGMA (Lebrun et al. 1991), BATSE (Wilson et al. 1992), OSSE (Strickman et al. 1995) and COMPTEL (Strong et al. 1993). For the latter, a $\sim 3\sigma$ indication was reported by Hermsen et al. (1994). Another indication (2.8σ) for pulsed emission was seen in the data of the ballon-borne FIGARO II experiment for the 0.15-0.48 MeV energy range based on an exposure of only 7 hours.

Present work summarizes the search for Geminga in the COMPTEL data for the first ~ 3.5 years of the CGRO mission.

2.2. Instrument and analysis techniques

The instrument consists of two detector layers, an upper layer (D1) and a lower layer (D2). Its detection principle is based on a two layer interaction : an incoming gamma-ray photon Compton scatters in a detector module of D1, while the scattered photon has another interaction in one of the D2 modules. The interaction loci in the involved D1 and D2 modules determine the direction of the scattered photon, which is specified as (χ, ψ) . From the energy deposits in the D1 - module, E_1 , and D2- module, E_2 , it is possible to determine the scatter angle $\overline{\varphi}$ and the total energy deposit $E_{tot} (= E_1 + E_2)$. The measured quantities $(\chi, \psi, \overline{\varphi}, E_{tot})$ constitute a 4-dimensional dataspace, in which we have to search for a "source signature". In practice the dimension of the dataspace is lowered by assuming a certain spectral shape of the sources to be searched for. The source signature (the Point Spread Function) in this reduced 3-d dataspace $(\chi, \psi, \overline{\varphi})$ is cone-shaped with its apex at the source position (χ_0, ψ_0) .

If a source position is a priori known it is also possible to determine the geometrical scatter angle φ_{geo} of an event from its scatter direction and the source direction. The difference angle (φ_{arm}) between $\overline{\varphi}$ and φ_{geo} is known as ARM (Angular Resolution Measure) angle and the ARM-distribution of the events in a background free environment is a narrowly peaked distribution at $\varphi_{arm} = 0$.

The search for sources in the previously mentioned 3-d dataspace is performed by applying a maximum likelihood analysis at each position in the COMPTEL field of view. Quantitative information on the detection significance and source position can be derived by the determination of a maximum likelihood ratio of two hypotheses \mathcal{H}_0 and \mathcal{H}_1 . In the zero hypothesis \mathcal{H}_0 the likelihood \mathcal{L}_0 is maximized for the case that the data are described by a background distribution alone (source contribution fixed at 0), while in the alternative hypothesis the likelihood \mathcal{L}_1 is maximized for a data description in terms of a background distribution and a point source. The quantity $-2 \ln(\mathcal{L}_0^{\max}/\mathcal{L}_1^{\max})$ behaves like a χ^2 -distribution for large sample sizes (see de Boer 1992). The background distribution has been determined from the data themselves using a smoothing method similar to that described in Bloemen et al. (1994). This complicates the classical interpretation of source detection significances because we are not dealing with an *independent* background

estimate. Extensive simulations have been performed to calibrate the likelihood method as used in the current analysis.

More detailed information about the instrument and its performance can be found in Schönfelder et al. (1993).

2.3. Observations

In this study all the COMPTEL observations between 28 April 1991 and 29 August 1994 have been used in which Geminga was less than 35° from the instrument z-axis. The CGRO viewing periods (VP) used in this study were 0.3-0.5, 1, 31, 36.0, 36.5, 39, 41, 44, 213, 221, 310, 321.1, 321.5 and 337. Although also VP 2.5 satisfies the aspect constraint, it was a target of opportunity observation of the Sun with the instrument set in a special mode, making its response interpretation more complicated. The data from this period were not included in the current analysis.

2.4. Timing analysis

The arrival times of the events at the spacecraft were recorded with an intrinsic resolution of 0.125 ms, sufficiently accurate for pulsar timing analysis. Before a timing analysis of COMPTEL data is performed the events were subjected to several selection criteria to reduce the background, including an ARM selection using the a priori known position of Geminga. An ARM selection of $|\varphi_{arm}| \leq 3^\circ$ turned out to be optimal, verified for the established MeV gamma-ray pulsars (Crab and Vela).

The arrival times of the selected events were transformed to arrival times at the Solar System Barycentre (SSB) using the known instantaneous spacecraft position, the source position and the solar system ephemeris (JPL DE200 Solar System Ephemeris). The pulse phase ϕ is calculated from :

$$\phi = \nu \cdot \Delta t + 1/2 \cdot \dot{\nu} \cdot \Delta t^2 + 1/6 \cdot \ddot{\nu} \cdot \Delta t^3 - \phi_0$$

in which $\Delta t = t^e - t^0$ with t^e the event SSB arrival time and t^0 the reference epoch. The values employed here for t^0 , ν , $\dot{\nu}$, $\ddot{\nu}$, ϕ_0 are given in Mattox et al. (1994).

Lightcurves (phase histograms) for the "standard" energy ranges 0.75-1 MeV, 1-3 MeV, 3-10 MeV and 10-30 MeV have been produced for the combination of all the observations mentioned above. The significance for a deviation from a statistically flat distribution has been determined using the Z_n^2 -test statistic (Buccheri et al. 1983). The significances for pulsed emission in the case of three harmonics are for all 4 energy intervals below 3σ , indicating that *no pulsed emission* has been detected from Geminga. A search for pulsed emission has also been performed for the individual observations when the aspect angle of Geminga was less than 20° . Also for these individual observations the search yields a negative result. The only case in which a result of about 3σ significance was obtained was for the 10 – 30 MeV range during observation period 0.3-0.5 (Hermsen et al. 1994). If this emission is genuine then it

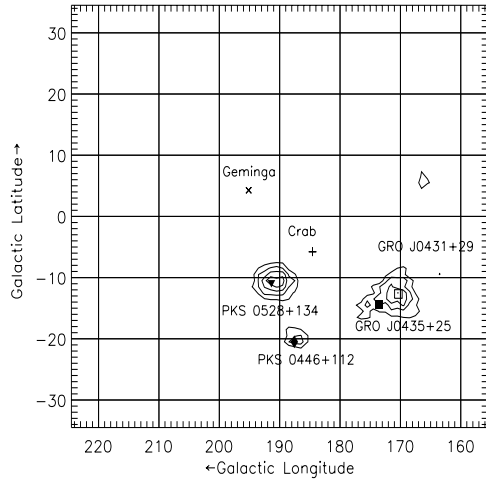


Fig. 2.1. COMPTEL 10-30 MeV MLR map of the Anti-Centre. Contour values start at 6 with stepsize 3. A value of 9 is equivalent with a $3\text{-}\sigma$ detection for a single trial. The Crab source has been subtracted.

seems to originate from the I2 part of the lightcurve defined in the analysis of COS-B data (Grenier et al. 1994).

2.5. Spatial analysis

2.5.1. Total spectrum

Because of the proximity of the Crab, which is the strongest source in the MeV domain, it is essential to properly incorporate its signature in the COMPTEL 3-d dataspace when searching for other potential candidate sources in the Anti-Centre. After sorting the events in the 4 standard energy intervals, a maximum likelihood analysis is applied to the various event sets taking care that the Crab is properly included in the background. This analysis yields simultaneously the detection significance and flux. An example of a resulting Maximum Likelihood Ratio (MLR) map is given in Fig. 2.1. Visible in this 10-30 MeV map is the positive signal of PKS 0528+134, PKS 0446+112 and a double structure consistent with 2 unidentified EGRET sources GRO J0431+29 and GRO J0435+25. However, there is no trace of Geminga.

Three 2σ -UL's and one flux value for the 4 standard energy ranges derived at the position of Geminga are shown in Fig. 2.2 along with the EGRET spectral points and spectral fit as given in Mayer-Hasselwander et al. (1994). The single flux value represents a weak excess ($\sim 2.3\sigma$) consistent in position with Geminga in the 3-10 MeV band. Selecting slightly different subsets of VP's as listed in Sect. 2.3 this excess sometimes exceeds 4σ significance. For example, Fig. 2.3 shows the 3-10 MeV MLR map for the combination of VP 1, 41, 44, 213, 221, 310 and 321.1/5. The apparent significant detection suggests time variable behaviour at MeV energies.

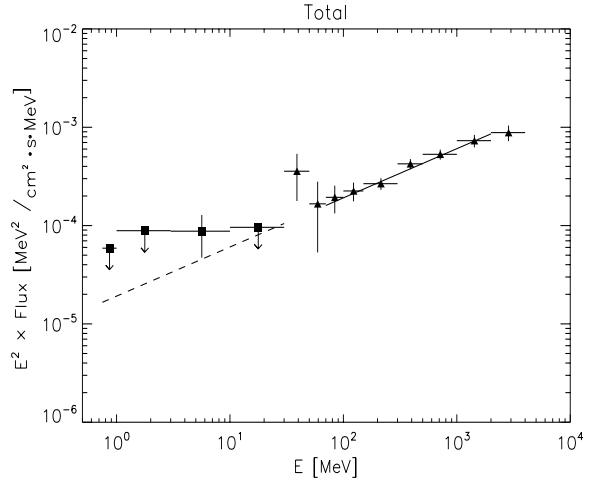


Fig. 2.2. EGRET (triangles; Mayer-Hasselwander et al. 1994) and time-averaged COMPTEL (squares) Geminga spectrum.

2.5.2. Spectra for different phase components

The events are subsequently sorted on both energy and pulse phase. For consistency the phase definitions as given by Mayer-Hasselwander et al. (1994) have been employed in this study (however, the boundaries of the 4 defined components (P1,I1,P2 and I2) are relative to the centre of peak-1). The results from the Likelihood analysis described above, but now for the 4 phase components are given in Tab. 2.1. If these flux values are combined with the EGRET flux values then it turns out that the COMPTEL 2σ UL's do not constrain the extrapolations of EGRET fits into the COMPTEL domain. Also, the indication found in the total 3-10 MeV map can primarily be ascribed to events from the I2 component.

Table 2.1. Phase-averaged flux values measured at the Geminga position for the different components. Flux values in units : 10^{-6} ph / cm^2s

	0.75-1 MeV	1-3 MeV	3-10 MeV	10-30 MeV
P1	-7.0 ± 5.5	$+0.8 \pm 8.0$	-2.9 ± 3.3	-0.6 ± 1.2
I1	-6.8 ± 9.3	$+9.4 \pm 13.6$	$+7.7 \pm 6.3$	-2.4 ± 2.2
P2	-8.5 ± 5.5	$+2.4 \pm 8.0$	$+4.3 \pm 3.9$	$+0.8 \pm 1.4$
I2	-2.5 ± 9.8	$+17.2 \pm 13.6$	$+16.8 \pm 6.3$	$+0.8 \pm 2.2$
All	-27.5 ± 15.0	$+32.0 \pm 22.0$	$+23.8 \pm 10.5$	-1.4 ± 3.6

2.6. Summary and Discussion

Employing the imaging capabilities of COMPTEL we have performed a deep search for MeV emission from Geminga. Indication for emission from Geminga has been found only in the 3-10 MeV range, mainly for events detected in the interpeak interval I2 of the phase his-

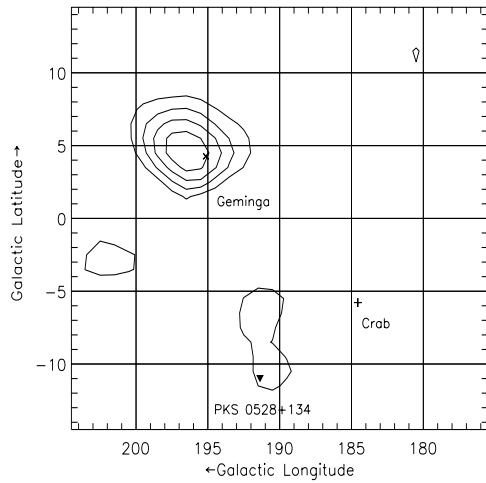


Fig. 2.3. COMPTEL 3-10 MeV Anti-Centre map using a subset of VP's. Contour values start at 9 with stepsize 3. See also caption Fig. 2.1.

togram. Such a hint was previously reported for the 10-30 MeV interval for the first COMPTEL observations of Geminga (Hermsen et al. 1994). It is interesting to note that the emission measured in this interval by EGRET (Mayer-Hasselwander et al. 1994) and COS-B (Grenier et al. 1994) represents the softest component of the lightcurve. The COMPTEL data do not require a spectral break in the COMPTEL domain extrapolating the EGRET spectra. In view of the observed long-term time-variability of the high-energy gamma-ray emission (Grenier et al. 1994, Ramanamurthy et al. 1995) and the suggestion at MeV energies (Fig. 2.3) future studies with COMPTEL remain important.

This study showed evidence for additional Anti-Centre sources. For example, the 10-30 MeV MLR map shown in Sect. 2.5.1 revealed evidence for PKS 0528+134, PKS 0446+112 and 2 unidentified EGRET sources. It should be noted that due to the combination of all data transient events (such as the flaring of PKS 0528+134) are suppressed in favour of steady sources.

Acknowledgements. The COMPTEL project is supported by NASA under contract NAS5-26645, by the Deutsche Agentur für Raumfahrtangelegenheiten (DARA) under grant 50 QV 90968 and by the Netherlands Organisation for Scientific Research (NWO).

References

- Bennett K., et al., 1977, A&A 56, 469
 Bertsch D.L., et al., 1992, Nat 357, 306
 Bignami G.F., Caraveo P.A., 1992, Nat 357, 287
 Caraveo P.A., et al., 1996, A&AS, This Volume
 Bloemen H., et al., 1994, ApJS 92, 419
 Buccheri R., et al., 1983, A&A 128, 245
 de Boer H., 1992, in: Data Analysis in Astronomy IV, Di Gesù, et al. (eds.). Plenum, New York, p. 241

- Grenier I.A., et al., 1991, Adv.Space Res. 11, (8)107-110
 Grenier I.A., et al., 1993, A&A 269, 209
 Grenier I.A., et al., 1994, ApJS 90, 813
 Halpern J.P., Holt S.S., 1992, Nat 357, 222
 Halpern J.P., Tytler D., 1988, ApJ 330, 201
 Hermsen W., et al., 1992, IAU Circ. 5541
 Hermsen W., Kuiper L., et al., 1994, ApJS 92, 559
 Kniffen D.A., et al., 1975, Proc. 14th Internat. Cosmic Ray Conf. 1,100 (Munich)
 Lebrun F., et al., 1991, Proc. 22th Internat. Cosmic Ray Conf. 1,165 (Dublin)
 Masnou J.L., et al., 1981, Proc. 17th Internat. Cosmic Ray Conf. 1,177 (Paris)
 Mattox J.R., et al., 1992, ApJ 401, L23
 Mattox J.R., et al., 1994, Proc. AIP Conf. 304, 77
 Mayer-Hasselwander H.A., et al., 1994, ApJ 421, 276
 Ramanamurthy P.V., et al., 1995, ApJ 450, 791
 Seiradakis J.H., 1992, IAU Circ. 5532
 Spoelstra T.A.Th., Hermsen W., 1984, A&A 135, 135
 Schönfelder V., et al., 1993, ApJS 86, 657
 Strickman M.S., et al., 1995, submitted to ApJ
 Strong A.W., et al., 1993, A&AS 97, 133
 Thompson D.J., et al., 1977, ApJ 213, 252
 Wilson R.B., et al., 1992, Proc. AIP conf. 280, 291 (St.Louis)

Chapter 3

Detection of pulsed MeV emission from PSR B1951+32 by COMPTEL

L. Kuiper², W. Hermsen², K. Bennett⁴, A. Carramiñana⁵, A. Lyne⁶, M. McConnell³, and V. Schönfelder¹

¹ Max-Planck Institut für Extraterrestrische Physik, D-8046 Garching, Germany

² SRON-Utrecht, Sorbonnelaan 2, NL 3584 CA Utrecht, The Netherlands

³ Space Science Centre, University of New Hampshire, Durham, NH 03824, U.S.A.

⁴ Astrophysics Division, European Space Research and Technology Centre, NL 2200 AG Noordwijk, The Netherlands

⁵ I.N.A.O.E., Apartado Postal 51 y 216, Puebla 72000, Puebla, México

⁶ University of Manchester, NRAL, Jodrell Bank, Cheshire SK11 9DL, United Kingdom

Astron. Astrophys. 337, 421-432 (1998)

Abstract. We report on the detection at MeV energies of the radio pulsar PSR B1951+32 by the Compton telescope COMPTEL aboard the COMPTON Gamma Ray Observatory (CGRO). Folding the event arrival times with the radio ephemerides, gives for the data collected during CGRO-mission Cycles I+II a pulsar-phase distribution with two peaks, consistent in phase with the pulses measured by EGRET for energies above 100 MeV. The overall significance is $\gtrsim 4.1\sigma$. For Cycle III-VI data, with similar exposure, no indication was found in the phase distribution. Assuming that the source is not variable, simulations show that fluctuations in the dominating background distribution at significance levels $\lesssim 3\sigma$ can explain the non-detection. In addition, evidence for the presence of the pulsar in the skymaps for energies above 3 MeV is found for all Cycles of the CGRO mission. Below 3 MeV the skymaps are dominated by the strong, soft-spectrum gamma-ray source Cyg X-1, located at only $\sim 2^\circ.6$ from PSR B1951+32. The flux $(7.7 \pm 4.6) \times 10^{-7} \text{ ph/cm}^2 \cdot \text{s} \cdot \text{MeV}$ measured by COMPTEL between 0.75 and 30 MeV is consistent with the measured EGRET spectrum. A single power-law fit to the combined EGRET-COMPTEL data (0.75 MeV – 30 GeV) gives a good fit with spectral index -1.89 ± 0.07 . Furthermore, a break in the pulsar spectrum at MeV energies appears to be required to reconcile the COMPTEL flux with upper limits reported below 1 MeV by OSSE and RXTE.

3.1. Introduction

Kulkarni et al. (1988) discovered PSR B1951+32, a fast 39.5 ms radio-pulsar in the core of the galactic supernova remnant CTB 80 (Angerhofer et al. 1981). The characteristic age and surface field strength assuming spin-down by magnetic dipole radiation are $1.1 \times 10^5 \text{ yr}$ and $5 \times 10^{11} \text{ Gauss}$ respectively (Fruchter et al. 1988). Its distance based

on both pulsar dispersion measure and estimates of the distance to the remnant is $\sim 2 \text{ kpc}$.

In the X-ray regime marginal detections of pulsed emission were claimed by Ögelman et al. (1987) and Angelini et al. (1988) in the EXOSAT data and by Cheng et al. (1994) in the *Einstein* data. Safi-Harb et al. (1995) published detailed results on the soft X-ray properties of PSR B1951+32 and CTB 80 using the ROSAT PSPC and HRI instruments. A combination of PSPC and HRI data yielded marginal evidence at a $\sim 99\%$ confidence level for pulsed emission at the radio period. Recently, at hard X-ray energies Chang et al. (1997) found indications for pulsed emission at $\sim 95\%$ confidence level in a 19 ks observation with the PCA aboard the Rossi X-ray timing explorer (RXTE).

Extrapolating the pulsar ephemeris (Fruchter et al. 1988, Foster et al. 1990, 1994) backwards, timing analysis of COS-B γ -ray data ($E > 50 \text{ MeV}$) yielded promising results (Li et al. 1990; Bennett et al. 1990).

Using γ -ray observations by the EGRET instrument aboard the COMPTON Gamma-Ray Observatory (CGRO) Ramanamurthy et al. (1995) firmly detected pulsed emission from PSR B1951+32 for energies above 100 MeV. The lightcurve showed 2 peaks separated 0.44 in phase with the first peak lagging the radio peak by 0.16. In an earlier systematic search for pulsed γ -ray emission from radio pulsars in CGRO Cycle I COMPTEL data (0.75 – 30 MeV) Carramiñana et al. (1995) found indications (random probability 0.62%) for a double-peak structure in the lightcurve, but had no information on the absolute phase.

In this paper we report now on the detection of PSR B1951+32 by COMPTEL using more data and absolute timing, and the results are compared with those from simultaneous EGRET observations. Preliminary results from this work were presented by Hermsen et al. (1997).

Table 3.1. COMPTEL observations of PSR B1951+32

VP #	Start Date dd-mm-yyyy	End Date dd-mm-yyyy	Pointing direction l(°) b(°)		Off-axis angle (°)	Eff.Exposure (3-10 MeV; $10^6 \text{ cm}^2 \text{ s}$)	EGRET spark- chamber status
Cycle I							
2.0	30-05-1991	08-06-1991	73.3	2.5	4.5	7.927	ON
7.0	08-08-1991	15-08-1991	70.5	-8.4	11.3	5.237	ON
20	06-02-1992	20-02-1992	39.8	0.7	29.1	4.853	ON
Cycle II							
203.0	01-12-1992	08-12-1992	77.8	0.7	9.3	⊥	ON
203.3	08-12-1992	15-12-1992	77.8	0.7	9.3	16.435	ON
203.6	15-12-1992	22-12-1992	77.8	0.7	9.3	⊥	ON
212	09-03-1993	23-03-1993	83.7	11.7	17.2	8.516	ON
Cycle III							
302.0	07-09-1993	09-09-1993	89.1	7.9	20.8	⊥	ON
303.2	22-09-1993	01-10-1993	89.1	7.9	20.8	3.717	ON
303.7	18-10-1993	19-10-1993	89.1	7.8	20.8	⊥	ON
318	01-02-1994	08-02-1994	68.4	-0.4	3.3	⊥	ON
328	24-05-1994	31-05-1994	64.9	0.0	4.8	11.247	ON
331.0	07-06-1994	10-06-1994	64.9	0.0	4.8	⊥	ON
331.5	14-06-1994	18-06-1994	64.9	0.0	4.8	2.948	ON
333	05-07-1994	12-07-1994	64.9	0.0	4.8	4.520	ON
Cycle IV							
429.5	27-09-1995	03-10-1995	86.3	-12.6	23.2	2.798	OFF
Cycle V							
522.5	14-06-1996	25-06-1996	65.7	2.8	3.1	8.064	OFF
Cycle VI							
601.1	15-10-1996	29-10-1996	69.7	-11.3	14.2	8.344	ON
612.5	28-01-1997	04-02-1997	71.3	3.1	2.6	5.204	OFF

3.2. Observations

In this study we have used COMPTEL data collected during CGRO Cycle I - VI observations in which the off-axis angle between PSR B1951+32 located at $(l, b) = (68^{\circ}77', 2^{\circ}82')$ and the pointing direction was less than 30° . Details of each viewing period (VP, in CGRO notation) satisfying the aspect angle constraint are given in Table 3.1. In this paper we depart from the official CGRO nomenclature by using Cycle I - VI instead of the confusing mixture of Phases and Cycles.

The last but one column gives the effective exposure in the 3-10 MeV band at the location of PSR B1951+32 assuming an E^{-2} power-law shape for the spectral distribution of the source events. Earth blocking effects are taken into account. Time periods in which the instrument detectors are off (e.g. anticipated during CGRO SAA passages) and in which there is no real time contact with the TDRS satellites are ignored in this calculation. The last column specifies the status of the EGRET sparkchamber, which is turned off regularly as of CGRO Cycle-IV observations in order to use the last refill of deteriorating gas for more restrictive observations spread over a longer time period. This means that there are no simultaneous EGRET observations for VP's 429.5, 522.5 and 612.5. EGRET data from VP 2.0

upto and including VP 333 have been retrieved from the Compton Science Support Center and used subsequently in our timing- and spatial analysis for verification purposes.

3.3. The COMPTEL instrument

COMPTEL is the imaging Compton Telescope aboard CGRO and is sensitive for γ -ray photons with energies in the 0.75-30 MeV range. Its energy resolution is 5-10% FWHM and due to its large field of view of typically 1 steradian it is possible to monitor a large part of the sky simultaneously with a location resolution of $\sim 1^{\circ}$. Its event-timing accuracy is 0.125 ms.

The COMPTEL instrument consists of two detector layers, an upper layer (D1) and a lower layer (D2). Its detection principle is based on a two layer interaction : an incoming γ -ray photon Compton scatters in one of the 7 detector modules of D1, while the scattered photon has another interaction in one of the 14 D2 modules. The interaction loci in D1 and D2 determine the direction of the scattered photon, which is specified as (χ, ψ) . From the energy deposits in the D1 - module, E_1 , and D2- module, E_2 , it is possible to determine the scatter angle $\bar{\varphi}$ ($= \arccos(1 - m_0c^2(1/E_1 - 1/(E_1 + E_2)))$), in which m_0c^2 is the electron rest energy) and the total energy deposit E_{tot}

Table 3.2. PSR B1951+32 radio-ephemerides used in current analysis

Pulsar position		Validity range		t^0	ν	$\dot{\nu}$	$\ddot{\nu}$	ϕ_0
α_{2000}	δ_{2000}	[MJD]		[MJD]	[Hz]	[Hz/s]	[Hz/s ²]	
19 52 58.322	32 52 41.88	48350	48678	48514 ^a	25.296909436979	-3.74070×10^{-12}	3.34×10^{-22}	0.7381
19 52 58.242	32 52 40.96	48898	49099	48998 ^b	25.2967530149361	-3.74216×10^{-12}	0.0	0.7103
19 52 58.242	32 52 40.96	49217	49574	49395 ^c	25.2966246804332	-3.74149×10^{-12}	-5.89×10^{-23}	0.8769
19 52 58.276	32 52 40.68	49954	50207	50080 ^c	25.2964033322986	-3.73751×10^{-12}	-6.18×10^{-22}	0.1300
19 52 58.276	32 52 40.68	50232	50513	50372 ^c	25.2963090136230	-3.73684×10^{-12}	-2.64×10^{-23}	0.7351

^aEntry from Princeton Database (Cordes et al. 1992)

^bEntry listed in Ramanamurthy et al. 1995

^cProvided by A.Lyne

(= $E_1 + E_2$). Other event parameters playing an important role in background discrimination are: the four veto domes anti-coincidence bits enabling the filtering of the charged particle triggers from the neutral particle triggers at efficiencies above 99.9%; the Time-of-Flight (TOF) measure (range 0-255) for which down-scattered γ -ray photons have well-defined values in a Gaussian shaped peak near channel 120; the Pulse-Shape-Discrimination (PSD) measure (range 0-255) of the signal built up in one of the 7 D1 detectors allowing further discrimination among photon- and neutron induced triggers (photons peak near channel 80, while neutrons peak near 120). In the event selection process also events which may originate from the Earth are ignored (Earth Horizon Angle (EHA) selection). The instrumental response takes this selection into account. More detailed information about the instrument, its detection principle and performance can be found in Schönfelder et al. (1993).

3.4. Analysis methods

The measured event parameters ($\chi, \psi, \bar{\varphi}, E_{tot}$) constitute a 4-dimensional data space, in which we have to search for a "source signature". In practice the dimension of the data space is lowered by assuming a certain spectral shape for the sources to be searched for. The event distribution of a point source (the Point Spread Function (PSF)) in this reduced 3-d data space ($\chi, \psi, \bar{\varphi}$) is concentrated in a cone-shaped structure with its apex at the source position (χ_0, ψ_0). If the position of a (potential) source is *a priori* known it is also possible to determine the geometrical scatter angle φ_{geo} of an event from its scatter direction and the source direction. The difference angle (φ_{arm}) between $\bar{\varphi}$ and φ_{geo} is known as ARM (Angular Resolution Measure) angle and the ARM-distribution of events from a point source is characterized by a narrowly peaked distribution at $\varphi_{arm} = 0$. This ARM angle is used in the event selection procedures for timing analyses.

3.4.1. Timing analysis

3.4.1.1. Procedures and ephemerides

In the timing analysis the event arrival times at the spacecraft recorded with an intrinsic resolution of 0.125 ms are transformed to arrival times at the Solar System Barycentre (SSB) using the known instantaneous spacecraft position, the source position and the solar system ephemeris (JPL DE200 Solar System Ephemeris). The pulse phase ϕ is calculated from the following timing model:

$$\phi = \nu \cdot \Delta t + 1/2 \cdot \dot{\nu} \cdot \Delta t^2 + 1/6 \cdot \ddot{\nu} \cdot \Delta t^3 - \phi_0 \quad (3.1)$$

In this formula Δt is given by $\Delta t = t^e - t^0$ with t^e the event SSB arrival time and t^0 the reference epoch. The values employed here for $t^0, \nu, \dot{\nu}, \ddot{\nu}, \phi_0$ are given in Table 3.2.

3.4.1.2. Detection significance of pulsed emission

The *modulation* significance i.e. the significance for a deviation from a statistically flat phase distribution is determined using the *bin free* Z_n^2 -test statistic (Buccheri et al. 1983). The statistics behaves as a χ^2 -distribution for $2n$ degrees of freedom (n =number of harmonics) in absence of any pulse signal, allowing the transformation from Z_n^2 -test statistic to Gaussian sigma's. This test is rotation invariant what means that a shifted pulse-phase distribution would yield the same modulation significance. A problem is the number of harmonics to be used in the test, if the underlying pulse-shape is unknown. Narrowly peaked pulse-phase distributions for example require more harmonics in the test than distributions with broad modulation patterns. In the current COMPTEL timing analysis we constrained the number of harmonics in the test to 2 and 3 in view of our expectations based on the double peaked EGRET lightcurve observed for energies > 100 MeV.

3.4.2. Spatial and spectral analyses

For spatial point-source searches the events are first sorted in the 3-dimensional data space spanned by the 2-scatter

directions (χ, ψ) and the calculated scatter angle $(\overline{\varphi})$ for a chosen measured energy interval. The search for the point source signature in this 3-d data space is performed by applying a maximum likelihood ratio (MLR) test at each scan position in the selected sky field of the instrument, rendering quantitative information on the source detection significance, position and flux (see de Boer et al. 1992). The ratio test is performed by maximizing the likelihood \mathcal{L}^{H_0} (1 degree of freedom (dof)) under the zero hypothesis \mathcal{H}_0 i.e. a description of the data by a background distribution alone and maximizing the likelihood \mathcal{L}^{H_1} (2 dof) under the alternative hypothesis \mathcal{H}_1 i.e. a data description in terms of a background model and a point source at the scan position. The quantity $Q = -2 \cdot \ln(\mathcal{L}^{H_0(max)} / \mathcal{L}^{H_1(max)})$ is distributed as a χ^2_1 for 1 dof at each scan position. Mathematically we write the expectation value for pixel (i, j, k) under \mathcal{H}_0 as $\mu_{ijk}^{H_0} = \beta \cdot B_{ijk}$ with B_{ijk} the background estimate for pixel (i, j, k) and β a scale factor, and under \mathcal{H}_1 as $\mu_{ijk}^{H_1} = \sigma \cdot P_{ijk} + \beta \cdot B_{ijk}$ with P_{ijk} the source contribution in pixel (i, j, k) with strength σ . The maximization process consists for e.g. the \mathcal{H}_1 case in finding the maximum of $\mathcal{L}^{H_1}(\sigma, \beta)$ given by:

$$\mathcal{L}^{H_1}(\sigma, \beta) = \prod_{ijk} \frac{\mu_{ijk}^{H_1}(\sigma, \beta)^{N_{ijk}} \cdot \exp(-\mu_{ijk}^{H_1}(\sigma, \beta))}{N_{ijk}!} \quad (3.2)$$

with respect to both σ and β simultaneously. In this formula N_{ijk} represents the measured number of counts in pixel (i, j, k) . From the optimized source scale factor σ^{\max} and the exposure at the scan position it is possible to derive source fluxes and corresponding uncertainties (3-d likelihood method). The dominating (instrumental) background distribution in the 3-d dataspace ($\sim 95\%$ of the events passing through our selection filters are still mainly instrumental background events) has been determined from the data themselves using a smoothing method similar to that described in Bloemen et al. (1994). If the position of the source is *a priori* known we can also apply an equivalent likelihood analysis, but now in a 2-d space $(\varphi_{geo}, \overline{\varphi})$ for each E_{tot} slice. This approach is in certain situations less sensitive to the background treatment, and is then particularly used for the generation of source spectra (2-d likelihood method).

In the case of a known timing signature, a third method can be applied to derive source flux information. This is based on the determination of the number of excess counts in an *a priori* chosen pulse-phase interval on top of a (flat) background level determined outside this pulse-phase interval in the lightcurve. The numbers of excess counts can be converted to flux values using the COMPTEL sensitivity to source events with measured ARM-values in the ARM-range applied in the event selection process for the timing analysis. It is important to note that the background estimates in the three methods are very different, in the latter case even completely independent from that in the spatial analyses, namely:

- The 3-d likelihood analysis for a chosen E_{tot} interval requires a background estimate for the full $(\chi, \psi, \overline{\varphi})$ -dataspace.
- The 2-d likelihood analysis for a chosen E_{tot} interval requires a background estimate for the $(\varphi_{geo}, \overline{\varphi})$ -dataspace.
- In the case of a pulsar timing signature, a statistically flat part of the lightcurve is selected (or an interval known to be “empty” from results of other instruments) to determine the background level.

3.5. Timing analysis results

3.5.1. COMPTEL Event selections

The following event selections have been applied:

$0.07 < E1/1 \text{ MeV} < 20.0, 0.65 < E2/1 \text{ MeV} < 30.0, 113 < TOF < 130, 0 < PSD < 110, \text{EHA-}\overline{\varphi} > 0$, no VETO flag bits set and finally an additional ARM selection of $|\varphi_{arm}| \leq 3^{\circ}5$. Except for the ARM selection the other event selections have also been applied in the spatial analysis. The applied ARM selection is in a narrow optimum range, as has been verified for the established MeV γ -ray pulsars Crab (Much et al 1995) and Vela (Kuiper et al. 1998).

3.5.2. Consistency of COMPTEL and EGRET lightcurves

In order to be sure that the calculated pulse-phase (see Eq. 3.1) is compatible with the published EGRET lightcurve for energies above 100 MeV (Ramanamurthy et al. 1995), the first three entries of the set of ephemerides shown in Table 3.2 have first been used in a timing analysis of archival EGRET data (from VP 2.0 upto and including VP 333; see Table 3.1). Applying the same energy- and cone selections as in Ramanamurthy et al. (1995) we could reproduce the EGRET > 100 MeV lightcurve for the slightly enlarged combination of observations, demonstrating the consistent functioning of our timing analysis tools. The result is shown in Fig. 3.1c, in which phase 0.0 corresponds to the radio peak. Superimposed is also the Kernel Density Estimator (KDE; de Jager 1986) and its $\pm 2\sigma$ uncertainty range determined from the unbinned set of pulse-phases. This provides an (asymptotically) unbiased view of the genuine underlying pulse-shape. The shaded areas indicate the “pulsed” interval defined by Ramanamurthy et al. (1995) as the combination of phase intervals 0.12-0.22 and 0.48-0.74 (P1+P2).

Next we repeated the analysis for the CGRO Cycle I COMPTEL data (i.e. data from VP 2.0, 7.0 and 20 combined) for which Carramiñana et al. (1995) found an indication for a narrow and a broad peak in the COMPTEL lightcurve at *unspecified* phases. The new radio-aligned COMPTEL lightcurve (see Fig.3.1a for a 12 bin – and Fig.3.1b for a 50 bin representation) for the total energy range 0.75-30 MeV shows two peaks co-aligned in phase with the peaks in the EGRET > 100 MeV lightcurve.

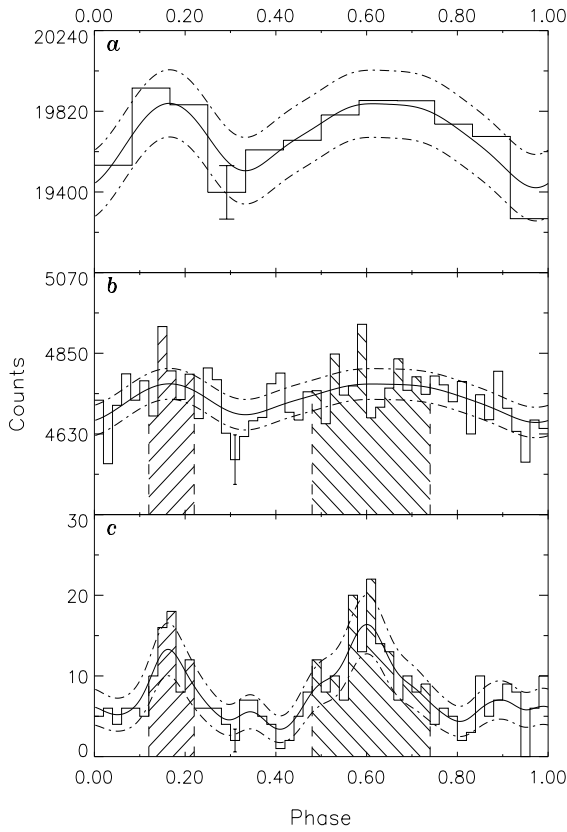


Fig. 3.1. *a)* Radio-aligned 0.75-30 MeV 12-bin COMPTEL lightcurve for CGRO Cycle I data only (same data as used by Carramiñana et al. 1995). The KDE and its $\pm 2\sigma$ uncertainty range are superposed. *b)* same as *a)* but now with 50 bins. The shaded area corresponds to the “pulsed” definition introduced by Ramanamurthy et al. (1995) based on the EGRET > 100 MeV lightcurve. *c)* EGRET 50 bin > 100 MeV lightcurve for the combination of the Cycle I, II and III viewing periods listed in Table 3.1. The KDE and its $\pm 2\sigma$ uncertainty range is superposed. The shaded area indicates the “pulsed” interval defined in Ramanamurthy et al. (1995). In all figures a typical 1σ error bar is indicated.

The Z_n^2 -test statistic gives for 3 harmonics a modulation significance of 3.42σ (see Sect. 3.4.1.2). Superimposed in both Fig. 3.1a,b are the KDE and its $\pm 2\sigma$ uncertainty range, while typical 1σ errors are indicated. It is striking that the two highest bins in the COMPTEL 0.75-30 MeV lightcurve (Fig. 3.1b) coincide with the pulse maxima in the EGRET > 100 MeV lightcurve (Fig. 3.1c). However, the significance of these two narrow peaks is too low to constrain significantly the KDE distribution.

3.5.3. Timing analysis for CGRO Cycles I–VI

The timing analysis has been performed using the data from all observations listed in Table 3.1. The derived *modulation* significances (see Sect. 3.4.1.2), irrespective of the peak

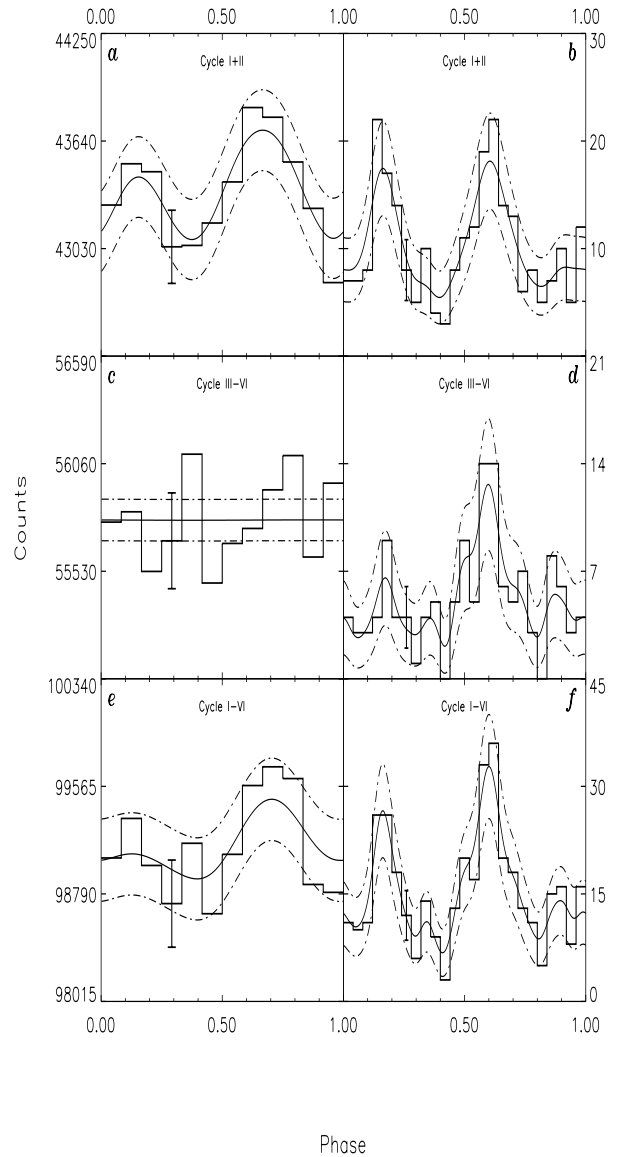


Fig. 3.2. The pulse-phase distributions for COMPTEL (0.75-30 MeV; left panels *a,c,e*) and EGRET (> 100 MeV; right panels *b,d,f*) shown for Cycles I+II and III-VI (comparable COMPTEL exposures), and the total (from top to bottom). In each frame the underlying unbiased estimate of the genuine pulse shape (KDE) is superposed as a solid line along with its $\pm 2\sigma$ uncertainty ranges (dashed-dotted lines). Typical 1σ error bars are indicated in each frame.

locations in the lightcurve, for both the COMPTEL 0.75-30 MeV and contemporaneous > 100 MeV EGRET pulse-phase distributions are shown in Table 3.3 for the individual CGRO Cycle VP combinations. Cycles IV-VI are combined to obtain an exposure comparable to the earlier Cycles. For COMPTEL also the excess counts in P1+P2 are listed. The same table lists these values for the combinations Cycle I+II, Cycle III-VI (comparable exposures) and the total I-VI. For the latter combinations the corresponding

Table 3.3. Modulation significances for PSR B1951+32 in COMPTEL and EGRET timing analyses, and the number of excess counts in the P1 and P2 phase intervals (see text) for different combinations of CGRO Cycles.

CGRO Cycle combination	n	COMPTEL 0.75 – 30 MeV		EGRET > 100 MeV
		Sign.	Excess counts	Sign.
I	2	2.95σ	1220 ± 295	2.32σ
	3	3.42σ		2.85σ
II	2	2.06σ	591 ± 321	4.05σ
	3	1.72σ		3.96σ
III	2	1.56σ	-545 ± 327	3.77σ
	3	1.81σ		4.32σ
IV-VI	2	0.05σ	-160 ± 367	—
	3	0.49σ		—
I+II	2	3.86σ	1813 ± 437	5.06σ
	3	3.52σ		5.45σ
III-VI	2	0.52σ	-705 ± 494	3.77σ
	3	0.76σ		4.32σ
I-VI	2	2.20σ	1109 ± 660	6.36σ
	3	1.78σ		7.23σ

COMPTEL and EGRET lightcurves are shown in Fig.3.2. The left panels (Fig.3.2a,c,e) show the COMPTEL 0.75-30 MeV 12-bin lightcurves with superposed the KDE and its $\pm 2\sigma$ uncertainty range along with a typical 1σ error bar. The right panels (Fig.3.2b,d,f) show the contemporaneous > 100 MeV EGRET lightcurves.

As mentioned above, the *modulation* significance for the COMPTEL Cycle I 0.75-30 MeV pulse-phase distribution approaches/exceeds the 3σ level: 2.95σ for $n=2$ harmonics and 3.42σ for $n=3$ (see Table 3.3). However, the corresponding chance probability values of $3.2 \cdot 10^{-3}$ and $6.4 \cdot 10^{-4}$ for $n=2,3$ do not take into account that the observed lightcurve co-aligns with the EGRET lightcurve. This means that the detection significance of the pulsed signal with peaks at the expected positions is in fact higher. The increase in significance can be determined through simulations, which is the subject of the next section. Also, the modulation significance of the COMPTEL 0.75-30 MeV Cycle I+II pulse-phase distribution, approaching the 4σ -level, is a conservative estimate, and will be above the 4σ -level. Unfortunately, adding more COMPTEL data does not improve the detection significance further. No timing signal is seen for Cycles III-VI. The simulations described in the next section will address this problem as well. Spatial analysis, however, see also below, gives evidence that the source is present during all Cycles of the CGRO mission. The $\sim 4\sigma$ -modulation significance of the 0.75-30 MeV Cycle I+II COMPTEL lightcurve with a double-peak pulse shape co-aligned with the EGRET lightcurve along with a point source in the maps (see below) consistent with the pulsars position led us already conclude that PSR B1951+32 was detected at MeV energies (Hermsen et al. 1997).

3.5.4. Lightcurve simulations

In order to study the effects of a weak pulsed signal atop of a dominating background distribution, we have now performed lightcurve simulations assuming a pulse-profile similar to the (KDE–KDE_{min}) of the EGRET > 100 MeV Cycle I+II+III lightcurve (see Fig.3.1c or equivalently Fig.3.2f). The fraction of counts falling in the P1 and P2 intervals as defined by Ramanamurthy et al. (1995) is 0.67. For the background level definition used in the actual analysis, namely the average level in the phase intervals complementary to the P1 and P2 intervals, the fraction of pulsed “excess” counts is lower, namely 0.48. A typical simulation consists in generating a background sample drawn from a uniform distribution and simulations of the pulsed signal drawing from the above described profile with a varying number of total pulsed counts. In the first set of simulations we have performed 6500 simulations for the case that we have not added a pulsed signal to the background sample (i.e. for the verification of the modulation significance determination) for a total number of counts of 235000, i.e. approximately the background level in the COMPTEL 0.75-30 MeV Cycle I pulse-phase distribution (see Fig.3.1a, b) and 1500, 1000 and 1000 simulations adding, respectively, sources for the following number of pulsed excess counts in P1+P2: 350, 700 and 1065 (i.e. approaching the number of excess counts in P1+P2 (=1220) as measured in the COMPTEL 0.75-30 MeV Cycle I lightcurve). For each simulation we have determined the modulation significance as the Z_3^2 -statistics value transformed to Gaussian sigmas and the *measured* number of excess counts in P1+P2 (N_E) using the complement of the P1+P2 phase interval as background interval.

The results of these simulations are shown in Fig. 3.3 for the different numbers of pulsed counts simulated in P1+P2. Along the x-axis the modulation significance is shown, and along the y-axis the number of excess counts in P1+P2 is given. The contour levels connect bins with the same probability level of occurrence. Figure 3.3 shows that in the presence of a pulsed signal the 2-d distributions become slanted indicating a correlation between the modulation significance and the number of excess counts measured in P1+P2. The centroids of the distributions, all intersected by the line specifying the number of simulated pulsed excess counts in P1+P2, shift towards higher Z_3^2 values the higher the number of pulsed counts put in P1+P2. From these 2-d distributions several important integral properties can be derived.

(i) For the background simulations (see Fig. 3.3 upper-left frame) the integral distribution of the Z_3^2 values (expressed in Gaussian sigmas; see Fig. 3.4) behaves, irrespective of the number of measured excess counts in P1 and P2, as the complementary error function, indicating that our modulation significance estimations have the *proper* calibration. We also showed this to be true when we used back-

ground samples from real flight data (Carramiñana et al. 1995).

(ii) In Fig. 3.5 (left panel) the Z_3^2 -distributions are shown for the background simulations (shaded) and for the simulations with 1065 excess counts in P1+P2 atop of the background (grey). Note the shift of the distribution maximum towards $Z_3^2 \sim 2.5\sigma$ for the latter case. In the right panel of Fig. 3.5 distributions of the excess counts are shown for the same simulations. Gaussian fits to each of the distributions are superimposed. The peak widths (σ) are of the order of ~ 375 counts indicating that the spread is completely dominated by background fluctuations. The probability to detect a source with a pulse profile as measured by EGRET with 1065 excess counts (total number of pulsed counts in the profile ~ 2200) with a significance above 3.5σ is similar to the probability to obtain a significance below 1.5σ . Therefore, a source with flux close to our detection threshold will predominantly be detected when its signal is enhanced by a constructive background fluctuation. Consequently, in most cases the best estimate for its flux will be too high.

(iii) In the previous section we reported a negative result for our Cycle III - VI observations. We investigated this as follows: The normalized 2-d distributions (Fig. 3.3) for a given number of background counts B and pulsed excess counts C_E simulated in P1+P2 can be specified by $F(\zeta, \epsilon|B, C_E)$, where ζ refers to the $Z_3^2(\sigma)$ variable and ϵ to the N_E variable. Then the probability of measuring a negative number for the excess counts in P1+P2 irrespective of the Z_3^2 -value is given by:

$$P(N_E < 0|B, C_E) = \int_{-\infty}^0 \int_{-\infty}^{\infty} F(\zeta, \epsilon|B, C_E) \cdot d\zeta \cdot d\epsilon \quad (3.3)$$

The results are summarized in Table 3.4. The columns include the number of simulated pulsed excess counts put in P1+P2 (C_E), the number of background counts (B), Z_3^2 value in Gaussian sigma at the centroid (ζ_C , the maximum), the measured number of excess counts in P1+P2 (N_E) at the centroid N_{E_C} , the standard deviation of the measured excess counts distribution W_{E_C} and finally the probability $P(N_E < 0|B, C_E)$ of measuring a negative number of excess counts in P1+P2 for a given background B and pulsed excess counts C_E simulated in P1+P2.

(iv) Finally, we would like to learn from the simulations the overall probability to measure a certain modulation probability and in addition a certain number of excess counts in a predefined phase window. In our case: What is the probability that random excesses in the COMPTEL phase distribution coincide with the pulses in the EGRET light curve? From $F(\zeta, \epsilon|B, C_E)$ we can calculate the following 2-d integral:

$$\mathcal{F}(\zeta_l, \zeta_u, \epsilon_l, \epsilon_u|B, C_E) = \int_{\zeta_l}^{\zeta_u} \int_{\epsilon_l}^{\epsilon_u} F(\zeta', \epsilon'|B, C_E) \cdot d\zeta' \cdot d\epsilon' \quad (3.4)$$

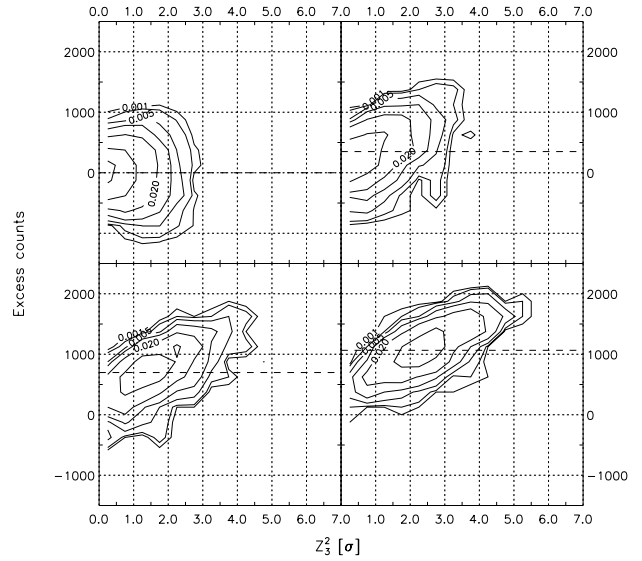


Fig. 3.3. Contour representation of lightcurve simulation results for different numbers of pulsed excess counts in the phase intervals 0.12-0.22 (P1) and 0.48-0.74 (P2) assuming an EGRET like pulse-phase distribution (used EGRET KDE of Fig.3.2) in a COMPTEL representative background environment with 235000 counts. *a)* (upper-left) 6500 pure background simulations; *b)* (upper-right) Adding source with 350 pulsed excess counts: 1500 simulations; *c)* (bottom left) Adding 700 pulsed excess counts: 1000 simulations. *d)* (bottom right) Adding 1065 pulsed excess counts: 1000 simulations. Dashed horizontal lines indicate the numbers of simulated pulsed excess counts in P1+P2.

Table 3.4. Global simulation results (see text)

C_E	B	ζ_C	N_{E_C}	W_{E_C}	$P(N_E < 0 B, C_E)$
0	235000	0.81σ	-7	371	0.500 ± 0.009
350	235000	1.00σ	349	376	0.166 ± 0.011
700	235000	1.60σ	716	379	0.035 ± 0.006
1065	235000	2.42σ	1085	355	0.001 ± 0.001
0	470000	0.79σ	-12	507	0.503 ± 0.015
700	470000	1.16σ	684	510	0.089 ± 0.008
1050	470000	1.57σ	1024	521	0.022 ± 0.005
1400	470000	2.18σ	1380	536	0.005 ± 0.002

and also the efficiency $\eta(\zeta_l, \epsilon_l|B, C_E)$ defined as:

$$\eta(\zeta_l, \epsilon_l|B, C_E) = \frac{\mathcal{F}(\zeta_l, \infty, \epsilon_l, \infty|B, C_E)}{\mathcal{F}(\zeta_l, \infty, -\infty, \infty|B, C_E)} \quad (3.5)$$

The quantity $\mathcal{F}(\zeta_l, \infty, -\infty, \infty|B, C_E)$ specifies the probability that we measure a modulation significance larger than ζ_l irrespective the number of measured excess counts in P1+P2 for given background B and pulsed excess counts C_E simulated in P1+P2. The efficiency $\eta(\zeta_l, \epsilon_l|B, C_E)$ specifies the fraction of $\mathcal{F}(\zeta_l, \infty, -\infty, \infty|B, C_E)$ having in addition measured excess counts in P1+P2 larger than ϵ_l . For the background simulations (see Table 3.5 upper 9

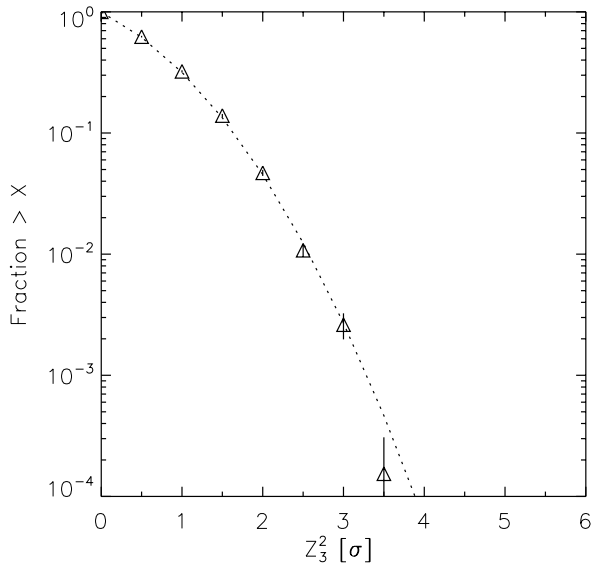


Fig. 3.4. The cumulative distribution of $Z_3^2(\sigma)$ for the 6500 background simulations. The triangles and error bars indicate the simulation results, while the dotted line represents the complementary error function - the expected functional shape of the cumulative distribution for lightcurve simulations of pure background.

rows) it turns out that this factor ranges from 0.05 to 0.12 demanding a measured number of excess counts larger than 800. This means that the chance probability of measuring a $n \cdot \sigma$ modulation significance along with the restriction of measuring more than 800 excess counts in P1+P2 decreases by this factor; the *detection* significance of the pulsed signal typically increases $0.6 - 1.0\sigma$ with respect to the modulation significance. As a result the detection significance of the 0.75-30 MeV COMPTEL Cycle I lightcurve showing a modulation significance of 3.4σ with ~ 1200 excess counts in P1+P2 is $\gtrsim 4.1\sigma$ ($6.7 \cdot 10^{-5}$ chance probability). For the COMPTEL Cycle I+II 0.75-30 MeV lightcurve (see simulation summary in Table 3.6) the significance becomes also above 4.1σ for 3 harmonics and $\gtrsim 4.5\sigma$ for 2 harmonics, justifying our earlier claim of detection of pulsed emission from PSR B1951+32 at MeV energies.

As noted before, the genuine number of pulsed counts in P1+P2 in the 0.75-30 MeV range for Cycle I/I+II can, however, be overestimated in case of a constructive background fluctuation. The non-detection of the pulsed signal in the 0.75-30 MeV range during Cycle III - VI, having a comparable exposure of the pulsar as during Cycle I+II, points in that direction. If the genuine number of pulsed counts in P1+P2 is ~ 950 on top of 470000 background counts (representative number in the timing analysis for COMPTEL 0.75-30 MeV Cycle I+II and Cycle III - VI, respectively) then the simulation results demonstrate that the detection of a pulsed signal (1800 counts) in the Cycle I+II data and the non-detection (-700 counts) in Cycle III - VI require statistical fluctuations in the dominating background of less than 3σ .

Table 3.5. Simulation results: background level representative for COMPTEL energy range 0.75-30 MeV in timing analyses of Cycle I, II and III and Cycle IV - VI viewing period combinations

C_E	B	ζ_l	ϵ_l	$\mathcal{F}(\zeta_l, \infty, -\infty, \infty B, C_E) / \eta(\zeta_l, \epsilon_l B, C_E)$
0	235000	2.0σ	800	0.0469 0.049
0	235000	2.0σ	1000	0.0469 0.026
0	235000	2.0σ	1200	0.0469 0.010
0	235000	2.5σ	800	0.0108 0.114
0	235000	2.5σ	1000	0.0108 0.085
0	235000	2.5σ	1200	0.0108 0.043
0	235000	3.0σ	800	0.0026 0.058
0	235000	3.0σ	1000	0.0026 0.000
0	235000	3.0σ	1200	0.0026 0.000
350	235000	2.5σ	800	0.0480 0.458
350	235000	2.5σ	1000	0.0480 0.250
350	235000	2.5σ	1200	0.0480 0.139
350	235000	3.0σ	800	0.0100 0.667
350	235000	3.0σ	1000	0.0100 0.467
350	235000	3.0σ	1200	0.0100 0.267
700	235000	2.5σ	800	0.1510 0.795
700	235000	2.5σ	1000	0.1510 0.629
700	235000	2.5σ	1200	0.1510 0.371
700	235000	3.0σ	800	0.0630 0.921
700	235000	3.0σ	1000	0.0630 0.762
700	235000	3.0σ	1200	0.0630 0.540
1065	235000	2.5σ	800	0.4590 0.959
1065	235000	2.5σ	1000	0.4590 0.839
1065	235000	2.5σ	1200	0.4590 0.654
1065	235000	3.0σ	800	0.2540 0.976
1065	235000	3.0σ	1000	0.2540 0.909
1065	235000	3.0σ	1200	0.2540 0.811

In summary the simulations demonstrate that:

- the pulsed signal in the COMPTEL 0.75-30 MeV range is detected at a $\gtrsim 4.1\sigma$ significance level (2 harmonics) with 1813 ± 437 excess counts for the combined Cycle I+II data.
- for an underlying background of 470000 counts there is a reasonable chance for a non-detection following this signal detection, if the genuine number of pulsed counts in P1+P2 is ~ 950 . Namely, a statistical fluctuation $\lesssim 2\sigma$ is required in order to measure a negative signal, and $\lesssim 3\sigma$ to reach as low as -700 counts.
- an alternative explanation is the detection of a time variable signal. However, the steady behaviour in the EGRET window of PSR B1951+32 as well as the other known γ -ray pulsars makes this interpretation less likely.

3.6. Spatial- and spectral analysis

3.6.1. Spatial analysis

The spatial analysis at MeV energies of the sky region around PSR B1951+32 is complicated by the proximity

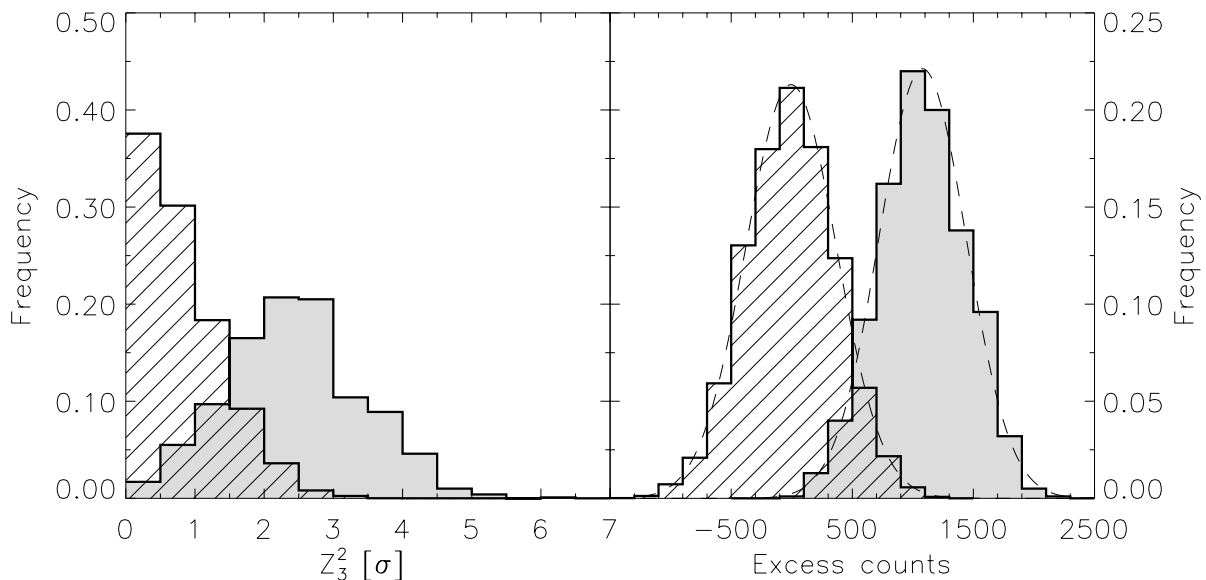


Fig. 3.5. Z_3^2 (left panel) and excess counts (right panel) distributions for two cases: background simulations (shaded) and simulations of 1065 pulsed counts put in P1+P2 atop a simulated background (grey).

of the black-hole X-ray binary Cyg X-1 at position $(l, b) = (71^{\circ}34, 3^{\circ}07)$ and at an angular distance of merely $\sim 2^{\circ}6$ (cf. spatial resolution of COMPTEL is $\sim 1^{\circ}$), preventing the resolution of both sources spatially. Previous COMPTEL studies of Cyg X-1 using data from Cycle I, II and III by Van Dijk (1996) and McConnell et al. (1997) showed that Cyg X-1 dominates the COMPTEL sky maps for energies below 3 MeV. Above 3 MeV the situation was less clear. A weak source feature was evident in the combined CGRO Cycle I, II and III data, statistically consistent with the location of Cygnus X-1. However, the centroid of this feature was seen to be consistently offset from the exact location of Cygnus X-1 in the direction of the pulsar location. The shift of the excess going from the 1-3 MeV range to the 3-10 MeV range is nicely illustrated in the upper panel of Fig. 3.6 showing MLR maps for the 1-3 MeV and 3-10 MeV energy ranges of the Cygnus region (Cyg X-1 and PSR B1951+32 indicated by + and \times signs, respectively) using all available COMPTEL data. This changing spatial morphology at MeV energies can be explained by a soft γ -ray source (Cyg X-1) located close to a hard γ -ray source (PSR B1951+32). The excess in the 3-10 MeV Cycle I - VI MLR map can be explained by the presence of the pulsar only. An explanation in terms of emission by Cyg X-1 only is less adequate leaving a strong ($\gtrsim 4.5\sigma$ for 1 dof) excess at lower longitudes near the pulsar position. This makes the pulsar the most likely candidate, but contributions from Cyg X-1 and other weak unidentified sources and/or emission of galactic diffuse origin with unknown spatial- and spectral distributions are likely. Analysing individually the Cycle I+II and Cycle III - VI datasets, which have similar exposures, indicates that this shift with energy persists

over all Cycles (see Fig. 3.6 middle and bottom panel). In the 3-10 MeV MLR map for Cycle III - VI (bottom right plot of Fig. 3.6) a local maximum consistent with the Cyg X-1 position is visible. A spatial analysis (3-d - and 2-d maximum likelihood methods) selecting events from the pulsed (P1+P2) and unpulsed (complement of P1+P2) phase intervals was applied by Hermsen et al. (1997) using Cycle I+II+III data. This yielded in the “pulsed” maps for the 0.75-10 MeV range a $\sim 3.3\sigma$ excess at the pulsar position on top of Cyg X-1 - and diffuse galactic emission (assumed to be spatially distributed as H1 and CO), while no excess was apparent in the “unpulsed” map. This combined timing and spatial analysis was performed particularly to derive flux information, but has been abandoned in this work. The above mentioned complicating factors – particularly the nearby strong time-variable source Cyg X-1 and the uncertain spatial- and spectral distribution of the emission of galactic diffuse origin – make the MLR map interpretation ambiguous. However, we have verified that at least the flux derived from the timing analysis (see below) is consistent with the flux derived from the 3-d - and 2-d spatial analyses.

3.6.2. Spectral analysis

In this work the flux information for PSR B1951+32 has been obtained from the determination of the excess counts in P1+P2 in the lightcurve (see Sect. 3.4.2), because in the phase-space all the complicating source components in the spatial analysis manifest themselves as statistically flat distributions. The disadvantage of this method, however, is that possible pulsed emission in the *a priori* defined un-

Table 3.6. Simulation results for a background level representative for the COMPTEL energy range 0.75-30 MeV in timing analyses of Cycle I+II and in Cycle III - VI viewing period combinations

C_E	B	ζ_l	ϵ_l	$\mathcal{F}(\zeta_l, \infty, -\infty, \infty B, C_E) / \eta(\zeta_l, \epsilon_l B, C_E)$	
0	470000	2.0σ	800	0.0418	0.096
0	470000	2.0σ	1000	0.0418	0.050
0	470000	2.0σ	1200	0.0418	0.042
0	470000	2.0σ	1400	0.0418	0.011
0	470000	2.5σ	800	0.0124	0.107
0	470000	2.5σ	1000	0.0124	0.036
0	470000	2.5σ	1200	0.0124	0.036
0	470000	2.5σ	1400	0.0124	0.036
0	470000	3.0σ	800	0.0022	0.200
0	470000	3.0σ	1000	0.0022	0.200
0	470000	3.0σ	1200	0.0022	0.200
0	470000	3.0σ	1400	0.0022	0.200
700	470000	3.0σ	800	0.0207	0.806
700	470000	3.0σ	1000	0.0207	0.710
700	470000	3.0σ	1200	0.0207	0.645
700	470000	3.0σ	1400	0.0207	0.484
700	470000	3.5σ	800	0.0060	0.556
700	470000	3.5σ	1000	0.0060	0.556
700	470000	3.5σ	1200	0.0060	0.444
700	470000	3.5σ	1400	0.0060	0.444
1400	470000	3.0σ	800	0.2010	1.000
1400	470000	3.0σ	1000	0.2010	0.990
1400	470000	3.0σ	1200	0.2010	0.970
1400	470000	3.0σ	1400	0.2010	0.920
1400	470000	3.5σ	800	0.0950	1.000
1400	470000	3.5σ	1000	0.0950	0.989
1400	470000	3.5σ	1200	0.0950	0.979
1400	470000	3.5σ	1400	0.0950	0.958

pulsed (here the EGRET definition was used) phase interval might raise the background level leading to an underestimation of the genuine pulsed flux. This cannot be ruled out in view of the observed changing spectral behaviour as a function of pulse-phase for e.g. the Crab, Vela and Geminga pulsars (Fierro 1995). Furthermore, DC-flux information can not be obtained by this method: this can only be determined through spatial analysis.

The source signature in the total dataset has become too weak to divide the total energy range in smaller energy bins. Therefore, we have used the 0.75-30 MeV Cycle I - VI lightcurve (see Fig. 3.2e) to derive our best estimate for the time-averaged pulsed 0.75-30 MeV flux from PSR B1951+32: $(7.7 \pm 4.6) \times 10^{-7} \text{ ph/cm}^2 \cdot \text{s} \cdot \text{MeV}$. This flux will increase when we select a wider pulsed phase interval, but then the phase selection is not identical to the EGRET definition. In addition, the systematic uncertainty in the overall COMPTEL sensitivity could be up to $\sim 25\%$. In a broader high-energy spectral perspective the COMPTEL flux point is shown in Fig. 3.7, where also spec-

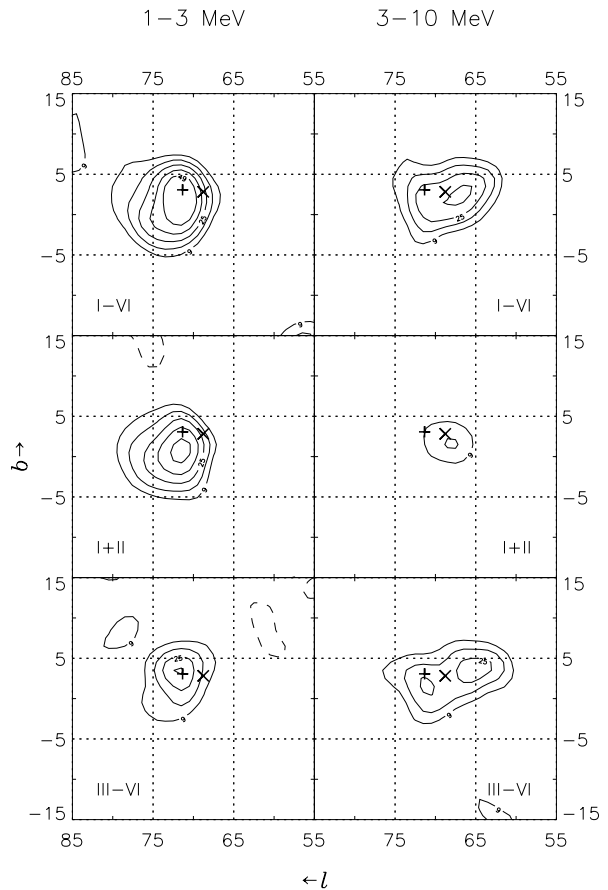


Fig. 3.6. MLR maps of the Cygnus region in two different energy intervals 1-3 MeV (left) and 3-10 MeV (right). From top to bottom are shown the maps for a combination of all data (upper panel; Cycle I - VI), for all Cycle I+II data (middle panel) and finally for all Cycle III - VI data (bottom panel). Contours starting at 3σ in steps of 1σ assuming 1 dof (corresponding maximum likelihood ratios are 9, 16, 25, etc.). Dashed contours indicate regions with negative point source correlations (levels at $-9, -16$). The maps below 3 MeV are dominated by Cyg X-1 (+), while the excess shifts towards the PSR B1951+32 location (x) for the 3-10 MeV energy window (see text).

tral information from other high-energy missions has been included: EGRET (Fierro 1995), OSSE (Schroeder et al. 1995), BATSE (Wilson et al. 1992) and RXTE (Chang et al. 1997).

3.7. Summary and discussion

The detection of a pulsed signal from PSR B1951+32 by COMPTEL can only be claimed based on earlier-mission data. Assuming that the MeV-emission from PSR B1951+32 is not time-variable, the COMPTEL detection of this pulsar in the data of CGRO-mission Cycles I and II (Hermesen et al. 1997) at a significance level $\gtrsim 4.1\sigma$ was fortunately high. The pulsar phase distribution exhibits two peaks, which are aligned in phase with the pulses measured

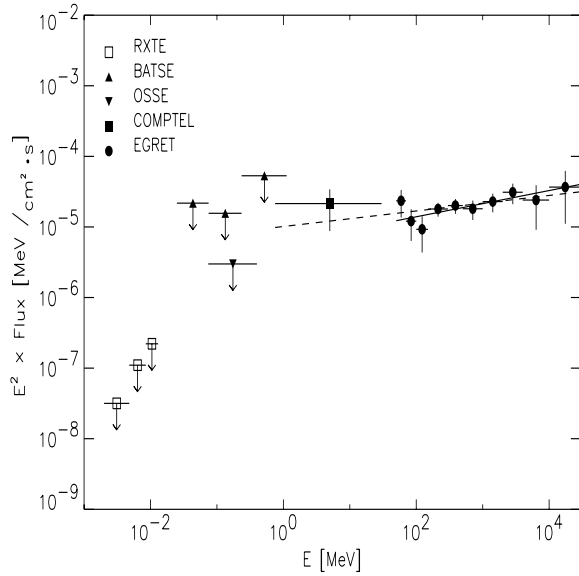


Fig. 3.7. Pulsed high-energy spectrum of PSR B1951+32 as observed by EGRET (Fierro, 1995), COMPTEL (this work), OSSE (Schroeder et al., 1995), BATSE (Wilson, 1992) and RXTE (Chang et al., 1997). The solid line shows the single power-law fit to the EGRET data points above 50 MeV; the dashed line the fit over the total COMPTEL and EGRET range.

by EGRET at high-energy γ -rays with a phase separation of ~ 0.44 . The subsequent non-detection in data of Cycles III - VI indicates that the source flux has to be close to the COMPTEL detection threshold. The time-averaged (Cycle I+II+III) flux values which we published earlier (Hermsen et al. 1997) are slightly higher (by $\sim 1\sigma$) than the new single flux value presented in Fig.3.7, including now also data from Cycle IV - VI. This integral (0.75–30 MeV) flux is consistent with the EGRET spectrum measured above 50 MeV, but suggests a flattening w.r.t. the single-power-law best fit to the EGRET data (index -1.81 ± 0.09). The latter fit predicts 275 pulsed counts in the COMPTEL data for Cycle I+II, and 1813 ± 437 were detected. A single power-law fit to the phase-averaged EGRET data points and the phase-averaged time-averaged COMPTEL flux, covering a total energy range of 0.75 MeV to 30 GeV, changes indeed the index to -1.89 ± 0.07 . The fit, see Fig.3.7, is good with a reduced χ^2 of 0.46 and it is represented (in units $ph/cm^2 \cdot s \cdot MeV$) by :

$$F(E_\gamma) = (1.10 \pm 0.12) \cdot 10^{-10} \times (E_\gamma/423.64)^{(-1.89 \pm 0.07)}$$

Obviously, a substantial spectral break is required in the extrapolation to the X-ray domain to satisfy the OSSE and RXTE upper limits.

PSR B1951+32 is one of the four older (age $\gtrsim 10^5$ yr) radio pulsars detected at γ -ray wavelengths, namely: PSR B1951+32 (1.1×10^5 yr), PSR B0656+14 (also 1.1×10^5 yr; weaker detection in γ -rays, see Ramanamurthy et al. 1996, Hermsen et al. 1997), Geminga (3.4×10^5 yr) and PSR

B1055-52 (5.3×10^5 yr). In this discussion we ignore the peculiar spectrum of PSR B0656+14 (which seems to have a narrow maximum in energy output in the range 10–30 MeV; Hermsen et al. 1997). In Fig.3.7, it is apparent that the measured luminosity of PSR B1951+32 between roughly 1 and 30 MeV is comparable to the luminosity in a similar logarithmic energy interval in high-energy γ -rays. This contrasts the situation for the other older radio pulsars Geminga and PSR B1055-52. The latter pulsars are measured with (much) higher fluxes by EGRET above 100 MeV with spectral indices of -1.42 ± 0.02 and -1.59 ± 0.12 , respectively (Fierro 1995), and no solid detections at COMPTEL energies could be reported so far (for Geminga see Kuiper et al. 1996). In this respect PSR B1951+32 resembles more the younger pulsars Crab and Vela (indices above 50 MeV -2.12 ± 0.03 and -1.62 ± 0.01 , respectively, Fierro 1995), although the total pulsar spectra of Crab and Vela differ significantly in their extrapolation to X-ray energies (see e.g. the review by Thompson et al. 1997). In fact, the spectral shape of PSR B1951+32 going from X-rays to γ -rays seems to have a shape rather similar to that of Vela. In this respect it is interesting to note that the efficiency in converting rotational energy loss into γ -rays (above 100 MeV) of PSR B1951+32 is $\sim 2 \times 10^{-3}$, roughly as efficient as the 10 times younger Vela pulsar. For the other older pulsars this efficiency is more than one order of magnitude higher.

Two types of models for pulsar γ -ray emission are discussed: Polar cap models (first proposed by Sturrock 1971; later extensions by Ruderman & Sutherland 1975; Harding 1981; Daugherty & Harding 1982; Arons 1983) and outer gap models (Cheng et al. 1986; Chiang & Romani 1992). The main difference between these scenarios is the region in which the γ -rays are produced. In the first this occurs in the vicinity of the star above the polar cap, in the latter, in vacuum gaps existing in the outer regions of the magnetosphere. In the most recent versions of these models a single pole picture is discussed, where the observer sees emission from one pole only. In polar cap models (Daugherty and Harding 1996; Sturmer et al. 1995) the γ -ray emission beam is a hollow cone centered on the magnetic pole. In outer gap models (Romani & Yadigaroglu 1995; Romani 1996), the γ -ray emission is a wide, curved fan beam that is formed by the surface of the last open field line in the outer magnetosphere. Both types of models have successes and difficulties in explaining the variety of parameters which can be derived for the eight pulsars seen in γ -rays so far. Below we will address only some points for which this COMPTEL detection of PSR B1951+32 has impact on the ongoing debate.

Daugherty & Harding model γ -ray emission originating in extended polar gap cascades. These extended photon-pair cascades are initiated by curvature radiation from electrons accelerated above the polar cap. In order to reproduce satisfactorily the double-pulse Vela light curve and its spectrum with a high-energy cut-off around 3 GeV and the relatively high level of emission below 100 MeV, the acceleration of

electrons above the polar cap had to start at a height of ~ 1 neutron star radius above the neutron star surface and to extend up to several neutron star radii. Earlier models assumed that the acceleration to high energies takes place just above the surface of the neutron star. The total high-energy spectrum of PSR B1951+32 (Fig.3.7) appears to have a higher energy cut-off compared to Vela's spectrum (around 10 GeV or higher) with also a relatively higher MeV flux. This spectrum is challenging the model even further.

In his most recent paper on radiation processes in the outer magnetosphere, Romani (1996) explains the low γ -ray efficiency above 100 MeV of PSR B1951+32 as being due to its low magnetic field, compared to the high magnetic fields and high efficiencies for Geminga and PSR B1055-52. Furthermore, his model identifies in the phase averaged spectrum a few components: A curvature radiation component dominating from ~ 30 MeV to ~ 10 GeV, a synchrotron component peaking at MeV energies, and at the extremes a thermal component at keV energies and Compton upscattering of the synchrotron spectrum on the primary e^\pm at TeV energies. In order to explain the high COMPTEL flux below 30 MeV, an enhanced synchrotron contribution seems to be required. However, this cannot be reconciled with the low magnetic field of PSR B1951+32.

Zhang & Cheng (1997) discuss the γ -ray production in thick outer gaps. For older pulsars the outer gaps become larger, as pointed out by Ruderman & Cheng (1988). However, PSR B1951+32 appears to have a medium size gap (Vela type), smaller than the other post-Vela type pulsars PSR B0656+14, Geminga and PSR B1055-52. Zhang & Cheng (1997) show that the Vela spectrum (100 keV – 10 GeV) cannot be explained by their thick gap model, but that the available spectra for Geminga, PSR B1055-52 and PSR B1951+32 can. However, the spectrum shown in Fig.3.7 with the new high COMPTEL flux is not consistent with their model spectrum, very similar to the Vela situation. For the latter they concluded that or the curvature radius of the top field line in the outer gap has to become larger, or that an explanation in terms of the thin outer gap model is required. This holds now also for PSR B1951+32.

Acknowledgements. The COMPTEL project is supported by NASA under contract NAS5-26645, by the Deutsche Agentur für Raumfahrtangelegenheiten (DARA) under grant 50 QV90968 and by the Netherlands Organisation for Scientific Research (NWO). AC research is sponsored by the CONACYT grant 4142-E.

References

Angelini, L., White, N.E., Parmar, A.N., et al. 1988, ApJ 330, L43
 Angerhofer, P.E., Strom, R.G., Velusamy, T., et al. 1981, A&A 94, 313
 Arons, J. 1983, ApJ 266, 215
 Bennett K., Buccheri, R., Bussetta, M., et al. 1990, Proc. 21st ICRC, 1, 181
 Bloemen H., Hermsen, W., Swanenburg, B.N., et al. 1994, ApJS 92, 419

Buccheri, R., Bennett, K., Bignami, G.F., et al. 1983, A&A 128, 245
 de Boer, H., Bennett, K., Bloemen, H., et al., 1992, in: Data Analysis in Astronomy IV, Di Gesù, et al. (eds.). Plenum, New York, p. 241
 Carramiñana, A., Bennett, K., Buccheri, R., et al. 1995, A&A 304, 258
 Chang, H.-K., Ho, C. 1997, ApJ 479, L125
 Cheng, L., Li, T., Sun, X., et al. 1994, Ap&SS 213, 135
 Cheng, K.S., Ho, C., Ruderman, M.A. 1986, ApJ 300, 500
 Chiang, J., Romani, R. 1992, ApJ 400, 629
 Cordes J.M., Backer, D. C., Foster, R. S., et al. 1992, GRO/radio timing data base, Princeton University.
 Daugherty, J.K., Harding, A.K. 1982, ApJ 252, 337
 Daugherty, J.K., Harding, A.K. 1996, ApJ 458, 278
 Fierro, J.M., 1995, Ph. D. thesis, Stanford University
 Foster, R.S., Backer, D.C., Wolszczan, A., 1990, ApJ 356, 243
 Foster, R.S., Lyne, A.G., Shemar, S.L., et al. 1994, AJ 108, 175
 Fruchter, A.S., Taylor, J.H., Backer, D.C., et al. 1988, Nat 331, 53
 Harding, A.K., 1981, ApJ 245, 267
 Hermsen, W., Kuiper, L., Schönfelder, V., et al. 1997, in: The Transparent Universe, Winkler et al. (eds), ESA-SP-382, p. 287
 de Jager, O.C., Swanepoel J.W.H., Raubenheimer B.C. 1986, A&A 170, 187
 Kuiper, L., Hermsen, W., Bennett, K., et al. 1996, A&AS 120, C73
 Kuiper, L., Hermsen, W., Schönfelder, V., et al. 1998, in: "The many faces of neutron stars", Buccheri et al. (eds), NATO ASI (in press)
 Kulkarni, S.R., Clifton, T.C., Backer, D.C., et al. 1988, Nat 331, 50
 Li, T., Li, J., Ma, Y., et al. 1990, Chin. Astron. Astrophys. 14, 10
 McConnell, M., Bennett, K., Bloemen, H., et al. 1997, Proc. AIP conf., 410, 829, "Proceedings of the Fourth Compton Symposium", eds. C.D. Dermer, M.S. Strickman, and J.D. Kurfess
 Much, R., Bennett, K., Buccheri, R., et al. 1995, A&A 299, 435
 Ögelman, H., Buccheri, R., 1987, A&A 186, L17
 Ramanamurthy, P.V., Bertsch, D.L., Dingus, B.L., et al. 1995, ApJ 447, L109
 Ramanamurthy, P.V., Fichtel, C.E., Kniffen, D.A., et al., 1996, ApJ 458, 755
 Romani, R.W. 1996, ApJ 470, 469
 Romani, R.W., Yadigaroglu, I.A. 1995, ApJ 438, 314
 Ruderman, M.A., Sutherland, P.G. 1975, ApJ 196, 51
 Ruderman, M.A., Cheng, K.S., 1988, ApJ 335, 306
 Safi-Harb, S., Ögelman, H., Finley, J.P., 1995, ApJ 439, 722
 Schönfelder, V., Aarts, H., Bennett, K., et al., 1993, ApJS 86, 657
 Schroeder, P.C., Ulmer, M.P., Matz, S.M., et al., 1995, ApJ 450, 784
 Sturmer, S.J., Dermer, C.D., Michel, F.C. 1995, ApJ 445, 736
 Sturrock, P.A. 1971, ApJ 164, 529
 Thompson, D.J., Harding, A.K., Hermsen, W., et al. 1997, Proc. AIP conf., 410, 39, "Proceedings of the Fourth Compton Symposium", eds. C.D. Dermer, M.S. Strickman, and J.D. Kurfess
 van Dijk, R., 1996, Ph. D. thesis, Univ. of Amsterdam
 Wilson, R.B., Fishman, G.J., Finger, M.H., et al. 1992, Proc. AIP conf., 280, 291, "Compton Gamma-ray Observatory", eds. M. Friedlander, N. Gehrels, and D.J. Macomb
 Zhang, L., Cheng, K.S. 1997, ApJ 487, 370

Chapter 4

COMPTEL detection of pulsed γ -ray emission from PSR B1509-58 up to at least 10 MeV

L. Kuiper², W. Hermsen², J.M. Krijger^{2,7}, K. Bennett³, A. Carramiñana⁴, V. Schönfelder¹, M. Bailes⁶, and R.N. Manchester⁵

¹ Max-Planck Institut für Extraterrestrische Physik, D-8046 Garching, Germany

² SRON-Utrecht, Sorbonnelaan 2, NL-3584 CA Utrecht, The Netherlands

³ Astrophysics Division, European Space Research and Technology Centre, NL-2200 AG Noordwijk, The Netherlands

⁴ I.N.A.O.E., Apartado Postal 51 y 216, Puebla 72000, Puebla, México

⁵ Australia Telescope National Facility, CSIRO, PO Box 76, Epping NSW 2121, Australia

⁶ Astrophysics and Supercomputing, Swinburne University of Technology, PO Box 218 Hawthorn, Victoria 3122 Australia

⁷ Astronomical Institute, Utrecht University, NL-3508 TA Utrecht, The Netherlands

Astron. Astrophys. 351, 119-132 (1999)

Abstract. We report on the first firm detection of pulsed γ -ray emission from PSR B1509-58 in the 0.75-30 MeV energy range in CGRO COMPTEL data collected over more than 6 years. The modulation significance in the 0.75-30 MeV pulse-phase distribution is 5.4σ and the lightcurve is similar to the lightcurves found earlier between 0.7 and 700 keV: a single broad asymmetric pulse reaching its maximum 0.38 ± 0.03 in phase after the radio peak, compared to the offset of 0.30 found in the CGRO BATSE soft gamma-ray data, and 0.27 ± 0.01 for RXTE (2-16 keV), compatible with ASCA (0.7-2.2 keV).

Analysis in narrower energy windows shows that the single broad pulse is significantly detected up to ~ 10 MeV. Above 10 MeV we do detect marginally significant (2.1σ) modulation with an indication for the broad pulse. However, imaging analysis shows the presence of a strong 5.6σ source at the position of the pulsar. To investigate this further, we have also analysed contemporaneous CGRO EGRET data (> 30 MeV) collected over a nearly 4 year period. In the 30-100 MeV energy window, adjacent to the COMPTEL 10-30 MeV range, a 4.4σ source can be attributed to PSR B1509-58. Timing analysis in this energy window yields an insignificant signal of 1.1σ , but with a shape somewhat similar to that of the COMPTEL 10-30 MeV lightcurve. Combining the two pulse-phase distributions results in a suggestive double-peaked pulsed signal above the background level estimated in the spatial analyses, with one broad peak near phase 0.38 (aligned with the pulse observed at lower energies) and a second narrower peak near phase 0.85, which is absent for energies below 10 MeV. The modulation significance is, however, only 2.3σ and needs confirmation.

Spectral analysis based on the excess counts in the broad pulse of the lightcurve shows that extrapolation of the OSSE power-law spectral fit with index -1.68 describes

our data well up to 10 MeV. Above 10 MeV the spectrum breaks abruptly. The precise location of the break/bend between 10 and 30 MeV depends on the interpretation of the structure in the lightcurve measured by COMPTEL and EGRET above 10 MeV.

Such a break in the spectrum of PSR B1509-58 has recently been interpreted in the framework of polar cap models for the explanation of gamma-ray pulsars, as a signature of the exotic photon splitting process in the strong magnetic field of PSR B1509-58. For that interpretation our new spectrum constrains the co-latitude to $\sim 2^\circ$, close to the “classical” radius of the polar cap. In the case of an outer-gap scenario, our spectrum requires a dominant synchrotron component.

4.1. Introduction

PSR B1509-58 was discovered as a 150 ms X-ray pulsar in the *Einstein* HRI and IPC (0.2-4 keV) data from observations performed in 1979 and 1980 of supernova remnant (SNR) MSH 15-52 (Seward & Harnden 1982). The pulsations and the large period derivative indicated in the X-ray data were soon confirmed at radio-wavelengths (Manchester et al. 1982), while the derived dispersion measure supports its association with the SNR. The inferred characteristic age is 1570 year and the component of the surface magnetic field perpendicular to the spin axis at the magnetic pole is 3.1×10^{13} Gauß, one of the highest among the steadily growing sample of radio-pulsars. Radio-data collected during an 11 yr time span showed that the pulsar did not glitch and made a detailed study of its slow-down possible (Kaspi et al. 1994). The measured braking index was $n = 2.837(1)$, close to $n = 3$ expected for a dipole.

Extensive X-ray studies of PSR B1509-58 and its environment have been performed in the early eighties at soft- and medium X-ray energies using the *Einstein* HRI, IPC and SSS (Seward et al. 1983,1984) and MPC (Weisskopf et al. 1983) instruments and in the late eighties using the EXOSAT ME and LE instruments (Trussoni et al. 1990). The morphology of MSH 15-52 at X-rays is complex with at the north western rim of the SNR an excess near the H α nebula RCW 89 and close to the middle of the SNR a clump containing the pulsar surrounded by a diffuse synchrotron nebula. The spectrum of the pulsar is hard with a photon power-law index of $\sim -1.1 \pm 0.1$ (Trussoni et al. 1990). The pulse is broad with a duty cycle of $\sim 50\%$ and rather asymmetric: a sharp rise followed by a gradual decline. At soft X-ray energies (< 2 keV) there is some indication that the broad pulse is composed of two smaller narrowly separated pulses (EXOSAT LE, Trussoni et al. 1990; ROSAT PSPC, Becker 1994).

More recently, the results from ROSAT PSPC/HRI (Greiveldinger et al. 1995, Trussoni et al. 1996, and Brazier & Becker 1997) and ASCA (Nagase et al. 1994, Tamura et al. 1996 and Saito et al. 1997) observations were presented. Using the high-spectral resolution of ASCA in combination with imaging (Tamura et al. 1996) and the high-spatial resolution of the ROSAT HRI (Brazier & Becker 1997) the morphology of the remnant can be explained by the presence of several components: the pulsar itself, a non-thermal nebula powered by the pulsar with collimated outflow structures (jets) and a hot thermal plasma at RCW 89 near the end of the jet. Assuming that the synchrotron nebula surrounding the pulsar can be described in terms of a torus and jets similar to the Crab pulsar, the morphology suggests a large angle between pulsar spin axis and line of sight.

The detection of pulsed emission at hard X-rays was first reported by Kawai et al. (1991) using Ginga LAC 2-60 keV data. They found that the X-ray pulse lags the radio pulse by 0.25 ± 0.02 in phase. The spectrum of the pulsed emission could be represented by a power-law with photon index -1.3 ± 0.05 confirming its hard nature (Kawai et al. 1993). Wilson et al. (1993a,1993b) showed that pulsed emission was even detectable in the soft γ -ray regime using CGRO BATSE data (20-740 keV), confirmed later by Ulmer et al. (1993) and Matz et al. (1994) using CGRO OSSE data. The OSSE/BATSE pulse phase distribution (lightcurve) showed a phase offset with respect to the radio-pulse of 0.32 ± 0.02 , slightly larger than the value obtained from the Ginga data. The OSSE spectrum above 50 keV of the pulsed emission could be described by a power-law with photon index -1.68 ± 0.09 , consistent with the spectral findings, $\alpha = -1.64 \pm 0.42$, from the balloon-borne Welcome instrument (94-240 keV) as reported by Gunji et al. (1994). The spectral measurements by EXOSAT, Ginga, Welcome, OSSE/BATSE suggest a spectral steepening (softening) towards higher energies.

Recently, Rossi XTE absolute timing results on PSR B1509-58 were presented by Rots et al. (1998) showing high resolution pulse profiles for energies between 2 and 128 keV. A comparison of the profiles measured by RXTE (2-16 keV) and BATSE (> 32 keV) was made and a 0.03 phase shift of the BATSE lightcurve w.r.t. the RXTE lightcurve, peaking at 0.27 ± 0.01 , was found by the authors. Rots et al. (1998) also performed a pulse-phase resolved spectral analysis using PCA and HEXTE data. The photon indices of the power-law fits to the 2 - 200 keV data in various 0.05 wide phase slices within the pulse are all consistent with one single value of $\alpha = -1.345 \pm 0.01$. This value is in line with the value of -1.3 ± 0.05 found by Kawai et al. (1991). RXTE spectral results for both the pulsed and unpulsed component are described in detail by Marsden et al. (1998): the spectrum of the pulsed component (radio phase range 0.17 and 0.53) could be represented by a power-law with index -1.358 ± 0.014 with no evidence for a spectral break seen up to ~ 200 keV, while the index of the unpulsed component was -2.215 ± 0.005 .

At high-energy gamma-rays (> 30 MeV) Brazier et al. 1994 reported only upper-limits for pulsed emission using CGRO EGRET data from 3 viewing periods (VP 12, 23 and 27; see e.g. Table 4.1) during the all-sky survey of CGRO. A study by Fierro (1995) analysing EGRET data from Cycle I-III yielded an interesting $\sim 4\sigma$ source feature for energies above 100 MeV consistent in position with the pulsar. Timing analyses resulted in non-detections for pulsed emission in the 30-100 MeV, > 100 MeV and > 1 GeV energy windows.

The detection of hard pulsed emission below ~ 700 keV and the non-detection above 30 MeV makes PSR B1509-58 a very interesting candidate for COMPTEL, the Compton Telescope aboard CGRO and sensitive to photons with energies between ~ 0.75 and 30 MeV. COMPTEL analysis using viewing period 23 (see Table 4.1) data only yielded an interesting $\gtrsim 3\sigma$ detection of pulsed emission in the 0.75-1 MeV energy window with a pulse aligned with the pulse observed by BATSE/OSSE (Hermesen et al. 1994, Carramiñana et al. 1995). However, a timing analysis of COMPTEL 0.75-30 MeV data from observations spread over more than 4 years yielded only a marginal detection of pulsed emission at energies below 3 MeV (Carramiñana et al. 1997). Here, we will report on the COMPTEL timing- and spatial analyses using all available data up to and including CGRO Cycle-6 data. Prompted by our results in the highest standard energy interval (10-30 MeV) in the COMPTEL analysis, we also (re)analysed all publicly available EGRET data on this source.

4.2. Instrument description and observations

COMPTEL is the imaging Compton Telescope aboard CGRO and is sensitive for γ -ray photons with energies in the 0.75-30 MeV range. Its detection principle relies on a two layer interaction: a Compton scatter in one of the

Table 4.1. COMPTEL observations used in current study with PSR B1509-58 less than 30° off-axis

VP #	Start Date TJD [†]	End Date TJD	Pointing direction		Off-axis angle ($^\circ$)	Eff.Exposure (3-10 MeV; $10^6 \text{ cm}^2 \text{ s}$)	EGRET spark- chamber status
			l($^\circ$)	b($^\circ$)			
Cycle I						18.70	
12.0	8546.620	8560.622	310.7	22.2	25.2	8.30	ON
23.0	8700.598	8714.534	322.2	3.0	4.6	3.74	ON
27.0	8740.573	8749.589	332.2	2.5	12.4	4.55	ON
35.0	8840.658	8845.038	335.1	-25.6	28.3	0.83	ON
38.0	8861.745	8866.192	335.1	-25.6	28.3	1.28	ON
Cycle II						11.71	
208.0	9020.627	9027.675	307.4	20.7	25.3	2.32	ON
215.0	9078.693	9083.810	311.7	22.9	25.5	4.32	ON
217.0	9089.577	9097.596	311.7	22.9	25.5	\perp	ON
232.0	9223.612	9225.197	347.5	0.0	27.2	5.07	ON
232.5	9225.219	9237.590	347.5	0.0	27.2	\perp	ON
Cycle III						23.97	
314.0	9355.682	9368.637	304.2	-1.0	16.1	9.21	ON
315.0	9368.656	9375.646	304.2	-1.0	16.1	5.32	ON
316.0	9375.671	9384.606	309.5	19.4	23.1	5.39	ON
336.5	9568.601	9573.884	340.4	2.9	20.5	3.11	ON
338.0	9593.637	9595.602	345.0	2.5	24.9	0.94	OFF
Cycle IV						27.01	
402.0	9643.633	9650.588	310.3	-5.0	10.7	12.71	ON
402.5	9650.614	9657.588	306.7	-3.8	13.9	\perp	ON
414.3	9805.592	9811.587	347.3	0.6	27.0	2.70	OFF
423.5	9898.619	9908.569	345.8	13.4	29.2	3.86	ON
424.0	9908.592	9923.596	312.7	19.0	21.5	7.74	ON
Cycle V						13.49	
516.1	10160.640	10163.650	341.1	5.5	21.8	1.71	ON [♣]
524.0	10273.592	10287.601	343.1	-3.6	22.9	7.22	OFF
529.5	10322.664	10332.579	345.0	2.4	24.9	4.56	ON [♣]
Cycle VI						42.95	
619.0	10574.621	10582.557	319.6	-1.6	0.9	6.86	OFF
619.4	10588.601	10596.510	319.6	-1.6	0.9	6.36	OFF
619.7	10603.617	10609.567	319.6	-1.6	0.9	5.21	OFF
632.1	10728.603	10755.605	307.9	-7.5	13.9	24.52	OFF

[†] TJD = JD - 2440000.5 = MJD - 40000

[♣] EGRET in narrow field mode; opening angle FoV is 19°

7 upper-detector (D1) modules followed by a second interaction in one of the 14 lower-detector (D2) modules. Main measured quantities are the angles (χ, ψ) specifying the direction of the scattered photon (from the interaction loci in D1 and D2) and the energy deposits in the D1/D2 modules where the interactions took place. From the last two quantities we can calculate the scatter angle $\bar{\varphi}$ and the total energy deposit E_{tot} (see for a full description Schönfelder et al. 1993).

Its energy resolution is 5-10% FWHM and due to its large field of view of typically 1 steradian it is possible to monitor a large part of the sky simultaneously with a position determination accuracy of $\sim 1^\circ$. The events are time tagged with an accuracy of 0.125 ms.

In this study we selected those CGRO Cycle I-VI viewing periods for which the angle between the pointing axis (co-aligned with the COMPTEL/EGRET z-axis) and PSR B1509-58 is less than 30° . Details for each individual observation can be found in Table 4.1. The last but one column specifies the effective exposure in the 3-10 MeV energy window assuming a E^{-2} dependency of the photon flux. The calculation took into account Earth blocking effects and utilizes the timeline information. The last column indicates the status of the sparkchamber of the EGRET high-energy (30 MeV - 30 GeV) instrument aboard CGRO. EGRET data (with the sparkchamber ON) from the first 4 CGRO observation Cycles have been retrieved from the COMPTON Science Support Center and have subsequently been used in spatial- and timing analyses.

Table 4.2. PSR B1509-58 radio-ephemerides

Pulsar position		Validity range		t^0	ν	$\dot{\nu}$	$\ddot{\nu}$	ϕ_0
α_{2000}	δ_{2000}	[MJD]		[MJD/TDB]	[Hz]	[Hz/s]	[Hz/s ²]	
†15 13 55.627	-59 08 9.54	48522	49956	49239	6.6324050404788	-6.75457×10^{-11}	1.96×10^{-21}	0.93162
‡15 13 55.620	-59 08 9.00	50114	50722	50418	6.6255346044703	-6.73467×10^{-11}	1.94×10^{-21}	0.64393

† Ephemeris has been provided by V. Kaspi (private communication).

‡ Ephemeris has been derived from radio timing data using the ATNF Parkes radio telescope.

(see also <http://www.atnf.csiro.au/research/pulsar/psr/archive/>)

The dispersion measure used in the calculation of absolute phases was 253.2 pc cm^{-3} .

4.3. COMPTEL timing analysis

4.3.1. Event selections

Prior to the actual timing analysis we have to specify the event selection criteria to which the events are subjected. The selection criteria applied here are the same as those in the timing analysis of PSR B1951+32 (see Kuiper 1998a) except for one selection parameter, namely φ_{arm} , the difference angle between the calculated scatter angle $\bar{\varphi}$ and the geometrical scatter angle φ_{geo} . The last quantity can be determined from the known source position ($(l, b) = (320^\circ.321, -1^\circ.162)$) and the scatter direction angles (χ, ψ). For a point-source the distribution of φ_{arm} (i.e. the ARM-distribution) is a narrowly peaked distribution with a maximum near $\varphi_{arm} = 0$ and a wing for positive φ_{arm} values due to incompletely absorbed events. The imaging capabilities of COMPTEL rely on this sharp asymmetric distribution of φ_{arm} . The relative contributions of the peak and wing, and the width of the peak are a function of input photon energy. This means that instead of fixing $|\varphi_{arm}|$ to a value in the range $2^\circ.5$ to $3^\circ.5$ irrespective of the selected energies, as turned out to be the optimum range from COMPTEL studies on the Crab (Much et al. 1995) and Vela (Kuiper et al. 1998b) pulsars, an energy window dependent ARM selection is more appropriate. In this study we have determined *a priori* the optimal value of $|\varphi_{arm}|$ for each energy window by estimating the maximum in the Signal-to-Noise vs. $|\varphi_{arm}|$ relation. The latter relation can be derived from a 3 dimensional ($\chi, \psi, \bar{\varphi}$) point source model for the energy window involved and the total measured 3d-event distribution in the same energy window, heavily dominated by instrumental background events (90-95%). The following energy dependent criteria on $|\varphi_{arm}|$ appeared to be appropriate: $3^\circ.5$ for the energy window 0.75-1 MeV and $2^\circ.5$ for the energy windows 1-3, 3-10 and 10-30 MeV. The fraction of counts from a point-source within the ARM-cut is typically $\sim 60\%$. It is also worth mentioning that the ARM cut applied in the timing analysis reduces the number of events handled in the timing analysis to typically 10% of the number of events available for the imaging or spatial analysis, in which the full 3d-dataspace is employed. For the 10-30 MeV interval we have departed from the ‘‘stan-

ard’’ Time of Flight (TOF) and Pulse Shape Discrimination (PSD) windows (see for a description of these event parameters Schönfelder et al. 1993) of 113-130 and 0-110 respectively, normally applied in the timing analysis (see e.g. Kuiper 1998a) and have used the optimum TOF and PSD windows derived by Collmar et al. (1997) in their study on optimum parameter cuts using the Crab pulsar/nebula signature in the COMPTEL event space.

4.3.2. Pulse phase folding

Once the event selection criteria were settled we proceeded as follows: the arrival times (recorded with an intrinsic resolution of 0.125 ms) of the events passing through our selection filters are converted to arrival times at the Solar System Barycentre (SSB) using the known instantaneous spacecraft position, the source position and the solar system ephemeris (JPL DE200 Solar System Ephemeris). The pulse phase ϕ is calculated from the following timing model:

$$\phi = \nu \cdot \Delta t + 1/2 \cdot \dot{\nu} \cdot \Delta t^2 + 1/6 \cdot \ddot{\nu} \cdot \Delta t^3 - \phi_0 \quad (4.1)$$

In this formula Δt is given by $\Delta t = t^e - t^0$ with t^e the event SSB arrival time and t^0 the reference epoch. The values employed here for $t^0, \nu, \dot{\nu}, \ddot{\nu}, \phi_0$ are given in Table 4.2. The RMS error of the timing models listed in Table 4.2 is typically 10 milli-periods or 1.5 ms, sufficiently accurate to keep coherency and allowing pulse phase folding over long time spans indicated by the validity range.

4.3.3. Pulse profiles in the 0.75-30 MeV energy range

The pulse phase distribution resulting from phase-folding COMPTEL Cycle I-VI 0.75-30 MeV data is shown in Fig. 4.1. The modulation significance of the unbinned sample of pulse-phases is 5.4σ employing a Z_n^2 -test (Buccheri et al. 1983) with 2 harmonics. This is the first *firm* detection of pulsed emission above 0.75 MeV from PSR B1509-58. The pulse is roughly aligned with the pulse observed by OSSE/BATSE (Ulmer et al. 1993) and peaks at phase 0.38 ± 0.03 (obtained from a Gaussian + background fit). We have split the integral energy window of 0.75-30 MeV up into 3 smaller energy windows, 0.75-3 MeV, 3-10

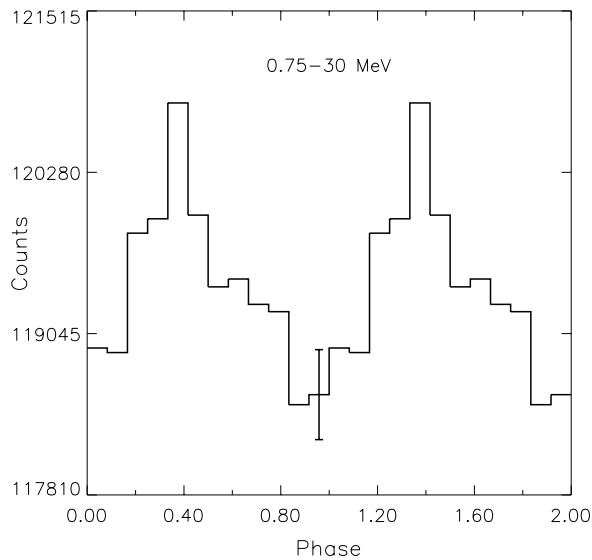


Fig. 4.1. Radio-aligned (radio pulse at phase 0) 0.75-30 MeV COMPTEL lightcurve of PSR B1509-58. A double cycle is shown for clarity. Data from Cycle I-VI observations (see Table 4.1) have been used. The modulation significance is 5.4σ adopting a Z_2^2 -test. A typical error bar is indicated.

MeV and 10-30 MeV and performed similar timing analyses. The modulation significances (Z_2^2 -test) found for the 3 energy windows are 3.7σ , 4.0σ and 2.1σ respectively, proving the detection of pulsed emission up to at least 10 MeV. The lightcurves are shown in Fig. 4.2. The 10-30 MeV lightcurve, having at face value a non-significant modulation, shows an indication for an enhancement in the phase range containing the pulse at lower energies. However, a narrower pulse might be visible near phase 0.85, which is absent at lower energies. A more detailed discussion on the 10-30 MeV lightcurve will be given once the spatial analysis, enabling the measurement of the *total* flux from a source, has been introduced.

4.3.4. Pulse profiles from soft X-rays to medium energy γ -rays

Rots et al. (1998) studied the pulse shape of PSR B1509-58 as a function of energy at medium and hard X-ray energies. He found that the RXTE 2-16 keV pulse peak lags the radio peak by 0.27 ± 0.01 in phase. This value is consistent with the lag of 0.25 ± 0.02 found in Ginga 2-60 keV data by Kawai et al. (1991). Ulmer et al. (1993) found at soft γ -ray energies a phase lag of 0.32 ± 0.02 in CGRO BATSE and OSSE data. The difference of 0.05 ± 0.022 (2.3σ effect) between these values was considered troublesome by Rots et al. (1998). It could not be attributed to a CGRO clock absolute timing uncertainty and this triggered Rots et al. (1998) to reprocess 5 years of BATSE data yielding now a slightly smaller phase lag of 0.30 consistent both

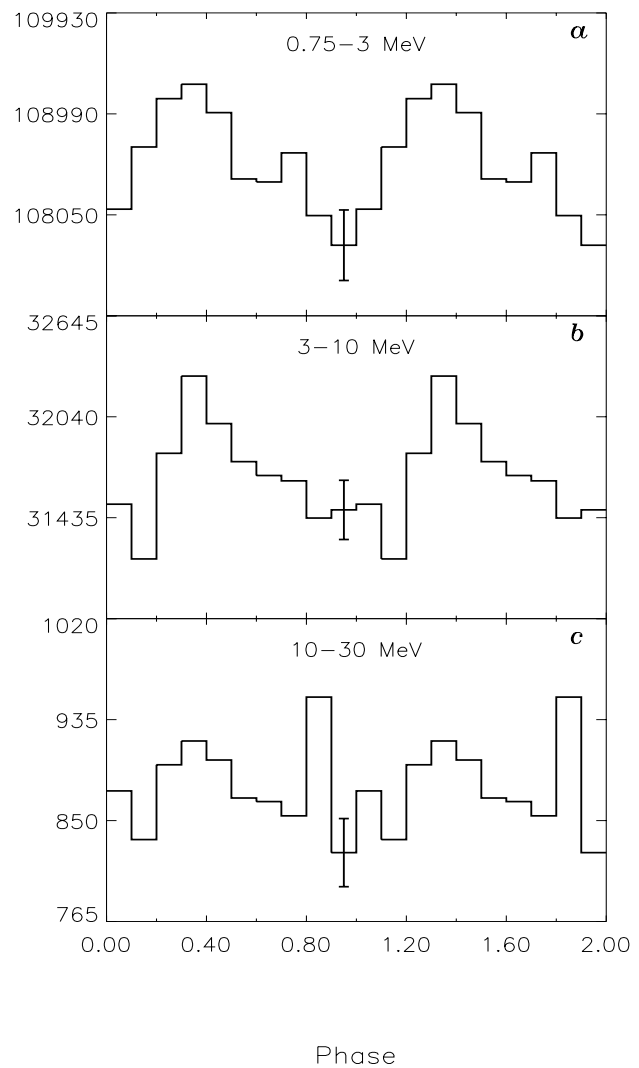


Fig. 4.2. Radio-aligned COMPTEL Cycle I-VI lightcurves of PSR B1509-58 for 3 different energy windows: 0.75-3 MeV (a), 3-10 MeV (b) and 10-30 MeV (c). Double cycles are shown for clarity, while typical error bars are indicated. The modulation significances adopting a Z_2^2 -test are 3.7σ , 4.0σ and 2.1σ for the energy windows 0.75-3 MeV, 3-10 MeV and 10-30 MeV respectively. This proves that pulsed emission is detected at least up to 10 MeV.

with Ulmer's previous estimate and also with the RXTE estimate.

The remaining (insignificant) difference of 0.03 ± 0.022 ($= 5$ ms) still seems to be too large to be explained by CGRO/RXTE clock uncertainties and could be due to intrinsic pulsar emission properties. Rots et al. (1998) also investigated the effect of the pulsar dispersion measure on the phase offset of the radio- and RXTE X-ray pulse. Using the most recent value of the dispersion measure of PSR B1509-58 of 255.3 ± 0.3 $pc\ cm^{-3}$ instead of the widely used value of 253.2 ± 1.9 $pc\ cm^{-3}$ results in an offset of 0.29 ± 0.01 , indicating that uncertainties in the dispersion measure can

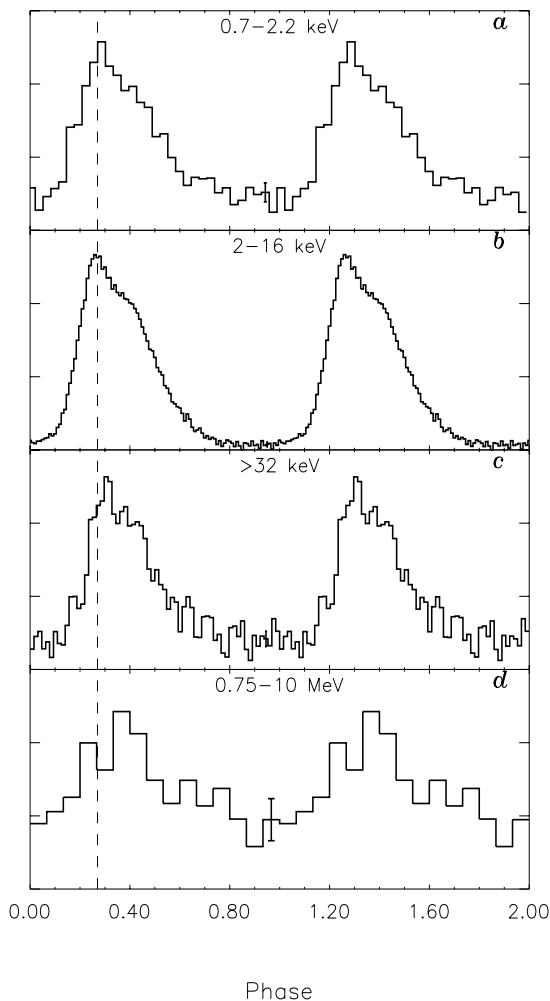


Fig. 4.3. Radio-aligned lightcurves of PSR B1509-58 from soft X-rays to medium energy γ -rays: **a)** ASCA 0.7-2.2 keV (Saito et al. 1997; private communication), **b)** RXTE 2-16 keV (Rots et al. 1998), **c)** BATSE > 32 keV (Rots et al. 1998) and **d)** COMPTEL 0.75-10 MeV. The dashed vertical line indicates the phase lag of 0.27 found in the RXTE lightcurves. Note that the “center of mass” of the pulse appears to shift towards higher pulse phases for higher energies, with the maximum of the pulse at MeV-energies (COMPTEL) coinciding in phase with the “shoulder” visible in the pulse shape at X-ray energies. Typical 1σ error bars are indicated in each figure at phase 0.95.

result in uncertainties in the radio/X-ray pulse phase lag of ~ 0.02 .

The RXTE 2-16 keV profile consists of a broad asymmetric pulse: a rapidly rising pulse reaching its maximum near phase 0.27 followed by a more gradual decline with a “shoulder” near phase 0.40. This profile is shown in Fig. 4.3b along with the X-ray/soft γ -ray profiles measured by different instruments in different energy windows. It is clear from this collage that the ASCA 0.7-2.2 keV soft X-ray profile is in detail very similar to the RXTE 2-16 keV hard X-ray profile. The BATSE > 32 keV soft γ -ray pro-

file also resembles the RXTE profile except for an apparent overall offset of 0.03 with respect to the RXTE profile. The COMPTEL 0.75-10 MeV lightcurve on the other hand reaches its maximum near 0.38 which coincides in phase with the shoulder clearly visible in the RXTE lightcurve. Whether this apparent offset has a statistical origin (cf. the typical error bar in the COMPTEL 0.75-10 MeV lightcurve which has a mean level of ~ 93000 counts in this 15 bin lightcurve) or is due to an intrinsic property of the pulsar’s high-energy emission is difficult to decide. The intrinsic timing-resolution of 0.125 ms of CGRO/COMPTEL is sufficiently accurate to allow the lightcurve to be binned in several hundreds of bins and can *not* be responsible for the offset. Also, BATSE and COMPTEL use the same CGRO clock.

In order to study the difference in morphology between the COMPTEL 0.75-10 MeV and RXTE 2-16 keV lightcurves we have fitted the RXTE 2-16 keV profile in terms of a background and two Gaussians (7 free parameters). This resulted in a narrow component peaking at phase 0.250 ± 0.008 with width 0.056 ± 0.008 and a broader component at 0.386 ± 0.012 and width 0.129 ± 0.006 . The first narrow pulse accounts for $25.7 \pm 4.3\%$ of the total pulsed emission. A similar fit has been performed on COMPTEL 0.75-10 MeV data, but now with positions and widths fixed to the values found in the RXTE 2-16 keV fit (3 free parameters). In this case the first narrow pulse can account for only $13 \pm 18\%$ of the total pulsed emission, consistent with being absent, and the profile can satisfactorily be described by just the broad second pulse near 0.39. This strongly suggests that the pulse shape changes from soft X-rays to medium energy γ -rays.

4.3.5. Pulsed 0.75-30 MeV fluxes from the excess counts in the lightcurves

Based on the RXTE 2-16 keV lightcurve we have defined a “pulsed” and an “unpulsed” phase interval in the pulse phase distribution: the pulsed interval extends from phase 0.15 to 0.65 and the unpulsed (background) interval from 0.65 to 1.15. This break-down is such that for a pulse shape as measured by RXTE 90.4% of the pulse is located in the “pulsed” interval.

Applying this definition to the COMPTEL data we can determine the pulsed excess counts in various energy slices by estimating the underlying background as the averaged level in the unpulsed part of the lightcurve. We derived these pulsed excess counts for the 0.75-3, 3-10 and 10-30 MeV energy windows and converted these to pulsed flux values taking into account efficiency correction factors due to the applied ARM cuts in the timing-analysis (see Table 4.3).

The weak 10-30 MeV flux value should be treated with care because we do not detect significant modulation (2.1σ). Moreover, the lightcurve shows indications for a second pulse in the “unpulsed”(background) phase interval.

Table 4.3. PSR B1509-58 pulsed fluxes derived from the timing analysis with the “pulsed” interval defined to be phases 0.15-0.65.

E -window	Flux $ph/cm^2 \cdot s \cdot MeV$
0.75 – 3 MeV	$(3.69 \pm 0.73) \times 10^{-5}$
3.0 – 10 MeV	$(4.52 \pm 0.77) \times 10^{-6}$
10.0 – 30 MeV	$(1.21 \pm 0.85) \times 10^{-7}$

If this pulse is genuine, then the true flux is underestimated (see next section).

4.4. COMPTEL spatial analysis

4.4.1. Analysis method

The measured event parameters $(\chi, \psi, \bar{\varphi}, E_{tot})$ constitute a 4-dimensional data space, in which we have to search for a “source signature”. In practice the dimension of the data space is lowered by integrating along the E_{tot} direction between user selected boundaries. The event distribution of a point source (the Point Spread Function, PSF) in this reduced 3-d data space $(\chi, \psi, \bar{\varphi})$ is concentrated in a cone-shaped structure with its apex at the source position (χ_0, ψ_0) . In the spatial or imaging analysis we proceed as follows: We generate a background model from the sparsely filled event dataspace (3d) through sophisticated smoothing techniques (see e.g. Bloemen et al. 1994). Because the measured events in the 3d-dataspace are primarily internally generated background events ($\sim 90 - 95\%$) this background model represents a good approximation of the genuine instrumental background. The search for point sources in the measured 3d-dataspace is accomplished by a maximum likelihood ratio (MLR) test at scan positions in the selected sky field. In the null hypothesis \mathcal{H}_0 the measured events are described in terms of a background model alone, while in the alternative hypothesis \mathcal{H}_1 the data are described in terms of a background model and a point source at a given scan position. From the parameter optimizations under \mathcal{H}_1 we can derive the source flux. From the optimized likelihoods under \mathcal{H}_1 and \mathcal{H}_0 we can determine the maximum likelihood ratio λ at each scan position, giving us information on the detection significance of a source. For more detailed information see Kuiper et al. (1998a).

4.4.1.1. Imaging results for energies < 10 MeV

For consistency purposes we have produced MLR maps for the same energy windows (0.75-3 and 3-10 MeV) as used in the timing analysis, and also made selections on pulse phase, the “pulsed” and “unpulsed” windows introduced in Sect. 4.3.5, while we also considered the total emission, the sum of both. In Fig. 4.4 the MLR images are shown for the “pulsed” and “unpulsed” phase intervals in the energy win-

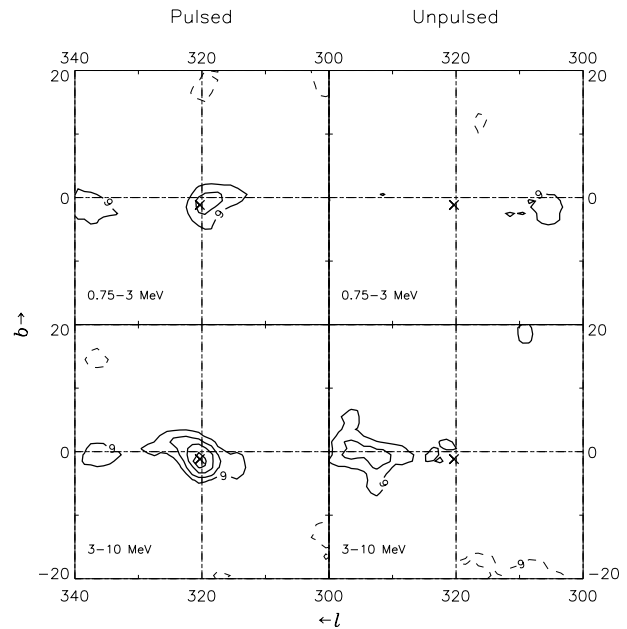


Fig. 4.4. COMPTEL “pulsed” (phases 0.15 - 0.65) and “unpulsed” (0.65 - 1.15) MLR maps for energies below 10 MeV. The upper panel shows the results for the 0.75-3 MeV energy window, the lower panel the 3-10 MeV analogon. The left side shows the pulsed maps and the right side the unpulsed maps. The solid contours start at the 3σ -significance level ($\lambda = 9$, 1 degree of freedom) in steps of 1σ . Significant emission at the pulsar position (\times symbol) is only observed in the “pulsed” maps.

dows 0.75-3 and 3-10 MeV. The contours start at an equivalent of 3σ in steps of 1σ for 1 degree of freedom (i.e. at $\lambda = 9, 16, 25, 36$ etc.), representative if the source position is *a priori* known.

From these maps it is evident that significant emission at the pulsar position (indicated by a “ \times ” mark) is only observed in the “pulsed” maps: 4.5σ in the 0.75-3 MeV energy window and 8σ in the 3-10 MeV window. From the maximum likelihood fits we can also obtain estimates for the source flux. However, in the maps shown in Fig. 4.4 the structured galactic diffuse emission is not included in the background model, and may contribute to the source flux. In addition, any pulsar/nebula DC-emission will contribute equally to the “pulsed” and “unpulsed” maps. Since λ is not zero at the source position in the “unpulsed” maps, we subtracted the measured fluxes (counts) in the “unpulsed” maps from those in the “pulsed” maps in order to obtain independent estimates of the “pulsed” fluxes. For the 0.75-3 MeV interval we found 7202 ± 1386 counts correlating with a point source at the pulsar position in the “pulsed” interval and 2264 ± 1382 in the “unpulsed” interval. The difference of 4938 ± 1960 is consistent with the pulsed excess counts in the timing analysis. The number of counts found in the “unpulsed” window can be fully attributed to contributions of galactic diffuse origin, as has been verified in a simulation of the galactic diffuse emission using the model com-

ponents and scale factors found by Bloemen et al. (1999). This means that there is no room for any significant pulsar or nebula DC-component in this energy window.

For the 3-10 MeV energy interval we obtained a similar picture. In this case we find 5233 ± 593 counts correlating with a point source at the pulsar position in the “pulsed” map and 2755 ± 590 in the “unpulsed” map. This leaves 2478 ± 840 counts for the genuinely pulsed emission, consistent with the timing analysis results. The “unpulsed” value can again be explained with being of galactic diffuse origin.

In conclusion, the fluxes derived from the spatial analysis for energies below 10 MeV are consistent with those derived from the timing analysis and there is no evidence for the detection of DC-emission from the pulsar or its nebula.

4.4.1.2. Imaging results for energies > 10 MeV

In the 10-30 MeV energy window we did not detect a significant (2.1σ) modulation in the light curve, but an enhancement is visible in the pulse phase interval in which the pulse is concentrated at lower energies, and in the “unpulsed” interval a high bin shows up near phase 0.85. A MLR image (total) in this energy window yielded somewhat surprisingly a strong source feature ($\sim 6\sigma$) consistent in position with the pulsar, by simply fitting the source contribution above the instrumental background model.

It should be noted here that the 10-30 MeV energy window is COMPTEL’s “cleanest” window not polluted by time-varying instrumental background lines contrary to the energy intervals below 10 MeV. Estimates for the galactic diffuse emission in this energy window can be considered reliable (e.g. Strong et al. 1994, Bloemen et al. 1999) and are consistent with extrapolations towards lower energies of EGRET > 30 MeV measurements.

When we now include also the total galactic diffuse background model in the total background, the source remains (see Fig. 4.5). At the pulsar position a detection significance of 5.6σ is reached. A break-down into “pulsed” and “unpulsed” maps yields sources at the pulsar position with statistically equal fluxes in both maps. This can mean that we either detected DC-emission from the pulsar and/or its surrounding synchrotron nebula or emission from a nearby unrelated source. But, in these cases we would expect to see emission below 10 MeV where COMPTEL is more sensitive. Another possibility is that we actually detected pulsed emission but with a different pulse profile.

We investigated the latter possibility further. In this respect it is instructive to go back to the 10-30 MeV lightcurve and superpose the background level as determined in the spatial analysis from the total number of counts correlating with a source at the pulsar position above the instrumental and galactic diffuse background. The lightcurve with this spatially determined background level (and its 1σ -errors) is shown in Fig. 4.8a. The exist-

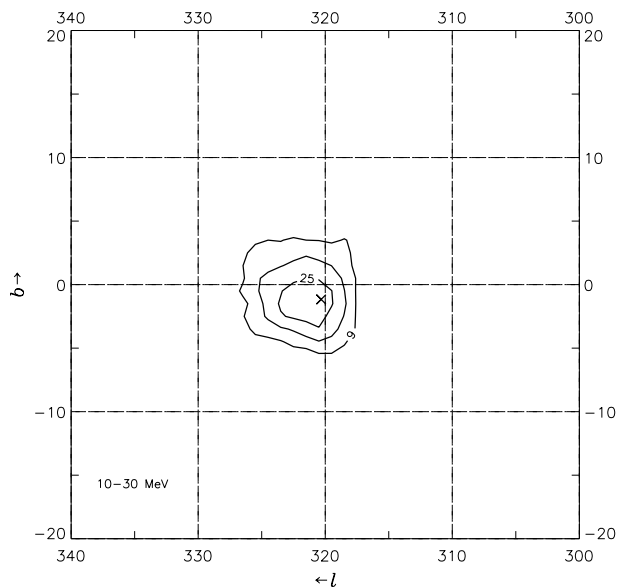


Fig. 4.5. COMPTEL “total” MLR map for the energy window 10-30 MeV, presenting the source detection significance above the instrumental and galactic diffuse background. A 5.6σ source is detected at the pulsar position. The solid contours start at the 3σ -significance level ($\lambda = 9$, 1 degree of freedom) in steps of 1σ . The pulsar position is marked by the \times symbol.

tence of the main pulse, definitely detected below 10 MeV, is again very suggestive for energies above 10 MeV. The number of excess counts in the “pulsed” interval (0.15-0.65) above of this spatially determined background level is 279 ± 57 counts, resulting in a flux of $(3.37 \pm 0.70) \cdot 10^{-7} \text{ ph/cm}^2 \cdot \text{s} \cdot \text{MeV}$. In the “unpulsed” region we find then a flux of $(2.16 \pm 0.70) \cdot 10^{-7} \text{ ph/cm}^2 \cdot \text{s} \cdot \text{MeV}$, predominantly due to the excess near phase 0.85. This $\sim 3\sigma$ feature above the spatially determined background, only shows up above 10 MeV and, if genuine, would indicate a new pulse component with a completely different spectral behaviour from that of the main pulse. This peculiar behaviour of the pulsed emission above 10 MeV in the COMPTEL energy range motivated us to analyze also the contemporaneous > 30 MeV EGRET data.

4.5. Analysis of EGRET data

No significant (pulsed) emission above 30 MeV has been reported from EGRET data, but, two papers (Brazier et al. 1994; Fierro 1995) report on weak (irregular) source features ($\sim 3\sigma$) near PSR B1509-58 for energies above 100 MeV. It is worth mentioning that in the first paper the analysis was constrained to data from CGRO Cycle I, namely VP’s 12, 23 and 27 (cf. Table 4.1), while in the second paper data from Cycles I to III were analyzed. Here, we reanalyzed all available Cycle I-IV EGRET data, the maximal exposure on the source. The observations used are those in Table 4.1 in which the spark chamber high-

voltage was enabled (see last column Table 4.1; the data of Cycle V do not contribute since EGRET operated in its narrow field mode with an effective FoV opening angle of 19°). Standard event selections were applied, however, the requirement of a minimum energy deposit of 6.5 MeV in the TASC was abandoned (for a description of EGRET see Thompson et al. 1993). This selection criterion is mainly effective for background suppression for measured total energies above 100 MeV. We verified using the Crab pulsar that for energies below 100 MeV the detection of the pulsed signal significantly increases when the TASC threshold of 6.5 MeV is ignored. In order to suppress Earth albedo γ -rays, standard Earth horizon angle cuts were applied for the differential energy ranges 30-50 MeV, 50-70 MeV and 70-100 MeV, which are roughly equivalent to a 3σ cut. For consistency, the same selections were applied in the spatial and timing analyses.

4.5.1. Spatial analysis

The imaging analysis of EGRET data is similar to that of COMPTEL data with the main difference that the EGRET analysis is performed in a 2-d dataspace. After reformatting the EGRET data and response for import in the COMPTEL Analysis and Software System COMPASS (de Vries 1994) we can use the same analysis programmes. One important difference is that the EGRET data are almost free of instrumental background. This means that the point source emission is searched for above of the dominating galactic and extragalactic γ -ray backgrounds only. The spatial structure of the first component, predominantly due to the interaction of cosmic rays and interstellar Hydrogen, is approximated by the measured total column density of atomic Hydrogen HI and molecular Hydrogen as traced by the CO-molecule, identical to our analysis of COMPTEL data. The latter component can simply be described by an isotropic model.

The MLR map for the 30-100 MeV energy window, adjacent to the COMPTEL 10-30 MeV window, combining all available Cycle I-IV data is presented in Fig. 4.6. A strong 6.7σ excess shows up near PSR B1509-58. Apart from the pulsar a few other identified and unidentified EGRET sources seem to be visible in the map (see figure caption).

The most likely sources responsible for the excess near $(l, b) = (320, 0)$ are PSR B1509-58 and 2EG J1443-6040 at $(l, b) = (316.28, -0.75)$. Fitting both sources simultaneously above of the galactic and extragalactic backgrounds, together with emissions from Cen-A and 2EGS J1429-4224 yields a 4.4σ excess at the position of PSR B1509-58 with a flux of $(3.3 \pm 1.0) \cdot 10^{-8} \text{ ph/cm}^2 \cdot \text{s} \cdot \text{MeV}$. This is shown in the MLR map of Fig. 4.7 in which the other three fitted sources and background emissions are “subtracted”. The detection significance of the source correlating with 2EG J1443-6040 is 2.6σ and has a flux of $(1.9 \pm 1.0) \cdot 10^{-8} \text{ ph/cm}^2 \cdot \text{s} \cdot \text{MeV}$. It should be noted that this unidentified EGRET source was only detectable

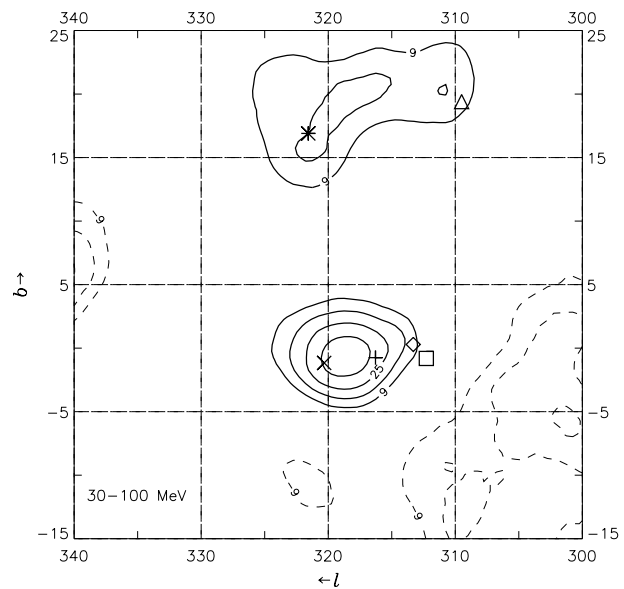


Fig. 4.6. EGRET “total” MLR map for the energy window 30-100 MeV, showing the likelihood of a source detection above of the galactic and extragalactic diffuse backgrounds. Contours of $\lambda = 9, 16, 25$ ($= 3, 4, 5 \sigma$); Solid contours positive values, broken ones negative values. Several identified and unidentified sources are indicated by different symbols: PSR B1509-58 (\times), Cen-A (Δ), and the unidentified EGRET sources 2EG J1412-6211 (\square), 2EG J1443-6040 ($+$), 2EGS J1418-6049 (\diamond) and 2EGS J1429-4224 ($*$) (see Thompson et al. 1995 and Thompson et al. 1996a). A 6.7σ source feature near $(l, b) = (320, 0)$ shows up and is likely composed of the contributions of PSR B1509-58 and the unidentified EGRET source 2EG J1443-6040.

in VP’s 12 and 27 and not during observations performed later on, indicating its likely transient behaviour. In fact, it does not appear anymore in the third EGRET source catalog (Hartman et al. 1999). (Note: After submission of this paper, the EGRET group, using analysis based on the third EGRET catalog, confirmed the finding of a 4.3σ significance source in the 30-100 MeV band, consistent in position with PSR B1509-58; D.J. Thompson, private communication).

We performed a similar imaging study in the 100-300 MeV energy window and found also a $\sim 2\sigma$ source feature near PSR B1509-58 above of the galactic and extra-galactic background, as well as the previously reported EGRET sources, consistent with the findings of Brazier et al. (1994) and Fierro (1995). The 100-300 MeV flux estimate for PSR B1509-58 is $(5.9 \pm 3.5) \cdot 10^{-10} \text{ ph/cm}^2 \cdot \text{s} \cdot \text{MeV}$. Even in the 300-1000 MeV window a marginal excess is visible consistent in position with PSR B1509-58 (flux $(4.5 \pm 3.6) \cdot 10^{-11} \text{ ph/cm}^2 \cdot \text{s} \cdot \text{MeV}$). Above 1000 MeV no excess is found. These low flux values can also be converted in upper-limits.

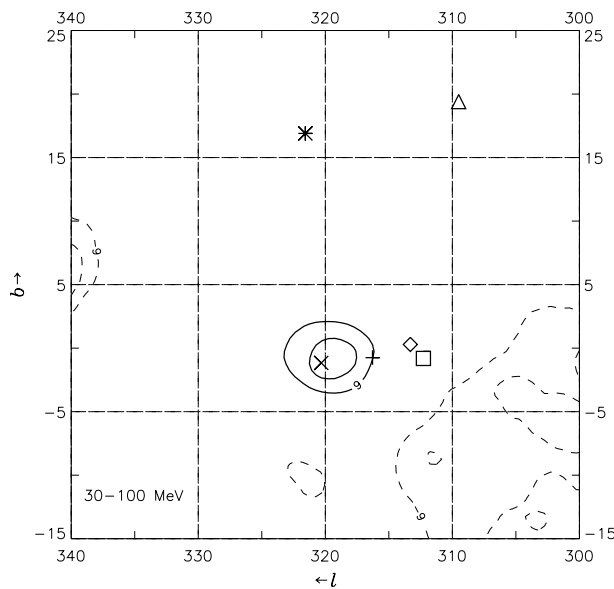


Fig. 4.7. EGRET MLR map for the energy window 30-100 MeV, as in Fig. 4.6. The contributions from 2EG J1443-6040, Cen-A and 2EGS J1429-4224 are subtracted. At the position of PSR B1509-58 (\times) a significance for a source detection of 4.4σ remains.

4.5.2. Timing analysis

Given the detection of a significant source in the spatial analysis for energies between 30 and 100 MeV, we first selected events in this energy range to search for the modulation. The event selection procedures in the EGRET timing analysis are equivalent to those applied in the COMPTEL timing analysis except that we are now dealing with a 2-dimensional dataspace. We applied an energy dependent cone selection (Thompson et al. 1996b) roughly selecting 68% of the source counts. In this 30-100 MeV energy interval we do not find significant modulation (1.1σ), although the shape of the pulse phase distribution bears some resemblance to the COMPTEL 10-30 MeV lightcurve. Both are shown in Fig. 4.8. Estimates of the underlying backgrounds as determined from the spatial analysis fitting PSR B1509-58 and 2EG J1443-6040 simultaneously are indicated. Also shown in the figure is the combined 10-100 MeV lightcurve, which has a modulation significance of 2.3σ for 2 harmonics in the Z_n^2 -test. Again, the summed background level determined in the spatial analyses is indicated, as well as the Kernel Density Estimator (KDE, de Jager et al. 1986) of the unbinned pulse-phase distribution with the $\pm 1\sigma$ error bounds. The KDE provides an (asymptotically) unbiased view on the genuine pulse shape. This lightcurve suggests a double-peaked profile: an enhancement in the previously defined “pulsed” interval, and a pulse near phase 0.85, which has become more pronounced in this summed lightcurve.

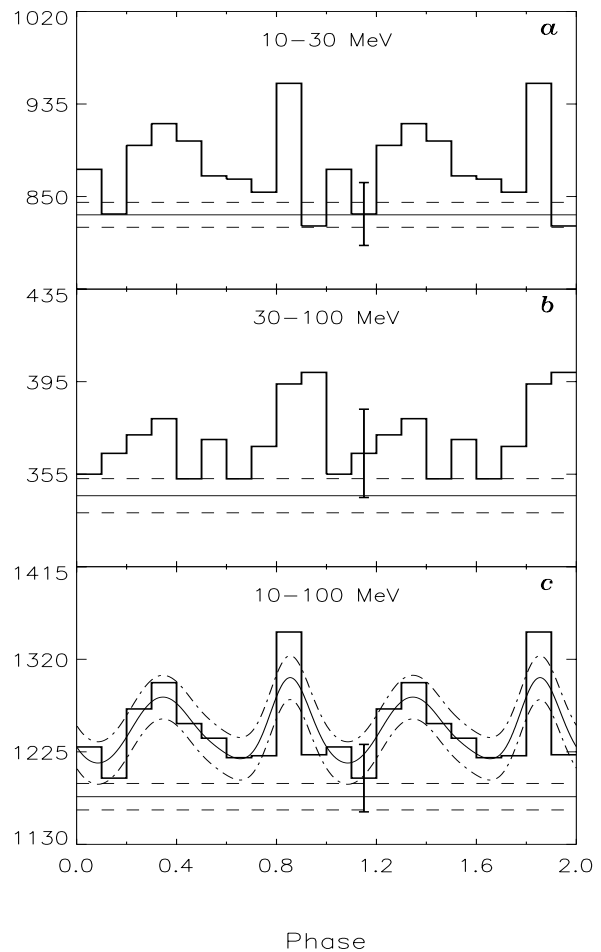


Fig. 4.8. **a** COMPTEL 10-30 MeV Cycle I-VI lightcurve (2.1σ): the background level and its $\pm 1\sigma$ error estimated from the spatial analysis are indicated as a solid straight line and dashed lines. **b** EGRET 30-100 MeV Cycle I-IV lightcurve (1.1σ): background level (and $\pm 1\sigma$ errors) are determined in a spatial analysis including point sources at the pulsar and 2EG J1443-6040 positions. **c** Combined COMPTEL 10-30 MeV and EGRET 30-100 MeV lightcurve (2.3σ or 1.9% chance probability). The summed background level from the spatial analyses is again indicated together with the smoothed curves representing the KDE and its $\pm 1\sigma$ error region. Typical error bars are indicated.

Even though the modulation significance of this 10-100 MeV lightcurve is still marginally significant, the apparent double-peaked structure above the background level estimated in the spatial analysis, makes it very suggestive that the source detected in the spatial analysis is PSR B1509-58 with pulsed emission up to the EGRET energies. At least, the spatial and timing analyses are consistent with this interpretation. If correct, the lightcurve morphology changed from one broad single pulse to a profile with an additional pulse near phase 0.85.

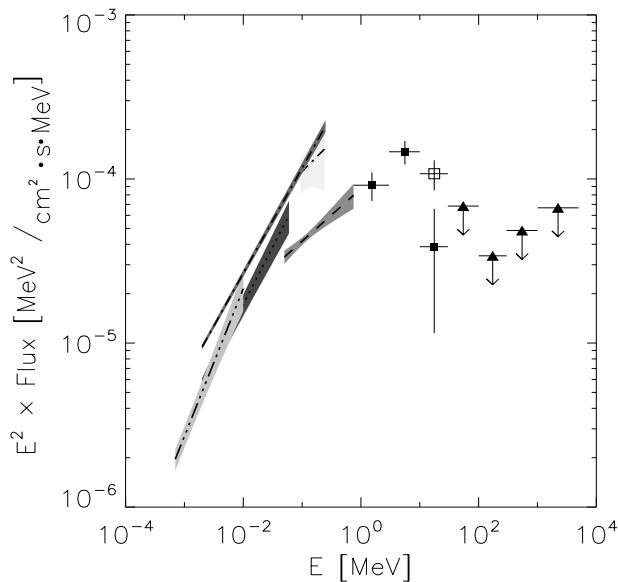


Fig. 4.9. The pulsed high-energy spectrum of PSR B1509-58 from soft X-rays to hard γ -rays. The filled squares are the COMPTEL flux points as derived from the excess counts in the 0.15 – 0.65 phase range (case *i*), from Sect. 4.3.5), while the open square represents the 10-30 MeV flux in the 0.15-0.65 phase interval above the spatially determined background (case *ii*). The filled triangles are the 2σ upper limits for the total fluxes in the EGRET energy domain (D. Thompson - private communication). The polygons represents the best fit 1σ error regions as measured by different instruments below the COMPTEL energy window: ASCA (0.7-10 keV; Saito et al. 1997); Ginga (2-60 keV; Kawai et al. 1993); OSSE (50-750 keV; Matz et al. 1994); WELCOME (94-240 keV; Gunji et al. 1994); RXTE (2-250 keV; Marsden et al. 1998). The softening of the spectrum from soft X-rays to MeV gamma rays is evident, as well as the spectral break above 10 MeV.

4.6. Spectral analysis

Energy spectra can be derived from the spatial analysis as well as from the timing analysis. Given that there is some ambiguity in the interpretation of the results on PSR B1509-58 for energies above 10 MeV, we consider three cases:

i) The COMPTEL “pulsed” spectrum of PSR B1509-58 (0.75-30 MeV) determined by the excess counts in the phase window 0.15-0.65 above the average level in the complementary phase interval. This represents the spectrum of the broad single pulse, which was already determined in Sect. 4.3.5 (Table 4.3). In Fig. 4.9 this spectrum is shown together with the spectra (power-law fits) derived by other instruments from 1 keV upto ~ 700 keV. Above 30 MeV are included the EGRET 2σ upper-limits (D.Thompson-private communication) derived from spatial analyses using a subset of the observations listed in Table 4.1. The new COMPTEL flux values are consistent with an extrapolation of the OSSE power-law fit (PL-index of -1.68) upto 10 MeV, followed by a drastic break, which will be discussed in Sect. 4.7.

ii) If the source detected by COMPTEL between 10 and 30 MeV is PSR B1509-58, then we have underestimated the flux of the single broad pulse in the 10 - 30 MeV interval. Determining then the flux (phases 0.15-0.65) above the spatially determined background (see Fig. 4.8) between 10 and 30 MeV, and inserting that in Fig. 4.9 gives a spectrum for the single broad pulse with a break energy between 10 and 30 MeV. In this case this spectrum does not represent the total pulsed spectrum for energies above 10 MeV.

iii) If the sources detected at the position of the pulsar by COMPTEL and EGRET in the spatial analyses above 10 MeV and 30 MeV, respectively, can be identified with the pulsar, then the *total* spectrum of PSR B1509-58 above 0.75 MeV can be derived by combining the COMPTEL flux values from the timing analysis below 10 MeV (consistent with 100% pulsed) with the flux values from the spatial analysis of COMPTEL 10-30 MeV data (Sect. 4.4.1.2) and EGRET data above 30 MeV (Sect. 4.5.1). This is shown in Fig. 4.10 together with the “pulsed” spectra measured at lower energies by other instruments as well as the flux estimate from the detection (4.1σ) by the CANGAROO collaboration in their spatial analysis for energies above 1.5 TeV in comparison with the spectrum shown in Fig. 4.9 is then mainly due to an additional pulse component near phase 0.85, having a completely different spectrum than the main pulse. For comparison is also shown the “unpulsed” spectrum of PSR B1509-58 measured by RXTE upto 240 keV (Marsden et al. 1998). It is evident that, if the “unpulsed” emission extrapolates according to the RXTE spectrum towards the γ -ray regime, the 10-30 MeV flux measured at the PSR B1509-58 position can *not* be the (nebula) DC emission, supporting the pulsar interpretation. Furthermore, the EGRET flux values above 100 MeV are consistent with the extrapolation of the fit to this “unpulsed” spectrum, which is even consistent with an extrapolation up to the claimed detection of the nebula by the CANGAROO collaboration at TeV energies. Therefore, the spectral compilation in Fig. 4.10 suggests that the combined COMPTEL / EGRET spectrum of PSR B1509-58 represents the transition from dominantly pulsed emission below ~ 30 MeV to dominantly DC-emission above ~ 100 MeV.

4.7. Summary and discussion

The major findings based on primarily COMPTEL and to a lesser extent EGRET γ -ray data presented in this paper can be summarized as follows:

I Pulsed γ -ray emission from PSR B1509-58 has been detected with high significance up to 10 MeV as a broad asymmetric single pulse located in the phase interval where also the pulse occurs for X-ray and soft γ -ray energies up to ~ 700 keV. The pulse measured by COMPTEL between 0.75 and 10 MeV reaches its maximum near radio phase 0.38, shifted w.r.t. the value 0.30 measured by Rots et al. (1998) in the BATSE data above 32

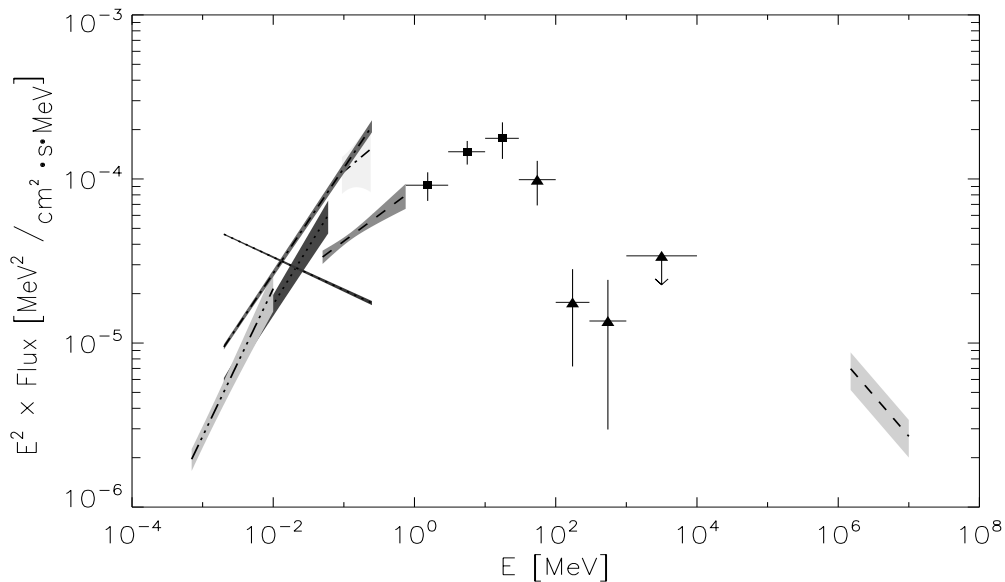


Fig. 4.10. The *total* COMPTEL and EGRET high-energy spectrum of PSR B1509-58 (> 0.75 MeV, case *iii*) including the spectral measurements below 0.75 MeV of the pulsed emission by other high-energy experiments (see caption Fig. 4.9). Furthermore, the “unpulsed” spectrum of PSR B1509-58 measured by RXTE (Marsden et al. 1998) is shown, as well as the > 1.5 TeV DC-flux measurement by the CANGAROO collaboration (assumed to have a photon index of -2.5). The *total* emission breaks now around 30 MeV due to the contribution from an additional pulse near phase 0.85 for energies in excess of 10 MeV.

keV. The COMPTEL maximum appears to coincide in phase with the “shoulder” clearly visible in the RXTE 2-16 keV data. The pulsed spectrum is consistent with a power-law extrapolation up to 10 MeV of the OSSE spectrum (PL-index of -1.68) measured at lower γ -ray energies.

- II** In the 10-30 MeV energy range we do detect a significant (5.6σ) source positionally consistent with PSR B1509-58, however, the timing analysis yields a modulation significance of $\sim 2\sigma$ only. Based on just the COMPTEL data we cannot discriminate with certainty between the following interpretations: *i*) DC emission from the pulsar or its nebula, *ii*) emission from a nearby source, or *iii*) pulsed emission: the light curve exhibits an excess in phase with the pulse measured below 10 MeV and there is an indication for a second narrow component near phase 0.85.
- III** In the adjacent 30-100 MeV EGRET energy band we detect a 6.7σ source positionally consistent with PSR B1509-58 which can be explained with contributions from PSR B1509-58 (4.4σ) and the nearby unidentified EGRET source 2EG J1443-6040 (2.6σ). Timing analysis of the 30-100 MeV events yields a modulation significance of 1.1σ only. The combined COMPTEL/EGRET 10-100 MeV lightcurve (modulation significance 2.3σ) shows also the double-peaked shape: again a main pulse coinciding with the pulse observed at lower energies and a weak narrower pulse near phase 0.85. The results of the spatial and timing analyses are

consistent with PSR B1509-58 being detected between 10 and 100 MeV, with a new pulse which is only visible between 10 and 100 MeV.

- IV** The pulsed spectrum of PSR B1509-58 shows a sharp break between 10 and 30 MeV. The break energy is close to 10 MeV for the broad main pulse, and shifts to ~ 30 MeV for the total spectrum if the second narrow component is genuine.

The implications of these new findings at medium and high-energy γ -ray energies will now be discussed. Theoretical models explaining the high-energy electro-magnetic radiation from highly magnetized rotating neutron stars can be distinguished in two different categories:

- a** Polar Cap models (PC) in which the acceleration of charged particles along the open magnetic field lines in the vicinity of the magnetic pole(s) and subsequent cascades through high-energy radiation processes gives rise to the emerging γ -ray spectrum.
- b** Outer Gap models (OG) in which the acceleration of charged particles and the production of γ -rays takes place in vacuum gaps between the null-charge surface defined by $\boldsymbol{\Omega} \cdot \mathbf{B} = 0$, with \mathbf{B} the local magnetic field and $\boldsymbol{\Omega}$ the pulsar spin vector, and the light cylinder ($R_{lc} = c/\Omega$) along the last closed field lines.

Both models rely on charge replenishment of the magnetosphere mainly through e^\pm pairs. The polar cap models can be subdivided further primarily based on the energy reached by the particles (primaries) in the accelera-

tion process. For primary particle energies $\Gamma \gtrsim 10^6$, with Γ the Lorentz factor or equivalently the dimensionless energy, energy loss in the form of high-energy γ -rays through *curvature radiation* is the most important radiation mechanism (CRPC models). For energies $10^4 \lesssim \Gamma \lesssim 10^6$ energy loss through *inverse Compton scattering* with either thermal X-ray photons from the polar cap or from non-thermal cascade processes in the magnetosphere will be more important (ICPC-models). Finally, for energies $50 \lesssim \Gamma \lesssim 10^4$ *resonant Compton scattering* will be the dominant energy loss mechanism. Irrespective of the underlying energy loss mechanism of the primary particles it is assumed that the emergent γ -ray spectrum is softened by magnetic pair production ($\gamma \xrightarrow{B} e^+ + e^-$; Sturrock process) in the strong magnetic fields present in the vicinity of the magnetic poles. These pairs (secondaries) are produced in excited Landau states, which decay by the emission of synchrotron photons which in turn can produce e^\pm pairs and a cascade can develop softening the initial γ -ray spectrum at each generation.

Daugherty & Harding (1996) assume in a recent version of their CRPC model that a distant observer sees the emission from just one polar cap. They also assume that the acceleration of the primaries occurs over an extended distance above the polar cap surface and that the magnetic inclination α (angle between Ω and magnetic moment μ) is comparable to the γ -ray beam opening angle θ_γ . The last two assumptions relax the requirement of both $\alpha \approx \theta_\gamma$ and a small α , i.e. a nearly aligned rotator, in earlier versions of their model (Daugherty & Harding 1994) to explain the γ -ray emission properties of pulsars.

Because the curvature radii R_{cr} of the open field lines, assuming a dipole configuration, originating from the polar cap rim near $\theta_{pc} \simeq \arcsin(\sqrt{R_{ns}/R_{lc}})$ are smaller than those originating at smaller polar angles (at the magnetic pole $R_{cr} \rightarrow \infty$ and no curvature emission can be produced) the initial CR γ -ray emission spectrum ($\propto 1/R_{cr}$) is most pronounced and hardest (maximum of CR-spectrum is reached at $\omega_{\max} \simeq 0.29 \cdot \omega_c \propto \Gamma^3/R_{cr}$) near the polar rim resulting in a hollow cone emission pattern. The mostly developed cascades originate near the polar rim which in turn soften the input CR-spectrum most efficiently.

This means that a distant observer not only sees a double peaked profile when the hollow γ -ray emission cone passes his line of sight, but also a soft-hard-soft variation of the emission is expected, because the CR-emission emanating nearer the magnetic pole is less softened by cascading. Grazing through the γ -ray emission cone will result in a single pulse profile highly softened by cascade processes. The last situation may be applicable for PSR B1509-58 requiring clear constraints on the geometrical aspects of both the system and the observer. In particular, it demands that the pulsar spin axis / line-of-sight angle ζ should approximately be equal to the sum of the magnetic inclination angle α and the γ -ray cone semi-angle θ_γ (beam radius). However, the

large duty cycle of the single pulse of ~ 0.4 poses an additional constraint, namely ζ should then be smaller than $\alpha + \theta_\gamma$. This can be estimated using the following equation:

$$\theta_\gamma = \arccos(\cos \beta - 2 \sin \alpha \sin(\alpha + \beta) \sin^2(\frac{\Delta\Phi}{4})) \quad (4.2)$$

which can be derived in the rotating vector model (e.g. Rankin 1993). $\Delta\Phi$ is the duty cycle of the pulse, while β is the impact parameter defined as $\beta \equiv \zeta - \alpha$. Radio-polarization data yield in the context of this rotating vector model (Crawford et al. 1997; private communication 1999) $\alpha \simeq 18_{-13}^{+18}$ degree and $\beta \simeq 20_{-20}^{+20}$ degree. If we use the best fit parameters, then $\theta_\gamma \simeq 36^\circ$. Eventhough the uncertainties are large, the emitting rim must be very broad to explain the broad single pulse.

The CRPC model also predicts a spectral cutoff in the γ -ray spectrum at several GeV. Another interesting feature is that a lower cutoff energy is expected for those pulsars with a higher magnetic field, because the softening by cascade processes is more efficient in these cases. Some of these general trends are indeed observed in some γ -ray pulsars (Thompson et al. 1997). The current implementation of geometrical and physical aspects, however, predicts lightcurves with a high degree of symmetry. This symmetry is a problem for e.g. the Vela pulsar high-energy lightcurve (Grenier et al. 1988; Kanbach et al. 1994) which shows rather asymmetric bridge emission.

For PSR B1509-58 this CRPC model *can not* explain the observed *low* spectral cutoff energy occuring between 10 and 30 MeV. However, the (very) strong polar surface magnetic field strength of $\sim 3.1 \times 10^{13}$ Gauß likely triggers another more exotic attenuation process to be active in the vicinity of the magnetic pole, namely *photon splitting* $\gamma \xrightarrow{B} \gamma I + \gamma II$, besides attenuation by magnetic pair production. Harding et al. (1997) showed that the photon splitting attenuation lengths can be shorter than the attenuation lengths for pair production for magnetic field strenghts $B \gtrsim 0.3 B_{cr}$ with $B_{cr} = m_e c^3 / e \hbar = 4.413 \times 10^{13}$ G. This means that photon splitting acts as the dominant attenuation process for such strong magnetic fields and can suppress the emission of high-energy photons. Contrary to the attenuation by magnetic pair production, photon splitting has *no* energy threshold and can degrade the photon energy also below the magnetic pair production threshold ($\omega \geq 2 m_e c^2 / \sin(\theta_{kB})$, θ_{kB} is the angle between photon propagation direction and local magnetic field). Depending on the splitting mode, partial and full splitting cascades are addressed, Harding et al. (1997) calculate the high-energy spectrum of PSR B1509-58 for various values of the model parameters θ_{kB} and θ , the magnetic co-latitude angle, assuming that the initial high-energy photon emission originates from the neutron star surface in a polar rim at colatitude θ . Our new medium-energy γ -ray data and in particular the spectrum of the main pulse severely constrain the magnetic co-latitude of the emission rim, irrespective of the

splitting mode. A co-latitude of $\sim 2^\circ$, close to the “classical” radius of the polar cap θ_{pc} , appears to be required in the model calculations to be consistent with the evident spectral break between 10 and 30 MeV in the combined COMPTEL-EGRET spectrum.

No detailed model calculations have been performed for PSR B1509-58 in the inverse Compton induced Polar Cap cascade scenario (Sturmer & Dermer 1994; Sturmer et al. 1995 and Sturmer 1995), although some interesting qualitative statements have been made. In particular, if $B > 10^{13}$ G and the neutron star surface temperature $T > 3 \cdot 10^6$ K the Lorentz factors of the electrons are limited to $\lesssim 10^3$, which might explain the low cutoff energy in the spectrum of PSR B1509-58 (Sturmer 1995). However, this type of PC-model also suffers from predicting too symmetric lightcurves. The model requirement of a nearly aligned rotator ($\alpha \sim \theta_\gamma \lesssim 5^\circ$) can formally not be excluded for the estimates of the magnetic inclination $\alpha \simeq 18_{-13}^{+18}$ degree (Crawford et al. 1997) and $\theta_\gamma \simeq 36_{-30}^{+32}$ degree.

In outer gap scenarios (see e.g. Cheng et al. 1986a, Cheng et al. 1986b and Ho 1989) it is believed that stable vacuum gaps (Holloway 1973) can be formed in the outer magnetosphere along the boundary of the last closed field lines which extend from the null-charge surface to the light cylinder. Voltage drops of typically $\sim 10^{13}$ V can be obtained across the gaps and accelerate e^\pm , created either in the gap or flowing in from beyond the light cylinder and from across the null-charge surface, to energies limited by curvature radiation and to a lesser extent inverse Compton scattering (off the ambient bath of lower energy photons). A geometrical calculation of the high-energy emission (beamed along the local magnetic field in the outer gap resulting in a “fan” beam) from an outer gap region was successful in reproducing qualitatively the observed γ -ray lightcurves of the known γ -ray pulsars (Chiang & Romani 1994). In a recent paper Romani (1996) modelled the emergent high-energy emission based on curvature radiation reaction limited accelerated charges in the outer magnetosphere. In his model the primary particles (e^\pm) emit curvature radiation with spectral cutoffs in the 1-10 GeV range. In order to tap the potential drop a small fraction (proportional to the optical depth $\tau_{\gamma\gamma}$ and of the order of $\lesssim 10^{-3}$ - 10^{-2}) of these curvature photons interact with low-energy photons, provided by thermal surface emission from the neutron star or produced in the gap itself by synchrotron emission processes, to produce e^\pm pairs. The perpendicular momentum of the produced pairs with respect to the local magnetic field is emitted in the form of synchrotron radiation peaking in the 1-10 MeV range. Part of the produced synchrotron radiation can inverse Compton scatter (ICS) off the primary particles to produce a TeV pulsed emission component (typically $\lesssim 1\%$ of the pulsed GeV flux). The composite of the various emission components constitute the high-energy pulsed spectrum. Although no quantitative estimates are presented, Romani (1996) argued that for short-period high-magnetic field pulsars like

PSR B1509-58 the synchrotron flux produced in the gap itself will dominate the thermal surface emission increasing $\tau_{\gamma\gamma}$ towards ~ 1 and thus significantly suppressing the GeV curvature component. This results in a synchrotron type spectrum peaking at MeV energies. From a geometrical point of view, the derived large values for the magnetic inclination and line-of-sight / pulsar spin axis angles seem to be naturally explained with an outer magnetospheric origin for the high-energy emission.

The above considerations for both the polar cap and outer gap scenarios show that further model calculations are required to make decisive statements on the production site and mechanisms of the high-energy pulsed radiation. In the small sample of detected high-energy pulsars PSR B1509-58 represents clearly a special case. This might now even be more so, given that in the above discussions we did not yet introduce the possible detection of an additional pulse in the lightcurve for energies above 10 MeV. This component must have a significantly harder spectrum than that of the broad main pulse. Such an additional narrow component may at first sight be more easily incorporated in an outer-gap scenario. In this respect it may be of interest to refer to earlier claims of detection of multiple and variable components in the lightcurve of PSR B1509-58 at TeV energies (> 1.5 TeV), which have been interpreted in the frame work of the outer gap scenario (de Jager et al. 1988, Nel et al. 1990). However, the earlier mentioned TeV observations by the CANGAROO collaboration do *not* confirm these claims, and provide a significantly lower upper-limit to the pulsed emission.

A long exposure of the source in the transition region of COMPTEL and EGRET is required to better study the change in morphology of the lightcurve. Additional COMPTEL observations of this source have been scheduled (CGRO Cycle 8) and are aimed to provide better insights in the source characteristics especially above 10 MeV.

Acknowledgements. The COMPTEL project is supported by NASA under contract NAS5-26645, by the Deutsche Agentur für Raumfahrtangelegenheiten (DARA) under grant 50 QV90968 and by the Netherlands Organisation for Scientific Research (NWO). AC research is sponsored by the CONACYT grant 4142-E. We thank Arnold Rots for providing the RXTE and BATSE lightcurves, Yoshitaka Saito for providing the ASCA spectral and timing results prior to publication and Fronev Crawford & Vicky Kaspi for corresponding radio polarization results. Finally, we thank Dave Thompson for discussions on the EGRET findings.

References

- Becker W., 1994, Ph.D. thesis, Ludwig-Maximilians-Universität München
- Bloemen H., Hermsen W., Swanenburg B., et al., 1994, ApJS 92, 419
- Bloemen H., Collmar W., Diehl R., et al., 1999, Proceedings third Integral Workshop “The Extreme Universe”, Overseas

- Publishers Association, *Astrophysical Letters & Communications*, in press
- Brazier K.T.S., Becker W., 1997, *MNRAS* 284, 335
- Brazier K.T.S., Bertsch D.L., Fichtel C.E., et al., 1994, *MNRAS* 268, 517
- Buccheri R., Bennett K., Bignami G.F., et al. 1983, *A&A* 128, 245
- Carramiñana A., Bennett K., Buccheri R., et al., 1995, *A&A* 304, 258
- Carramiñana A., Bennett K., Hermsen W., et al., 1997, *AIP Conf. Proc.* 410, p. 583, Eds. Dermer, C.D., Strickman, M.S. and Kurfess, J.D.
- Cheng K.S., Ho C., Ruderman M., 1986a, *ApJ* 300, 500
- Cheng K.S., Ho C., Ruderman M., 1986b, *ApJ* 300, 522
- Chiang J., Romani R.W., 1994, *ApJ* 436, 754
- Collmar W., Wessolowski U., Schönfelder V., et al., 1997, *AIP Conf. Proc.* 410, p. 1587, Eds. Dermer C.D., Strickman M.S. and Kurfess J.D.
- Crawford F., Kaspi V.M., Manchester R.N., Lyne A.G. 1997, *BAAS*, 191, 1120
- Daugherty J.K., Harding A.K., 1994, *ApJ* 429, 325
- Daugherty J.K., Harding A.K., 1996, *ApJ* 458, 278
- de Jager O.C., Swanepoel J.W.H., Raubenheimer B.C., 1986, *A&A* 170, 187
- de Jager O.C., Raubenheimer B.C., North A.R., et al. 1988, *ApJ* 329, 831
- de Vries C.P., 1994, *A.S.P. Conf. Series* 61, 399, eds. Crabtree D.R., Hanisch R.J. and Barnes J.
- Fierro J.M., 1995, Ph. D. thesis, Stanford University
- Greiveldinger C., Caucino S., Massaglia S., et al., 1995, *ApJ* 454, 855
- Grenier I.A., Hermsen W., Clear J., et al., 1988, *A&A* 204, 117
- Gunji S., Hirayama M., Kamae T., et al., 1994, *ApJ* 428, 284
- Harding A., Baring M., Gonthier P., 1997, *ApJ* 476, 246
- Hartman R.C., Bertsch D.L., Bloom S.D., 1999, *ApJS*, in press
- Hermsen W., Kuiper L., Diehl R., et al., 1994, *ApJS* 92, 559
- Ho C., 1989, *ApJ* 342, 396
- Holloway N.J., 1973, *Nat. Phys. Sci.* 246, 6
- Kanbach G., Arzoumanian Z., Bertsch D.L., et al., 1994, *A&A* 289, 855
- Kaspi V.M., Manchester R.N., Siegman B., et al., 1994, *ApJ* 422, L83
- Kawai N., Okayasu R., Brinkmann W., et al., 1991, *ApJ* 383, L65
- Kawai N., Okayasu R., Sekimoto Y., 1993, *AIP Conf. Proc.* 280, p. 213, Eds. Friedlander M., Gehrels N. and Macomb D.
- Kuiper L., Hermsen W., Bennett K., et al., 1998a, *A&A* 337, 421
- Kuiper L., Hermsen W., Schönfelder V., et al. 1998b, in: "The many faces of neutron stars", Buccheri et al. (eds), *NATO ASI Series C*, Vol. 515, 211
- Manchester R.N., Tuohy I.R., D'Amico N., 1982, *ApJ* 262, L31
- Marsden D., Blanco P.R., Gruber D.E., et al. 1998, *ApJ* 491, L39
- Matz S.M., Ulmer M.P., Grabelsky D.A., et al. 1994, *ApJ* 434, 288
- Much R., Bennett K., Buccheri R., et al. 1995, *A&A* 299, 435
- Nagase F., Zylstra G., Mihara T., 1994, p. 57, in "New horizon of X-ray astronomy", Universal Academy Press, Inc. - Tokyo, Japan
- Nel H.I., de Jager O.C., Raubenheimer B.C., et al. 1990, *ApJ* 361, 181
- Rankin J.M., 1993, *ApJ* 405, 285
- Romani R.W., 1996, *ApJ* 470, 469
- Rots A.H., Jahoda K., Macomb D.J., et al., 1998, *ApJ* 501, 749
- Saito Y., Kawai N., Kamae T., et al., 1997, *AIP Conf. Proc.* 410, p. 628, Eds. Dermer C.D., Strickman M.S. and Kurfess J.D.
- Sako, T., 1998, in *Neutron Stars and Pulsars - 30 years after the discovery*, Eds. Shibasaki N., Kawai N., Shibata S. and Kifune T., Universal Academy Press, Tokyo, Japan, 1998
- Schönfelder V., Aarts H., Bennett K., et al., 1993, *ApJS* 86, 657
- Seward F.D., Harnden Jr. F.R., 1982, *ApJ* 256, L45
- Seward F.D., Harnden Jr. F.R., Murdin P., 1983, *ApJ* 267, 698
- Seward F.D., Harnden Jr. F.R., Szymkowiak A., et al., 1984, *ApJ* 281, 650
- Strong A., Bennett K., Bloemen H., et al., 1994, *A&A* 292, 82
- Sturmer S.J., 1995, *ApJ* 446, 292
- Sturmer S.J., Dermer C.D., 1994, *ApJ* 420, L79
- Sturmer S.J., Dermer C.D., Michel F.C., 1995, *ApJ* 445, 736
- Tamura K., Kawai N., Yoshida A., et al., 1996, *PASJ* 48, L33
- Thompson D.J., Bertsch D.L., Fichtel C.E., et al., 1993, *ApJS* 86, 629
- Thompson D.J., Bertsch D.L., Dingus B.L., et al., 1995, *ApJS* 101, 259
- Thompson D.J., Bertsch D.L., Dingus B.L., et al., 1996a, *ApJS* 107, 227
- Thompson D.J., Bailes M., Bertsch D.L., et al., 1996b, *ApJ* 465, 385
- Thompson D.J., Harding A.K., Hermsen W., et al., 1997, *AIP Conf. Proc.* 410, p. 39, Eds. Dermer C., Strickman M., and Kurfess J.
- Trussoni E., Brinkmann W., Ögelman H., et al., 1990, *A&A* 234, 403
- Trussoni E., Massaglia S., Caucino S., et al., 1996, *A&A* 306, 581
- Ulmer M.P., Matz S.M., Wilson R.B., et al., 1993, *ApJ* 417, 738
- Weisskopf M.C., Elsner R.F., Darbro W., et al., 1983, *ApJ* 267, 711
- Wilson R.B., Finger M.H., Pendleton G.N., et al., 1993a, p. 257, in "Isolated Pulsars", Taos, New Mexico, Eds. Van Riper K.A. and Ho C., Cambridge Univ. Press
- Wilson R.B., Fishman G.J., Finger M.H., et al., 1993b, *AIP Conf. Proc.* 280, p. 291, Eds. Friedlander M., Gehrels N. and Macomb D.

Chapter 5

The Crab pulsar in the 0.75-30 MeV range as seen by COMPTEL

A coherent high-energy picture from soft X-rays up to high-energy γ -rays

L. Kuiper², W. Hermsen², G. Cusumano⁵, R. Diehl¹, V. Schönfelder¹, A. Strong¹, K. Bennett³, and M.L. McConnell⁴

¹ Max-Planck -Institut für Extraterrestrische Physik, D-85741 Garching, Germany

² SRON-Utrecht, Sorbonnelaan 2, NL-3584 CA Utrecht, The Netherlands

³ Astrophysics Division, European Space Research and Technology Centre, 2200 AG, Noordwijk, The Netherlands

⁴ Space Science Centre, University of New Hampshire, Durham, NH 03824, USA

⁵ Istituto di Fisica Cosmica ed Applicazioni all'Informatica CNR, Via U. La Malfa 153, I-90146, Palermo, Italy

Submitted to Astron. Astrophys. (2001)

Abstract. We present the time-averaged characteristics of the Crab pulsar in the 0.75-30 MeV energy window using data from the imaging Compton telescope COMPTEL aboard the Compton Gamma-Ray Observatory (CGRO) collected over its 9 year mission. Exploiting the exceptionally long COMPTEL exposure on the Crab allowed us to derive significantly improved COMPTEL spectra for the Crab nebula and pulsar emissions, and for the first time to accurately determine at low-energy γ -rays the pulse profile as a function of energy. These timing data, showing the well-known main pulse and interpulse at a phase separation of ~ 0.4 with strong bridge emission, are studied together with data obtained at soft/hard X-ray energies from the ROSAT HRI, BeppoSAX LECS, MECS and PDS, at soft γ -rays from CGRO BATSE and at high-energy γ -rays from CGRO EGRET in order to obtain a coherent high-energy picture of the Crab pulsar from 0.1 keV up to 10 GeV. The morphology of the pulse profile of the Crab pulsar is continuously changing as a function of energy: the intensities of both the second peak (interpulse) and the bridge emission increase relative to that of the first pulse for increasing energies up to ~ 1 MeV. Over the COMPTEL energy range above 1 MeV an abrupt morphology change happens: the first pulse becomes again dominant over the interpulse and the bridge emission loses significance such that the pulse profile above 30 MeV mimics the one observed at optical wavelengths. A pulse phase resolved spectral analysis performed in 7 narrow phase slices consistently applied over the 0.1 keV - 10 GeV energy interval shows that the pulsed emission can empirically be described with 3 distinct spectral components: i) a power-law emission component (1 keV - 5 GeV; photon index -2.069 ± 0.003) which is present in the phase intervals of the two pulses; ii) a curved spectral component required to describe soft ($\lesssim 100$ keV) excess emission present in the same pulse phase intervals;

iii) a broad curved spectral component reflecting the bridge emission from 0.1 keV to ~ 10 MeV. This broad spectral component extends in phase over the full pulse profile in an approximately triangular shape, peaking under the interpulse. Finally, at high-energy γ -rays ($\gtrsim 100$ MeV) there are indications for an additional very hard spectral component coinciding in phase with the leading wing of the interpulse. Recent model calculations for a three-dimensional pulsar magnetosphere with outer magnetospheric gap acceleration by Cheng et al. (2000) appears at present most successful in explaining the above complex high-energy characteristics of the Crab pulsar.

5.1. Introduction

The Crab nebula (3C 144; NGC 1952; CTB 18) is a filled-center type supernova remnant (plerion) associated with a supernova explosion which appeared in the constellation Taurus on 4 July 1054 A.D. Due to its visibility from radio to high-energy γ -rays it serves as a “standard” calibration target for many astronomical detector systems sensitive to radiation across the complete electro-magnetic spectrum. This makes it one of the best studied celestial objects in astronomy.

Near the center of the $3' \times 2'$ nebula a fast 33 ms radio-pulsar NP 0532 (nowadays named PSR B0531+21; PSR J0534+2000) was found in 1968 (Staelin & Reifenstein 1968; Richards & Comella 1969) soon after the discovery of the first radio-pulsar in July 1967. The unambiguous association of the pulsar with the supernova remnant provided crucial information for the theory of stellar evolution of massive stars.

The radio pulse profile is characterized by two pulses: a main pulse and in radio jargon a so called interpulse, sepa-

Chapter 5

The Crab pulsar in the 0.75-30 MeV range as seen by COMPTEL

A coherent high-energy picture from soft X-rays up to high-energy γ -rays

L. Kuiper², W. Hermsen², G. Cusumano⁵, R. Diehl¹, V. Schönfelder¹, A. Strong¹, K. Bennett³, and M.L. McConnell⁴

¹ Max-Planck -Institut für Extraterrestrische Physik, D-85741 Garching, Germany

² SRON-Utrecht, Sorbonnelaan 2, NL-3584 CA Utrecht, The Netherlands

³ Astrophysics Division, European Space Research and Technology Centre, 2200 AG, Noordwijk, The Netherlands

⁴ Space Science Centre, University of New Hampshire, Durham, NH 03824, USA

⁵ Istituto di Fisica Cosmica ed Applicazioni all'Informatica CNR, Via U. La Malfa 153, I-90146, Palermo, Italy

Submitted to Astron. Astrophys. (2001)

Abstract. We present the time-averaged characteristics of the Crab pulsar in the 0.75-30 MeV energy window using data from the imaging Compton telescope COMPTEL aboard the Compton Gamma-Ray Observatory (CGRO) collected over its 9 year mission. Exploiting the exceptionally long COMPTEL exposure on the Crab allowed us to derive significantly improved COMPTEL spectra for the Crab nebula and pulsar emissions, and for the first time to accurately determine at low-energy γ -rays the pulse profile as a function of energy. These timing data, showing the well-known main pulse and interpulse at a phase separation of ~ 0.4 with strong bridge emission, are studied together with data obtained at soft/hard X-ray energies from the ROSAT HRI, BeppoSAX LECS, MECS and PDS, at soft γ -rays from CGRO BATSE and at high-energy γ -rays from CGRO EGRET in order to obtain a coherent high-energy picture of the Crab pulsar from 0.1 keV up to 10 GeV. The morphology of the pulse profile of the Crab pulsar is continuously changing as a function of energy: the intensities of both the second peak (interpulse) and the bridge emission increase relative to that of the first pulse for increasing energies up to ~ 1 MeV. Over the COMPTEL energy range above 1 MeV an abrupt morphology change happens: the first pulse becomes again dominant over the interpulse and the bridge emission loses significance such that the pulse profile above 30 MeV mimics the one observed at optical wavelengths. A pulse phase resolved spectral analysis performed in 7 narrow phase slices consistently applied over the 0.1 keV - 10 GeV energy interval shows that the pulsed emission can empirically be described with 3 distinct spectral components: i) a power-law emission component (1 keV - 5 GeV; photon index -2.069 ± 0.003) which is present in the phase intervals of the two pulses; ii) a curved spectral component required to describe soft ($\lesssim 100$ keV) excess emission present in the same pulse phase intervals;

iii) a broad curved spectral component reflecting the bridge emission from 0.1 keV to ~ 10 MeV. This broad spectral component extends in phase over the full pulse profile in an approximately triangular shape, peaking under the interpulse. Finally, at high-energy γ -rays ($\gtrsim 100$ MeV) there are indications for an additional very hard spectral component coinciding in phase with the leading wing of the interpulse. Recent model calculations for a three-dimensional pulsar magnetosphere with outer magnetospheric gap acceleration by Cheng et al. (2000) appears at present most successful in explaining the above complex high-energy characteristics of the Crab pulsar.

5.1. Introduction

The Crab nebula (3C 144; NGC 1952; CTB 18) is a filled-center type supernova remnant (plerion) associated with a supernova explosion which appeared in the constellation Taurus on 4 July 1054 A.D. Due to its visibility from radio to high-energy γ -rays it serves as a “standard” calibration target for many astronomical detector systems sensitive to radiation across the complete electro-magnetic spectrum. This makes it one of the best studied celestial objects in astronomy.

Near the center of the $3' \times 2'$ nebula a fast 33 ms radio-pulsar NP 0532 (nowadays named PSR B0531+21; PSR J0534+2000) was found in 1968 (Staelin & Reifenstein 1968; Richards & Comella 1969) soon after the discovery of the first radio-pulsar in July 1967. The unambiguous association of the pulsar with the supernova remnant provided crucial information for the theory of stellar evolution of massive stars.

The radio pulse profile is characterized by two pulses: a main pulse and in radio jargon a so called interpulse, sepa-

rated ~ 0.4 in pulse phase. Observations at different radio frequencies show that there is a considerable morphology change of the profile as a function of radio frequency (see e.g. Moffett & Hankins 1996). At frequencies below ~ 800 MHz the main pulse is preceded by a precursor pulse, while at higher radio frequencies (> 4.7 GHz) pulses emerge in the otherwise featureless phase interval beyond the second pulse (=interpulse).

The synchrotron type nebula spectrum is believed to originate from interactions of relativistic electrons with the ambient nebular magnetic field. It is generally accepted that these particles are produced and accelerated in the “open” field line zone of a rapidly spinning neutron star with a strong dipolar magnetic field and manifest as a relativistic pulsar wind.

In the open field line zone along the last closed field lines in the magnetosphere non-thermal pulsed high-energy radiation can be produced. At optical wavelengths this component has first been detected in 1969 by Cocke et al. (1969) (see also Nather et al. 1969), in the X-ray regime followed by detections in 1969 by Fritz et al. (1969 ; ~ 1 -13 keV) and Bradt et al. (1969 ; 1.5-10 keV), although an earlier rocket (Boldt et al. 1969 ; 2-10 keV) and balloon borne hard X-ray experiment (Fishman et al. 1969; 35-560 keV) already recorded, but did not recognize, the X-ray pulses. Since these pioneering observations much more details of the pulsar emission characteristics at optical and X-ray wavelengths have been obtained from subsequent observations by more sensitive instruments.

At optical wavelengths most notable among the published papers are the results by Smith (1988,1996) scrutinizing the optical polarization properties, by Percival et al. (1993) using the HSP aboard the Hubble Space telescope (HST) to study the optical and UV spectrum of the Crab pulsar in detail, by Gull et al. (1998) and by Sollerman et al. (2000) both using the timetag mode of the STIS instrument aboard HST to obtain spectral characteristics in the near-UV and Far-UV. Golden et al. (2000), using a high-speed two-dimensional photometer, found significant unpulsed optical emission from the Crab pulsar in the “off” pulse part of the light curve, the spectrum of which appears to be softer than the spectra from other parts of the light curve.

In the X-ray/soft γ -ray domain many interesting results on the Crab pulsar emission properties have been published based on observations by balloon-borne, sounding rocket and satellite experiments performed since the early seventies. The significant detection of pulsed soft γ -ray emission by Kurfess (1971; 100-400 keV) in data from a balloon-borne experiment performed in 1970 is worth mentioning. Following important results obtained by Kestenbaum et al. (1976; 0.6-23 keV) and Toor & Seward (1977; 0.5-16 keV) from sounding rocket experiments a great boost forward was made by the X-ray instruments on board the OSO-8

(Pravdo & Serlemitsos 1981; 2-50 keV, noticing the spectral variations of the pulsed emission as a function of pulse phase) , HEAO-1 (Knight 1982, 18-200 keV; introducing the possible existence of at least 2 pulsed emission components: one associated with the 2 main peaks and one with the bridge, the interval between the two peaks) and HEAO-2 (Einstein) satellites (Harnden & Seward 1984, 0.1-4.5 keV; producing the first high-resolution ($\sim 4''$) image of the Crab nebula/pulsar in X-rays along with a high-resolution soft X-ray pulse profile). Recently, Pravdo et al. (1997) presented the details of a pulse-phase resolved spectral analysis of the pulsed emission in the 5-200 keV interval based on RXTE PCA and HEXTE data. They found systematic spectral changes in the photon power-law index as a function of pulse phase across the interval of the pulsed emission. Their work is confirmed by the findings presented by Massaro et al. (2000), who used data from the narrow field instruments aboard BeppoSAX (0.1-300 keV). These authors also made an attempt to disentangle the two emission components, introduced by Knight (1982), assuming for one component (reflecting the emission in the 2 peaks) the shape of the optical pulse profile and for the other component (the bridge emission) a shape from an analytical model with adjustable parameters.

At soft/medium γ -ray energies the first detection of pulsed radiation (0.6-9 MeV) from the Crab pulsar was reported by Hillier et al. (1970). Worth mentioning are the subsequent explorations of this energy range by Walraven et al. (1975), Graser & Schönfelder (1982), Mahoney et al. (1984) and Agrinier et al. (1990).

In the high-energy γ -ray domain ($\gtrsim 30$ MeV) the first indications for pulsed emission from the Crab pulsar were obtained from data collected by balloon-borne spark chambers or gas Cherenkov detector systems (see e.g. Browning et al. 1971, Albats et al. 1972, Parlier et al. 1973, McBreen et al. 1973). A big step forward in this energy range was made by the SAS-2 spark chamber experiment in the early seventies. In these data (20 MeV - 1 GeV) significant pulsed emission was reported by Kniffen et al. (1974) and Thompson et al. (1977). The most detailed information on the pulsed high-energy γ -ray properties of the Crab pulsar was, however, provided by the data from the spark chamber on board the European COS-B satellite (Bennett et al. 1977; Wills et al. 1982; Clear et al. 1987). Significant bridge emission was discovered in the combined COS-B Crab dataset, and the spectral characteristics of the pulsed and unpulsed (nebula) emission turned out to be quite diverse.

One striking feature emerges comparing the pulse profiles from the radio regime up to high-energy γ -rays: over this very wide energy interval the main pulse (P1) keeps its alignment. This fact is only observed for the Crab pulsar among the total sample of γ -ray pulsars (see e.g. Wills et al. 1982 and more recently Thompson et al. 1997).

The launch of the Compton Gamma-Ray Observatory (CGRO; 20 keV-30 GeV) in April 1991 brought about an

enormous improvement in the statistical quality of the γ -ray data. During its exceptionally long lifetime of more than 9 years Crab pulsar data collected by the Energetic Gamma-Ray Experiment (EGRET; 20 MeV - 30 GeV) showed clearly different spectral behaviour as a function of pulse phase (Nolan et al. 1993; Fierro 1995; Fierro et al. 1998). The phase region between the narrow pulses appeared to possess the hardest spectrum across the pulse profile. The findings from the Oriented Scintillation Spectrometer Experiment OSSE (50 keV-10 MeV), were presented by Ulmer et al. (1994). The imaging Compton Telescope COMPTEL (0.75 - 30 MeV) aboard CGRO had the Crab region in its field of view several times during its more than 9 years period of continuous operations. The results based on data from an early set of observations performed during the all-sky survey of the CGRO mission had been published by Much et al. (1995) and Carramiñana et al. (1994). The addition of data from subsequent COMPTEL observations (up to VP 502; see Table 5.1) improved the data quality considerably (Much et al. 1997), but the analyses could still not include the full database, did not use the improved response estimates nowadays available and did not yet apply optimum event selection windows.

In this paper the final COMPTEL 0.75-30 MeV results on the Crab pulsar/nebula are presented using i) data from nearly all¹ available COMPTEL Crab observations, ii) upgraded/improved response estimates and iii) improved data selection criteria. In order to obtain a broad high-energy picture, we also consistently analysed in detail Crab data from the Italian/Dutch BeppoSAX satellite at lower energies (0.1–300 keV) and from EGRET at higher energies (30 MeV–10 GeV). For some parts of the work we analysed additional data (e.g. soft γ -ray/X-ray data from the CGRO Burst and Transient Source Experiment, BATSE, and the ROSAT HRI; and for comparisons optical and UV data).

5.2. Instrument description and observations

COMPTEL is the imaging Compton Telescope aboard CGRO and operates in the 0.75-30 MeV energy range. Its detection principle relies on a two layer interaction: a Compton scatter in one of the 7 upper-detector (D1) modules followed by a second interaction in one of the 14 lower-detector (D2) modules. Main measured quantities are the angles (χ , ψ) specifying the direction of the scattered photon (from the interaction loci in D1 and D2) and the energy deposits in the D1/D2 modules where the interactions took place. From the last two quantities we can calculate the scatter angle $\bar{\varphi}$ and the total energy deposit E_{tot} (for a full description see Schönfelder et al. 1993). Its energy resolution is 5-10% FWHM and, due to its large field of view of typically 1 steradian, it is possible to monitor a large part

¹ At the very end of the CGRO mission 2 additional COMPTEL observations, VP 918.5 and VP 919.5, had been performed with the Crab in the field of view. The data from these observations were not available during the preparation of this paper.

Table 5.1. COMPTEL observation summary with PSR B0531+21 within 30° from the pointing axis

VP #	Start Date TJD [†]	End Date TJD	Off angle ($^\circ$)	Exposure (1-3 MeV; $10^6 \text{ cm}^2 \text{ s}$)
Cycle 0				
0.3	8374.853	8377.686	8.98	⊥
0.4	8377.894	8380.678	8.98	8.677
0.5	8380.886	8383.662	0.13	⊥
Cycle I				
1	8392.903	8406.785	6.51	10.725
31	8784.730	8798.554	27.78	9.614
36.0	8845.170	8846.765	15.55	⊥
36.5	8846.806	8854.644	16.64	12.802
39	8866.263	8882.637	17.52	⊥
Cycle II				
213	9069.778	9075.544	3.19	2.764
221	9120.708	9131.637	3.00	4.615
Cycle III				
310	9322.653	9334.635	14.59	6.387
321.1/5	9391.663	9400.636	4.49	7.622
337	9573.925	9593.594	21.38	11.143
Cycle IV				
412	9776.688	9783.672	6.48	4.307
413	9783.690	9797.589	7.54	9.161
419.1	9811.629	9818.586	25.92	4.071
419.5	9846.614	9860.634	29.17	6.221
420	9860.654	9874.688	18.28	9.462
426	9937.618	9951.581	0.13	9.629
Cycle V				
502	10007.590	10021.594	8.38	10.877
520	10210.681	10224.556	24.18	8.310
523	10259.621	10273.551	26.70	7.462
526/527/528	10294.630	10322.616	5.04 [‡]	20.969
Cycle VI				
616.1	10497.670	10525.647	8.56	20.046
Cycle VII				
724.5	11001.609	11015.620	9.60	9.852
Cycle VIII				
816	11309.621	11323.581	14.59	8.132
829	11435.584	11449.597	3.00	10.826
Cycle IX				
903.1	11533.662	11540.639	16.78	4.212

[†] TJD = JD - 2440000.5 = MJD - 40000

[‡] weighted mean of 3 observations

of the sky simultaneously with a position determination accuracy of $\sim 1^\circ$. The events are time tagged with an accuracy of 0.125 ms and are converted to Coordinated Universal Time (UTC) with an absolute accuracy better than 100 μs using the on board master clock, serving also the other 3 CGRO instruments BATSE, OSSE and EGRET.

In this study we selected those CGRO Cycle 0-IX viewing periods for which the angle between the pointing axis

(co-aligned with the COMPTEL/EGRET z-axis) and the Crab pulsar is less than 30° . Details for each individual observation can be found in Table 5.1, which is self-explanatory.

Because we have also included extensively archival EGRET data in the current study, a brief summary of this CGRO instrument is given as well. EGRET has a (gas-filled) sparkchamber and is sensitive to γ -rays with energies in the range 30 MeV to 30 GeV. In the mode used for most of the observations the field of view is approximately 80° in diameter. Its effective area is approximately 1500 cm^2 between 200 and 1000 MeV. The angular resolution is strongly energy dependent: the 67% confinement angle at 35 MeV, 500 MeV and 3 GeV are $10^\circ 9'$, $1^\circ 9'$ and $0^\circ 5'$ respectively. The energy resolution $\Delta E/E$ is $\sim 20\%$ (FWHM) over the central part of the energy range. The relative timing accuracy is $8 \mu\text{s}$ and the absolute accuracy is better than $100 \mu\text{s}$. For a detailed overview of the EGRET detection principle and instrument characteristics, see Thompson et al. (1993).

The X-ray data most extensively used in this work had been collected with the 4 narrow field instruments aboard BeppoSAX: the low-energy (0.1-10 keV) and medium energy (1.6-10 keV) concentrator spectrometers, LECS and MECS respectively, the High-Pressure Gas Scintillation Proportional Counter, HPGSPC (4-60 keV) and the Phoswich Detector System PDS sensitive in the 15-300 keV energy range. Detailed instrument descriptions for the 4 narrow field instruments can be found in Parmar et al. (1997), Boella et al. (1997), Manzo et al. (1997) and Frontera et al. (1997) for the LECS, MECS, HPGSPC and PDS respectively.

5.3. Timing analysis

The first step in the timing analysis is to subject the events registered during an observation to an event selection filter. In the case of COMPTEL the most important selection parameters are the time-of-flight TOF, the pulse shape discriminator PSD (see e.g. Schönfelder et al. 1993), the “spatial” parameters χ , ψ , $\bar{\varphi}$ and the total energy deposit E_{tot} . Given the a priori known position of the Crab pulsar it is possible to determine for each event the so-called φ_{geo} angle, i.e the angle between the scattered photon and the source. The $\bar{\varphi}$ angle provides an equivalent measure of this angle, but now only based on the energy deposits in both detector layers. The difference angle $\varphi_{arm} = \bar{\varphi} - \varphi_{geo}$ is called the Angular Resolution Measure (ARM) and forms the base of the spatial response of COMPTEL and its distribution is narrowly peaked near $\varphi_{arm} = 0$ with asymmetric (energy dependent) wings. The definite and significant timing signature of the Crab pulsar in the COMPTEL energy range (Much et al. 1995; Much et al. 1997) provides a very useful tool to determine the optimum event parameter windows for celestial sources. In this study we have determined and used subsequently the optimum (total energy de-

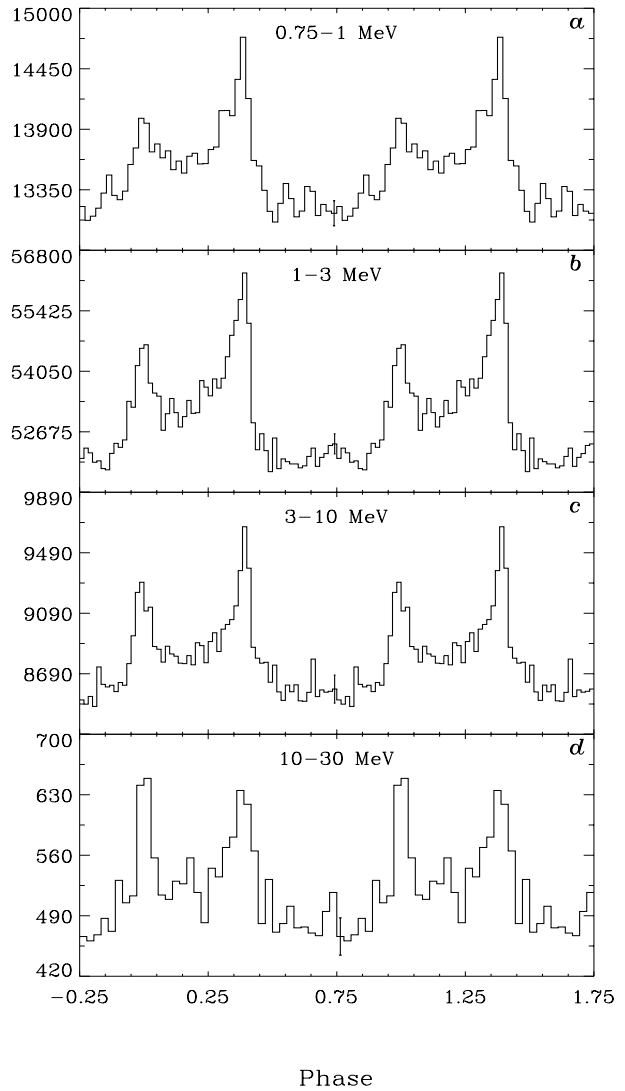


Fig. 5.1. Pulse profiles (double cycles) of PSR B0531+21 as measured by CGRO COMPTEL in 4 differential energy intervals: 0.75-1, 1-3, 3-10 and 10-30 MeV. Typical error bars are shown near phase 0.75. A clear morphology change of the pulse profiles is visible: below 10 MeV the second peak (near phase 0.4) dominates, and emission in the interpulse phase interval is significant, while above 10 MeV the first peak (near phase 0.0) dominates with strongly reduced interpulse emission.

posit dependent) parameter windows for the TOF and PSD. The optimum windows for the φ_{arm} angle turn out to be asymmetric around 0 and a function of total energy deposit (as expected). Also, these optimum windows have been applied. Finally, for the given combination of viewing periods (see Table 5.1) we compared the measured $\bar{\varphi}$ distribution, dominated by background photons, with the distribution expected for a point source at the Crab position. This allows for a determination of the optimum window for selection on $\bar{\varphi}$ (a function of the total energy deposit).

Table 5.2. Phase component definitions for the Crab pulsar adopted in this study

Component	Abbreviation	Phase interval	Width
Leading Wing 1	LW1	0.88 - 0.94	0.06
Peak 1	P1	0.94 - 1.04	0.10
Trailing Wing 1	TW1	0.04 - 0.14	0.10
Bridge	Bridge	0.14 - 0.25	0.11
Leading Wing 2	LW2	0.25 - 0.32	0.07
Peak 2	P2	0.32 - 0.43	0.11
Trailing Wing 2	TW2	0.43 - 0.52	0.09
Off Pulse	OP	0.52 - 0.88	0.36
Total Pulse	TP	0.88 - 1.52	0.64

Events, not vetoed by any of the 4 anti-coincidence domes surrounding the COMPTEL detector layers, and having a very low probability of originating from the Earth (“Earth Horizon selection”) and passing through our optimized event selection windows are finally used in the timing analysis.

The event arrival times (at the spacecraft) of these accepted events are converted to arrival times at the barycenter of the solar system (SSB) using the JPL DE200 solar system ephemeris and the Crab pulsar position. This process yields SSB arrival times with an absolute timing accuracy of less than $100 \mu s$. Subsequent phase folding using the Crab pulsar ephemeris data (CGRO timing database; Arzoumanian 1992) yields the pulse profile. Because the Crab pulsar shows a lot of timing noise (young pulsar) the ephemerides have only a limited validity interval. Therefore, in the phase folding process we used different timing solutions (ephemerides) for (almost) each observation given in Table 5.1. The derived pulse profiles (double cycles for clarity) in the 4 “standard” COMPTEL energy intervals – 0.75-1, 1-3, 3-10 and 10-30 MeV – combining all observations given in Table 5.1 are shown in Fig. 5.1. The two expected peaks, separated ~ 0.4 in phase, with clear emission between the peaks (bridge emission) are visible in each of the four panels of Fig. 5.1.

The significances for deviations from uniformity applying the Z_n^2 -test (Buccheri et al. 1983) with 8 harmonics on the unbinned set of pulse phases yields the following numbers (expressed in Gaussian sigma’s) for the 0.75-1, 1-3, 3-10 and 10-30 MeV energy windows: 17.1σ , 30.8σ , 17.0σ and 9.8σ respectively. Comparing the profiles with those presented in Much (1997) (the previous Crab pulsar publication using COMPTEL data) shows the enormous increase in statistical quality, especially for energies above 3 MeV, due to the longer exposure in combination with our improved event selection procedures. We witness a clear morphology change of the pulse profile in the COMPTEL 0.75-30 MeV energy range: below ~ 10 MeV the second peak (near phase 0.4) dominates the first peak (near 0), and the bridge emission is significant, while above ~ 10 MeV

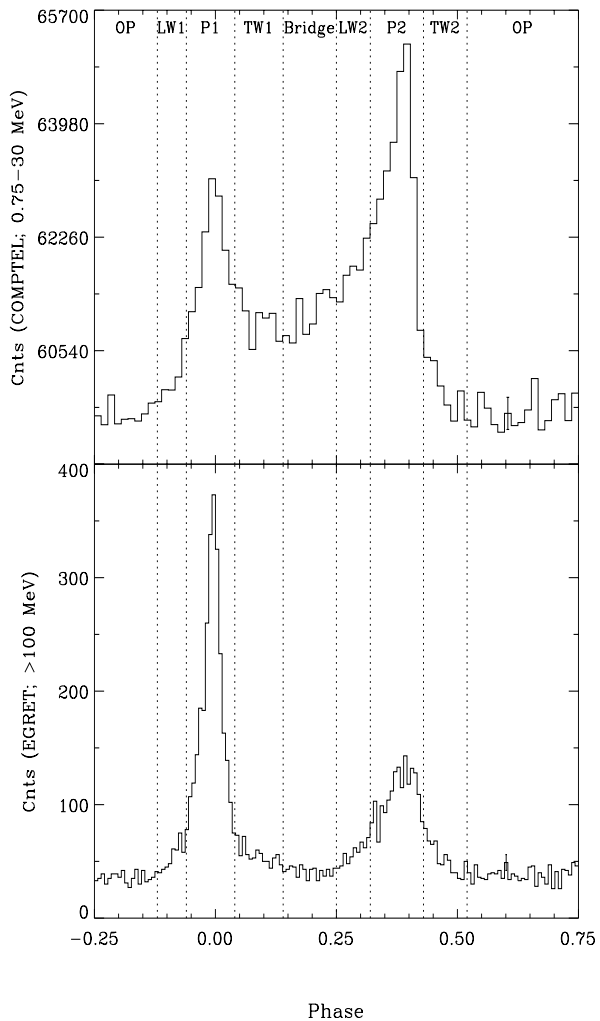


Fig. 5.2. Pulse profiles of PSR B0531+21 as observed by CGRO COMPTEL in the 0.75-30 MeV energy interval (top) and CGRO EGRET (bottom) for energies > 100 MeV. The boundaries of the pulse phase intervals defined by Fierro et al. (1998) are indicated by the dotted vertical lines. Notice the morphology change: at energies between 0.75-30 MeV the second peak dominates, while at energies above 100 MeV the first peak dominates. Moreover, in the 0.75-30 MeV interval there is considerable bridge emission in between the two peaks, which is hardly present at energies above 100 MeV.

the first peak dominates and the bridge emission is strongly reduced. This change was expected, but now actually seen, based on the pulse profile of the Crab pulsar observed at high-energy (> 30 MeV) γ -rays (see e.g. Thompson et al. 1977 and Clear et al. 1987 for the SAS-2 and COS-B Crab pulsar results, and Nolan et al. 1993, Fierro et al. 1998, or Fig. 5.2 for recent CGRO EGRET results) where emission in the first peak is more intense than in the second peak with strongly reduced bridge emission.

For the first time the statistics in the COMPTEL 0.75-30 MeV window are sufficiently good to perform accu-

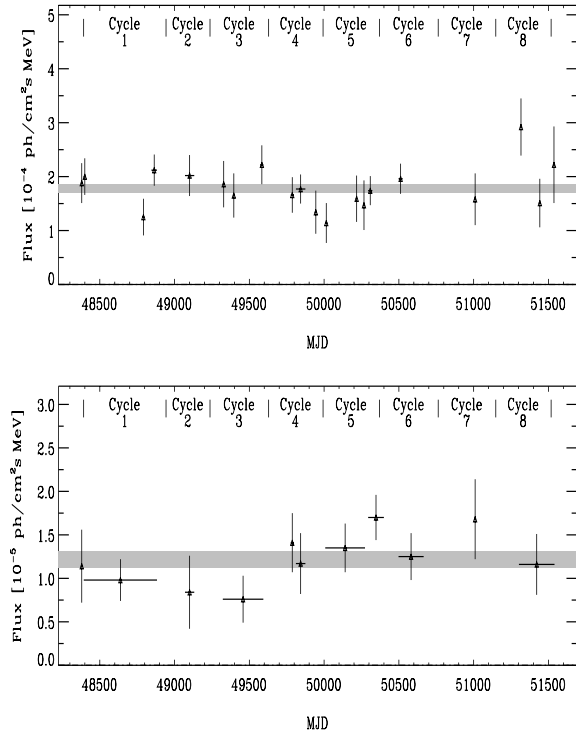


Fig. 5.3. “Total Pulsed” flux from the Crab pulsar as a function of time in the 1-3 MeV (top) and 3-10 MeV (bottom) energy intervals. The $\pm 1\sigma$ uncertainty intervals assuming a constant flux are indicated by the shaded regions in both figures. The χ^2_ν -values for the fits assuming the flux being constant are ~ 0.5 , thus there is no indication for “Total Pulsed” flux variability in both the 1-3 and 3-10 MeV energy intervals.

rate phase resolved spectral analyses. In order to allow direct comparisons with published CGRO EGRET results at higher γ -ray energies (Fierro 1995), we adopted the pulse phase interval definitions used in the latter work. These definitions, used consistently throughout this study, are given in Table 5.2. A visual representation is provided in Fig. 5.2, where both the COMPTEL 0.75-30 MeV pulse profile and the EGRET > 100 MeV profile are shown along with the pulse phase interval boundaries (dashed vertical lines). The COMPTEL 0.75-30 MeV profile is merely the sum of the profiles shown in the differential energy windows in Fig. 5.1 and represents the statistically most significant pulse profile of the Crab pulsar at medium energy γ -rays. We compiled the > 100 MeV EGRET profile from archival Cycle 0 to VI EGRET viewing periods with the Crab pulsar within 35° from the pointing axis, and in which the spark chamber was switched on. This study utilizes a substantially larger data base than the recent EGRET publication on the Crab pulsar (Fierro et al. 1998; Cycle 0-III data). The same ephemerides have been used (the Princeton database, Arzoumanian et al. 1992) as for the COMPTEL analysis.

The γ -ray profiles in Fig. 5.2 are time-averaged profiles, compiled over many years. Before analysing the pro-

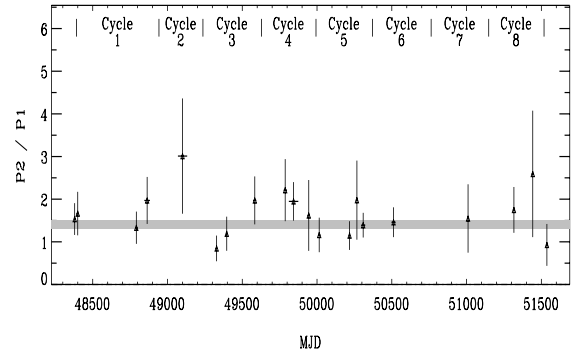


Fig. 5.4. The P2/P1 flux ratio of the Crab pulsar in the 1-3 MeV energy interval as a function of time. The $\pm 1\sigma$ uncertainty interval assuming a constant ratio is indicated by the shaded region. The P2/P1 ratio is consistent with being constant.

files further, we first verified the long-term stability of the γ -ray signature (flux and pulse shape).

5.4. Long-term variability

5.4.1. Flux variations: total pulsed flux in the 1-10 MeV range

We studied the time variability of the emission from the Crab pulsar by determining the “pulsed” flux in differential energy windows as a function of time. The “pulsed” flux has been derived from the number of excess counts in the Total Pulse phase interval (see Table 5.2) atop the average emission level in the Off Pulse phase interval. For the latter interval we assume that the emission originates from the nebula only, although a DC-contribution from the pulsar can not be ruled out. We show as examples the 1-3 and 3-10 MeV results. These results over the almost 9 year baseline (April 1991/December 1999) are shown in Fig. 5.3. For the 1-3 MeV energy interval typical integration times are 2/3 weeks, while in the 3-10 MeV interval longer integration times are used given the strongly reduced statistics. The χ^2_ν values for the fits assuming a constant flux level are typically ~ 0.5 for both energy ranges, indicating that there is no evidence for time variability. Fierro (1995) also studied the Crab long-term variability for energies above 100 MeV and also concluded that the emission from the Crab pulsar is stable.

5.4.2. Pulse shape variations: P2/P1 ratio in the 1-3 MeV range

The time variability of the pulse shape was investigated in the 1-3 MeV (best statistics) energy window by determining the P2/P1 ratio for each observation. This ratio is derived by measuring the number of excess counts in the P2 and P1 phase intervals (see Table 5.2) atop the level in the Off Pulse interval. This ratio is shown in Fig. 5.4. The χ^2_ν value for a fit assuming a constant P2/P1 ratio is ~ 0.8 .

Therefore, there is no indication for a time dependency of the pulse shape at medium energy γ -ray energies consistent with the findings presented by Carramiñana et al. (1994). For energies above 30 MeV Fierro (1995) studied the long-term temporal variation of the P2/P1 ratio and found also no evidence for a (systematic) variation over the Cycle 0-III EGRET observations. Tompkins et al. (1997) came to a similar conclusion using an extended EGRET data base including also Cycle IV-V EGRET observations.

5.4.3. Variations in arrival time of P1 at energies above 30 MeV

Another test on the stability of the pulse shape is a test for variations of the arrival time/phase of P1 (maximum), particularly remembering that different ephemerides had to be used over the CGRO mission lifetime. For this purpose we used the high signal-to-noise EGRET > 30 MeV data. We determined for each observation the arrival phase of P1 by fitting a symmetric Lorentzian profile plus a constant background to the measured event distribution in a relatively broad (0.3) phase window centered around phase 0. In Fig. 5.5 the arrival phases of P1 are shown as a function of time over a ~ 7.5 year baseline (VP 0.2 up to and including VP 724.5). The error bars on the individual datapoints are composed of a statistical contribution from the profile fit and of a systematic component of about $100 \mu\text{s}$ (1σ) reflecting the uncertainties in the dispersion measure from the radio pulsar timing observations (see explanatory supplement *README.txt* in the Princeton CGRO database directory). The P1 arrival phases have been fitted by a constant value yielding as optimum value -0.0072 ± 0.0009 for an acceptable χ^2_ν value of 1.59 for 19 degrees of freedom. This offset in the phase domain translates to an offset of $-241 \pm 29 \mu\text{s}$ in the time domain and indicates that the high energy γ -ray photons from the main pulse arrive *earlier* than the fiducial point in the radio pulse profile template, which was defined to be the maximum of the main radio pulse (P1). This value of $-241 \mu\text{s}$ is significantly larger than the quoted CGRO absolute timing uncertainty of better than $100 \mu\text{s}$ and denotes a genuine deviation. This result is consistent with the findings presented by Rots et al. (2000) using X-ray data from RXTE Crab monitoring observations. They found a time lag between radio and X-rays of about $250 \mu\text{s}$.

The statistics in the COMPTEL data are not sufficiently good to repeat the above analysis done for single observations. The analysis can be performed for the integral COMPTEL time-averaged profile (Fig. 5.2), but is more complicated: the P1 profile is asymmetric due to the high bridge emission. Nevertheless, fitting a symmetric Lorentzian plus background the maximum appears to be slightly shifted with respect to the EGRET P1 position, but is consistent with no shift ($-55 \pm 68 \mu\text{s}$) with respect to the radio maximum. In Sect. 5.7 it will be shown that a broad underlying bridge component can explain the shift of

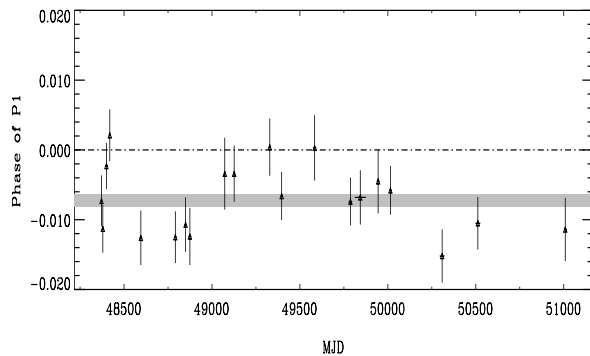


Fig. 5.5. The P1 arrival phase vs time for photon energies in excess of 30 MeV. The $\pm 1\sigma$ uncertainty interval assuming a constant arrival phase is indicated by the hatched region. The high-energy γ -rays arrive $241 \pm 29 \mu\text{s}$ earlier than the fiducial point in the radio template.

the COMPTEL maximum with respect to the neighbouring X-ray and high-energy γ -ray P1 profiles.

5.5. Pulse profiles of PSR B0531+21 from 0.1 keV up to 10 GeV

The γ -ray pulse profiles in Figs. 5.1 & 5.2 show that the pulse morphology changes significantly over the COMPTEL energy window (0.75-30 MeV), i.e. the emission spectra vary significantly with phase. Phase-resolved spectral analyses have earlier been performed at X-ray and γ -ray energies for different data sets and/or different narrow energy intervals. However, for each study, different phase selections have been made such that a consistent full high-energy picture of the Crab pulsar can not be compiled from published results. Therefore, we extended our energy window by analysing consistently not only the CGRO EGRET (30 MeV - 10 GeV) high-energy γ -ray data, but also X-ray data from the ROSAT HRI (0.1-2.4 keV), BeppoSAX LECS (0.1-10 keV), MECS (1.6-10 keV) and PDS (15-300 keV), and CGRO BATSE (20 keV- 1 MeV). Firstly, we compiled Crab profiles over the energy range 0.1 keV to 10 GeV.

The soft X-ray ROSAT HRI data were collected during an observation of the Crab pulsar/nebula performed from 4 March 1995 to 15 March 1995 yielding a net exposure time of 7.98 ks. Because the data are spread over 115 different orbital intervals over the 11 day observation period the pretty large ROSAT clock drift will result in a messy pattern when combining the pulse phases from the entire observation. We could identify 4 consecutive sets of orbital intervals in which the observed pulse profile is stable. The 0.1-2.4 keV pulse profile shown in Fig. 5.6 a was obtained cross-correlating 3 of the 4 profiles with the profile chosen as template, correcting for the observed mutual phase shifts and fixing the zero phase at the centre of the main peak.

The BeppoSAX LECS, MECS and PDS data have been collected during a calibration observation of the Narrow

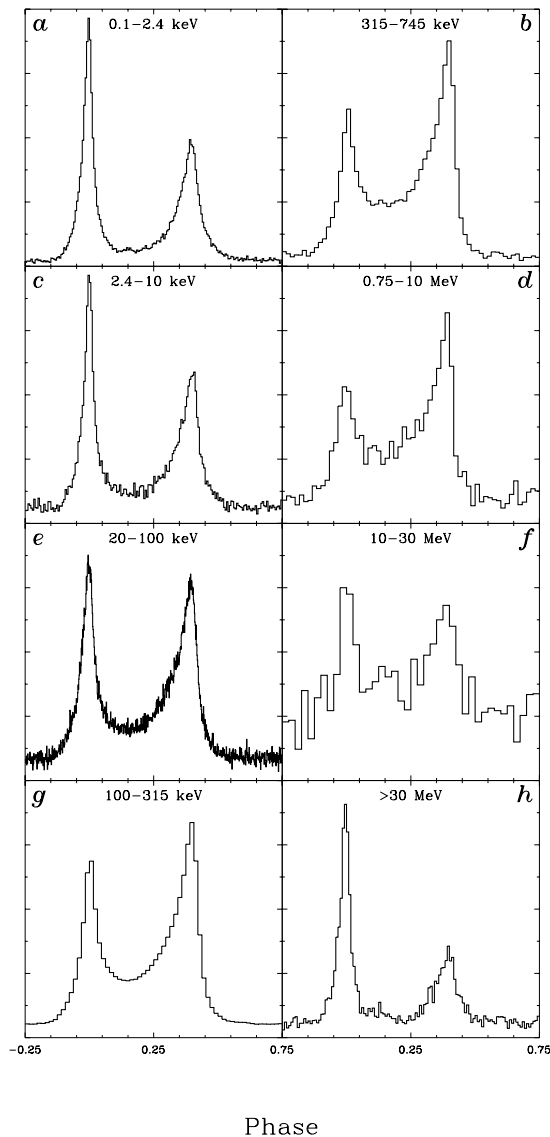


Fig. 5.6. High-energy pulse profiles of PSR B0531+21 from 0.1 keV up to 10 GeV. Data have been used from the following instruments: ROSAT HRI (0.1-2.4 keV; panel **a**), BeppoSAX MECS (2.4-10 keV; panel **c**), BeppoSAX PDS (20-100 keV; panel **e**), CGRO BATSE (100-315 keV & 315-750 keV; panels **b,g**), CGRO COMPTEL (0.75-10 MeV & 10-30 MeV; panels **d,f**) and CGRO EGRET (> 30 MeV; panel **h**). The morphology change of the profiles as a function of energy is striking.

Field instruments aboard BeppoSAX performed on 25-26 September 1999 yielding (screened) effective exposure times of 7.75 ks, 32.6 ks and 30.7 ks for the LECS, MECS (unit-2) and PDS clusters A & B, respectively. In Fig. 5.6 **c** and **e** the Crab pulse profiles are shown as observed by the MECS in the 2.4-10 keV energy window and by the PDS in the 20-100 keV energy window, respectively.

In the hard X-ray/soft γ -ray band (0.05-1 MeV) we have used archival data from the CGRO BATSE Large Area De-

tectors collected during observations performed between MJD 48392 and 50273 in the onboard folding mode. Typical integration times were 2/3 weeks per included observation (64 observations have been used in this study). The profiles had been produced in 64 bins per cycle in 16 different energy channels for each individual observation run. We determined the shifts of the pulse profiles of the individual observation runs with respect to the profile obtained during the observation run 48392-48406 in channel 9 (~ 165 -230 keV) by cross-correlation. Applying the shifts in the combination of the pulse profiles and putting the first peak at phase 0 yields high quality pulse profiles in the 20 keV - 2 MeV range. In Fig. 5.6 **g** and **b** the profiles are shown for the 100-315 keV (channels 7-10) and 315-745 keV (channels 11-13) energy windows, respectively.

At medium energy γ -rays the CGRO COMPTEL pulse profiles derived in this work are shown for the 0.75-10 and 10-30 MeV energy windows in Fig. 5.6 **d** and **f**, respectively. Finally, in Fig. 5.6 **h** the CGRO EGRET pulse profile is given for energies above 30 MeV, also derived in this work.

From the (high-energy) pulse profile compilation shown in Fig. 5.6 we can immediately observe some striking features. The appearance of the second peak (near phase 0.4) becomes more and more pronounced for increasing energies. However, above ~ 10 MeV the first peak becomes dominant again. The “Bridge” emission shows the same behaviour as the second peak. Emission in this phase interval gradually increases reaching a maximum level at MeV energies, beyond which a rapid decline is observed towards a strongly reduced level at high-energy γ -rays. A more quantitative evaluation of this morphology change of the profile as a function of energy will be presented in the next subsection.

5.5.1. P2/P1 and Bridge/P1 ratios as a function of energy

From the pulse phase distributions measured by the above mentioned high-energy instruments we can derive more quantitative information such as intensity ratios of pulse phase components as a function of energy. We determined in this way the intensity ratios for P2/P1 and Bridge/P1 as a function of energy over the entire 0.1 keV to 10 GeV energy interval, adopting the phase interval definitions of Table 5.2. The emission in each interval has been separated from the underlying nebula/DC emission by subtracting the (properly scaled) emission from the OP phase interval. The results are visualized in Figs. 5.7 & 5.8 for the P2/P1 and Bridge/P1 ratios, respectively. In these plots we have also included the ratios derived from the optical profile in the 3800 to 6500 Å wavelength interval obtained by Much et al. (2000) using the UCL MIC detector. The ratios in the Far-Ultraviolet (1140-1720 Å) and Near-Ultraviolet (1600-3200 Å) as obtained from (time-tagged) data taken by the HST STIS instrument (Sollerman et al. 2000, Gull et al. 1998) are presented too. In all optical ranges we ap-

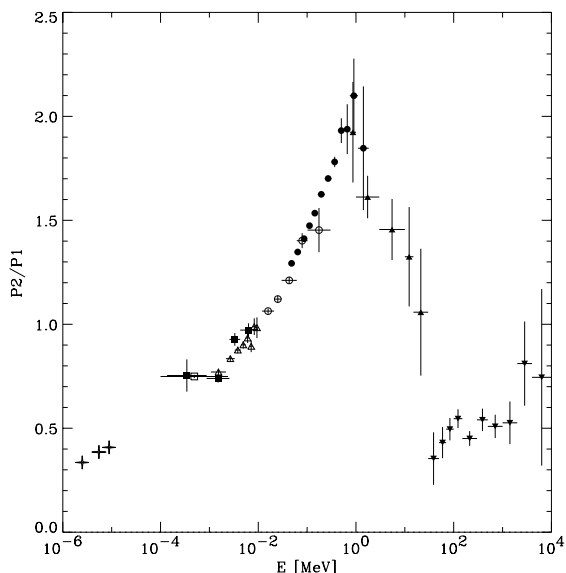


Fig. 5.7. P2/P1 ratio as a function of energy from optical wavelengths up to high-energy γ -rays. Data from the following instruments have been used: optical wavelengths, UCL MIC detector (star symbol), NUV/FUV HST STIS (star symbols); X-ray energies, ROSAT HRI (open square), BSAX LECS (filled square), BSAX MECS (open triangle); Hard X-rays/soft γ -rays, BSAX PDS (open circles), CGRO BATSE (filled circles); Medium/hard γ -ray energies, CGRO COMPTEL (filled upwards pointing triangle), CGRO EGRET (filled downwards pointing triangle). The gradual increase of the P2/P1 ratio up to ~ 1 MeV is striking, a sharp decline in the 1-30 MeV energy range follows and a recovery to the optical ratio value settles above ~ 30 MeV.

plied again the consistent phase interval definitions. Unfortunately, the interstellar extinction in the Extreme Ultraviolet (100-1000 \AA , covered by the Extreme UltraViolet Explorer EUVE) in the Crab direction is so large that the gap shown in both Figs. 5.7 & 5.8 between the FUV and soft X-rays can never be filled in by space-borne instruments.

The P2/P1 ratio as a function of energy (Fig. 5.7) gradually increases from the optical wavelength range to ~ 1 MeV, followed by a rapid decrease in the 1-30 MeV interval (the COMPTEL energy window) towards a more or less constant value of ~ 0.5 for energies above 30 MeV (the EGRET energy window). The Bridge/P1 ratio vs. energy (Fig. 5.8) exhibits a very similar shape as for the P2/P1 ratio. However, the values of the latter ratio in the optical and high-energy γ -ray domains, become very small (0.017) indicating that the Bridge emission practically vanishes. It is only substantial in the ~ 1 keV to ~ 10 MeV energy window in contrast with the emissions from the 2 peaks which are always present. This behaviour suggests that we are dealing with an emission component distinct from the emission from both peaks. This hypothesis (see e.g. also Knight 1982, Hasinger 1984,1985 and Massaro 2000) is further strengthened in the phase-resolved spectral analysis presented in the next section.

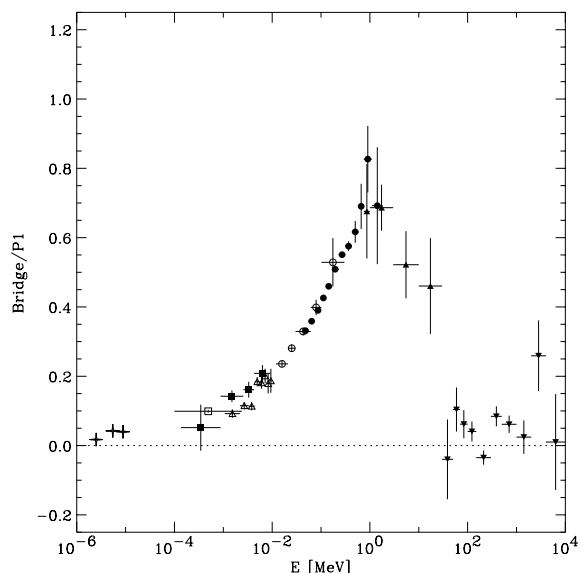


Fig. 5.8. Bridge/P1 ratio as a function of energy from optical wavelengths up to high-energy γ -rays. See the caption of Fig. 5.7 for the meaning of the symbols. The Bridge/P1 ratio is almost 0 at optical wavelengths, but gradually reaches a maximum near 1 MeV, followed by a drastic break in the 1-30 MeV energy range. Above ~ 30 MeV the Bridge/P1 ratio approaches the optical value of ~ 0.017 .

Similar analyses have been presented in the past by other authors (e.g. Toor & Seward 1977, Hasinger 1984,1985, Ulmer et al. 1994, Mineo et al. 1997 and Massaro et al. 1998,2000), generally over more restricted energy windows with poorer data coverage, and/or often using data of much less statistical quality than is available now. Particularly the “transition” region of the COMPTEL MeV window is well covered for the first time.

5.6. Spectral analysis

In this section we will first present the spectra of the nebula emission and the Total Pulse emission (excess emission in Total Pulse interval; see Table 5.2). Then we will show the results from the phase resolved spectral analysis for the narrow phase intervals. Like for the timing analysis, we did not limit ourselves to the analysis of the COMPTEL data, but we collected data over a very wide spectral band to derive a consistent overall high-energy picture of the Crab. Combining spectra derived by different instruments, we had to assess possible systematic effects in the flux estimates, and their impact on our analysis and conclusions. For this purpose, we used the nebula spectra to estimate possible (in)consistencies.

5.6.1. Crab nebula spectrum

To determine the Crab nebula spectrum from our COMPTEL (0.75-30 MeV) Cycle 0-IX observations (see Table

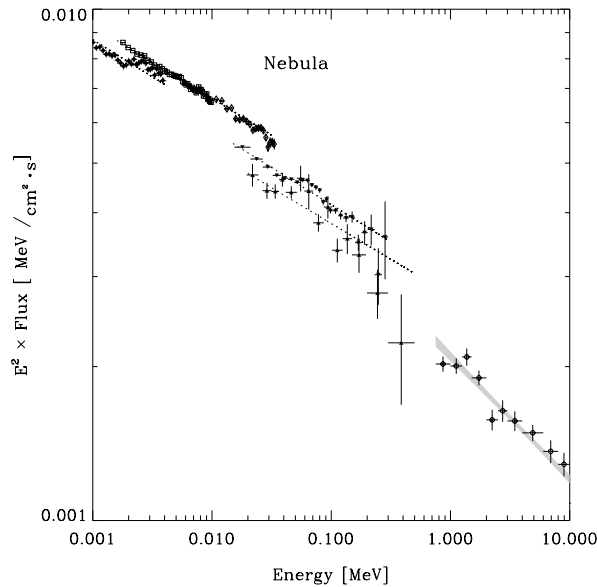


Fig. 5.9. The Crab nebula spectrum in the 1 keV - 10 MeV energy interval. Flux measurements from BeppoSAX LECS (filled diamonds; 1-4 keV), MECS (open squares; 1.6-10 keV), HPGSPC (open diamonds; 10-32 keV) and PDS (downwards filled pointing triangles; 15-300 keV), GRIS (upwards pointing filled triangles; 20-500 keV) and COMPTEL (open circles; 0.75-10 MeV) are shown. The dotted lines show the best power-law fits for the combined BeppoSAX instruments and for GRIS. Note the apparent systematic deviation from the power-law fit in the LECS spectral data. The shaded band indicates the $\pm 1\sigma$ uncertainty interval around the optimum power-law fit for COMPTEL (0.75-30 MeV). Clear discrete jumps are visible between the various BeppoSAX instruments and GRIS reflecting uncertainties in absolute sensitivity.

5.1) we selected events recorded in the Off Pulse phase interval (see Table 5.2), assuming that any pulsar DC emission is negligible, and applied a maximum likelihood method using the spatial signature of a point source in the (φ, φ_{arm}) plane as a function of measured energy. This work yielded an improved spectrum for the nebula emission in the COMPTEL energy range compared to the COMPTEL Crab nebula spectrum published earlier by van der Meulen et al. (1998). In the latter work a smaller database was used, as well as preliminary response characteristics, which have since been improved upon. The new COMPTEL spectrum is given in Table 5.3.

To cover the neighbouring soft X-ray to soft γ -ray band, we derived ourselves the BeppoSAX LECS, MECS, HPGSPC and PDS nebula spectra applying the most recent (December 1999 issue for the LECS and HPGSPC and November 1998 issue for the MECS and PDS) response characteristics (sensitive area, energy redistribution matrices and spatial response). We fitted the Sept. 1999 Off Pulse Crab data from these 4 BeppoSAX instruments over the full 0.1-300 keV energy range with an absorbed power-law model taking into account the mutual uncertainties in abso-

Table 5.3. COMPTEL spectra of the Crab nebula and the pulsar (Total Pulse)

Energy window [MeV]	Nebula Flux [$ph/cm^2 s MeV$]	Total Pulse Flux [$ph/cm^2 s MeV$]
0.75 1.00	$(2.715 \pm 0.092)E-3$	$(0.643 \pm 0.074)E-3$
1.00 1.25	$(1.611 \pm 0.056)E-3$	$(0.467 \pm 0.045)E-3$
1.25 1.50	$(1.117 \pm 0.044)E-3$	$(0.284 \pm 0.035)E-3$
1.50 2.00	$(0.638 \pm 0.021)E-3$	$(0.162 \pm 0.017)E-3$
2.00 2.50	$(0.316 \pm 0.015)E-3$	$(0.080 \pm 0.012)E-3$
2.50 3.00	$(0.219 \pm 0.011)E-3$	$(0.050 \pm 0.009)E-3$
3.00 4.00	$(1.313 \pm 0.058)E-4$	$(0.279 \pm 0.046)E-4$
4.00 6.00	$(0.626 \pm 0.023)E-4$	$(0.118 \pm 0.018)E-4$
6.00 8.00	$(0.286 \pm 0.015)E-4$	$(0.061 \pm 0.012)E-4$
8.00 10.0	$(1.616 \pm 0.085)E-5$	$(0.301 \pm 0.069)E-5$
10.0 15.0	$(0.730 \pm 0.035)E-5$	$(0.250 \pm 0.028)E-5$
15.0 30.0	$(0.201 \pm 0.014)E-5$	$(0.041 \pm 0.011)E-5$

lute flux calibrations by including in the fit 3 free relative normalization scale factors (MECS scale factor fixed to 1). The best photon index and Hydrogen column density N_H , assuming solar abundances for the other elements absorbing soft X-rays, resulting from this fit are -2.145 ± 0.001 and $3.61(2) \times 10^{21} \text{ cm}^{-2}$, respectively. Massaro et al. (2000) reported recently a significantly lower value for N_H of $3.23(2) \times 10^{21} \text{ cm}^{-2}$ analysing a much larger BeppoSAX Crab database. The apparent discrepancy can be explained by their use of an older version of the LECS response description in combination with fitting LECS 0.1-4 keV data only, thus constraining to a lesser extent the photon index. We verified this by reproducing our values for N_H , the normalization and the photon index for this Off Pulse emission repeating our analysis for the database used by Massaro et al. (2000). Our value for N_H of $3.61(2) \times 10^{21} \text{ cm}^{-2}$ is consistent with the X-ray based value of $3.45(42) \times 10^{21} \text{ cm}^{-2}$ obtained by Schattenburg & Canizares (1986) using the Focal Plane Crystal Spectrometer on the Einstein observatory and with a radio based estimate of $\sim 3.65 \times 10^{21} \text{ cm}^{-2}$ (Dickey & Lockman 1990).

In the fit to the data of the 4 BeppoSAX NFI instruments we derived for the sensitivity normalization scale factors, relative to the MECS (factor set to 1): LECS 0.93, HPGSPC 1.01 and PDS 0.87. This means that the LECS and PDS calibrations of their overall sensitivities deviate from that of the MECS by 7% and 13%, respectively. This is clearly visible in Fig. 5.9, which presents the nebula spectrum in an $E^2 \times F$ representation between 1 keV and 10 MeV as measured with the 4 BeppoSAX NFI instruments and COMPTEL, in which no normalization correction factors have been applied. Also shown is the Crab nebula spectrum in the 0.02-1 MeV energy range as measured by the balloon borne GRIS (Ge detectors; Bartlett et al. 1994a). The combined BeppoSAX spectra as well as the GRIS spec-

trum are best fitted with a power-law spectral shape with a consistent slope of ~ -2.14 over the 1-700 keV interval. However, the normalization factor for GRIS, relative to the MECS is even as low as 0.78, to be compared with the estimated GRIS systematic uncertainties of $+12\%$ and -6% by Bartlett (1994b). Allowing spectral curvature in the multi-instrument BeppoSAX nebula fit by introducing an energy dependent power-law index does not improve the fit significantly. The same is true for the GRIS spectrum. However, some gradual softening above a few 100 keV is required to connect to the softer spectrum measured by COMPTEL at energies above 1 MeV (cf. Fig. 5.9; power-law photon index in the 0.75-30 MeV interval is -2.240 ± 0.014). The statistical uncertainties in the above quoted normalization correction factors are typically better than 1%. Therefore, it is obvious that the differences in absolute normalizations are systematic, and it is discouraging to note that between the two instruments for which the calibrations were expected to be most accurate (MECS and GRIS), the discrepancy appears to be largest. We cannot decide unambiguously on this controversy. Therefore, we feel that in the presentation and analysis of the above spectral data in combined broad band spectra, this problem should not be hidden by making arbitrary choices on normalization. We should note that also COMPTEL has an overall uncertainty on its flux estimates of the order of 20%. For the adjacent EGRET high-energy (30-30000 MeV) γ -ray range we did not derive ourselves new spectra using all available EGRET data on the Crab, like we did for the timing analysis. Due to the problem of gas aging, the spark chamber efficiency degraded significantly during the later Cycles of the EGRET CGRO observations, and the EGRET team did not yet publish for the later Cycles energy and time dependent correction factors. Therefore, we compare our new COMPTEL spectrum (like in van der Meulen et al. 1998) with the EGRET spectrum of Fierro (1995), who analysed Cycle 0-III data. The EGRET spectral data are claimed to be accurate down to a $\sim 10\%$ level (Thompson et al. 1995).

The Crab nebula spectrum from 0.1 keV up to 50 TeV is shown in an $E^2 \times F$ representation in Fig. 5.10. The BeppoSAX, GRIS, COMPTEL and EGRET spectra (no normalization factors) are included, together with ground-based TeV data (STACEE-32 > 0.19 TeV, Oser et al. 2000; HEGRA 1-20 TeV, Aharonian et al. 2000; Whipple 0.5-8 TeV, Hillas et al. 1998; CANGAROO 7-50 TeV, Tanimori et al. 1998). Similarly to the spectrum shown in van der Meulen et al. (1998), but now even more clearly, we see a continuous and smooth decrease from soft X-rays up to medium energy γ -rays, irrespective of the uncertainties in the absolute sensitivities of the instruments, followed by a steep gradient beyond ~ 30 MeV till ~ 300 MeV. Above ~ 300 MeV an additional emission feature seems to emerge reaching a maximum between 10 and 100 GeV, a window not yet accessible for space-borne and ground-based experiments. For an interpretation of this spectral shape, see e.g. de Jager et al. (1996).

5.6.2. Crab Total Pulse spectrum

In the 0.75-30 MeV energy range we determined the pulsed flux values from all CGRO COMPTEL observations (see Table 5.1) in two distinct manners. In the first method, the number of (pulsed) excess counts in the broad Total Pulse interval (see Table 5.2) above the mean level in the Off Pulse interval is determined as a function of measured energy. These excess counts are then converted to flux values using the COMPTEL response and the total exposure. The second approach is based on the maximum likelihood method in the spatial domain as introduced in Sect. 5.6.1. Applying the latter approach for pulse phase selected events and subtracting the properly scaled Off Pulse contribution (containing only the DC/nebula source with a point source signature) yields the pulsed fluxes as a function of energy for the selected pulse phase intervals. We verified for the Total Pulse interval, having the best statistics, that the fluxes derived from both methods are compatible within 5 – 20%, giving a measure of the systematic uncertainties. The COMPTEL Total Pulse fluxes from the spatial analysis (remember, nebula emission subtracted) are also included in Table 5.3 and shown in Fig. 5.11.

For comparison, we include in Fig. 5.11 the published total Crab pulsar spectra from EGRET (30 MeV-10 GeV, Cycle 0-III; Fierro 1995) and GRIS (20 keV - 1 MeV; Bartlett 1994a). A feature in the COMPTEL Total Pulse spectrum becomes apparent: the high flux value in the 10-15 MeV interval, consistently derived in both the timing and spatial methods. A response anomaly is excluded, e.g. the nebula 0.75-30 MeV spectrum (cf. Fig. 5.10) exhibits a very smooth behaviour over its full range, nor has such an effect been seen in other COMPTEL analyses. Fitting the COMPTEL flux points with a power-law spectral model, excluding the deviant 10-15 MeV flux point, yields a good fit with photon index of -2.36 ± 0.06 ($\chi^2_\nu = 0.57$ for 9 d.o.f.), connecting smoothly at both ends to the GRIS and EGRET flux measurements. The excess flux in the 10-15 MeV interval above this power-law model fit reaches a significance of 3.6σ . Including the deviant 10-15 MeV flux point in the spectral fit yields a worse fit ($\chi^2_\nu = 1.57$ for 10 d.o.f) with a power-law index of -2.24 ± 0.04 , which does not connect smoothly to the neighbouring measurements, particularly by EGRET. The 10-15 MeV excess flux above this fit has a significance of only 2.1σ . We do not regard the 10-15 MeV flux enhancement as a firm detection of a new spectral feature, and have no possible astrophysical interpretation, but we find it interesting to note that contributions to this flux enhancement appear to come from those (narrow) phase intervals in which a broad spectral (Bridge) component dominates the spectrum (see Sect. 5.6.3). If genuine, it could therefore be related to this spectral component. Unfortunately, no new missions with good sensitivity between 10 and 30 MeV have so far been scheduled.

For the BeppoSAX LECS, MECS and PDS we determined the number of (pulsed) excess counts above the mean

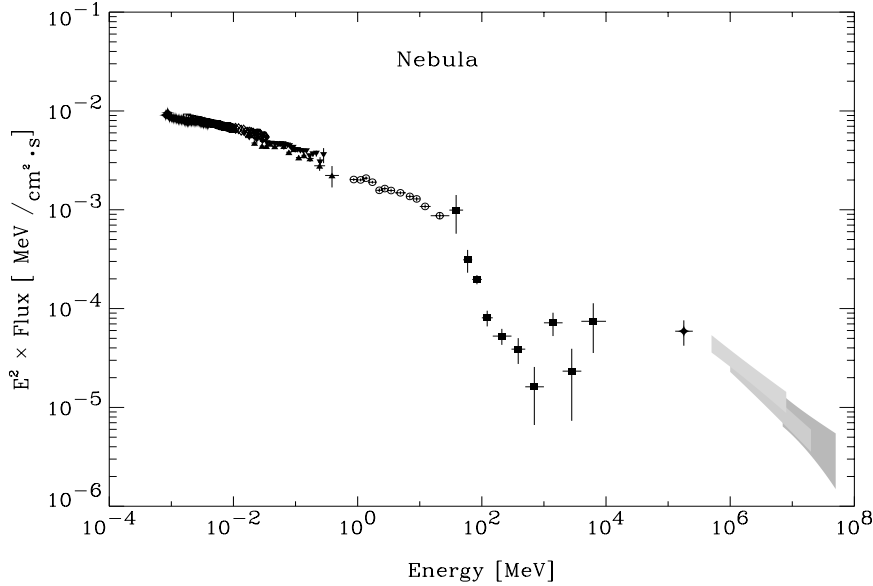


Fig. 5.10. The Crab nebula spectrum from soft X-rays up to TeV γ -rays. See the caption of Fig. 5.9 for the meaning of the data point symbols at energies between 10^{-3} and 30 MeV. The EGRET (30-30000 MeV) data points are indicated by filled squares. The TeV data point near 1.6×10^5 MeV is taken from Oser et al. (2000) and the hatched bands represent the flux measurements and corresponding 1σ uncertainty estimates at TeV energies (for references, see text).

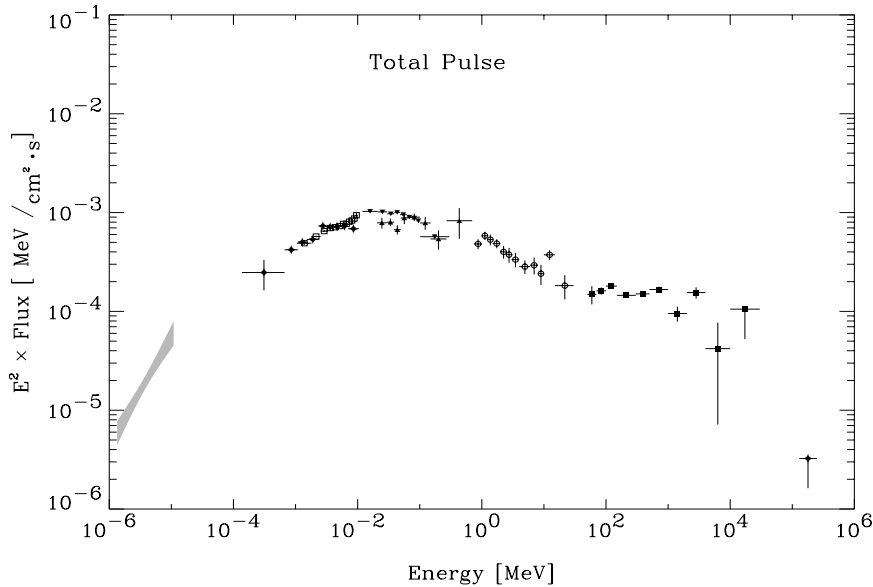


Fig. 5.11. The Total Pulse emission of the Crab pulsar from optical wavelengths up to high-energy γ -rays. The nebula emission has been subtracted. The optical spectral data (10^{-6} - 10^{-5} MeV) are taken from Sollerman et al. (2000); For a meaning of the data point symbols see the caption of Fig. 5.10.

level in the Off Pulse phase interval, similarly to the first COMPTEL method. These excess counts have been converted to flux measures applying the most recent response characteristics assuming intrinsic power-law type emission absorbed in a column of density $N_{\text{H}} = 3.61(2) \times 10^{21} \text{ cm}^{-2}$ (see Sect.5.6.1). In this way we obtained the Total Pulse spectrum over the 0.1-300 keV energy interval.

In Fig. 5.11 we show the high-energy X-ray, γ -ray spectrum of the Crab pulsar in the broad Total Pulse phase interval. We augmented the energy coverage by including the pulsed spectra obtained at optical/NUV/FUV wavelengths by Sollerman et al. (2000). In this $E^2 \times F$ representation, the total pulsed emission shows a gradual increase from the optical range towards a plateau of maximum luminosity extending from ~ 10 keV to ~ 1

MeV. Beyond ~ 1 MeV the emission softens until ~ 70 MeV, above which a second plateau appears with an emission spectrum having a photon power-law index close to -2 . Between 5 and 10 GeV the pulsar spectrum appears to break/soften drastically to account for the recently derived upper limits for pulsed emission at TeV γ -ray energies (see e.g. Vacanti et al. 1991, Borione et al. 1997, Aharonian et al. 1999, Lessard et al. 2000 and Oser et al. 2000). Its spectral behaviour is completely different from that of the nebula (cf. Fig. 5.10). Notice the dominance of the nebula emission component over the pulsed emission component for energies below ~ 100 MeV and above ~ 10 GeV, comparing Figs. 5.10 & 5.11. Only in a small window at high-energy γ -rays between ~ 100 MeV and ~ 10 GeV the pulsed component exceeds the underlying nebula com-

ponent. This Total Pulse spectrum is clearly complex. For detailed theoretical interpretations one should take into account the systematic uncertainties between the different instruments, as discussed in the previous section. In the next section we will attempt to disentangle this total spectrum in contributions from different phase components of the pulse profile, obviously important for detailed modelling.

5.6.3. Spectral behaviour in the narrow pulse phase intervals

A similar broad band spectral analysis (0.1 keV - 10 GeV), as presented in Sect. 5.6.2 for the Total Pulse interval, has been performed for the 7 narrow pulse phase intervals defined within the Total Pulse phase interval (see Table 5.2). We analyzed data from the BeppoSAX LECS, MECS and PDS and CGRO COMPTEL instruments and used the EGRET results derived by Fierro (1995) for the identical phase window selections. Since we planned to make empirical fits to the multi-instrument spectra, we wished to avoid fitting the systematic discrete jumps in the overlapping spectra of the BeppoSAX LECS, MECS and PDS, as shown in Fig. 5.9. In order to investigate the effect of these relative normalizations, we analysed the spectral data using two different approaches to the normalization. We first normalized the three spectra to the mean of the 3 BeppoSAX instruments, the “high” (relative to the COMPTEL and EGRET spectra) normalization, leading to the following flux normalization correction factors: LECS 0.998, MECS 0.937 and PDS 1.073. Then we applied a “low” normalization, in which the BeppoSAX spectra were substantially moved downwards, normalizing to the GRIS spectrum, to verify whether this influences our conclusions.

Applying the “high” normalization factors, the spectral results for the seven different intervals are shown in Fig. 5.12. This compilation clearly shows that the spectral shape varies strongly with pulsar phase. For example, the spectra of the P1 and the Bridge intervals differ dramatically. Emission from the latter is hardly discernible at energies below 1 keV and above 100 MeV; this emission is confined within a restricted energy window roughly between these energies in a broad “bump” shaped fashion in this $E^2 \times F$ representation. On the other hand, the emission in the P1 interval remains very strong in the γ -ray domain above 1 MeV (COMPTEL and EGRET data), exhibiting a power-law photon distribution up to a spectral break at GeV energies. Extrapolation of such a power-law spectral shape to X-ray energies, reveals a narrower “bump” shaped excess above the power-law extrapolation, with a maximum power output well below 100 keV. The P2 spectrum is rather similar to the spectrum of P1, but a spectral component similar in shape to that of the Bridge interval seems to enhance the P2 spectrum at MeV energies, relative to the P1 spectrum. Finally, the Trailing Wing 1 (TW1) and Leading Wing 2 (LW2) spectra are amazingly similar in shape, and appear to be some mixture of shapes of P1 and the Bridge intervals.

This should not be a surprise, because the adopted separation in phase intervals (Table 5.2) will most likely not coincide exactly with genuine physical components (different dominating production mechanisms and/or production sites in the Crab magnetosphere). However, the vastly different spectral behaviour exhibited in the Bridge phase interval suggests a physically distinct emission component as proposed earlier by e.g. Knight (1982) and Hasinger (1985).

5.6.4. Parametrization of the emission in the narrow pulse phase intervals

Exploiting our high statistics and eight-decades wide high-energy phase resolved spectra, we made an attempt to empirically disentangle in phase and energy space underlying physical components. Assuming again that the Bridge spectrum represents the shape of a distinct emission component, we modelled its spectral behaviour in terms of two spectral components, a “modified” power-law with an energy dependent index and a simple power-law: $F_{\text{ph}} = \alpha \cdot E^{-(\beta+\gamma \cdot \ln E)} + \delta \cdot E^{-\epsilon}$. In this formula F_{ph} denotes the photon flux in units $\text{ph}/\text{cm}^2 \cdot \text{s} \cdot \text{MeV}$, while E is given in MeV. As expected, the normalization parameter δ for the simple power-law component was consistent with zero, although a weak level of high-energy γ -ray emission is measured up to GeV energies. The same approach has been followed for the emission in the P1 interval. The resulting simple power-law fit, describing entirely the high-energy end of the spectrum has an index -2.069 ± 0.003 . We note that this power-law spectrum has to break near the boundaries of the energy window shown in Fig. 5.12 (see also Fig. 5.11). The resulting best fit values of the “modified” power-law components for the P1 and Bridge emissions are given in Table 5.4. From these values we can derive the following positions for the maxima (in the $E^2 \times F$ flux representation): 0.022 ± 0.005 MeV and 0.14 ± 0.02 MeV for the P1 and Bridge phase intervals, respectively. The widths of the “modified” power-law components are specified by the FWHM values in the $^{10} \log(E)$ domain and are about 1.3 and 2.5 for the P1 and Bridge intervals, respectively. With this approach we have identified three distinctly different spectral shapes, which can describe the P1 and Bridge spectra.

Table 5.4. Best fit parameter values of the “modified” power-law components for the P1 and Bridge phase intervals

Interval	α	β	γ
P1	$(2.38 \pm 0.65) \cdot 10^{-6}$	4.28 ± 0.13	0.299 ± 0.017
Bridge	$(7.97 \pm 0.52) \cdot 10^{-5}$	2.33 ± 0.03	0.084 ± 0.005

In the next step we made an attempt to describe the measured spectral distributions in the narrow pulse phase intervals in terms of just these 3 models each with a free scaling

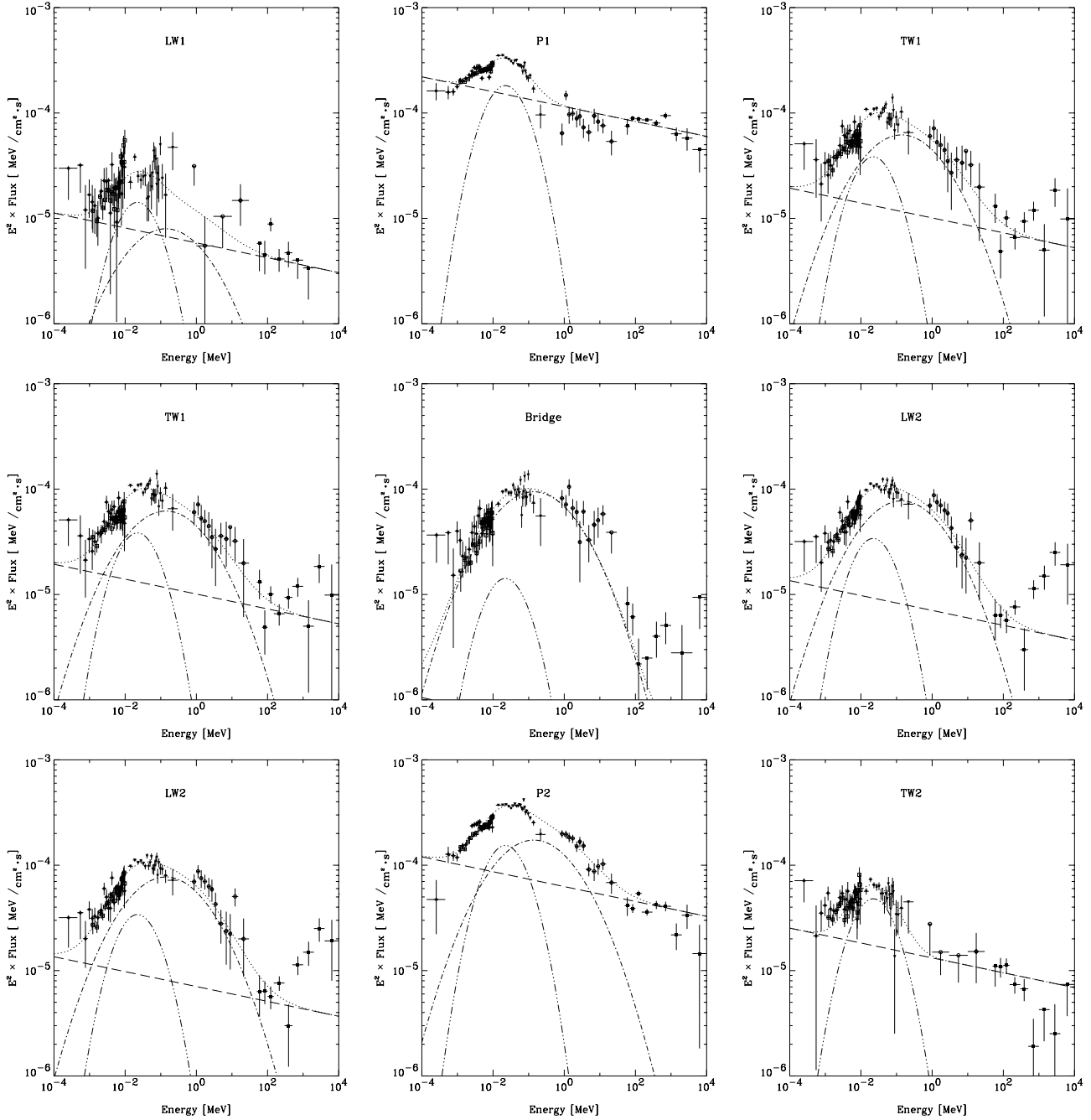


Fig. 5.12. The high-energy emission of the Crab pulsar in the 7 narrow pulse phase intervals (see Table 5.2) from 0.1 keV up to 10 GeV. Two spectra (for the TW1 and LW2 phase intervals) are displayed twice, to facilitate a better visual comparison of the different spectra (see discussion). See Fig. 5.11 for the origin of the data points. The different contributions (P1 curved model, dash-dot-dot-dot line; Bridge curved model, dash-dot line; power-law model, dash line) to the composite model fits (dotted lines) have all been superimposed for the optimum scaling parameters (histogram) shown in Fig. 5.13.

parameter. Interestingly, the resulting fits are very satisfactory for all phase intervals as shown in Fig. 5.12 in which the total model and the individual components are superimposed on the measured spectra. The fits are acceptable in all cases, although the χ^2_ν values obtained for the high statistics P1 and P2 intervals are rather high, likely also re-

flecting remaining systematic uncertainties in the absolute flux calibrations.

The fit results for the 3 scale parameters are visualized in Fig. 5.13. These scale parameters have been normalized to the emission in the Bridge interval because of the different phase extents of the intervals. Fig. 5.13 shows effectively the “light curves” of these model components: two

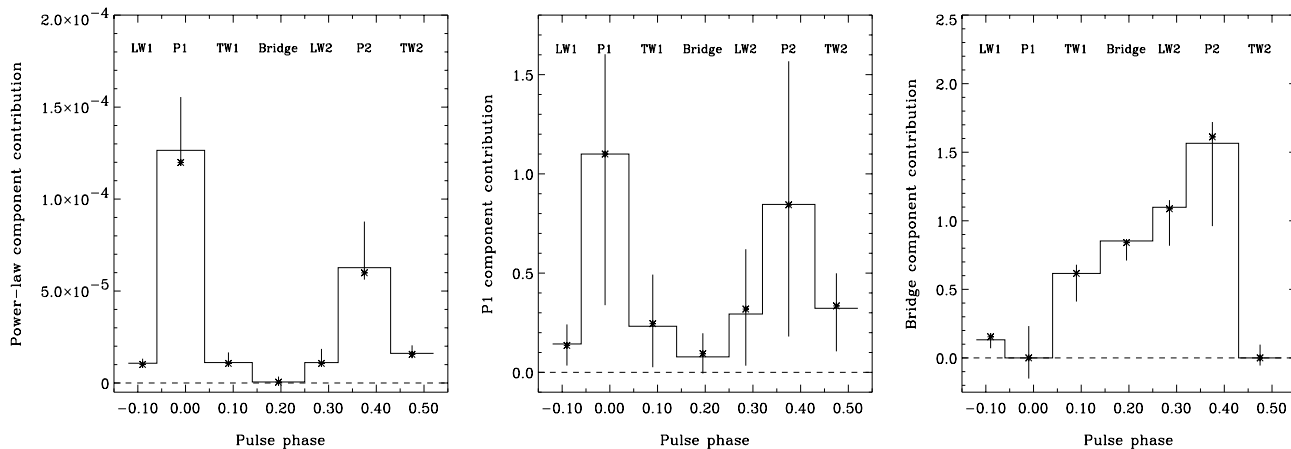


Fig. 5.13. Scale factors of the 3 empirical spectral models as a function of phase for the case of “high” normalization of the data points below the COMPTEL range (see text): left panel, power-law model scale factor; middle panel, “narrow” bump (P1 curved component) scale factor; right panel, “broad” bump (Bridge curved component) scale factor. The histograms are drawn through the optimum fit values i.e. obtained by using the optimum parameters for the curved components as listed in Table 5.4. The asymmetric error bars indicate the 90% interval for the scale factor in question obtained by varying the (4) shape parameters of the 2 curved models at their $-1, 0, 1\sigma$ values. The * symbols indicate the optimum fit values for the “low” normalization case.

components are clearly related to the emission in the two main pulses (the power-law component and the “narrow bump”) and the “Bridge component” or “broad bump” extends apparently from the LW1 till under P2 in a triangular shape. In a fit leaving only the scaling parameters free, the statistical errors become unrealistically small. In order to get more realistic error estimates we varied all parameters, including those describing the “broad” and “narrow” bump models given in Table 5.4, within their $\pm 1\sigma$ errors and determined the range over which the scaling parameters vary. The latter range (90% confidence) is shown as an (asymmetric) error bar in Fig. 5.13 around the histogram which is drawn through the optimum fit values.

The “light curves” in Fig. 5.13 can also be clearly discerned in the 9 panels of Fig. 5.12. The upper row centered on P1 shows how the components of P1 extend into the wings; the middle row shows how the Bridge spectrum dominates in all three intervals and how the power-law component and the “narrow bump” contributions are symmetrically distributed on either side of the Bridge interval. Finally, the lowest row centered on P2 looks very much like the upper row, but the Bridge spectral component reaches a maximum value in P2. We have apparently succeeded in identifying likely genuine underlying physical components in phase and energy space.

Finally, we studied the impact of a different choice of the normalization “correction” factors for the 3 NFI BepoSAX and GRIS instruments. For this purpose we applied the “low” normalization factors (normalizing on the GRIS spectrum, as explained above), and repeated the total fitting procedure. We do not see significant departures from the phase dependencies shown in Fig. 5.13 for the 3 scale factors. The best fit values hardly change (see Fig. 5.13), the

differences are confined within the error intervals. Therefore our main conclusions appear not to be affected.

5.6.5. Likely hard high-energy γ -ray component in front of P2

The most apparent and significant (5.3σ for energies above 300 MeV) deviation from the composite fits in Fig. 5.12 is visible in the LW2 spectrum in the EGRET range above 100 MeV. Fierro (1995) reported for this phase interval the hardest pulsed γ -ray spectrum (photon index -1.69 ± 0.08) fitting his data points (CGRO Cycles 0-III) which are also shown in Fig. 5.12. For our timing analysis we used CGRO EGRET Cycle 0-VI data, almost doubling the statistics for energies above 1 GeV (for energies lower than 1 GeV the increase in statistics is less due to the energy and time dependent EGRET sensitivity caused by spark-chamber gas aging). To verify whether the phase distributions in the GeV energy range indeed show evidence for a separate hard spectral component in front of P2 we produced the pulse profiles of Fig. 5.14. In this figure we show the 1-10 GeV pulse profile superimposed on the 100-300 MeV pulse profile both with high statistics using EGRET Cycle 0-VI observations. Typical error bars for both distributions are shown. The two distributions are normalized on the P1 phase interval. A clear increase of emission in the LW2 phase interval is visible for the highest energies, while also the core of the P2 phase interval shows some increased emission (cf. Fig. 5.7). In summary, also within this enlarged database there is evidence for a “new” feature in the phase distribution at GeV energies in the LW2 phase interval. If there is a genuine new component then this new component must be even harder than derived by

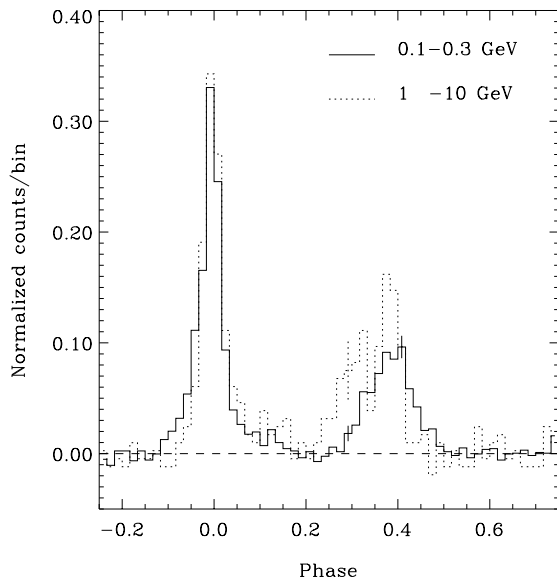


Fig. 5.14. EGRET pulse profiles (60 bins) using CGRO EGRET Cycle 0-VI data: 1-10 GeV, dotted line; 100-300 MeV, solid line. The profiles are normalized on their emission in P1. Typical error bars are indicated for both profiles. A clear increase is visible in the LW2 phase interval for the 1-10 GeV energy interval with respect to the 100-300 MeV interval.

Fierro (1995). Fitting for the LW2 phase interval another power-law model with both a free normalization and a free index atop the model composed of the broad and narrow spectral components and the power-law component with a fixed index of -2.069 , we find for the additional power-law model a very hard photon index of -1.34 ± 0.15 . However, our data are not of sufficient quality to discriminate between an additional very hard power-law component, which must break somewhere above 10 GeV to be consistent with the non-detections of pulsed emission at TeV energies, or e.g. an additional high-energy “bump”. This can be studied in detail with the next generation high-energy γ -ray telescopes AGILE and particularly GLAST (see e.g. <http://glast.gsfc.nasa.gov>), which is ~ 30 times more sensitive than EGRET over a much wider energy interval extending to 300 GeV.

5.7. P1 arrival time/phase at MeV energies

In Sect. 5.4.3 we showed that the arrival phase of P1 (maximum) for energies above 30 MeV precedes the main radio pulse by $241 \pm 29 \mu\text{s}$, consistent with the time lag between the P1 radio and X-ray pulses of about $250 \mu\text{s}$ (RXTE; Rots et al. 2000). The phase of the COMPTEL maximum of P1 was consistent with no time lag. If we assume that the sum of the P1 power-law component and the P1 “narrow” bump (see Fig. 5.13) are related to the P1 pulses measured by EGRET and RXTE (e.g. originating from the same sites in the pulsar magnetosphere) then it is inter-

esting to verify whether a P1 pulse consisting of the two components at MeV energies can have a time lag consistent with those measured at lower and higher energies by RXTE and EGRET. Clearly, the presence of an additional bridge component with a triangular shape as shown in Fig. 5.13 tends to shift the maximum in the P1 interval towards larger phase values. Therefore, we have fitted a Lorentzian profile plus a first order polynomial to the measured 0.75-30 MeV Cycle 0-IX COMPTEL pulse profile over the phase interval $[0.8, 1.2]$ to take into account the known bridge behaviour. We find that P1 in the 0.75-30 MeV range arrives $117 \pm 73 \mu\text{s}$ earlier than the fiducial point in the radio template. This value is consistent within 1.2σ with the value of $241 \pm 29 \mu\text{s}$ derived for the EGRET > 30 MeV data, although the pretty large (systematic) uncertainty in the COMPTEL derived value does not allow making more stringent statements.

5.8. Summary and discussion

In this work we derived the time-averaged characteristics of the Crab pulsar at medium γ -ray energies (0.75-30 MeV) using COMPTEL data collected over its 9 year mission. We first verified that our data do not show indications for time-variable behaviour of the Crab pulsed emission in this energy range, neither in intensity nor in pulse shape. Our high-statistics integral (0.75-30 MeV) pulse profile shows the well-known morphology of two peaks with a phase separation of ~ 0.4 , one coinciding with the main radio pulse and the other with the radio interpulse. The second γ -ray pulse dominates the first pulse, while intense emission is present between the 2 pulses (bridge emission). Over this 0.75-30 MeV interval, however, we witness a clear morphology change of the pulse profile as a function of energy: for energies above ~ 10 MeV the first pulse starts to dominate the second pulse again, and the bridge emission loses significance quickly with increasing energy. This is clear evidence for drastic spectral variations with pulsar phase over the COMPTEL energy window. Indications for such variations were found in the earlier COMPTEL analysis by Much et al. (1995).

Using our large COMPTEL data base we derived an improved Crab nebula spectrum, which has a power-law spectral shape between 0.75 and 30 MeV with index -2.240 ± 0.014 . Also our new COMPTEL spectrum for the total pulsed emission (nebula/DC emission subtracted) can be described with a power-law spectral shape between 0.75 and 30 MeV with index -2.24 ± 0.04 . If the indication for enhanced emission in the 10-15 MeV interval is genuine, then the index becomes, -2.36 ± 0.06 .

These improved COMPTEL findings have been put in a much broader context by including in our analysis data from instruments sensitive at the neighbouring X-ray/soft γ -ray energies, particularly from the BeppoSAX LECS, MECS and PDS instruments, and at high γ -ray energies from CGRO EGRET. We first compiled a Crab nebula spec-

trum from 0.1 keV up to 50 TeV (Fig. 5.10), which we mainly used to derive an estimate for the systematic uncertainties in the absolute sensitivities of the contributing instruments. Nevertheless, this new high-energy spectrum shows more clearly the drastic spectral break at ~ 30 MeV, above which the spectrum (from EGRET) is much softer than in the COMPTEL range. Above ~ 300 MeV the spectrum hardens again and reaches a local maximum (in $E^2 \times F$ representation; luminosity per decade in energy) between 10 and 100 GeV to connect smoothly to the ground based TeV measurements. The spectral break between the COMPTEL and EGRET ranges at ~ 30 MeV can be explained with a model including Inverse Compton (IC) and synchrotron emission with an exponential cut-off (de Jager et al. 1996), as was also shown in van der Meulen et al. (1998).

Secondly, we compiled a new spectrum of the Crab pulsed emission from the optical/NUV/FUV wavelengths up to the high-energy γ -rays at 10 GeV with an upper limit at TeV energies (Fig. 5.11). This emission reaches a level of maximum luminosity per decade in energy from ~ 5 keV to 50 keV, the exact location being uncertain due to the systematic uncertainties in the absolute sensitivities of the instruments sensitive around this energy window. Beyond this maximum a gradual softening sets in reaching a plateau (photon power-law index of ~ -2) near ~ 30 MeV which continues to ~ 10 GeV. Above ~ 10 GeV the spectrum must break rapidly in order to be consistent with the stringent TeV upper limits for pulsed emission. Possible interpretations of this complex spectrum will be discussed below.

Phase resolved spectral analysis can provide important constraints for pulsar modelling, particularly to help identifying different production mechanisms and sites in the pulsars magnetosphere. Therefore, we derived consistently over a broad energy range from 0.1 keV up to 10 GeV (BeppoSAX LECS, MECS, PDS, CGRO COMPTEL and EGRET) for seven narrow phase intervals phase resolved spectra. These spectra exhibited very different spectral shapes, most notably the spectra for the narrow Bridge and Peak 1 intervals. We could disentangle the pulsed emission in energy and phase space, by exploiting the vastly different spectral shapes, particularly over the COMPTEL energy window, by making empirical fits, and found that the pulsed emission can be described with 3 distinctly different spectral components:

- 1- a power-law emission component from ~ 1 keV to ~ 5 GeV, photon index -2.069 ± 0.003 , which is present in the phase intervals of the two pulses.
- 2- a curved spectral component required to describe soft (≤ 100 keV) excess emission present in the same pulse phase intervals.
- 3- a broad curved spectral component reflecting the bridge emission from 0.1 keV to ~ 10 MeV. This broad spectral component extends in phase over the full pulse

profile in an approximately triangular shape, peaking under the second pulse.

- 4- in addition, the LW2 phase interval contains a very hard spectral component, most notably at GeV energies.

These derived phase dependencies suggest indeed different origins for the spectral ‘‘components’’ likely produced at different sites and by different production mechanisms in the pulsar’s magnetosphere. In a somewhat different approach and using only BeppoSAX data between 0.1 and 300 keV, Massaro et al. (2000) identified recently two components: the first is the combination of the two components as described above under -1- and -2- and the second corresponds to the one described under -3-. In their narrower energy window differences in spectral shapes can be well approximated by variations in power-law index.

Since the discovery of γ -ray emission from radio pulsars in the early seventies, the most popular and competing models attempting to explain the high-energy radiation from highly magnetized rotating neutron stars can be divided in two distinct categories: the so-called Polar Cap (PC) models and Outer Gap (OG) models.

In the Polar Cap models charged particles (mainly e^\pm) are accelerated along the open field lines in the vicinity of the magnetic poles. Subsequent cascade processes initiated by the creation of high-energy photons through either the curvature radiation mechanism (CRPC; Daugherty & Harding 1982, Daugherty & Harding 1994) or inverse Compton scattering (ICPC; Sturmer & Dermer 1994) give rise to the emergent high-energy spectrum. In the most recent versions of this type of model the high-energy emission is confined in a hollow cone centered on the direction of the magnetic moment vector μ . A distant observer whose line of sight passes through this hollow cone sees a double peaked profile. A requirement for these models is that the magnetic inclination α i.e. the angle between the pulsar spin axis Ω and magnetic moment axis is comparable to the half-angle Θ_γ of the γ beam. More detailed information on this kind of models, especially the CRPC model, can be found in the most recent papers, Daugherty & Harding (1996) and Zhang & Harding (2000).

In Outer Gap models the acceleration of charged particles and production of high-energy radiation takes place in charge depleted gaps between the null-charge surface, defined by $\Omega \cdot B = 0$ with B the local magnetic field, and the light cylinder (with radius $R_{lc} = c/\Omega$) above the last close field lines. Pioneering work on this type of models has been presented by Cheng et al. (1986a,b) and Ho (1989). Further extensions, modifications and refinements of these initial ideas have been made by e.g. Chiang & Romani (1994), Romani & Yadigaroglu (1995), Romani (1996) and Yadigaroglu (1997). Recently, Cheng et al. (2000) presented a three-dimensional outer gap model building on the work of Romani and co-workers. The emission patterns from these outer gap models resemble fan beams, and double peak pro-

files with (strong) bridge emission can commonly be generated for the cases that emission is seen from only one pole, e.g. Romani (1996), as well as from both poles, e.g. most recently Cheng et al. (2000). Irrespective the model category the observed pulsar's emission morphology depends strongly on the viewing angle ζ , the angle between the spin axis and the observer's line of sight, and the magnetic inclination α .

This geometrical information can in principle be derived from polarization measurements at radio and optical wavelengths. Based on optical polarization data Narayan & Vivekanand (1982) obtained, adopting the Rotating Vector Model (RVM; see Radhakrishnan & Cooke 1969 for pioneering work on this subject), for the Crab pulsar a magnetic inclination angle α of 86° and different observer impact angles β ($= \zeta - \alpha$) for the main and interpulse pulse, $\sim -9^\circ 6$ and $\sim +18^\circ$, respectively. Subsequent optical/Ultra-Violet polarization position angle measurements by Smith et al. (1988) and Graham-Smith et al. (1996) support a model, ascribing the double pulse optical emission from regions above the two magnetic poles, with both α and ζ close to 60° . Recently, Moffett & Hankins (1999) derived the two geometrical angles adopting the RVM model based on high frequency (1.4-8.4 GHz) radio data. They found for the magnetic inclination α and impact angle β the following values, 56° and 51° (for the interpulse), respectively. Although not fully compatible with each other (see e.g. Everett & Weisberg (2000) for a critical assessment of RVM fitting technics) these estimates for α and ζ indicate a very oblique rotator which is viewed at a large aspect angle. A large aspect angle ζ of $\sim 60^\circ$ is also suggested from HST/ROSAT HRI (Hester et al. 1995) and Chandra HETG-ACIS-S observations (Weisskopf et al. 2000) assuming that the apparent symmetry axis corresponds to the pulsar spin axis.

These large angles for both α and ζ are troublesome for PC models because this would require a very large cone half-angle Θ_γ of the gamma-ray beam of about 70° . Even in the extended polar cap scenarios (Daugherty & Harding 1996) this cone half-angle is unrealistically high. Moreover, for the extended polar cap model the predicted polarization position angle swing is in severe conflict with the observed optical/radio position angle swing(s).

For OG models these difficulties with large α and ζ angles do not exist. This is e.g. shown by Chiang & Romani (1994) for a geometrical model of an outer gap configuration in which the magnetic field line directions (the high-energy radiation is beamed in the local field direction for emission by relativistic particles moving along these field lines) passing through the outer gap were projected onto the sky taking into account the effects of relativistic aberration and travel time delays within the magnetosphere. This provided very useful insights in the pulse profiles which can be expected under different geometrical conditions. Crab like pulse profiles i.e. double peaked

profiles with bridge emission can easily be produced from a geometrical point of view for the observed (large) geometrical angles α and ζ . Moreover, phase offsets of the radio and high-energy pulses can be explained in a natural way. This kind of models is also successful in reproducing the observed polarization position angle swings of the Crab pulsar at optical wavelengths (Romani & Yadigaroglu 1995).

Early attempts to model the Crab Total Pulse spectrum in an OG scenario using various radiative processes like the curvature, synchrotron and inverse Compton radiation mechanisms assumed to play a key role in the outer gap physics, were made by Cheng et al. (1986b) and Ho (1989). The latter employed a self-consistent iterative procedure with one varying parameter, the ratio of gap height and curvature radius of the field lines, and it is interesting to note that the calculated high-energy spectrum bears reasonably good overall similarity with the observed one (cf. Fig. 4 of Ho (1989) with Fig. 5.11 of this paper). Chiang & Romani (1994) made refinements to the above calculations and attempted to model the Crab Total Pulse spectrum and the spectral variation with phase, which they considered to be a clear mapping of location in the magnetosphere to pulse phase. They divided the outer gap in different subzones taking into account the transport of radiation and particles from subzone to subzone. Convergence to a self-consistent solution, however, resulted to spectra significantly lacking photon flux below several GeV. Romani (1996) described a revised picture of gap closure and radiation physics in the outer magnetosphere to overcome difficulties in the scheme of Cheng et al. (1986b), and addressed also spectral variations with pulsar phase from the optical to the high-energy γ -ray spectrum. For the Crab pulsar, he made some qualitative statements on the expected spectral properties. So will synchrotron photons significantly contribute to the EGRET flux. This could probably explain the observed underlying power-law component from soft X-rays up to high energy γ -rays, although the observed photon index of ~ -2 is considerably softer than the expected value of ~ -1 .

Building on the work of Romani and co-workers, Cheng et al. (2000) also used a three-dimensional pulsar magnetosphere to study the geometry of outer magnetospheric gap accelerators. However, the physics of both models is strikingly different. For the single outer gap model (Chiang & Romani 1994), the emission comes from the outward direction in an outer gap above one pole; the emission regions for the two peaks of the pulse profile are those close to the null charge surface and to the light cylinder radius, respectively. In the model of Cheng et al. (2000), photon emission consists of emission outward and inward from regions in outer gaps above both poles, the gaps being limited along the azimuthal direction by e^\pm pair production of inward-flowing photons from the outer gap. It is shown that both models can produce the same (Crab-like) pulse profiles. Cheng et al. (2000) also calculated phase-resolved spectra of the Crab pulsar. They

determined the locations of the emission regions in the outer gaps in the open field line zone of the Crab magnetosphere as a function of pulse phase. It can be seen in their Fig. 9 that high-energy emission from the P1 interval is produced high in the magnetosphere ($0.8 < r/R_{lc} < 1.0$) where curvature radiation dominates, resulting in a spectrum which extends to the GeV regime. In the interval between the pulses (TW1 and Bridge interval) high-energy radiation is predominantly produced deep in the magnetosphere where a soft synchrotron component is expected to dominate, roughly in accordance with the observations. Moving towards the P2 interval, emissions from regions high and low in the magnetosphere contribute, resulting in a overall spectrum composed of a hard curvature component and a much softer synchrotron component. In the P2 interval high-energy radiation is coming in essence from emitting regions extending from $\sim 0.2R_{lc}$ to $\sim 1.0R_{lc}$ which gives rise to a hard spectral component extending into the GeV domain and a soft component. Crossing the bridge interval moving from P1 to P2 a gradual decrease from $\sim 0.6R_{lc}$ to $\sim 0.2R_{lc}$ is seen for the lower bound of the emission region in the outer gap. According to Eq. 33 of Cheng et al. (2000) the dominating synchrotron emission from these regions deep in the outer gap in the pulsar's magnetosphere becomes increasingly intense moving towards P2, because the magnetic field strength becomes stronger deeper in the magnetosphere. This offers an explanation for the observed phase dependence of the bridge/broad bump spectral component, shown in Fig. 5.13. Beyond P2 (and before P1) this soft synchrotron component should be absent which is in agreement with the observations. Thus the model proposed by Cheng et al. (2000) seems to provide a viable and promising theoretical description of the physics responsible for the production of the Crab high-energy radiation with characteristics as shown in Figs. 5.11, 5.12 and 5.13. A direct quantitative confrontation of this model with our observed 0.1 keV - 10 GeV phase-resolved spectra is therefore strongly recommended. Cheng et al. (2000) compared in their paper the model calculations with phase-resolved Crab spectra from EGRET (> 30 MeV, Fierro et al. 1998). By mistake, EGRET spectra from the phase resolved spatial analysis were used, which also comprise the underlying nebula component. This explains the large discrepancies between the model calculations and the observed spectra for energies between 30 and 100 MeV. Cheng et al. (2000) also show a broad band (0.1 keV - 10 GeV) model spectrum for the phase-averaged Crab pulsar spectrum, which can be compared with our spectrum in Fig. 5.11. The overall shape of the model spectrum follows the observed spectral characteristics reasonably well, although for energies below ~ 100 keV the model underestimates the observed X-ray fluxes, i.e. it seems that the component which we empirically described as a narrow spectral "bump" peaking around 20 keV in an $E^2 \times F$ representation, is not accounted for. This can be best studied in the phase-resolved analysis.

Future observations of the Crab pulsar by high-energy missions are important. In particular the spectral characteristics in the 300-1000 keV interval must be determined much more accurately. Here, data from both IBIS and SPIE aboard INTEGRAL will contribute significantly. At high γ -ray energies data from the AGILE and GLAST missions can provide sufficient statistics to study the peculiar spectral behaviour in the LW2 phase interval in much more detail for energies above 1 GeV. Moreover, these instruments can, for the first time, study the pulsed emission for energies above 10 GeV (upper edge of the sensitivity window is 50 GeV and 300 GeV for AGILE and GLAST, respectively). At medium γ -ray energies no mission is planned for the coming 10-15 years. It is, however, in this energy region where interesting spectral transitions occurs and where we have indications for enhanced pulsed emission in the 10-15 MeV range. Future space borne Compton telescopes having 10-100 times better sensitivity than CGRO COMPTEL are required to allow further progress.

Acknowledgements. The COMPTEL project is supported by the German Ministerium für Bildung und Forschung through DLR grant 50 QV 90968 and by the Netherlands Organisation for Scientific Research (NWO). We are grateful to Jesper Sollerman, who kindly provided the HST STIS pulse profiles of the Crab pulsar, and to Rudolf Much for making the optical UCL MIC Crab data accessible. We thank Dave Thompson for providing the EGRET pulsed spectral analysis data as derived by Joe Fierro in his thesis work.

References

- Agrinier B., Masnou J.L., Parlier B., et al., 1990, ApJ 355, 645
 Aharonian F.A., Akhperjanian A.G., Barrio J.A., et al., 1999, A&A 346, 913
 Aharonian F.A., Akhperjanian A.G., Barrio J.A., et al., 2000, ApJ 539, 317
 Albats P., Frye G.M. Jr., Zych A.D., et al., 1972, Nat 240, 221
 Arzoumanian Z., Nice D., Taylor J. H., 1992, GRO/radio timing data base, Princeton University.
 Bartlett L.M., Barthelmy S.D., Gehrels N., et al., 1994, AIP Conf. Proc. 304, 67; "The Second COMPTON Symposium, College Park MD, 1993", eds. Fichtel C.E, Gehrels N. and Norris J.P.
 Bartlett L.M., Ph.D. thesis, The University of Maryland
 Bennett K., Bignami G.F., Boella G., et al., 1977, A&A 61, 279
 Borione A., Catanese M.A., Chantell M.C., et al., 1997, ApJ 481, 313
 Boella G., Chiappetti L., Conti G., et al., 1997, A&AS 122, 327
 Boldt E.A., Desai U.D., Holt S.S., et al., 1969, Nat 223, 280
 Bradt H., Rappaport S., Mayer W., et al., 1969, Nat 222, 728
 Browning R., Ramsden D., Wright P.J., 1971, Nat 232, 99
 Buccheri R., Bennett K., Bignami G., et al., 1983, A&A 128, 245
 Carramiñana A., Bennett K., Buccheri R., et al., 1994, A&A 290, 487
 Cheng K.S., Ho C., Ruderman M., 1986a, ApJ 300, 500
 Cheng K.S., Ho C., Ruderman M., 1986b, ApJ 300, 522
 Cheng K.S., Ruderman M., Zhang L., 2000, ApJ 537, 964
 Chiang J., Romani R.W., 1994, ApJ 436, 754
 Clear J., Bennett K., Buccheri R., et al., 1987, A&A 174, 85

- Cocke W.J., Disney M.J., Taylor D.J., 1969, *Nat* 221, 525
- de Jager O.C., Harding A.K., Michelson P.F., et al., 1996, *ApJ* 457, 253
- Daugherty J. K., Harding A. K., 1982, *ApJ* 252, 337
- Daugherty J. K., Harding A. K., 1994, *ApJ* 429, 325
- Daugherty J. K., Harding A. K., 1996, *ApJ* 458, 278
- Dickey J.M., Lockman F.J., 1990, *ARA&A* ,215
- Everett J.E., Weisberg J.M., 2000, *ApJ* submitted; <http://arXiv.org/abs/astro-ph/0009266>
- Fierro J., PhD. thesis, 1995, Stanford University
- Fierro J., Michelson P.F., Nolan P.L., et al., 1998, *ApJ* 494, 734
- Fishman G.J., Harnden F.R. Jr., Haymes R.C. , 1969, *ApJ* 156, L107
- Fritz G., Henry R.C., Meekins J.F., et al., 1969, *Sci* 164, 709
- Frontera F., Costa E., dal Fiume D., et al., 1997, *A&AS* 122, 357
- Golden A., Shearer A., Beskin G.M., 2000, *ApJ* 535, 373
- Graser U., Schönfelder V., 1982, *ApJ* 263, 677
- Gull T.R., Lindler D.J., Crenshaw D.M., et al., 1998, *ApJ* 495, L51
- Harnden F.R., Seward F.D., 1984, *ApJ* 283, 279
- Hasinger G., 1984, Ph.D. thesis, Ludwig-Maximilians-Universität München
- Hasinger G., 1985, In: *The Crab Nebula and Related Supernova Remnants*, eds. Kafatos & Henry, Cambridge University Press
- Hester J.J., Scowen P.A., Sankrit R., et al., 1995, *ApJ* 448, 240
- Hillas A.M., Akerlof C.W., Biller S.D., et al., 1998, *ApJ* 503, 744
- Hillier R.R., Jackson W.R., Murray A., et al., 1970, *ApJ* 162, L177
- Ho C., 1989, *ApJ* 342, 396
- Kestenbaum H.L., Ku W., Novick R., et al., 1976, *ApJ* 203, L57
- Knight F.K., 1982, *ApJ* 260, 538
- Kniffen D.A., Hartman R.C., Thompson D.J., et al., 1974, *Nat* 251, 397
- Kurfess J.D., 1971, *ApJ* 168, L39
- Lessard R.W., Bond I.H., Bradbury S.M., et al., 2000, *ApJ* 531, 942
- Mahoney W.A., Ling J.C., Jacobson A.S., 1984, *ApJ* 278, 784
- Manzo G., Giarrusso S., Santangelo A., 1997, *A&AS* 122, 341
- Massaro E., Feroci M., Costa E., et al., 1998, *A&A* 338, 184
- Massaro E., Cusumano G., Litterio M., et al., 2000, *A&A* 361, 695
- McBreen B., Ball S.E. Jr., Campbell M. , et al., 1973, *ApJ* 184, 1973
- Mineo T., Cusumano G., Segreto A., et al., 1997, *A&A* 327, 21
- Moffett D.A., Hankins T.H., 1996, *ApJ* 468, 779
- Moffett D.A., Hankins T.H., 1999, *ApJ* 522, 1046
- Much R., Bennett K., Buccheri R., et al., 1995, *A&A* 299, 435
- Much R., Bennett K., Winkler C., et al., 1997, *AIP Conference Proc.* 410: Proceedings of the fourth Compton Symposium, Williamsburg, VA, eds. Dermer, C.D., Strickman, M.S. and Kurfess J.D.
- Much R., Carramiñana A., Fordham J.L.A., 2000, *ASP Conf. Series*, 202, 85, "in *Pulsar Astronomy — 2000 and beyond: IAU Colloquium 177*"
- Narayan R., Vivekanand M., 1982, *A&A* 113, L3
- Nather R.E., Warner B., Macfarlane M., 1969, *Nat* 221, 527
- Nolan P.L., Arzoumanian Z., Bertsch D.L., et al., 1993, *ApJ* 409, 697
- Oser S., Bhattacharya D., Boone L.M., et al., 2000, to appear in *ApJ (astro-ph/0006304; 21 June 2000)*
- Parlier B., Agrinier B., Forichon M., et al., 1973, *Nat Phys. Sci.* 242, 117
- Parmar A.N., Martin D.D., Favata F., et al., 1997, *A&AS* 122, 309
- Percival J.W., Biggs J.D., Dolan J.F., et al., 1993, *ApJ* 407, 276
- Pravdo S.H., Serlemitsos P.J., 1981, *ApJ* 246, 484
- Pravdo S.H., Angelini L., Harding A. K., 1997, *ApJ* 491, 808
- Richards D.W., Comella J.M., 1969, *Nat* 222, 551
- Radhakrishnan V., Cooke D.J., 1969, *ApJ* 3, L225
- Romani R.W., 1996, *ApJ* 470, 469
- Romani R.W., Yadigaroglu I. A., 1995, *ApJ* 438, 314
- Rots A., Jahoda K., Lyne A.G., et al., 2000, "ROSSI 2000; Astrophysics with the Rossi X-ray Timing Explorer", March 22-24, 2000, NASA's GSFC, Greenbelt, MD, USA
- Schattenburg M.L., Canizares C.R., *ApJ* 301, 759
- Schönfelder V., Aarts H., Bennett K., et al., 1993, *ApJS* 86, 657
- Smith F.G., Jones D.H.P., Dick J.S.B., et al., 1988, *MNRAS* 233, 305
- Graham-Smith F., Dolan J.F., Boyd P.T., et al., 1996, *MNRAS* 282, 1354
- Sollerman J., Lundqvist P., Lindler D., et al., 2000, *ApJ* 537, 861
- Staelin D.H., Reifenstein E.C., 1968, *Sci* 162, 1481
- Sturmer S.J., Dermer C.D., 1994, *ApJ* 420, L79
- Tanimori T., Sakurazawa K., Dazeley S.A., et al., 1998, *ApJ* 492, L33
- Thompson D.J., Fichtel C.E., Hartman R.C., et al., 1977, *ApJ* 213, 252
- Thompson D.J., Bertsch D.L., Fichtel C.E., et al., 1993, *ApJS* 86, 629
- Thompson D.J., Bertsch D.L., Dingus B.L., et al., 1995, *ApJS* 101, 259
- Thompson D.J., Harding A.K., Hermsen W., et al., 1997, *AIP Conference Proceedings* 410, 39; *Proc. of the IV-th Compton Symposium*, Williamsburg VA, 1997
- Tompkins W.F., Jones B.B., Nolan P.L., et al., 1997, *ApJ* 487, 385
- Toor A., Seward F.D., 1977, *ApJ* 216, 560
- Ulmer M.P., Lomatch S., Matz S.M., et al., 1994, *ApJ* 432, 228
- Ulmer M.P., Matz S.M., Grabelsky D.A., et al., 1995, *ApJ* 448, 356
- Vacanti G., Cawley M.F., Colombo E., et al., 1991, *ApJ* 377, 467
- van der Meulen R.D., Bloemen H., Bennett K., et al., 1998, *A&A* 330, 321
- Walraven G.D., Hall R.D., Meegan C.A., et al., 1975, *ApJ* 202, 502
- Weisskopf M.C., Hester J.J., Tennant A.F., et al., 2000, *ApJ* 536, L81
- Wills R.D., Bennett K., Bignami G.F., et al., 1982, *Nat* 296, 723
- Yadigaroglu I.-A., 1997, Ph.D. thesis, Stanford University
- Zhang B., Harding A. K., 2000, *ApJ* 532, 1150

Part II

High-energy radiation from the recycled pulsars:
the case PSR J0218+4232

Chapter 6

High-energy observations of the millisecond pulsar PSR J0218+4232

Frank Verbunt¹, Lucien Kuiper², Tomaso Belloni³, Helen M. Johnston^{1,4}, A.G. de Bruyn^{5,6}, Wim Hermsen², and Michiel van der Klis³

¹ Astronomical Institute, Utrecht University, P.O.Box 80000, NL-3508 TA Utrecht, the Netherlands

² SRON-Utrecht, Sorbonnelaan 2, NL-3584 CA Utrecht, the Netherlands

³ Astronomical Institute Anton Pannekoek and Center for High-Energy Astrophysics, Kruislaan 403, 1098 SJ Amsterdam, the Netherlands

⁴ Anglo-Australian Observatory, P.O. Box 296, Epping NSW 2121, Australia

⁵ Netherlands Foundation for Research in Astronomy, P.O.Box 2, 7990 AA Dwingeloo, the Netherlands

⁶ Kapteyn Astronomical Institute, Postbus 800, 9700 AV Groningen, the Netherlands

Astron. Astrophys. 311, L9-L12 (1996)

Abstract. The very luminous millisecond binary radio pulsar PSR J0218+4232 has been detected in soft X-rays, at a luminosity of 8.4×10^{32} erg/s between 0.1–2.4 keV. The EGRET source 2EG J0220+4228 has a position which is consistent with that of PSR J0218+4232. Both the X-ray source and the gamma-ray source show indications for variations at the pulse period. If the gamma-ray source is indeed the radio pulsar, then the energy loss in gamma-rays corresponds to about 10% of the spin-down luminosity. The X-ray luminosity of PSR J0218+4232 is high, but in line with the luminosities of other radio pulsars. We also determine an upper limit to the X-ray luminosity of PSR B1937+21 of $\sim 2.3 \times 10^{32}$ erg/s.

6.1. Introduction

Recently, Navarro et al. (1995) discovered a 2.3 msec radio pulsar, PSR J0218+4232, in a 2.0 d orbit around a low-mass companion. This recycled pulsar is very luminous, at $L_{400\text{MHz}} > 2700$ mJy kpc². (For comparison: 36 out of 561 pulsars with known luminosities in the catalog by Taylor et al. (1993) are brighter than 2700 mJy kpc²; amongst these there is only one pulsar in a binary, i.e. PSR J0045–7319 which accompanies a B star in the Small Magellanic Cloud, and only one millisecond pulsar, i.e. PSR B1937+21, at 3110 mJy kpc².) An interesting feature of PSR J0218+4232 is that its radio emission is detected throughout the pulse period; this is taken by Navarro et al. (1995) as an indication that the magnetic field is almost aligned with the rotation axis. From the dispersion measure, a minimum distance of 5.7 kpc is derived.

We describe our X-ray observations of this pulsar, and of the millisecond radio pulsar PSR B1937+21, with the High Resolution Imager of ROSAT. The observations and data reduction are described in Sect. 6.2, including the anal-

ysis of archival ROSAT PSPC data. Section 6.3 presents the analysis of archival high-energy γ -ray data from EGRET, aboard the Compton Gamma-Ray Observatory (CGRO). Our results are discussed in Sect. 6.4.

6.2. X-ray observations and data reduction

The observations were obtained with the X-ray telescope HRI combination of ROSAT (David et al. 1995), which was pointed at PSR J0218+4232 on 18/19 Aug 1995 for an effective exposure time of 22209 s, at an offset of 12' from the image center, and at PSR B1937+21 between 13 April and 16 May 1995 for an effective exposure time of 6274 s, and between 15 Oct and 11 Nov 1995 for 17956 s.

The HRI images were analyzed with the standard interactive analysis package EXSAS (Zimmerman et al. 1994), which utilizes a maximum likelihood source detection and parameter estimation algorithm taking account of each photon separately (Craddock et al. 1988). In the Aug 1995 observation we detect a source of 45 ± 9 cts at a position of $\alpha(2000) = 2^{\text{h}} 18^{\text{m}} 06.05^{\text{s}}$ and $\delta = +42^{\circ} 32' 21.0''$. The error in this position, $8''3$, is a combination of the statistical accuracy of the center of the photon distribution, $5''8$, and a systematic uncertainty in the satellite pointing, $6''$. The X-ray position is at a nominal distance of $4''9$ of the position determined from the pulsed radio signal of PSR J0218+4232, and we conclude that we have detected the pulsar. The background- and vignetting-corrected number of photons is 47, corresponding to a countrate of $(2.1 \pm 0.4) \times 10^{-3}$ cts/s.

We do not detect PSR B1937+21 in either of the two observations. The $3\text{-}\sigma$ upper limit to the countrate is 6.6×10^{-4} cts/s (corresponding to about 16 photons in both observations together).

The conversion of countrates to flux depends on the spectrum incident on the detector, i.e. on the intrinsic spectrum of the source and on the interstellar absorption.

To estimate the amount of interstellar absorption, we note that the maximum colour excess in the direction of PSR J0218+4232 is $E(B - V) = 0.09$ on the maps of Burstein & Heiles (1982). With $A_V = 3.1E(B - V)$ and $N_H = 1.79 \times 10^{21} A_V$ (Predehl & Schmitt 1995), this corresponds to a hydrogen column $N_H = 0.5 \times 10^{21} \text{cm}^{-2}$. PSR B1937+21 lies in the Galactic Plane. For pulsars in globular clusters with similar dispersion measures, the visual absorption ranges from $A_V = 0.16$ for M 15 to $A_V = 1.24$ for M 4. With the above relation between N_H and A_V these values correspond to $N_H = (0.28 - 2.2) \times 10^{21} \text{cm}^{-2}$.

For the intrinsic spectrum we assume the spectrum observed for PSR J0437–4715, which is a combination of a powerlaw with energy index 1.85, responsible for 74% of the flux in the range 0.1–2.4 keV, and a blackbody with temperature 0.147 keV, responsible for the remaining 26% of the flux (Becker & Trümper 1993).

For this spectrum, absorbed by a column $N_H = 0.5 \times 10^{21} \text{cm}^{-2}$, the countrate of PSR J0218+4232 of $2.14 \times 10^{-3} \text{cts/s}$ corresponds to a luminosity of $8.4 \times 10^{32} \text{erg s}^{-1}$ at a distance of 5.7 kpc. For the same spectrum, absorbed by a column $N_H = (0.28 - 2.2) \times 10^{21} \text{cm}^{-2}$, the upper limit of $0.66 \times 10^{-3} \text{cts/s}$ to the countrate of PSR B1937+21 corresponds to an X-ray luminosity at 3.6 kpc of $L_x \simeq (0.8 - 2.3) \times 10^{32} \text{erg s}^{-1}$.

For our timing analysis, we selected all photons detected with the HRI within a circle centered on the pulsar position, with a radius twice the radius within which 50% of source photons are expected to fall, i.e. $2 \times 10''$. This extraction radius was chosen because the countrate is source dominated. The solar-system barycentric UTC arrival times (determined from a fifth order polynomial fit of the spacecraft clock times to UTC) are converted to barycentric dynamical time scale, and subsequently the arrival times are folded according to the radio ephemeris given in Navarro et al. (1995), taking into account the time delays arising from its binary orbit (Blandford & Teukolsky 1976). (We have verified our software for this procedure by reproducing the lightcurve of the binary pulsar PSR J0437–4715 from a ROSAT PSPC photon list kindly supplied by W.Becker.)

The HRI X-ray pulse lightcurve for PSR J0218+4232 is shown in Fig. 6.1a. According to the Z_n^2 test statistic, which does not depend on binning of the data (Buccheri et al. 1983), the photon distribution for PSR J0218+4232 deviates from a statistically flat distribution at $\sim 94\%$ significance, for two harmonics, i.e. for two maxima during each pulse period. (Note that the radio pulse has two peaks.)

Encouraged by this result, we checked the ROSAT data archive, and found a 24880 s exposure on NGC 891 in which PSR J0218+4232 is near the edge of the field of view of the PSPC detector. The pulsar is just detectable at its

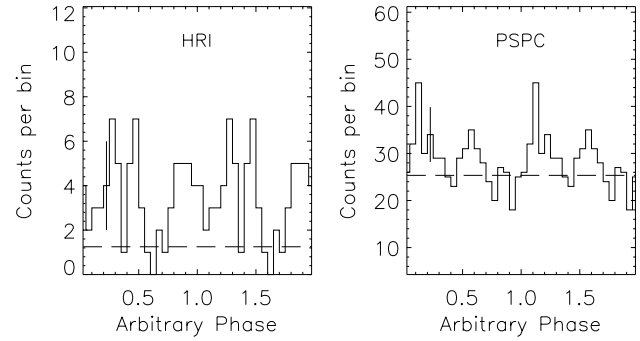


Fig. 6.1. The X-ray lightcurves of PSR J0218+4232 as obtained with our HRI observation (left) and with an archival PSPC observation (right). The dashed lines indicate background levels estimated in a spatial analysis. The pulse period is shown twice, phases are arbitrary; the phase connection between the HRI and PSPC data is not known. Typical error bars are indicated.

known radio position. The data were obtained within one day, on August 18, 1991. (A second PSPC observation on SN 1986J in NGC 891 is not suitable for timing analysis, because the fit residuals of the spacecraft clock to UTC calibration are too large – ~ 1.5 millisecond – during the 20 days over which the exposure was spread.) Photons detected with the PSPC were selected from a circle centered on the pulsar position, with a radius equal to the radius within which 50% of source photons are expected to fall, i.e. $170''$; the PSPC countrate is dominated by background. The PSPC X-ray pulse lightcurve for PSR J0218+4232 is shown in Fig. 6.1b. According to the Z_n^2 test statistic, the PSPC photon distribution for PSR J0218+4232 deviates from a statistically flat distribution at $\sim 99\%$ significance, again for two harmonics. Within the appreciable uncertainty, the PSPC countrate is compatible with what would be predicted from the HRI countrate and the assumed spectrum.

Both the HRI and PSPC lightcurves as shown in Fig. 6.1 are for arbitrary phase, and the phase connection between the two lightcurves is unknown. Thus the evidence from the two lightcurves cannot be combined, and our detection of pulsed variation in the X-ray emission remains tentative.

6.3. High-energy γ -ray data and analysis

We note that the position of the source 2EG J0220+4228 in “The Second EGRET Catalog of High-Energy Gamma-Ray Sources” (Thompson et al. 1995) is spatially consistent with that of PSR J0218+4232, being located at the $\sim 80\%$ confidence location contour. In fact, the possible counterpart listed in the catalog, the BL Lac system 0219+428 (3C66A) is located at the 99% confidence contour. EGRET, sensitive in the range 30 MeV – 30 GeV, detected 2EG J0220+4228 above 100 MeV with a time-averaged flux of $(16.7 \pm 3.7) \times 10^{-8} \text{photons cm}^{-2} \text{s}^{-1}$ during Phase I (1991 April to 1992 November) and Phase II (1992 November to 1993 September) of the CGRO mission.

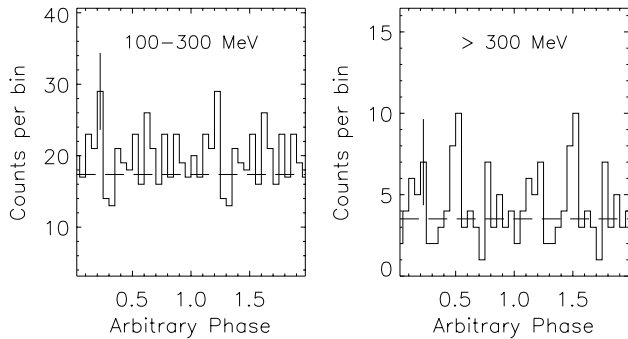


Fig. 6.2. The γ -ray lightcurves of PSR J0218+4232 as obtained from EGRET data from Phases I–III. The dashed lines indicate the background levels estimated in a spatial analysis. The pulse period is shown twice, phases are arbitrary, but the same in the two panels. Typical error bars are indicated.

We selected from EGRET archival data the viewing periods for which the source was within 20 degrees from the pointing direction, namely viewing periods 15, 211 and 325. The latter period is in CGRO Phase III, and we confirmed the presence of the source in a spatial analysis. For the combined data set we performed then the timing analysis analogous to that described above for the ROSAT data. To optimize the signal-to-noise ratio, events were selected from an energy-dependent cone about the known pulsar position (see e.g. Fierro et al. 1995). Since we do not know the γ -ray duty cycle or pulse shape, we cannot select a priori the number of harmonics for the Z_n^2 statistic. Therefore these were calculated for $n=1$ till 20 harmonics. The maximal significances obtained were 3.5σ (for all photons with $E > 100$ MeV), 2.6σ ($E > 150$ MeV) and 2.5σ ($E > 300$ MeV), for varying numbers of harmonics. For 43 of the total of 60 “trials” the significance was above 2σ , which indicates that any genuine pulsed signal is not a single sharp profile. If we consider the power in all harmonics with an H_m test (de Jager et al. 1989), not the most sensitive test for broad duty cycles, then the significances are reduced to 5.3%, 13.4% and 5.1%, respectively. Figure 6.2 shows the phase distributions for two energy ranges. In these distributions background levels are indicated, determined by demanding that the number of source counts detected in the spatial analysis equals the number of excess counts in the phase distributions (taking into account the correction for the 67% energy-dependent cone selection). This shows that the source excess is consistent with being 100% pulsed.

6.4. Discussion

To compare the X-ray luminosity of PSR J0218+4232 and PSR B1937+21 with those of other pulsars, we consider their locations in two diagrams. In the first of these, shown in Fig. 6.3 (after Trümper 1995) the X-ray luminosities of radio pulsars are plotted as a function of characteristic age $\tau_c \equiv P/(2\dot{P})$. The X-ray data in this Figure

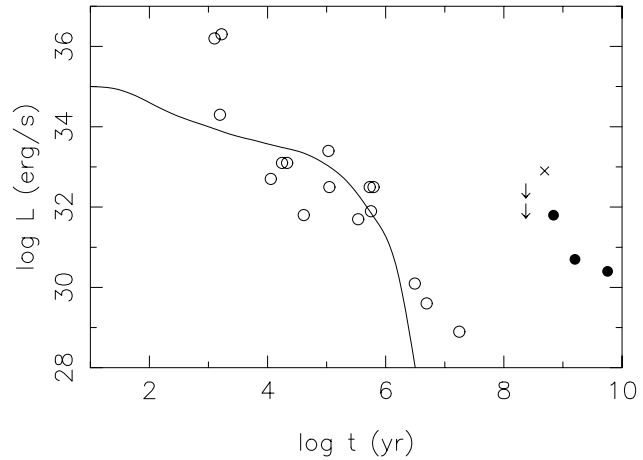


Fig. 6.3. The X-ray luminosity in the range 0.1 – 2.4 keV of PSR J0218+4232 (\times) and the upper limit of PSR B1937+21 (\downarrow , for two assumed values of the interstellar absorption) compared with the X-ray luminosities of other radio pulsars (\circ ordinary pulsars, \bullet recycled pulsars) as a function of their characteristic age $t_c \equiv P/(2\dot{P})$. A standard cooling curve is also shown. After Trümper (1995).

are from Becker (1995), and (for PSR J1012+5307) from Halpern (1996); the characteristic ages from the Princeton Pulsar Database (see Taylor et al. 1993). Our detection of PSR J0218+4232 and our upper limit for PSR B1937+21 are added. A theoretical lightcurve for a cooling neutron star, from Umeda et al. (1993), is also shown. X-ray emission above this curve may be interpreted as magnetospheric and/or due to a re-heated polar cap. In particular, none of the X-ray emission from recycled pulsars, recognizable in this diagram by their ages $\tau_c > 10^8$ yr, can be due to cooling. In this diagram, PSR J0218+4232 is seen to be very bright for its age, especially if it is taken into account that its luminosity is calculated for a lower limit to its distance. We speculate that this is related to the fact that the Earth is inside the cone of radio emission throughout the radio pulse.

In the second diagram, Fig. 6.4, after Seward & Wang (1988), the X-ray luminosity of radio pulsars is shown as a function of the total spin-down luminosity. Over a range of 7 decades, the X-ray luminosity is seen to be of the order of 10^{-3} of the spindown luminosity. Remarkably, this is true for pulsars close to the cooling curve in Fig. 6.3 as well as for those well above it, so that young ordinary pulsars and old recycled pulsars follow the same relation. The Figure shows that an upper bound to the X-ray luminosity of a radio pulsar is given roughly by ~ 0.01 of the spin-down luminosity; with only one upper limit shown in the figure, we do not know whether there is a lower bound.

Turning now to the γ -ray observations, we note that if PSR J0218+4232 were the radio counterpart of 2EG J0220+4228, then the γ -ray luminosity represents about 10% of the total pulsar spin-down luminosity at the minimum distance of 5.7 kpc, and for

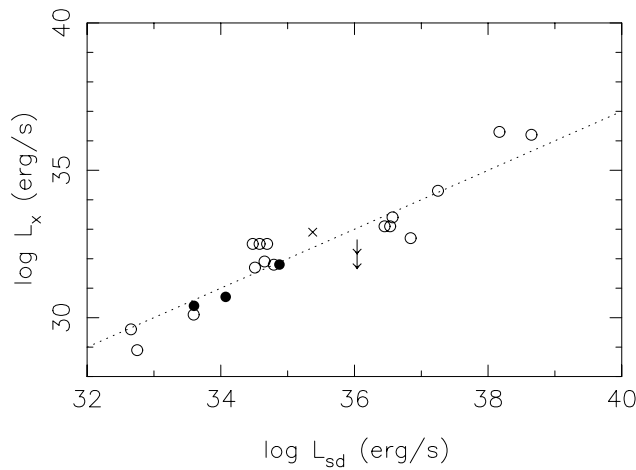


Fig. 6.4. The X-ray luminosity of radio pulsars in the range 0.1 – 2.4 keV as a function of the spindown luminosity $L_{sd} \equiv I(2\pi)^2 \dot{P}/P^3$. Symbols as in Fig. 6.3. The dashed line indicates $L_x = 10^{-3} L_{sd}$.

the energy range 100 MeV - 2 GeV and an assumed beaming angle of 1.0 sr. This is about as high as was measured for the most efficient γ -ray pulsar detected so far, PSR B1055–52 (Fierro et al. 1993). Models for γ -ray emission by radio pulsars can be divided in polar cap models (e.g. Daugherty & Harding 1996) and outer gap models (e.g. Romani & Yadigaroglu 1995). Sturmer & Dermer (1994) have extended these models to the regime of millisecond radio pulsars to predict their γ -ray luminosity. According to the latter, only the outer gap model predicts that PSR J0218+4232 is sufficiently luminous for detection.

Fierro et al. (1995) recently searched for millisecond pulsars in the EGRET high-energy γ -ray data (30 MeV – 30 GeV). With the H_m test statistic in a search for a pulsed signal, only one indication for a pulsar detection (PSR J0034-0534) with a random probability of occurrence of 6.4 % was reported from a list of 28 millisecond pulsars, but no statistically significant source was visible in the sky map. Thus, confirmation of the identity of 2EG J0220+4228 with PSR J0218+4232, by strengthening our 2 – 3.5 σ indication for a pulsed signal in the timing analysis, would make this pulsar the first millisecond radio pulsar detected in the high-energy γ -rays. The brightness in γ -rays of PSR J0218+4232 could then be due to the same reason why this pulsar is so bright in radio and in X-rays, i.e. to the fact that the Earth is inside the cone of radio emission throughout the radio pulse.

Whereas the X-ray detection of the pulsar may be considered secure, we note that variation of the X-rays with the pulse phase needs to be confirmed.

Acknowledgements. This research was supported in part by the Netherlands Organization for Scientific Research NWO under grant PGS 78-277. We are grateful to Werner Becker for his help

in the timing analysis; and to Fernando Camilo for remarks on the manuscript.

References

- Becker W., 1995, Ph.D. thesis, Ludwig Maximilian Universität München, MPE Report 260, p. 131
 Becker W., Trümper J., 1993, Nat 365, 528
 Blandford R., Teukolsky S., 1976, ApJ 205, 580
 Bucccheri R., Bennett K., Bignami G., et al., 1983, A&A 128, 245
 Burstein D., Heiles C., 1982, AJ 87, 1165
 Cruddace R., Hasinger G., Schmitt J., 1988, in F. Murtagh, A. Heck (eds.), Astronomy from large databases, p.177
 Daugherty J.K., Harding A.K., 1996, ApJ 458, 278
 David L., Harnden Jr. F., Kearns K., et al., 1995, The ROSAT High Resolution Imager (HRI), Technical report, U.S. ROSAT Science Data Center/SAO
 de Jager O.C., Swanepoel J.W.H., Raubenheimer B.C., 1989, A&A 221, 180
 Fierro J.M., Bertsch D.L., Brazier K.T., et al., 1993, ApJ 413, L27
 Fierro J.M., Arzoumanian Z., Bailes M., et al., 1995, ApJ 447, 807
 Halpern J.P., 1996, ApJ 459, L9
 Navarro J., de Bruyn A. G., Frail D., et al., ApJ 455, L55
 Predehl P., Schmitt J., A&A 293, 889
 Romani R., Yadigaroglu I.A., 1995, ApJ 438, 314
 Seward F., Wang Z-R., 1988, ApJ 332, 199
 Sturmer S.J., Dermer C.D., 1994, A&A 281, L101
 Taylor J.H., Manchester R.N., Lyne A., 1993, ApJS 88, 529
 Thompson D.J., Bertsch D.L., Dingus B.L., et al., 1995, ApJS 101, 259
 Trümper J., 1995, Reviews in modern astronomy 8, 1
 Umeda H., Shibazaki N., Nomoto K., et al., 1993, ApJ 408, 186
 Zimmerman H., Becker W., Belloni T., et al., 1994, EXSAS User's Guide, Technical Report 257, MPE

Chapter 7

Detection of pulsed X-ray emission from the binary millisecond pulsar PSR J0218+4232

L. Kuiper¹, W. Hermsen¹, F. Verbunt², and T. Belloni³

¹ SRON-Utrecht, Sorbonnelaan 2, NL-3584 CA Utrecht, The Netherlands

² Astronomical Institute, Utrecht University, P.O.Box 80000, NL-3508 TA Utrecht, The Netherlands

³ Astronomical Institute Anton Pannekoek and Center for High-Energy Astrophysics, Kruislaan 403, NL-1098 SJ Amsterdam, The Netherlands

Astron. Astrophys. 336, 545-552 (1998)

Abstract. We report the detection of pulsed X-ray emission from the binary millisecond pulsar PSR J0218+4232 in a 100 ks ROSAT HRI observation. The lightcurve deviates from a flat distribution at a $\sim 4.8\sigma$ level, showing a sharp main pulse with a duty cycle of ~ 0.15 ($350\mu s$), compatible with smearing due to the scatter in the ROSAT clock calibration. The intrinsic width can be smaller than $100\mu s$. There is an indication for a second peak at a phase separation of 0.47 ± 0.01 . The pulsed fraction is $37 \pm 13\%$. No indication for a modulation at the orbital period of the binary system is found. This is the fourth millisecond pulsar showing modulation in X-rays at the radio-pulsar period. The sharp pulses, very similar to those of PSR B1821-24 and the Crab pulsar, point to a magnetospheric origin of the pulsed X-ray emission. The observed and derived parameters of PSR J0218+4232 and PSR B1821-24 are very consistent with the exception of the small pulsed fraction of PSR J0218+4232. The large unpulsed component in X-rays and that reported earlier in the radio domain can be explained by emission from a compact nebula with diameter $\sim 14''$.

7.1. Introduction

PSR J0218+4232 was discovered by Navarro et al. (1995) as a highly luminous 2.3 ms radio-pulsar in a 2.0 day orbit. This millisecond (ms) pulsar has an extremely broad pulse-profile and about half of the radio emission is unpulsed; this is taken by Navarro et al. (1995) as an indication that the magnetic field is almost aligned with the rotation axis. From the dispersion measure a lower limit on the distance of 5.7 kpc is derived.

Van Kerkwijk (1997) reported the detection of an optical counterpart for this recycled ms-pulsar. The pulsar mass function as given by Navarro et al. (1995) suggests a companion mass of $\sim 0.2M_{\odot}$.

Recently, Verbunt et al. (1996) detected soft X-ray emission from this source in a 22 ksec ROSAT HRI observation. A timing analysis yielded a 6% probability that the observed phase distribution was due to random processes. They also found indications for pulsed emission in an archival ROSAT PSPC observation with the pulsar at an unfavourable off-axis angle of $40'$. The significance for pulsed emission ranged from 2.5σ to 4σ depending on the size of the event extraction radius. Verbunt et al. (1996) con-

servatively reported a value of 2.5σ since the usage of an extraction radius is in this case not an optimum selection criterion in view of the "horse-shoe" - shaped far off-axis PSPC point spread function. Therefore the detection of pulsed emission was considered tentative. The ROSAT HRI and PSPC lightcurves suggested a double-peaked lightcurve.

Pulsed X-ray emission has been firmly detected sofar from only 3 ms-pulsars, namely PSR J0437-4715 (Becker & Trümper 1993), PSR B1821-24 (Saito et al. 1997) and PSR J2124-3358 (Becker & Trümper 1997).

It was also noticed by Verbunt et al. (1996) that the EGRET high-energy γ -ray source 2EG J0220+4228 (Thompson et al. 1995), detected above 100 MeV at a $> 5\sigma$ significance is positionally consistent with the pulsar. A timing analysis using archival EGRET > 100 MeV data yielded indications for pulsed emission above 100 MeV at significance levels slightly below 3σ , making 2EG J0220+4228 a potential high-energy gamma-ray counterpart for PSR J0218+4232.

In this paper the results are presented from a 100 ks follow-up observation of PSR J0218+4232 with the ROSAT XRT/HRI combination aimed at clarifying its soft X-ray (0.1-2.4 keV) timing properties.

7.2. X-ray data and data analysis

7.2.1. ROSAT HRI Observation

PSR J0218+4232 was observed nearly on-axis with the ROSAT XRT/HRI combination between 23 July 1997 and 31 July 1997 yielding a net exposure of 98069 s. A standard analysis of the HRI image confirmed the detection by Verbunt et al. (1996) of a source consistent in position with the radio-pulsar. The measured offset of $4''.2$ is smaller than the systematic uncertainty in the satellite pointing of $6''.0$. Figure 7.1 shows the measured event distribution and the position of the radio-pulsar without bore-sight correction.

7.2.2. Spatial analysis

The standard analysis was applied to determine the centroid of the source event distribution using a Gaussian shaped Point Spread Function (PSF) with a predetermined standard deviation (Zimmermann et al. 1997). However, the in-flight PSF could have a

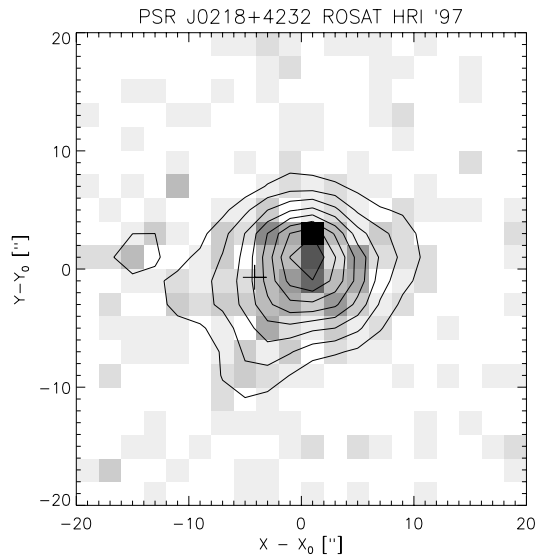


Fig. 7.1. Measured (x,y) -distribution (in $2''.0 \times 2''.0$ pixels) centered on the position of the X-ray counterpart of PSR J0218+4232. The position of the pulsar, indicated by a '+' sign, is consistent with the position of the X-ray source which has a systematic uncertainty of $\sim 6''.0$. Superposed is the smoothed distribution (equidistant contour levels) obtained after convolving the measured distribution with a 2-dimensional Gaussian with $\sigma = 2''.0$, approximately the width of the point-spread function derived from ground-based calibrations and in-flight measurements (David et al. 1997). The highest pixel contains 14 counts.

somewhat different shape and width. In addition, we have to verify whether the source distribution is consistent with a single point source. To derive this in-flight distribution we have determined the radial distribution with respect to the centroid ($r=0$) of the number of events per arcsec square. This distribution is shown in Fig. 7.2a. For radii beyond $20''.0$ the background level is evidently reached. We found for the latter a value of $(0.093 \pm 0.004) \text{ cnts/arcsec}^2$ by choosing the background region between r is $20''.0$ and $50''.0$. By subtracting this underlying background contribution from the measured (including both source and background events) radial distribution we can determine the cumulative radial distribution of the source events. This distribution saturates at a value of $\sim 182 \text{ cnts}$, corresponding to the total number of source counts, and its shape is compatible with a Gaussian having a standard deviation of $4''.75$ (see Fig. 7.2b; empirically derived source distribution).

This value is larger than expected from the on-axis PSF derived from ground-based calibrations and in-flight observations (David et al. 1997). The latter is described as the sum of two Gaussians and an exponential and gives on average a good representation. Due to random errors in the aspect solution of the spacecraft, the width of the core of the measured response can vary. David et al. (1997) give a range for the widths of the Gaussian components as derived from in-flight observations. In Figs. 7.2a,b the expected profiles are shown for comparison ($\sigma_1 = 2''.19$ and $\sigma_2 = 4''.04$; see David et al. 1997). It is evident that the measured profile is significantly broader than that expected for a point source. This can be due to the detection of a point source plus extended emission,

unless systematic effects have broadened the profile excessively. We will investigate these possibilities below.

In order to derive a measure for the overall significance and flux of the total excess, we repeated the spatial analysis by applying a maximum likelihood ratio test using the empirically derived source distribution. This maximum likelihood ratio test is based on parameter optimization under two different hypotheses, one describing the measured (x,y) - event distribution by background only (\mathcal{H}_0) and the alternative (\mathcal{H}_1) describing the event distribution by background and a point source (the empirical source distribution) at a given scan position. This test yielded a 21σ source detection. The number of counts S assigned to the total excess and background B per arcsec square is $(181.4 \pm 15.0) \text{ cnts}$ and $(0.094 \pm 0.004) \text{ cnts/arcsec}^2$, respectively, fully consistent with the above estimates. The countrate is $(1.84 \pm 0.15) \cdot 10^{-3} \text{ cnts/s}$, which is consistent with the value of $(2.1 \pm 0.4) \cdot 10^{-3} \text{ cnts/s}$ from our previous 22 ks ROSAT/HRI observation (Verbunt et al. 1996).

Having decoupled the source and background distributions we were able to determine the Signal-to-Noise ratio ($S/N = (Q(r) - \pi \cdot B \cdot r^2) / \sqrt{Q(r)}$) as a function of distance r from the centroid (Fig. 7.2c). The quantity $Q(r)$ represents the measured cumulative count distribution as function of distance r including both source and background events. The optimum radius $r_{opt} = 11''.25$ is used as *extraction* radius in the subsequent timing analyses.

7.2.3. Timing analyses

7.2.3.1. Modulation at the pulsar period

In the search for modulation at the pulsar period we selected events within a radius r_{opt} , the optimum radius determined above, from the X-ray source position. The solar-system barycentered (SSB) UTC arrival times were converted to barycentric dynamical time scale (TDB). These SSB UTC arrival times in turn were obtained by converting the spacecraft clock (SCC) arrival times to UTC times using a fourth order polynomial fit of the SCC-calibration points to UTC, and subsequently determining the source -, space-craft - and SSB position dependent parts. Because our observation was spread over more than 8 days the stability of the SCC - UTC fit over the observation period is crucial for a successful modulation search at *millisecond* periods. We have been fortunate, the average scatter around the mean of the fit residuals over the entire observation was in an acceptable range ($\lesssim 0.20 \text{ ms}$, corresponding to a scatter in pulse-phase of $\lesssim 0.1$). (see e.g. ROSAT Service Area; chapter on Calibration sub. Timing; http://ftp.rosat.mpe-garching.mpg.de/rosat_svc/calibration/timing/). The next step in our analysis was pulse-phase folding the TDB-arrival times according to the radio ephemeris given by Navarro et al. (1995) taking into account the time-delays due to the orbital motion. We verified that the uncertainty in the predicted period is sufficiently small to justify a single trial at the expected radio parameters.

The obtained pulse-phase distribution deviates from a statistically flat distribution at a $\sim 4.8\sigma$ level (chance probability of $1.96 \cdot 10^{-6}$) for two harmonics ($n = 2$) applying a Z_n^2 - test (see Bucccheri et al. 1983) on the unbinned set of pulse-phases. An H-test (de Jager et al. 1989), also on the unbinned set of pulse-phases and more appropriate if the pulse-shape is unknown, yields a chance probability of $1.94 \cdot 10^{-5}$ corresponding to a $\sim 4.4\sigma$ deviation. We verified the association of the pulsed emission with the

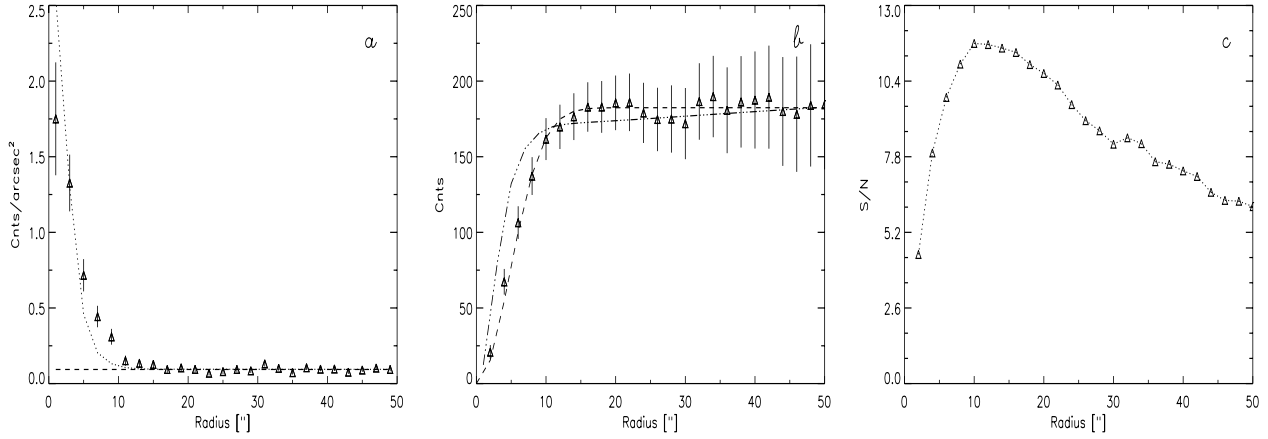


Fig. 7.2. **a)** Radial distribution of the surface density centered on the X-ray counterpart of PSR J0218+4232. The dashed line indicates the background level determined from the distribution for radii between $20''0$ and $50''0$. The dotted line shows the expected profile for a point source (David et al. 1997). **b)** Cumulative background- subtracted distribution for the X-ray counterpart of PSR J0218+4232. The dashed line shows the distribution for a Gaussian shaped source distribution with $\sigma = 4''.75$ and 182 source counts. The dashed-dotted line shows the expected cumulative distribution for a point source having 182 counts. **c)** The Signal-to-Noise distribution as a function of the event extraction radius r . This distribution peaks at $r = r_{opt} = 11''.25$, the optimum extraction radius for timing studies.

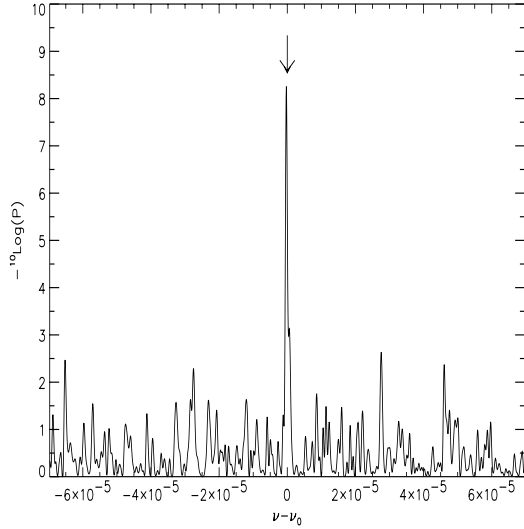


Fig. 7.3. Periodogram for our HRI'97 observation at frequencies in the vicinity of the expected radio-pulse frequency ν_0 . Along the y-axis is shown the chance probability from the Z_2^2 -test. The expected frequency (downwards arrow) falls within the measured peak with a characteristic width $\Delta\nu$ of $\sim 1/\tau = 1.4 \cdot 10^{-6}$ Hz with τ the total observation interval ($8^d.3$).

pulsar by performing a similar timing analysis but now selecting events having radii larger than r_{opt} . No modulation is present in this sample. Furthermore, the periodogram in Fig. 7.3 shows that the detected pulsar modulation is only visible around the expected frequency $\nu_0 = 430.461066552(7)$ Hz with a width $\Delta\nu$ consistent with the total observation interval. The lightcurve (binned representation of the pulse-phase distribution) obtained after phase-folding at the expected radio frequency (single trial) is shown in Fig. 7.4 for two cycles with superimposed its Kernel Density Es-

imator (de Jager 1986; solid smooth line) and its 1σ -uncertainty range (dashed-dotted lines). The phase in Fig. 7.4 is arbitrary, for we can not relate the X-ray phase to the radio-phase due to the limited accuracy of the ROSAT timing. Indicated as a dashed line is the background level determined from the spatial analysis. It is evident that a considerable fraction of the source photons is unpulsed (DC). In order to quantify the pulsed fraction we have applied a method based on bootstrapping of the (unbinned) data to determine the strength of the pulsed signal and the unpulsed interval in an unbiased manner as outlined in Swanepoel et al. (1996). This method assigns the pulse-phase interval $[0.12 - 0.39]$ as the unpulsed interval (statistically flat) and the pulsed fraction $\mathcal{R} = N_P / (N_P + N_{DC})$ obtained by this recipe is 0.37 ± 0.13 , where N_P and N_{DC} are the number of pulsed and DC counts, respectively.

The dominant emission feature above the DC-flux level (in phase range 0.45-0.60) has a remarkably small duty cycle of ~ 0.15 ($350\mu s$) which is compatible with the effect of smearing due to the scatter in the SCC - UTC clock calibration (see above). The intrinsic width can be significantly less than $100\mu s$.

There appears to be a second pulse (near 1.0 in phase), although it is marginally significant in this 100 ks ROSAT HRI observation: the improvement in likelihood of a pulse-phase distribution description in terms of a background and 2 Gaussians with respect to a description in terms of a background and 1 Gaussian corresponds to 1.6σ . The 2 Gaussians have a phase separation of 0.47 ± 0.01 . Our earlier HRI and PSPC lightcurves suggested also two pulses (Verbunt et al. 1996). Unfortunately, all lightcurves have arbitrary phase, so we can not directly sum the distributions. To derive the phase shifts from the lightcurves we cross-correlated the ROSAT/HRI 1995 and ROSAT/PSPC lightcurves with the ROSAT/HRI 1997 lightcurve and select the global maxima. Applying these shifts we obtain the co-added lightcurve shown in Fig. 7.5. It is remarkable to see how this combined lightcurve strengthens the features visible in Fig. 7.4: The main pulse becomes more significant with a similar or smaller pulse width; the second pulse becomes also more pronounced with similar width; the phase sep-

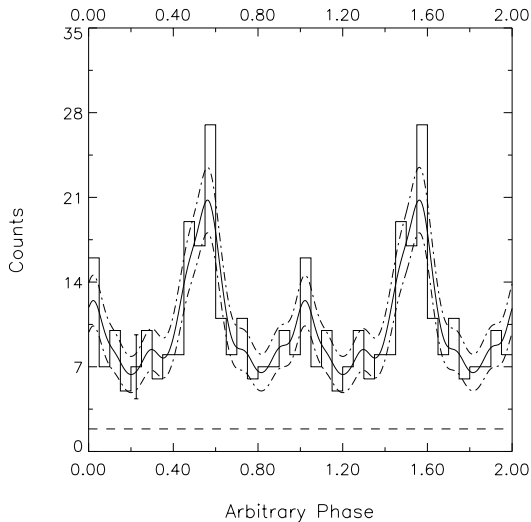


Fig. 7.4. Lightcurve for the 100 ks ROSAT HRI 1997 observation of PSR J0218+4232. Two cycles are shown for clarity. A typical error bar is shown. The significance for a deviation from a statistically flat distribution is $\sim 4.8\sigma$. The dashed line indicates the background level determined from the spatial analysis. The pulsed fraction is estimated to be $(37 \pm 13\%)$. The smooth solid curve represents the Kernel Density Estimator and the dashed-dotted lines indicate the 1σ uncertainty range.

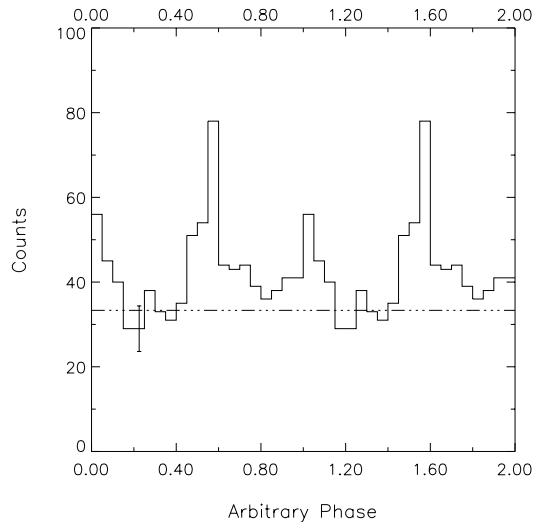


Fig. 7.5. Co-added HRI '97, HRI '95 and PSPC lightcurve obtained after applying the phase-shifts at cross-correlation maxima (see text). A typical error bar is indicated. The dashed line represents the level of unpulsed emission determined in the phase range $[0.12-0.39]$. The features visible in Fig. 7.4 become more pronounced. The second peak (phase range $[-0.12-0.12]$) contains 50 ± 14 excess counts corresponding to a $\sim 3.6\sigma$ detection.

aration is again 0.47 ; and the background region identified by the bootstrapping method in the lightcurve of the HRI 1997 observation represents even more clearly the unpulsed level. This level is drawn in Fig. 7.5 as a dashed-dotted line adopting the unpulsed interval $[0.12 - 0.39]$ as determined above. The number of counts in the second peak (phase range $[-0.12, 0.12]$) above the unpulsed level is 50 ± 14 ($\sim 3.6\sigma$) giving additional support for the presence of a second peak. In fact, this phase distribution mimics the well-known X-ray lightcurve of the Crab pulsar which exhibits also two peaks with phase separation 0.40 and emission between the peaks.

7.2.3.2. Modulation at the orbital period

We also searched for a possible modulation at the binary period of $2^d.0288$. In this case we have to divide the number of counts detected within r_{opt} per orbital phase bin by its exposure to obtain the countrate corrected for the inhomogeneous exposure. Dividing the orbital cycle in 10 and 20 bins we found no indication for orbital modulation ($\chi_r^2 = 1.05$ and $\chi_r^2 = 1.12$, respectively, fitting a constant countrate). An X-ray eclipse could be expected near $\phi_{orb} = 0.25$ ($\phi_{orb} = 0$ corresponds to the time of the ascending node). The flux measurement around this phase does not show any suppression.

7.2.4. Indications for extended emission

In Sect. 7.2.2 we concluded from Fig.7.2a,b that the excess in the skymap has an extent which is larger than expected for a point source based on ground-based calibrations and in-flight observations (David et al. 1997). The detection of a pulsed signal in the timing analysis with a pulsed fraction of $37 \pm 13\%$ proves that

at least a significant fraction originates in a point source. For the remaining unpulsed component of $\sim 63\%$ there are two explanations possible: 1) Point-like emission from the pulsar, but then the PSF of the pulsed and unpulsed emission would be excessively broadened by systematic effects; 2) extended emission.

In order to investigate these possibilities, we produced a “pulsed” map selecting events in the pulse-phase interval of the main pulse (phase range 0.45-0.60; see Fig. 7.4) and an “unpulsed” map for the complementary phase range (0.0-0.45 and 0.6-1.0). If systematic effects are not responsible for the broad total profile, then the profile in the pulsed map should be narrower, because in that case we selected an event sample with a pulsed fraction of $70 \pm 6\%$. This pulsed fraction has been determined from the number of excess counts in the main peak above the level in the unpulsed phase interval 0.12-0.39 (see Sect. 7.2.3.1; bootstrap method as outlined in Swanepoel et al. 1996). Note that the pulsed fraction in the complementary phase interval is also non-zero: $13 \pm 11\%$.

Figure 7.6 displays for the pulsed and unpulsed maps the differential radial profiles analogous to Fig. 7.2a for the total data. Indeed, the distribution in the pulsed map (Fig. 7.6a) is sharper, only slightly broader than expected for a point source. In order to investigate this more quantitatively, we compared the measured distributions with the expected profile for the (weighted) sum of two components: A point source plus an extended distribution, assumed to have the shape of a cylinder. The latter distribution has been convolved with the expected PSF for a point source (David et al. 1997).

To derive an estimate of the diameter of the extended emission, we made a fit to the total radial profile (Fig. 7.2a) in terms of a point source with a *fixed* contribution of 37% and an extended model (63%) yielding for the diameter of the extended emission

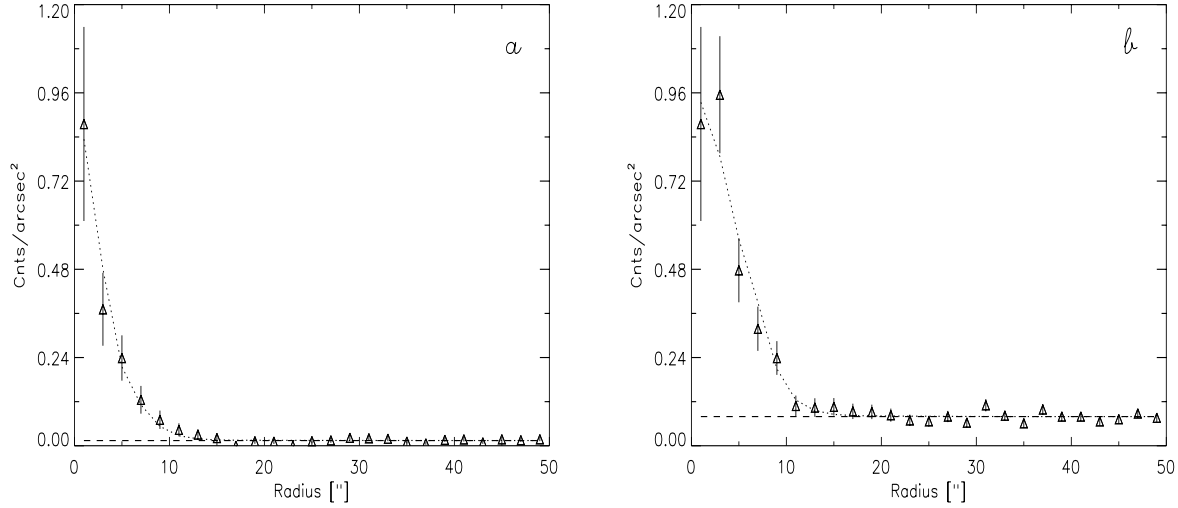


Fig. 7.6. a) Radial event distribution of the X-ray counterpart of PSR J0218+4232 selecting events with pulse-phases in the range 0.45–0.60 (main peak). The dotted line shows the distribution expected from a point-source with weight factor 0.7 and an extended model (cylinder model with radius $7''$) with weight factor 0.3. **b)** Radial event distribution of the X-ray counterpart of PSR J0218+4232 selecting events with pulse-phases in range 0.0-0.45 and 0.60-1.0. The dotted line shows the distribution expected from a point-source with weight factor 0.13 and the extended model with weight factor 0.87. Note the sharper shape of the radial distribution of the main peak shown in **a** in comparison with the shape of the complementary distribution shown in **b**.

a 1σ -confidence interval of $[12'' - 15'']$ with an optimum value near $14''$.

Figures 7.6a and b show that also these distributions are fully consistent with the sums of the expected profiles for a point source (weight factors 0.70 and 0.13, respectively) and extended emission with diameter $14''$ (weight factors 0.30 and 0.87, respectively). The obtained reduced χ^2 -values were 0.58 and 0.85, respectively, both for 5 degrees of freedom (d.o.f.; the effective fit range was $0''0 < r < 12''0$, which includes 6 datapoints). In order to quantify the differences between the distributions we have also fit the radial distribution of the pulsed events in Fig. 7.6a with the profile used in the fit of the complementary distribution in Fig.7.6b. The reduced χ^2 was then 2.21, again for 5 d.o.f. The chance probability for such a large value of the reduced χ^2 is $\sim 5\%$, indicating that the fit is rejectable at the 95%- confidence level.

Finally, we also investigated whether the weight of the point source can be increased fitting again the total radial profile (Fig.7.2a), leaving both the radius of the extended emission and the point source fraction free, to see how much DC emission from the point source is allowed in addition to the extended emission. We do not find a significant detection, the 1σ -confidence interval for the *total* point source fraction being $[0.2-0.65]$ to be compared with that for the pulsed fraction from the timing analysis $[0.24-0.50]$.

An independent method to study the extent of the in-flight PSF consists in identifying point-sources with high photon statistics in the vicinity (within $\sim 10'$) of PSR J0218+4232 and subsequently analyzing their radial profiles. We only found 3 weak sources, all weaker than PSR J0218+4232 and therefore less appropriate for this kind of study. None of these show the same broadening as PSR J0218+4232.

From the above findings we can conclude that we found indications for extended emission with an angular scale of $\sim 14''$, centered on the pulsar position.

7.2.5. Flux calculation

The ROSAT HRI has no spectral resolving power, making spectral modelling impossible. However, assuming a spectral model and a measure of the Hydrogen column density (N_H) in the direction of the source, it is possible to convert the total measured count rate to an unabsorbed flux value (David et al. 1997). For a power-law photon spectrum as found for peak 1 of PSR B1821-24 (Saito et al. 1997) with photon-index $\Gamma = -1.5$ between $0.7 - 10$ keV (energy index α is -0.5) and $N_H = 5 \cdot 10^{20} \text{ cm}^{-2}$ (see Verbunt et al. 1996) the observed count rate translates in an unabsorbed $0.1-2.4$ keV flux of $(1.05 \pm 0.09) \cdot 10^{-13} \text{ ergs/cm}^2 \text{ s}$. Varying the power-law photon index from -1.0 to -3.0 we obtain flux values between $0.97 \cdot 10^{-13}$ and $2.96 \cdot 10^{-13} \text{ ergs/cm}^2 \text{ s}$. Varying also N_H to a value of $7.5 \cdot 10^{20} \text{ cm}^{-2}$ found from the H I-survey performed by Heiles & Habing (1974), increases the fluxes by 8 to 24% for power-law indices ranging from -1.0 to -3.0 , respectively. Assuming, a fortiori, that the pulsed and unpulsed components have the same spectral shape, we can divide the total flux of $(1.05 \pm 0.09) \cdot 10^{-13} \text{ ergs/cm}^2 \text{ s}$ for $N_H = 5 \cdot 10^{20} \text{ cm}^2$, $\Gamma = -1.5$ and a pulsed fraction of $37 \pm 13\%$ in a pulsed component of $(3.9 \pm 1.4) \cdot 10^{-14} \text{ ergs/cm}^2 \text{ s}$ and an unpulsed/extended component of $(6.6 \pm 1.5) \cdot 10^{-14} \text{ ergs/cm}^2 \text{ s}$.

7.3. Discussion

The detection of pulsed X-ray emission from PSR J0218+4232 makes this the fourth ms-pulsar for which modulation at the pulse-period is observed. Of the three other ms-pulsars showing spin-modulated X-ray emission, namely PSR J0437-4715 (Becker & Trümper 1993; Halpern et al. 1996; Kawai et al. 1998), PSR B1821-24 (Danner et al. 1994, 1997; Saito et al. 1997; Rots et al. 1998; Becker & Trümper 1997) and PSR J2124-3358 (Becker & Trümper 1997), only PSR B1821-24 shows narrow pulses in its lightcurve similar to PSR J0218+4232. The other two ms-

pulsars, PSR J0437-4715 and PSR J2124-3358, show both broad and smooth X-ray lightcurves. In addition, the latter have luminosities in the ROSAT 0.1-2.4 keV band about 3 orders of magnitude lower than the first two. Therefore we concentrate in the remainder of the discussion on the comparison of PSR J0218+4232 with PSR B1821-24, which have the smallest characteristic ages ($\tau_c = P/2\dot{P}$), by 1-2 orders of magnitude, of the ms-pulsars detected at X-rays so far.

PSR B1821-24 has been studied in detail by Saito et al. (1997) using ASCA data. They showed that the narrow ($\sim 100\mu s$) first pulse after subtraction of the DC-component has a very hard spectrum (photon index -1.2 between 0.7 and 10 keV), which has to be of magnetospheric origin. Interestingly, the phase separation 0.444 ± 0.014 or alternatively 0.556 (Rots et al. 1998) between the two pulses of PSR B1821-24 is very similar to the 0.47 ± 0.01 measured by us for PSR J0218+4232. In addition, the first pulse in the lightcurve of Figs. 7.4 and 7.5 can be intrinsically be narrower than 1 bin, which is also $\sim 100\mu s$. Unfortunately, we cannot derive spectra from our ROSAT HRI observation, but the narrow pulses detected from PSR J0218+4232 make us believe that these are also of magnetospheric origin. The origin of the substantial unpulsed component (see Fig. 7.4) is less obvious. This could be thermal emission from the neutron star surface as well as of magnetospheric origin. However, this unpulsed component can also be assigned to extended emission from e.g. a compact nebula, as is shown in Sect. 7.2.4. This will be discussed below.

Most striking are the differences in the shapes of the radio pulses of the two ms-pulsars. Backer & Sallmen (1997) show for PSR B1821-24 two narrow pulses and one broader radio pulse (at 800 and 1395 MHz), very different from the extremely broad radio pulse of PSR J0218+4232 detected throughout the pulsar period (Fig. 7.7). As mentioned in the introduction, the broad radio-pulse from PSR J0218+4232 was explained with the geometry of an aligned rotator (Navarro et al. 1995), but the two narrow peaks with the indication of bridge emission between them as seen in the X-ray lightcurve (see Figs. 7.4,7.5), require at least a small angle between the magnetic - and rotation axis. Namely: Such double-peaked pulses with bridge emission are currently explained by models in which the high-energy emission is seen from one magnetic pole. In polar cap models (most recently: Sturmer et al. 1995; Daugherty & Harding 1996) the non-thermal beam is a hollow cone centered on the magnetic pole. In outer gap models (most recently Romani 1996) the emission occurs in a wide fan beam that is formed by the surface of the last open field line in the outer magnetosphere. For both models a double-peaked pulse can only be observed when the rotator is not completely aligned and the edge of the cone is visible to the observer twice per rotation. Unfortunately, we cannot compare the radio and X-ray profiles of PSR J0218+4232 in absolute timing, nor is it possible to identify a common pulse for tentative more detailed discussions like has been done for PSR B1821-24 by Backer & Sallmen (1997). Saito et al. (1997) compared the physical parameters of PSR B1821-24 with those of the Crab pulsar to understand the production of hard emission in the magnetosphere of a ms-pulsar for which the magnetic field strength is orders of magnitude weaker than for normal rotational pulsars. They pointed out that in the magnetosphere near the light-cylinder radius (R_L), the radius at which the magnetosphere, if corotating with the neutron star, will have a speed equal to the speed of light, the magnetic field strength ($B_L = B_S \cdot (R_S/R_L)^3$ with B_S and R_S the averaged magnetic field strength at the neutron star surface and the neutron star radius respectively) comes

out to be very close to that for the Crab. In addition, R_L of ms-pulsars is 1-2 orders of magnitude smaller than those of the young normal pulsars, increasing strongly the curvature of the magnetic field lines which enhances the production of non-thermal emission (see Ho 1989). With our firm detection of pulsed emission from PSR J0218+4232 with a lightcurve similar to those of the Crab pulsar and the isolated ms-pulsar PSR B1821-24 it is interesting to compare now the physical parameters of the two ms-pulsars in more detail (see Table 7.1). They have very similar periods, PSR J0218+4232 rotating a bit faster, but PSR B1821-24 is ~ 15 times younger, has a rotational energy loss $\dot{E} \sim 9$ times higher and a surface magnetic field strength $B_S \sim 5$ times stronger. This suggests that the X-ray luminosity of PSR B1821-24 will be higher, as is indeed the case. The pulsed X-ray luminosities in the ROSAT band (0.1-2.4 keV) differ at most a factor of ~ 10 , proportional to the difference in \dot{E} , but the total X-ray luminosities differ at most by a factor of 4.

The derived total radio luminosity of PSR J0218+4232 is about a factor of three higher, while the luminosities of the pulsed radio components are, within the uncertainties on the distance estimates, about the same. It is interesting to note that the magnetic field strength B_L at the light-cylinder of PSR J0218+4232 is only a factor of ~ 2 smaller than that of PSR B1821-24 due to its smaller R_L (~ 110 km vs ~ 146 km). More remarkably, B_L of PSR J0218+4232 is only a factor of ~ 3 smaller than B_L of the Crab pulsar, while B_S differs in this case more than 4 orders of magnitude (see also Saito et al. 1997).

The main difference in characteristics is the remarkably large fraction of unpulsed emission of $\sim 60\%$ in X-rays (see Fig. 7.4) and $\sim 50\%$ in radio (see Fig. 7.7; systematically over the range 400-1400 MHz, Navarro et al. 1995) for PSR J0218+4232. We showed above that this X-ray emission might be extended with angular scale of $\sim 14''$. Navarro et al. (1995) noted that it is possible that the observed unpulsed emission in the radio comes from a compact nebula close to the pulsar. This nebula would then have the same steep spectral index as the pulsed emission and the nebula would have to be smaller than the VLA beam size of $16''$. The latter constraint is consistent with the possible extent found here in X-rays. Navarro et al. (1995) preferred the explanation for which the unpulsed emission comes from the pulsar, however, given our results above, we prefer now the explanation that the unpulsed X-ray and radio emissions are both manifestations of a compact nebula around the pulsar.

Danner et al. (1997) report the detection of an extended source next to PSR B1821-24. The shape of this source is "identical" to the distribution shown in Fig. 7.1, with the same angular extent. Since the estimated distances are comparable, even the absolute extent is similar, ~ 0.4 pc. The main difference is that Danner et al. (1997) determine a separation between the pulsar and the extended source of $9''3$. PSR B1821-24 is located near the edge of the globular cluster M28. Since the extended source appeared to be only slightly offset from the centre of the cluster, Danner et al. (1997) preferred an interpretation as a collection of low-luminosity accreting X-ray binaries in the cluster, over the interpretation as a synchrotron nebula. They considered the synchrotron nebula to be powered by a recent (of the order of 200 years ago) outburst of an unknown source, inconsistent with the pulsar age. However, if the pulsar is powering the nebula it is doing this continuously and no outburst is required. Therefore the interpretation as a synchrotron nebula remains a viable option. The binary ms-pulsar PSR J0218+4232 is not located in a globular

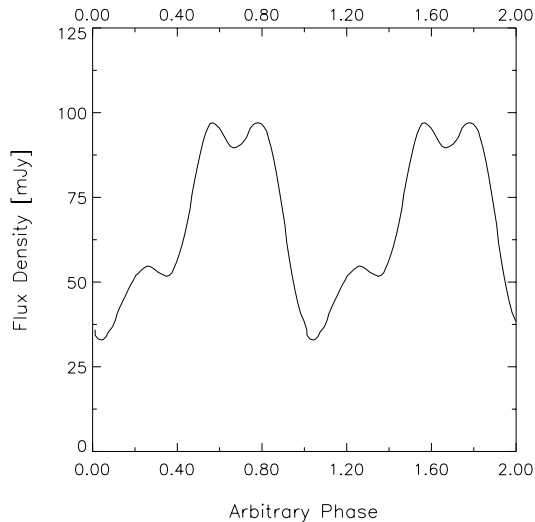


Fig. 7.7. Radio-profile at 410 MHz of PSR J0218+4232 as shown in Navarro et al. (1995). The pulse shape is broad and complex. Notice that there is no flat baseline to the profile at any phase. The pulsed fraction is about 50%.

cluster. Of the two options mentioned above only the interpretation as a synchrotron nebula remains. Kawai & Tamura (1997) searched for diffuse sources in the vicinity of normal radio pulsars using ASCA X-ray data. They found such sources with high probability for many pulsars, leading to the suggestion that they exist universally for all the active pulsars, and that they are powered by the pulsars. The extended sources near PSR B1821-24 and PSR J0218+4232 add two more candidates, now concerning recycled ms-pulsars.

Wei et al. (1996) discuss the production processes of pulsed and unpulsed gamma-ray emission in ms-pulsars using the outer gap model. They assume that the unpulsed gamma-rays come from a compact region, a couple of light cylinder radii from the pulsar rather than from an extended nebula. This unpulsed non-thermal emission (up to TeV energies) is produced in the interaction of the primary electrons/positrons from one gap interacting with the low-energy photons from another gap, which one expects to cross over just beyond the light cylinder. If we assume that the unpulsed X-ray emission measured from PSR J0218+4232 is the low-energy end of the spectrum of this component, rather than from a small nebula, then one would expect the signature of a point source in our maps. This seems not to be the case. Furthermore, the observed and derived parameters of PSR J0218+4232 and PSR B1821-24 are very consistent. Therefore it is unlikely that the first can produce such a strong unpulsed point-like X-ray component at the pulsar position while there is no evidence for such a component for the second.

Wei et al. (1996) produced pulsed and unpulsed spectra showing that at high-energy gamma-rays the unpulsed component becomes particularly important. In our earlier paper (Verbunt et al. 1996) we noted that the EGRET source 2EG J0220+4228 (Thompson et al. 1995) can be the counterpart of PSR J0218+4232, and we found indications for variation at the pulse period, however, consistent with being 100% pulsed. In fact, also PSR B1821-24 is located close to a possible EGRET source (Fierro 1995), but the identification is less certain, since

Table 7.1. Parameter comparison between PSR J0218+4232 and PSR B1821-24 (from Navarro et al. 1995, Saito et al. 1997 and this work)

Parameter	J0218+4232	B1821-24
Period (ms)	2.323	3.054
Period derivative (s/s)	$8.00 \cdot 10^{-20}$	$161.88 \cdot 10^{-20}$
Age $P/2\dot{P}$ (yr)	$4.6 \cdot 10^8$	$3.0 \cdot 10^7$
\dot{E} (ergs/s)	$2.5 \cdot 10^{35}$	$2.2 \cdot 10^{36}$
R_L (km)	110.8	145.7
B_S (G)	$4.4 \cdot 10^8$	$2.2 \cdot 10^9$ [∇]
B_L (G)	$3.2 \cdot 10^5$	$7.3 \cdot 10^5$
Distance (kpc)	≥ 5.7	5.1 [♣]
L_X (0.1-2.4 keV; ergs/s)		
Total	$\geq 4.1 \cdot 10^{32}$	$1.1^{\dagger} - 1.7^{\ddagger} \cdot 10^{33}$
Pulsed	$\geq 1.5 \cdot 10^{32}$	$1.1^{\dagger} - 1.7^{\ddagger} \cdot 10^{33}$
L_{Radio} (400 MHz; mJy · kpc ²)		
Total	> 2700	835 [♠]
Pulsed	> 1137	≤ 835

[†] X-ray luminosity given by Danner et al. (1997)

[‡] X-ray luminosity given by Becker & Trümper (1997)

[♠] 400 MHz radio luminosity given by Foster et al. (1991) multiplied by $(5.1/5.8)^2$

[♣] Rees & Cudworth (1991)

[∇] The magnetic field strength at the surface calculated by us is a factor of 2 lower than the value given by Saito et al. (1997). The difference can be traced back to the use of a factor of $\frac{1}{2}$ by Saito et al. in the formula relating the magnetic dipole moment to B_S and R_S . Our factor of 1 is consistent with that widely used in the pulsar community (e.g. Taylor et al. 1993, Becker & Trümper 1997, Navarro et al. 1995).

PSR B1821-24 is just outside the 99% location confidence contour.

At high-energy γ -rays progress can be expected from our scheduled 3 weeks CGRO EGRET exposure in summer 1998 aimed at confirming our indications for pulsed emission above 100 MeV from PSR J0218+4232.

As mentioned above, due to the lack of spectral resolving power of the ROSAT HRI we can not perform a spectral analysis for PSR J0218+4232. Spectral information on the pulsed and DC components can only be obtained by long exposures using ASCA, SAX LECS/MECS and the future AXAF and XMM X-ray observatories.

Acknowledgements. This research was partly supported by the Netherlands Organization for Scientific Research NWO.

References

- Backer D.C., Sallmen S., 1997, AJ 114, 1539
 Becker W., Trümper J., 1993, Nat 365, 528
 Becker W., Trümper J., 1997, A&A 326, 682
 Buccheri R., Bennett K., Bignami G., et al., 1983, A&A 128, 245
 Danner R., Kulkarni S.R., Thorsett S.E., 1994, ApJ 436, L153
 Danner R., Kulkarni S.R., Saito Y., Kawai N., 1997, Nat 388, 751
 David L.P., Harnden F.R., Kearns K.E., et al., 1997, The ROSAT High Resolution Imager (HRI) Calibration Report, U.S. ROSAT Science Data Center/SAO (

www.harvard.edu/rosat/rsdc/www/HRI_CAL_REPORT/hri.html)

- Daugherty J.K., Harding A.K., 1996, ApJ 458, 278
Fierro J.M., 1995, Ph.D. thesis, Stanford University
Foster R. S., Fairhead L., Backer D.C., 1991, ApJ 378, 687
Halpern J.P., Christopher M., Marshall H.L., 1996, ApJ 462, 908
Heiles C., Habing H.J., 1974, A&AS 14, 1
Ho C., 1989, ApJ 342, 396
de Jager O.C., Swanepoel J.W.H., Raubenheimer B.C., 1986, A&A 170, 187
de Jager O.C., Swanepoel J.W.H., Raubenheimer B.C., 1989, A&A 221, 180
Kawai N., Tamura K., 1997, Proc. IAU Coll. 160, 367
Kawai N., Tamura K., Saito Y., 1998, Adv. in Space Research 21, in press
van Kerkwijk M.H., Proc. IAU Coll. 160, 489
Navarro J., de Bruyn A.G., Frail D.A., Kulkarni S.R., Lyne A.G., 1995, ApJ 455, L55
Rees R.F., Cudworth K.M., 1991, AJ 102, 152
Romani R.W., 1996, ApJ 470, 469
Rots A.H., Jahoda K., Macomb D.J., et al., 1998, ApJ submitted
Saito Y., Kawai N., Kamae T., et al., 1997, ApL 477, L37
Sturmer S.J., Dermer C.D., Michel F.C., 1995, ApJ 445, 736
Swanepoel J.W.H., de Beer C.F., Loots H., 1996, ApJ 467, 261
Taylor J.H., Manchester R.N., Lyne A.G., 1993, ApJS 88, 529
Thompson D.J., Bertsch D.L., Dingus B.L., et al., 1995, ApJS 101, 259
Verbunt F., Kuiper L., Belloni T., et al., 1996, A&A 311, L9
Wei D.M., Cheng K.S., Lu T., 1996, ApJ 468, 207
Zimmermann U., Becker W., Belloni T., et al., 1997, EXSAS User's guide, MPE Report

Chapter 8

The pulse shape and spectrum of the millisecond pulsar PSR J0218+4232 in the energy band 1-10 keV observed with BeppoSAX

T. Mineo¹, G. Cusumano¹, L. Kuiper², W. Hermsen², E. Massaro³, W. Becker⁴, L. Nicastro¹, B. Sacco¹, F. Verbunt⁵, A.G. Lyne⁶, I.H. Stairs⁶, and S. Shibata⁷

¹ Istituto di Fisica Cosmica ed Applicazioni all'Informatica CNR, Via U. La Malfa 153, I-90146, Palermo, Italy

² SRON-Utrecht, Sorbonnelaan 2, 3584 CA Utrecht, The Netherlands

³ Istituto Astronomico, Unita' GIFCO Roma-1, Universita' "La Sapienza", Via Lancisi 29, I-00161, Roma, Italy

⁴ Max-Planck-Institut für Extraterrestrische Physik, D-85740 Garching bei München, Germany

⁵ Astronomical Institute Utrecht University, P.O. Box 80000, 3508 TA Utrecht, The Netherlands

⁶ University of Manchester, Jodrell Bank, Macclesfield SK11 9DL, United Kingdom

⁷ Department of Physics, Yamagata University, Kojirakawa, Yamagata 990-8560, Japan

Astron. Astrophys. 355, 1053-1059 (2000)

Abstract. We present the results of a BeppoSAX observation of PSR J0218+4232 which, for the first time, provides detailed information on the pulsar's temporal and spectral emission properties in the broad band 1–10 keV. We detected X-ray pulses with a pulsed fraction of 73 ± 12 %. The pulse profile is characterized by two peaks phase separated by $\Delta\phi = 0.47 \pm 0.05$. The pulsed spectrum is best described by a power-law of photon index 0.61 ± 0.32 with an unabsorbed (2–10 keV) X-ray flux of 4.1×10^{-13} erg cm⁻² s⁻¹ implying a luminosity of $L_x = 1.3 \times 10^{32} \Theta (d/5.7 \text{ kpc})^2$ erg s⁻¹ and an X-ray efficiency of $L_x/\dot{E} = 4.8 \times 10^{-4} \Theta (d/5.7 \text{ kpc})^2$ where Θ is the solid angle spanned by the emission beam.

8.1. Introduction

PSR J0218+4232 is a 2.3 ms pulsar in a two day orbit around a $\sim 0.2 M_\odot$ white dwarf companion (Navarro et al. 1995) with a period derivative of $\dot{P} = 8 \times 10^{-20}$ s s⁻¹. The pulsar has a spin-down energy of $\dot{E} = 2.5 \times 10^{35}$ erg s⁻¹, a dipolar magnetic field component at the star surface of $B_\perp = 4.3 \times 10^8$ G and a spin-down age of $\leq 4.6 \times 10^8$ years. The pulsar distance inferred from its dispersion measure and from the electron density model of Taylor & Cordes (1993) is ≥ 5.7 kpc. A detection of the companion star at optical wavelength was reported recently by Van Kerkwijk (1996).

Soft X-ray emission from the pulsar was first detected by Verbunt et al. (1996) using the ROSAT HRI. A follow-up observation confirmed the detection and discovered X-ray pulsation at a significance of about 5σ using 200 HRI counts (Kuiper et al. 1998). The X-ray pulse profile deduced from those data is characterized by a sharp main pulse with an indication of a second peak at a phase separation of $\Delta\phi \sim 0.47$. The pulsed fraction inferred from the ROSAT HRI data is 37 ± 13 %. Furthermore, Kuiper et al. (1998) show that the measured large DC component is consistent with a $\sim 14''$ diameter compact nebula surrounding the pulsar, but con-

firmation is required. However, it is interesting to note that also in the radio domain the source exhibits an unusually high DC component of ~ 50 % (Navarro et al. 1995). The HRI provides no spectral information and the number of counts recorded in a serendipitous off-axis PSPC observation does not allow spectral modeling.

Also ASCA detected this source, however, the observation was too short: no pulsation could be seen, and a spectral fit with a power-law photon index of 1.6 ± 0.6 could only be made to the weak total excess (Kawai & Saito 1999). Therefore, no detailed spectral information on the pulsed X-ray emission was available prior to the BeppoSAX observation reported in this paper (see Becker & Trümper 1999 for a review of the X-ray properties of millisecond pulsars).

Noting the spatial coincidence of PSR J0218+4232 with the EGRET source 2EG J0220+4228, Verbunt et al. (1996) tentatively identified the pulsar with the high-energy γ -ray source. Using some additional EGRET observations, and applying a combination of spatial and timing analysis, Kuiper et al. (1999) conclude that 2EG J0220+4228 is probably a multiple source: between 0.1 and 1 GeV PSR J0218+4232 is the most likely counterpart, and above 1 GeV the bright BL Lac 3C 66A is the best candidate counterpart. The third EGRET catalog (Hartman et al. 1999), which is based on more viewing periods than the 2EG catalog, identifies 3EG J0222+4253 (2EG J0220+4228) with 3C 66A, rather than with the ms-pulsar. However, in a note on this source, they indicate that the identification with 3C 66A stems from the catalog position based on the > 1 GeV map. Furthermore, they confirm that for lower energies (100-300 MeV) the EGRET map is consistent with all the source flux coming from the pulsar, 3C 66A being statistically excluded.

In this paper we present the results of a BeppoSAX observation of PSR J0218+4232 which, for the first time, provides detailed information on the pulsar's temporal and spectral emission properties across a wide band from 1 to 10 keV.

8.2. Observation

PSR J0218+4232 was observed on January 1999 14–16 by the Narrow Field Instruments (NFIs) aboard BeppoSAX satellite (Boella et al. 1997a). We report in this paper only results from data collected with the MECS instrument (Boella et al. 1997b), sensitive in the energy range 1–10 keV; the net exposure time was 82 795 s. The LECS instrument (0.1–10 keV; Parmar et al. 1997) observed the source for a much shorter time due to the constraint on operating only during spacecraft night. The HPGSPC (4–60 keV; Manzo et al. 1997) was not working during the observation. A signal detected with the PDS (13–200 keV; Frontera et al. 1997) will be shortly discussed in Sect. 8.5. No pulsed signals have been detected in the LECS and PDS data.

During the observation only two of the three MECS detectors were operating (MECS2 and MECS3). MECS has a field of view of $56'$ and an angular resolution of about $1'2$ at 6 keV. During the observation of PSR J0218+4232 the instrument operated in direct mode, transmitting to ground information on each individual photon. Standard procedures and selection criteria were applied on the observation data to avoid the South Atlantic Anomaly, solar, bright Earth and particle contaminations¹. Event reduction has been performed using the SAXDAS v.2.0.0 package.

8.3. Spatial analysis

A 100 ks ROSAT HRI (0.1–2.4 keV) observation of PSR J0218+4232 (see Kuiper et al. 1998) revealed 7 X-ray sources within a radius of $\sim 5'$ around our target (see Fig. 8.1). Given the extended tails of the MECS Point-Spread Function (PSF), accurate spatial analysis is required to separate the signal of PSR J0218+4232 from that of any neighbouring sources. We used a Maximum Likelihood approach in searching for individual sources on top of a background model, as well as for analyzing simultaneously several sources and a background model.

The search is applied on various equidistant trial positions within a selected part of the instrument field of view, where it checks for the presence of a source taking into account the Poissonian nature of the data. Maximum Likelihood Ratio (MLR) tests are performed describing in the zero \mathcal{H}_0 hypothesis the 2-d event distribution in terms of a flat background model only, while in the alternative \mathcal{H}_1 hypothesis the data is described in terms of a point source at the trial position and a flat background model (see e.g. Kuiper et al. 1998 for a more detailed description).

The improvement in the likelihood \mathcal{L} between \mathcal{H}_0 and \mathcal{H}_1 computed from the quantity $Q = -2 \ln(\mathcal{L}^{\mathcal{H}_0} / \mathcal{L}^{\mathcal{H}_1})$ yields simultaneously the detection significance and strength of the source. The probability distribution of Q is that of a χ^2 for $n_1 - n_0$ degree of freedom (d.o.f.) where n_0 and n_1 are the d.o.f. for the \mathcal{H}_0 and \mathcal{H}_1 hypotheses, respectively. In searching for sources $n_1 - n_0 = 3$, while in a detection test of a known source $n_1 - n_0 = 1$. The distribution of Q as a function of trial position is the MLR–map.

We applied the above approach to the MECS data without energy selection allowing for maximum source statistics. We used an energy averaged PSF assuming a power–law spectral shape of index 1.5, given by the following expression:

$$PSF(x, y) =$$

Table 8.1. Ephemeris of PSR J0218+4232

Parameter	Value
Right Ascension (J2000)	02 ^h 18 ^m 6 ^s .350
Declination (J2000)	42° 32' 17".44
Epoch validity start/end (MJD)	49092 – 50900
Frequency	430.4610674213 Hz
Frequency derivative	-1.4342×10^{-14} Hz s ⁻¹
Epoch of the period (MJD)	49996.000000023
Orbital period	175292.3020 s
$a_p \sin i$	1.98444 (lt-s)
Eccentricity	0
Longitude of periastron	0
Time of ascending node (MJD)	49996.637640

$$\frac{\int_0^\infty E^{-1.5} \cdot (S_2(E) + S_3(E)) \cdot PSF(x, y | E) \cdot dE}{\int_0^\infty E^{-1.5} \cdot (S_2(E) + S_3(E)) \cdot dE}, \quad (1)$$

where $S_2(E)$ and $S_3(E)$ are the sensitive areas of the two operating MECS units. The $PSF(x, y | E)$ is modelled using the parametric form given in Boella et al. (1997b). Furthermore, we investigated the impact of the assumed power–law index on the MLR results and found that this is negligible, as expected by the moderate dependence on energy of the PSF.

The resulting MLR map/image is shown in Fig. 8.1a. The maximum value in this figure ($> 21 \sigma$) is reached at a position consistent with that determined by the ROSAT HRI for PSR J0218+4232 (indicated by a star symbol). It is, however, evident that several of the sources detected by ROSAT below 2.4 keV (indicated by filled triangles) contribute significantly to the extended excess. We can show this better, by repeating the search for sources on top of a flat background model *and* a point source at the pulsar position (effectively “subtracting” the counts from PSR J0218+4232 from Fig. 8.1a). The remaining extended feature (Fig. 8.1b) clearly follows the distribution of the nearby sources, reaching detection significances up to about 10σ . Figure 8.1c shows the MLR map resulting from a point source search on top of a flat background and 9 sources fixed at the ROSAT HRI source positions: no significant residual emission remains. The total number of counts assigned by this analysis to PSR J0218+4232 is 403 ± 29 .

The position of PSR J0218+4232 determined from the MLR map shown in Fig. 8.1a is shifted by $\sim 23''$ with respect to the radio position, well within the systematic uncertainty of the accuracy of the BeppoSAX pointing reconstruction².

The spatial analysis allows also the evaluation of an optimum event extraction radius by computing the Signal-to-Noise ratio as a function of radial distance r from the source position. Taking as source radial profile the PSF, and as noise the *measured* radial count distribution, we obtained the value $r = 100''$. Note that none of the nearby sources fall within this radius. The selected region contains 62 % (250 counts) of the MECS source signal; the number of background events in the same area is 92 with a contribution from the neighbouring sources of 12 counts.

¹ see <http://www.sdc.asi.it/software/cookbook> as a reference about the data analysis software and reduction procedures.

² see <http://www.sdc.asi.it/software/cookbook/attitude.html>

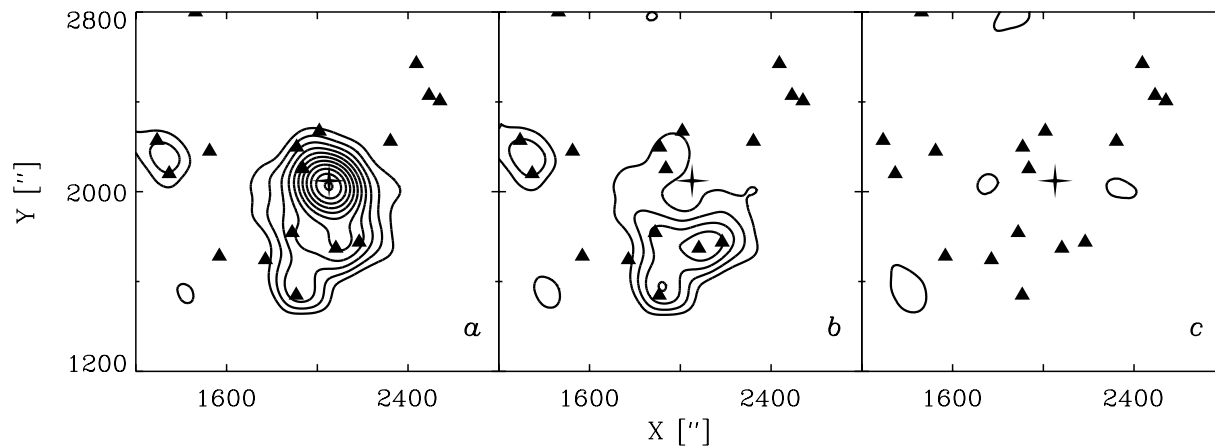


Fig. 8.1. Maximum Likelihood Ratio maps in instrumental coordinates (X ["], Y ["]) using all MECS data (~ 1 – 10 keV) for the sky region around PSR J0218+4232 (star). The contours start at a value of 3σ source detection significance with a stepsize of 2σ (for 1 d.o.f.) or equivalently at Q values (see text) of 9, 25, 49, The positions of all sources detected by the ROSAT HRI observation below 2.4 keV are indicated by filled triangles. *a*) Evidence for sources above a flat background showing PSR J0218+4232 ($\sim 21\sigma$) on top of an extended excess. *b*) Like *a*), but PSR J0218+4232 has now been “subtracted”. *c*) No significant excesses are left when 9 ROSAT sources are added to the background model.

8.4. Timing analysis

The arrival times of all selected events were converted to the Solar System Barycentric Frame using BARYCONV³, then folded according to the radio ephemeris (see Table 8.1), correcting for the pulsar binary motion. The pulse phase distribution deviates from a statistically flat distribution at a 6.8σ level applying a Z^2 test (Buccheri et al. 1983) using the first two harmonics.

The MECS timing resolution is dominated by the precision of the OBT (On Board Time)-UTC conversion: an inspection of the residuals of the OBT-UTC linear fit reveals a systematic scatter with an rms of the order of ~ 0.2 ms that cannot be reduced by fitting higher order polynomials. This effect corresponds to an uncertainty in the photon phases of 0.087.

The light curve resulting from folding all MECS events (1–10 keV) with a phase resolution of 18 bins (~ 0.13 ms) is shown in Fig. 8.2 (top panel): two cycles are plotted for clarity. The MECS background level, indicated with a grey band ($\pm 1\sigma$ errors), is determined in the spatial analysis and therefore includes the contributions from the neighbouring sources. In the same figure (bottom panel) the 610 MHz profile as derived by Stairs et al. (1999) is also presented. The phase relation between the two profiles is unknown for the time being: they have been arbitrarily aligned. Notice that, like in the radio light curve, the MECS profile is not simple: it has a prominent double peak structure with a relative phase separation (centre to centre) of 0.47 ± 0.05 , confirming the value derived by Kuiper et al. (1998) from ROSAT data below 2.4 keV.

The phase histograms for 1.6–4 keV and 4–10 keV are shown respectively in the middle and bottom panels of Fig. 8.3. The ROSAT (0.1–2.4 keV) profile (Kuiper et al. 1998), shifted in phase to obtain the highest peak coincident with the most significant one in the MECS softer light curve (middle panel), is also shown for comparison in the top panel of Fig. 8.3. These profiles clearly show a change of the relative peak intensities. The peak at phase 0.8 is stronger in the low energy histograms (top and middle pan-

els), while that at phase 0.3 is more prominent at high energies (bottom panel).

The structure measured in the MECS light curves of two peaks separated by narrow valleys and the uncertainty due to the OBT-UTC conversion residuals make it difficult to establish an unpulsed interval: slightly different values could affect the unpulsed level. Notice, moreover, that while in the ROSAT profile a DC component is apparent above the background level, the same does not hold for the 4–10 keV profile, where the background level is consistent with those measured in the valleys of the light curve. In the intermediate energy profile, at face value, there might be some evidence of a DC component but not as high as in the ROSAT profile. Such effect could be due to the presence of a quite soft unpulsed emission. In an attempt to quantify the evidence for a DC component, we applied the bootstrap method proposed by Swanepoel et al. (1996), which allows to estimate the DC level, and therefore also the pulsed fraction, working directly on the phases of individual photons. However, in the available form, this method is able to find only one unpulsed interval and cannot account for systematic errors. One should therefore realize that the quoted errors on the calculated parameters are only statistical. Using this algorithm we found, for the whole MECS energy band, an unpulsed interval of 0.47–0.61 and a corresponding pulsed fraction of 0.73 ± 0.12 (1σ error). Notice that the average count level in the interval -0.08 – 0.15 is statistically not different from that measured in the former interval. The resulting DC-fractions for the three bands of Fig. 8.3 are shown in Fig. 8.4. The decrease with energy is clearly visible, but the error bars are large and the trend deviates only at the 2.4σ level from a flat distribution. Given the large error bars and the systematic uncertainties, we did not derive a detailed spectrum of the DC component.

The relatively high scatter in the residuals of our timing solution (up to ~ 0.2 ms) does not allow to determine accurately the intrinsic widths of the two pulses. The total scatter in the event arrival times at the SSB might even be consistent with the measured width of P1 in Fig. 8.2.

³ see <http://www.sdc.asi.it/software/saxdas/baryconv.html>

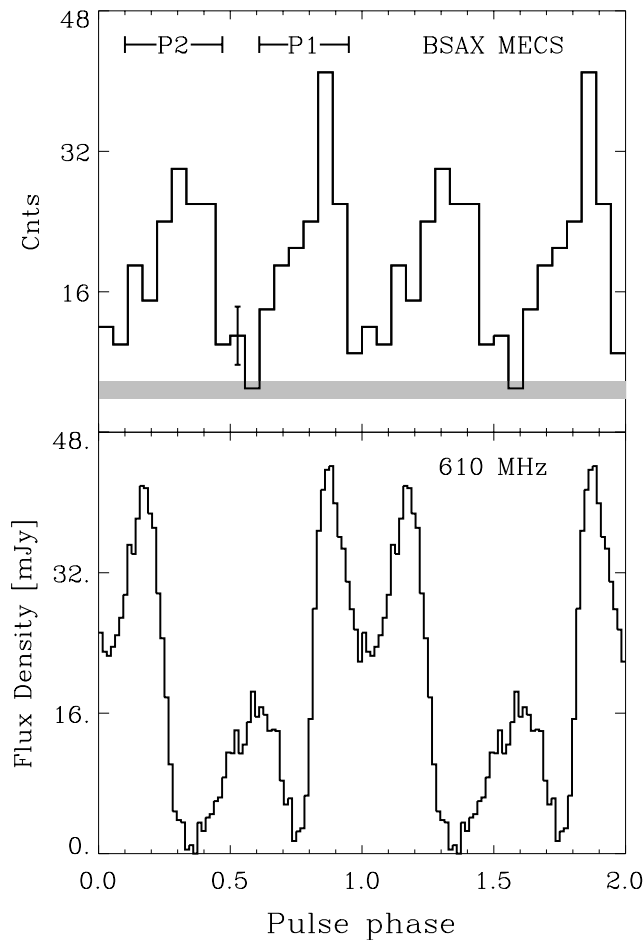


Fig. 8.2. PSR J0218+4232 light curve in the 1–10 keV range as observed by the MECS (top panel) and at 610 MHz (bottom panel, Stairs et al. 1999). In the top panel a typical statistical 1σ error bar is shown and the MECS background level as determined in the spatial analysis is indicated as a grey band, representing the $\pm 1\sigma$ widths. The two horizontal bars above the MECS profile indicate the definitions of the phase intervals for the two peaks, Peak 1 (P1) and Peak 2 (P2), as explained in the text. The alignment between the two curves is arbitrary.

We defined the phase intervals containing the two pulses as follows: Peak 1 (P1) phase interval 0.61–0.95 and Peak 2 (P2) 0.10–0.47, where P1 is identified with the obvious ROSAT peak and appears to have a softer spectrum than P2. The statistical significance of the suggested change in morphology of the phase histogram with energy can be evaluated by the P2/P1 ratio. This ratio, computed in the energy bands 1.6–4 keV and 4–10 keV after background subtraction, is shown in Fig. 8.5. The ROSAT point derived from the data of Kuiper et al. (1998), indicated by a filled circle, is evaluated using the same phase definitions. Including the ROSAT point, a correlation of P2/P1 with energy is evident, but the statistical significance is only 2σ , and confirmation is needed.

8.5. Spectral analysis

Spectral fits were performed on the background subtracted MECS data binned logarithmically after checking that each single energy

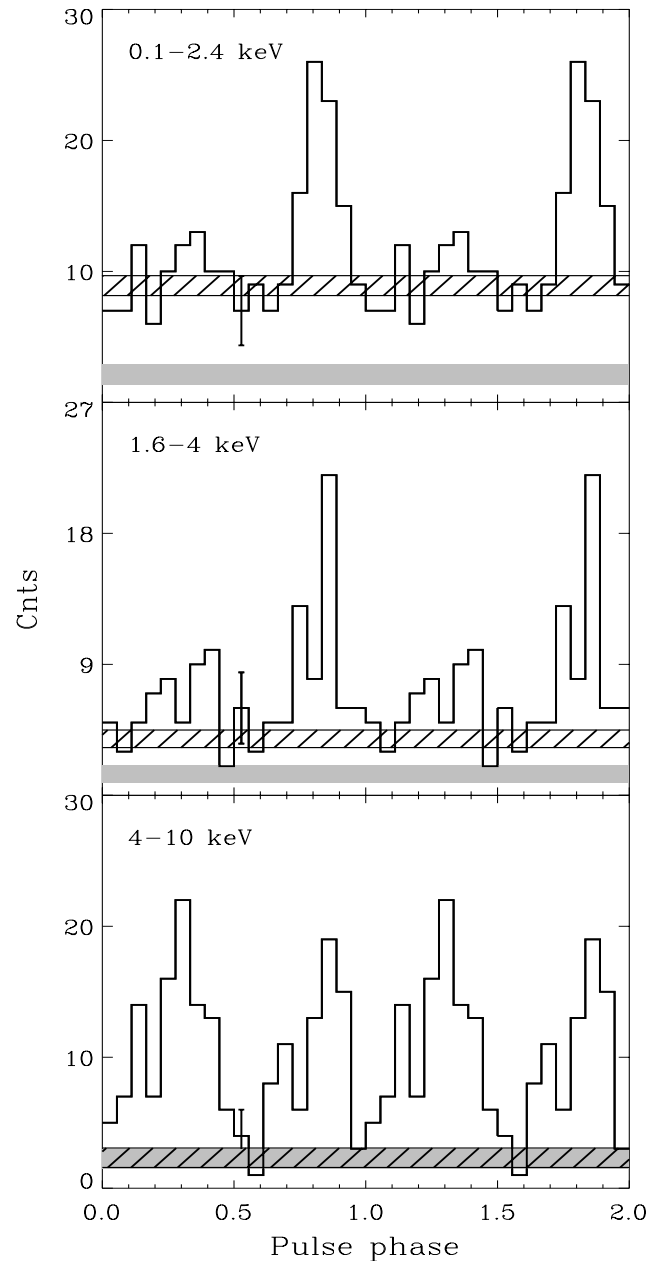


Fig. 8.3. PSR J0218+4232 phase histograms: energy range 0.1–2.4 keV from the ROSAT HRI (Kuiper et al. 1998); energy ranges 1.6–4 keV and 4–10 keV from the BeppoSAX MECS (this work). Note the increase of the P2 peak strength with respect to P1 with energy. The hatched area represents the unpulsed level ($\pm 1\sigma$) determined in a bootstrapping analysis of the phase histogram, while the grey area represents the background level with 1σ errors determined in the spatial analysis.

channel contains at least 20 photons. The N_H was fixed to the value of $5 \times 10^{20} \text{ cm}^{-2}$ (see Verbunt et al. 1996). We fitted the total pulsed spectrum, i.e. the excess counts above the unpulsed level in the phase histogram, with a power-law model, taking into account the energy dependent interstellar absorption. The resulting photon index is $\alpha = 0.61 \pm 0.32$, with a 2–10 keV flux $F = 4.1 \times 10^{-13}$

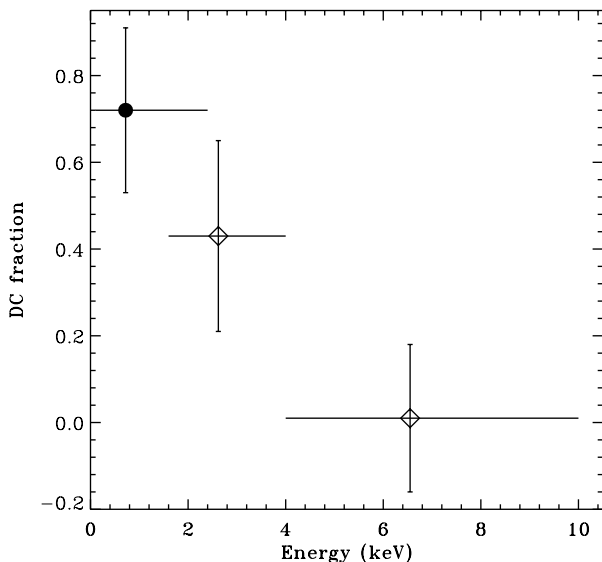


Fig. 8.4. The DC-fraction as a function of energy. The ROSAT point (filled circle) was derived using the same width of the unpulsed interval as obtained for the whole MECS range.

$\text{erg cm}^{-2} \text{ s}^{-1}$, and a reduced χ_r^2 of 0.7 (3 dof). A fit with a black body spectral distribution gives $kT = 2.3 \pm 0.5$ keV, with a $\chi_r^2 = 1.4$ (3 dof). Both the χ^2 values are acceptable, the black body temperature $T = 2.6 \times 10^7$ K, however, is quite higher than the values measured for the thermal components of other pulsars that typically does not exceed $\sim 5 \times 10^6$ K (Greiveldinger et al. 1996, Becker & Trümper 1997, 1999). Fig. 8.6 also shows the spectra for the pulses P1 and P2 separately, using the same energy bins as for the total pulsed spectrum. We fitted again power-law models for each of the spectra, but the low statistics result in large errors in the estimated parameters. The measured spectral indices of P1 and P2 are 0.84 ± 0.35 and 0.42 ± 0.36 respectively, in agreement with the trend seen in the P2/P1 ratio.

Finally, we determined the total spectrum (pulsed plus DC) applying the Maximum Likelihood approach to the spatial distributions in smaller energy intervals (see also Fig. 8.6). The fit with a power-law gives a photon spectral index $\alpha = 0.94 \pm 0.22$ with a 2–10 keV flux $F = 4.3 \times 10^{-13} \text{ erg cm}^{-2} \text{ s}^{-1}$, about 10 % higher than the pulsed value given above, and a reduced χ_r^2 of 0.56 (8 dof).

Given the hard spectra found above, we also analysed the PDS data to investigate whether there was any signal from PSR J0218+4232 at higher energies, even though an extrapolation of the total spectrum measured in the MECS to the PDS range predicts a flux well below the PDS sensitivity threshold. Indeed, no pulsed signal was found, but in the 17–25 keV band a DC signal was detected at the $\sim 4 \sigma$ level. Moreover the fit of MECS+PDS spectra with a power-law plus a constant factor to take into account the intercalibration uncertainties between the two instruments leads to a spectral index of 1.4 and to a value for the constant ~ 8 , well above the expected range of variability (0.7–1, Cusumano et al. 2000). Furthermore, the PDS light curve shows that most of the source counts are concentrated in the first half of the observation. Therefore, it is likely that we observed a variable source in the large field of view of the PDS collimators ($1^\circ 3 \times 1^\circ 3$

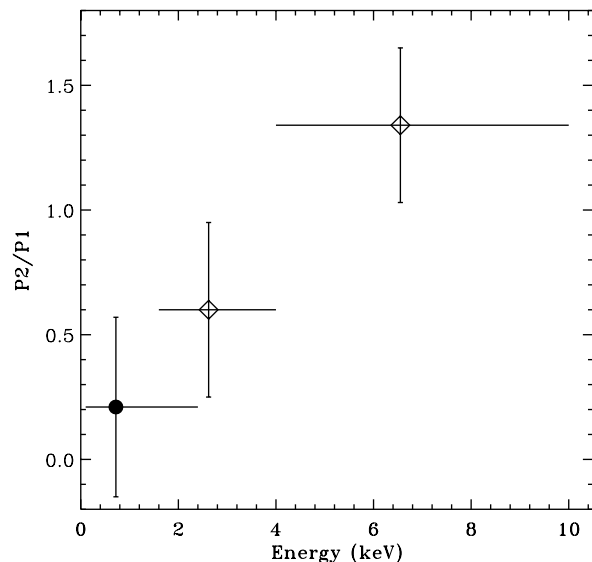


Fig. 8.5. The energy dependence of P2/P1, according to the phase interval defined in the text. The ROSAT point is indicated by a filled circle.

FWHM). Note that there are several sources within a 3° region in the soft X-ray catalogs, but none in the hard X-ray ones.

8.6. Discussion

The BeppoSAX observation of PSR J0218+4232 provided the first detection of pulsed emission from this millisecond pulsar for energies up to 10 keV. The source shows a double peaked pulse shape with a remarkably flat (photon index ~ 0.6) spectral distribution and indications that the peak intensity ratio depends on photon energy. In particular, the P2 peak, which is not prominent in the ROSAT low energy phase histogram, becomes the dominant feature above 5 keV.

Our fit for a black body spectrum gives the quite high value of 2.6×10^7 K for the temperature of the emitting region. If we assume that the radiation comes from the pulsar polar cap, heated, for instance, by the interactions with starwards moving high energy particles, we can compute the expected luminosity. The polar cap area of PSR J0218+4232, defined as usual by the open field lines, is of the order of $A \simeq 2\pi R^2 [1 - \sqrt{(1 - R\Omega/c)}] = 2.9 \times 10^{11} \text{ cm}^2$, where R is the stellar radius; from the Stefan's law we obtain a bolometric luminosity of $5 \times 10^{36} \text{ erg s}^{-1}$, a value that must be doubled if the other cap is taken into account. Such luminosity is several orders of magnitude higher than that derived from the phase averaged flux $L_x = 1.3 \times 10^{32} \Theta (d/5.7 \text{ kpc})^2 \text{ erg s}^{-1}$ (corresponding to an X-ray efficiency of $L_x/\dot{E} = 4.8 \times 10^{-4} \Theta (d/5.7 \text{ kpc})^2$) where Θ is the solid angle spanned by the emission beam. It is moreover significantly greater than the spin-down energy loss rate. This inconsistency could be solved with the assumption that the emission spot covers a very small fraction, of the order of about 10^{-4} or even less, of the whole cap. The flux of heating particles should be then collimated within a very narrow angle of ~ 0.2 or smaller. Furthermore, the heating flux into the two polar caps must be different to explain the spectral

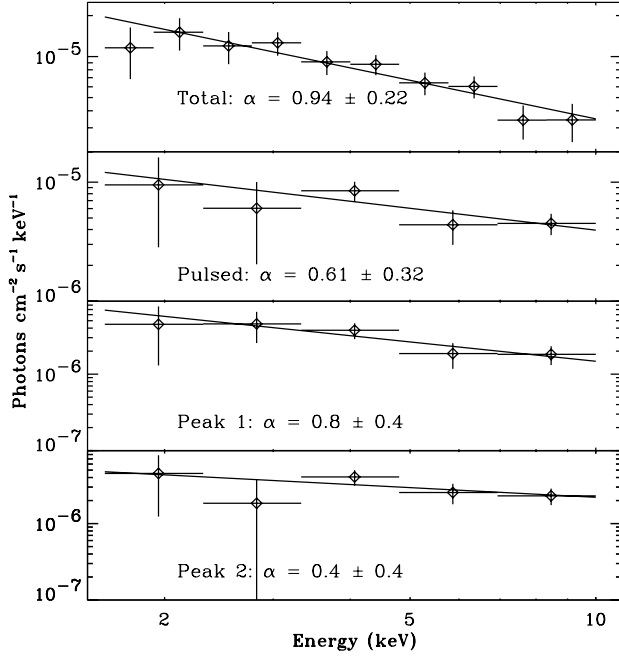


Fig. 8.6. PSR J0218+4232 spectra as detected by the MECS. The lines represent the power-law used as fitting model

difference of the two peaks. A non-thermal origin of the X-ray emission seems therefore more convincing.

The variation of the peak ratio with energy recalls a similar effect observed for the Crab pulsar (see, for instance, the recent BeppoSAX data described by Mineo et al. 1997). The possibility of detecting such effect could be due to a particular orientation among the rotation and magnetic axes and the line of sight. The Crab has an orthogonal alignment, however, Navarro et al. (1995), on the basis of the radio pulse shape, inferred for PSR J0218+4232 a nearly aligned rotator. The same conclusion is reached by Stairs et al. (1999) who analyzed high-precision, coherently-dispersed polarization profiles at the two frequencies of 410 and 610 MHz. Their Rotating Vector Model (RVM) fits support the classification of PSR J0218+4232 as a nearly aligned rotator with magnetic inclination consistent with 0° , namely (8 ± 11) deg at 410 MHz and (8 ± 15) at 610 MHz. Unfortunately, the impact angle parameters for their RVM fits have large uncertainties and therefore the line-of-sight inclination is unconstrained.

The Crab-like double pulse X-ray profile of PSR J0218+4232 and its hard non-thermal spectrum suggests a common magnetospheric origin of the high-energy emission. The comparison with Crab is additionally enforced by the similar values of the magnetic field at the light cylinder, as already pointed out by Kuiper et al. (1998) and Kawai & Saito (1999). This follows directly from the classical assumption that the pulsar braking is entirely due to the Poynting flux at the light cylinder, independently of the actual structure of the magnetic field in the magnetosphere:

$$B_L \simeq 4\pi^2 \left(\frac{I}{c^3}\right)^{\frac{1}{2}} P^{-\frac{5}{2}} \dot{P}^{\frac{1}{2}}, \quad (2)$$

where I is the moment of inertia. For the two pulsars we obtain then:

$$B_L = B_{L,Cr} \left(\frac{I}{I_{Cr}}\right)^{\frac{1}{2}} \left(\frac{P}{P_{Cr}}\right)^{-\frac{5}{2}} \left(\frac{\dot{P}}{\dot{P}_{Cr}}\right)^{\frac{1}{2}}, \quad (3)$$

where the suffix Cr is referred to Crab. Assuming that the moments of inertia of the two pulsars are equal, we found $B_L \simeq \frac{1}{3} B_{L,Cr} \simeq 3 \times 10^5$ Gauss.

The nature of the non-thermal mechanism responsible for the X-ray emission is still unclear. A possibility is that X-ray photons are produced by curvature radiation from relativistic electrons moving outwards along the field lines in proximity of the light cylinder. The Lorentz factor of these particles to radiate photons of frequency ν is given by

$$\gamma = \left(\frac{4\pi \nu \rho}{3c}\right)^{\frac{1}{3}}, \quad (4)$$

where $\rho \simeq c/(3\Omega)$ is the curvature radius of the last closed line near the light cylinder in a dipole field. For $\nu = 10^{18}$ Hz, corresponding to ~ 4 keV, we have:

$$\gamma \simeq \left(\frac{2}{9} \nu P\right)^{\frac{1}{3}} = 8 \times 10^4. \quad (5)$$

The radiative life time of the electrons is long enough to allow them to reach the light cylinder, namely:

$$\tau_c = \frac{\gamma}{|d\gamma/dt|} = \frac{9}{8\pi} \frac{\rho}{r_e \nu} = 2 \times 10^{21} \frac{P}{\nu}, \quad (6)$$

where r_e is the classical radius of the electron; for $P = 2.3$ ms and $\nu = 10^{18}$ Hz we have $\tau_c \simeq 5$ s. These electrons could be accelerated either in the outer gaps or above the polar caps. In the latter case, we expect that a copious number of electron-positron pairs will reach, after suffering radiation losses, the light cylinder with energy high enough for X-ray emission.

An origin of the high-energy X-rays in a narrow outer gap can also explain the narrow profile (intrinsically < 0.04 phase; Kuiper et al. 1998) measured in the ROSAT light curve, as well as the double peak profile, e.g. for the wide fan-beam geometry proposed by Romani (1996). However, an additional constraint is needed: the length of the gap over which the hard X-rays are produced should be small. In fact, the very strong curvature of the magnetic field lines would produce a broader pulse profile for a long gap. However, as Ho (1989) pointed out, strongly curved magnetic field lines, as in millisecond pulsars, enhance the production of non-thermal emission, allowing outer gaps shorter than those of normal radio pulsars.

According Kuiper et al. (1999), PSR J0218+4232 is the most likely counterpart of the high-energy EGRET source 2EG J0220+4232 / 3EG J0222+4253 for energies between 100 MeV and 1 GeV. This would suggest a cut-off energy at least four orders of magnitude higher than the maximum energy of 10 keV to which the BeppoSAX data showed evidence for the detection of this source. Further high sensitivity observations at hard X-ray energies up to the high-energy γ -rays are therefore particularly relevant for the understanding of the physics of this and other millisecond pulsars.

Acknowledgements. TM acknowledges G.Vizzini for his technical support on data handling.

References

Becker W., Trümper J., 1997, A&A 326, 682

Becker W., Trümper J., 1999, A&A 341, 803
Boella G., Butler R.C., Perola G.C., et al., 1997a, A&AS 122, 299
Boella G., Chiappetti L., Conti G., et al., 1997b, A&AS 122, 327
Buccheri R., Bennett K., Bignami G., et al., 1983, A&A 128, 367
Cusumano G., Mineo T., Guainazzi M., et al., 2000, in preparation
Frontera F., Costa E., Dal Fiume D., et al., 1997, A&AS 122, 357
Greiveldinger C., Camerini U., Fry W., et al., 1996, ApJL 465, 35
Hartman R.C., Bertsch D.L., Bloom S.D., et al., 1999, ApJS, in
press
Ho C., 1989, ApJ 342, 396
Kawai N., Saito Y., 1999, 3rd INTEGRAL Workshop "The Ex-
treme Universe", Sept. 1998, Taormina, Italy, in press
Kuiper L., Hermsen W., Verbunt F., Belloni T., 1998, A&A 336,
545
Kuiper L., Hermsen W., Verbunt F., et al., 1999, 3rd INTEGRAL
Workshop "The Extreme Universe", Sept. 1998, Taormina,
Italy, in press
Manzo G., Giarusso S., Santangelo A., et al., 1997, A&AS 122,
341
Mineo T., Cusumano G., Segreto A., et al., 1997, A&A 327, L21
Navarro J., de Bruyn A.G., Frail D.A., Kulkarni S.R., Lyne A.G.,
1995, ApJ 455, L55
Parmar A.N., Martin D.D.E., Bavdaz M., et al., 1997, A&AS 122,
309
Romani R.W., 1996, ApJ 470, 469
Stairs I.H., Thorsett S.E., Camilo F., 1999, ApJS 123, 627
Swanepoel J.W.H., de Beer C.F., Loots H., 1996, ApJ 467, 261
Taylor J.H., Cordes J.M., 1993, ApJ 411, 674
Van Kerkwijk M.H., 1996, Proc. IAU Coll. 160, 489
Verbunt F., Kuiper L., Belloni T., et al., 1996, A&A 311, L9

Chapter 9

The likely detection of pulsed high-energy γ -ray emission from millisecond pulsar PSR J0218+4232

L. Kuiper¹, W. Hermsen¹, F. Verbunt², D.J. Thompson³, I. H. Stairs⁴, A. G. Lyne⁴, M. S. Strickman⁵, and G. Cusumano⁶

¹ SRON-Utrecht, Sorbonnelaan 2, NL-3584 CA Utrecht, The Netherlands

² Astronomical Institute, Utrecht University, NL-3508 TA Utrecht, The Netherlands

³ Code 661, Laboratory for High Energy Astrophysics, NASA Goddard Space Flight Center, Greenbelt, MD 20771, United States of America

⁴ University of Manchester, Jodrell Bank, Macclesfield SK11 9DL, United Kingdom

⁵ Naval Research Laboratory, Washington DC, United States of America

⁶ Istituto di Fisica Cosmica ed Applicazioni all'Informatica CNR, Via U. La Malfa 153, I-90146, Palermo, Italy

Astron. Astrophys. 359, 615-626 (2000)

Abstract. We report circumstantial evidence for the first detection of pulsed high-energy γ -ray emission from a millisecond pulsar, PSR J0218+4232, using data collected with the Energetic Gamma Ray Experiment (EGRET) on board the Compton Gamma Ray Observatory (CGRO). The EGRET source 3EG J0222+4253 is shown to be spatially consistent with PSR J0218+4232 for the energy range 100 - 300 MeV. Above 1 GeV the nearby BL Lac 3C 66A is the evident counterpart, and between 300 MeV and 1 GeV both sources contribute to the γ -ray excess. Folding the 100-1000 MeV photons with an accurate radio ephemeris of PSR J0218+4232 yields a double peaked pulse profile with a $\sim 3.5\sigma$ modulation significance and with a peak separation of ~ 0.45 similar to the 0.1-10 keV pulse profile. A comparison in absolute phase with the 610 MHz radio profile shows alignment of the γ -ray pulses with two of three radio pulses. The luminosity of the pulsed emission (0.1-1 GeV) amounts $L_\gamma = 1.64 \cdot 10^{34} \cdot (\Delta\Omega/1 \text{ sr}) \cdot (d/5.7 \text{ kpc})^2 \text{ erg s}^{-1}$ which is $\sim 7\%$ of the pulsar's total spin-down luminosity. The similarity of the X-ray and γ -ray pulse profile shapes of PSR J0218+4232, and the apparent alignment of the γ -ray pulses with two radio pulses at 610 MHz, bears resemblance to the well-known picture for the Crab pulsar. This similarity, and the fact that PSR J0218+4232 is one of three millisecond pulsars (the others are PSR B1821-24 and PSR B1937+21) which exhibit very hard, highly non-thermal, high-luminosity X-ray emission in narrow pulses led us to discuss these millisecond pulsars as a class, noting that each of these has a magnetic field strength near the light cylinder comparable to that for the Crab. None of the current models for γ -ray emission from radio pulsars can explain the γ -ray spectrum and luminosity of PSR J0218+4232.

9.1. Introduction

Pulsed high-energy emission from millisecond (ms) pulsars has so far been detected at X-ray energies below ~ 10 keV for only five pulsars: PSR J0437-4715 (Becker & Trümper 1993), PSR J2124-3358 (Becker & Trümper 1999), PSR B1821-24 (Saito et al. 1997), PSR J0218+4232 (Kuiper et al. 1998) and PSR

B1937+21 (Takahashi et al. 1999). The first two exhibit broad X-ray pulses, have soft spectra and relatively low luminosities in the X-ray window, about 3 orders of magnitude lower than derived for the latter three ($L_X^{1-10 \text{ keV}} \sim 10^{32} \text{ erg s}^{-1}$ assuming emission in a 1 sr beam). In addition to the higher luminosity, these have very narrow X-ray pulses (intrinsically $\sim 100\mu\text{s}$ or narrower) and hard power-law shape spectra measured up to ~ 10 keV (Saito et al. 1997, Mineo et al. 2000, Takahashi et al. 1999, respectively), the two hardest spectra having indices as hard as ~ -0.65 . This short observational summary suggests that this small sample can be divided in two distinct classes of ms pulsars: *Class I*, ms pulsars with soft, low-luminosity X-ray emission in broad pulses; *Class II*, with highly non-thermal, high-luminosity X-ray emission in narrow pulses.

Millisecond pulsars not only differ from normal radio pulsars in that their spin periods are 1 to 2 orders of magnitude shorter, reducing correspondingly their light cylinder radii, but particularly their surface magnetic field strengths are 3 to 4 orders of magnitude weaker. Nevertheless, Bhattacharya & Srinivasan (1991) and Sturmer & Dermer (1994) showed that both of the competing classes of models for the production of γ -rays (polar cap and outer gap models) predict the production of detectable non-thermal emission up to the high-energy γ -rays for a sizable number of ms pulsars. An early systematic search for pulsed high-energy γ -ray emission from ms pulsars rendered, however, only upper limits (Fierro 1995). In this paper we will present circumstantial evidence for the first detection of pulsed high-energy gamma-ray emission from a *Class II* ms pulsar: PSR J0218+4232.

PSR J0218+4232 is a 2.3 ms pulsar in a two day orbit around a low mass ($\sim 0.2 M_\odot$) white dwarf companion (Navarro et al. 1995; van Kerkwijk 1997). The dipolar perpendicular magnetic field strength (B_\perp) at the surface of the neutron star is estimated to be 4.3×10^8 G and the spin-down age is $\sim 4.6 \times 10^8$ years. The spin-down energy loss L_{sd} of the pulsar amounts $\sim 2.5 \times 10^{35} \text{ erg s}^{-1}$. The pulsar distance inferred from its dispersion measure and from the electron density model of Taylor & Cordes (1993) is ≥ 5.7 kpc.

Soft X-ray emission from the pulsar was first detected by Verbunt et al. (1996) in a 20 ks ROSAT HRI observation. In a 100

ks follow-up observation X-ray pulsations were discovered at a significance of about 5σ (Kuiper et al. 1998). The X-ray pulse profile is characterized by a sharp main pulse with an indication for a second peak at a phase separation of $\Delta\phi \sim 0.47$. The pulsed fraction inferred from the ROSAT HRI (0.1-2.4 keV) data is $37 \pm 13\%$. It is interesting to note that also in the radio domain the source exhibits an unusually high unpulsed component of $\sim 50\%$ (Navarro et al. 1995).

The ROSAT HRI provides no spectral information and the number of counts recorded in a far off-axis PSPC observation does not allow spectral modeling in the soft X-ray regime (0.1-2.4 keV). Also ASCA detected this source, however, the observation was too short: no pulsation could be detected, and a spectral fit to the weak total excess resulted in a power-law photon index of -1.6 ± 0.6 (Kawai & Saito 1999).

The spectral information for PSR J0218+4232 improved enormously analyzing the data from a 83 ks BeppoSAX MECS (1.6-10 keV) observation performed early 1999 (Mineo et al. 2000). Pulsed emission was detected up to 10 keV, the pulse profile clearly showing two peaks at the same phase separation of 0.47 which we reported earlier combining ROSAT HRI and PSPC observations (Kuiper et al. 1998). The BeppoSAX MECS observation reveals that PSR J0218+4232 exhibits the hardest pulsar X-ray spectra measured so far: Between 1.6 and 10 keV one peak has a spectrum consistent with a power-law photon index of -0.84 and the other with an index of -0.42 . The total pulsed spectrum can be described with an index -0.61 (Mineo et al. 2000).

At high-energy γ -rays, Verbunt et al. (1996) noticed the positional coincidence of PSR J0218+4232 with the second EGRET catalog source 2EG J0220+4228 (Thompson et al. 1995), which was identified in the catalog and other publications with the BL Lac 3C 66A (Dingus et al. 1996; Mukherjee et al. 1997; Lamb & Macomb 1997). Using some additional EGRET observations, and applying a combination of spatial and timing analyses, Kuiper et al. (1999a) conclude that 2EG J0220+4228 is probably multiple: between 100 and 1000 MeV PSR J0218+4232 is the most likely counterpart, and above 1000 MeV 3C 66A is the best candidate counterpart. The third EGRET catalog (Hartman et al. 1999), which is based on more viewing periods than the 2EG catalog, also identifies 3EG J0222+4253 (2EG J0220+4228) with 3C 66A, rather than with the ms-pulsar. However, in a note on this source, they indicate that the identification with 3C 66A stems from the catalog position based on the > 1 GeV map. Furthermore, they confirm that for lower energies (100-300 MeV) the EGRET map is consistent with all the source flux coming from the pulsar, 3C 66A being statistically excluded.

In this paper we present the results of spatial, timing and pulse-phase resolved spatial analyses using all available EGRET (30 MeV - 30 GeV) data collected between November 1991 and November 1998 in 5 observations with PSR J0218+4232 within 25° of the pointing axis. Analysis of radio monitoring data of this pulsar provided us with an ephemeris valid over the total period of 7 years covering the EGRET observations, allowing phase folding of all selected EGRET events in a single trial. The resulting high-energy γ -ray pulse profile is compared with pulse profiles detected at X-ray energies up to 10 keV, and in absolute phase with the radio profile at 610 MHz. The results are finally discussed in relation to the *Class II* ms pulsars and the Crab, as well as with recent theoretical predictions for the production of X-ray and γ -ray emission in the magnetospheres of ms pulsars.

9.2. Instrument description and observations

EGRET (the Energetic Gamma Ray Experiment Telescope) aboard the Compton Gamma Ray Observatory (CGRO) has a (gas-filled) sparkchamber and is sensitive to gamma-rays with energies in the range 30 MeV to 30 GeV. In the mode used for most of the observations the field of view is approximately 80° in diameter, although the instrument point-spread function (PSF) and the effective area degrade considerably beyond 30° off-axis. Its effective area is approximately 1500 cm^2 between 200 and 1000 MeV, falling off at lower and higher energies. The angular resolution is strongly energy dependent: the 67% confinement angle at 35 MeV, 500 MeV and 3 GeV are $10^\circ.9$, $1^\circ.9$ and $0^\circ.5$ respectively. The energy resolution $\Delta E/E$ is $\sim 20\%$ (FWHM) over the central part of the energy range. Each registered event is time tagged by the on-board clock, serving also the other 3 CGRO instruments BATSE, OSSE and COMPTEL. The on-board time is converted to Coordinated Universal Time (UTC) with an absolute accuracy better than $100\ \mu\text{s}$, and a relative accuracy of $8\ \mu\text{s}$. For a continued proper sparkchamber performance regular gas replenishments of the sparkchamber are required in order to restore the efficiency after the gas has aged. The sparkchamber efficiency is therefore a function of time and energy. For a detailed overview of the EGRET detection principle and instrument characteristics, see Thompson et al. (1993). The inflight calibration and performance are presented in detail by Esposito et al. (1999). In this work we selected those CGRO Cycle I-VII Viewing Periods (VP) in which PSR J0218+4232, located at (l,b) = (139.508, -17.527), was less than 25° off-axis. In Table 9.1 the details of each selected VP are given.

COMPTEL, the imaging Compton Telescope aboard CGRO, is co-aligned with EGRET and had PSR J0218+4232 in its field of view during the same VP's as EGRET. COMPTEL operates in the 0.75-30 MeV energy window and has an energy resolution of about 5-10% FWHM, a large field of view (~ 1 steradian) and a location accuracy of $\sim 1^\circ$ (see Schönfelder et al. 1993). Events are time-tagged with a 0.125 ms resolution. A timing analysis of PSR J0218+4232 in the COMPTEL energy window did not yield a significant timing signal and subsequent imaging studies of the sky region containing PSR J0218+4232 did not show a source detection at the pulsar position. Therefore, only the flux upper limits are presented in this paper (see Sect. 9.8).

OSSE, the Oriented Scintillation Spectrometer Experiment aboard CGRO, is a non-imaging detector system consisting of 4 independent actively shielded NaI(Tl)-Cs(Na) phoswich detectors operating in the 0.05 to 10 MeV energy range, each having a $3^\circ.8 \times 11^\circ.4$ (FWHM) field of view (see Johnson et al. 1993). PSR J0218+4232 was the primary target of OSSE during VP 728.7 and VP 728.9 and was observed in event-by-event mode in the 50-150 keV energy band with a timing accuracy of 0.125 ms. Like in the case for COMPTEL, also OSSE did not detect a timing signature. Flux upper limits are given in Sect. 9.8.

9.3. Spatial analysis

Events arriving from within 30° off axis when EGRET is in full FoV mode and 19° in narrow field mode, are sorted in a 3 dimensional data cube with galactic longitude, latitude and energy as axes. The longitude and latitude bin widths are $0^\circ.5$, and 10 narrow "standard" energy ranges are selected: 30-50, 50-70, 70-100, 100-150, 150-300, 300-500, 500-1000 MeV, 1-2, 2-4 and 4-10 GeV.

Table 9.1. EGRET observations used in this study with PSR J0218+4232 less than 25° off-axis

VP #	Start Date TJD [†]	End Date TJD	Pointing direction		Off-axis angle ($^\circ$)	Eff.Exposure (100-300 MeV; cm^2s)	Sparkchamber efficiency (100-150 MeV) / (1-2 GeV)
			l ($^\circ$)	b ($^\circ$)			
15.0	8588.535	8602.696	152.75	-13.40	13.4	3.209×10^8	0.962 / 0.981
211.0	9043.646	9055.631	125.86	-4.70	18.5	1.661×10^8	0.870 / 0.935
325.0	9468.592	9482.625	147.08	-9.06	11.2	2.512×10^8	0.820 / 0.909
427.0	9951.603	9967.581	153.71	-9.95	15.7	0.690×10^8	0.269 / 0.632
♠728.7/9	11078.646	11120.603	139.36	-18.70	1.2	0.887×10^8	0.180 / 0.250

[†] TJD = JD - 2440000.5 = MJD - 40000

♠ EGRET in narrow field mode; opening angle FoV is 19°

Because the Earth atmosphere is the largest source of non-celestial γ -rays the events are subjected to an energy dependent zenith angle cut. We used the “standard” values for the 10 selected energy windows. The corresponding energy dependent exposure maps are calculated using the “exposure history” files taking into account the instrument calibration characteristics, the instantaneous timeline, the operation mode of the instrument and the time dependent spark chamber sensitivity factors (see Esposito et al. 1999 and Table 9.1).

To be consistent with the selection criteria used in the generation of the exposure matrices we demand that the energy deposit in the TASC (Total Absorption Shower Counter) measured by at least one of its PHA’s is above a threshold of ~ 6.5 MeV.

The imaging method employed here is based on our Maximum Likelihood Ratio (MLR) program, part of the COMPTEL analysis software package COMPASS (de Vries 1994). In this program point sources are searched for on top of a diffuse background model which describes the galactic and extra-galactic γ -ray emission separately. The galactic component originating in cosmic-ray interactions with the protons of the atomic and molecular Hydrogen gas, as well as inverse Compton interactions of cosmic-ray electrons with the ambient photon field, is described by a combination of 2 different models: one results from the convolution of the EGRET PSF with the spatial distribution of the atomic Hydrogen column density and the second from the convolution with the spatial distribution of CO used as tracer for the molecular Hydrogen gas in the galaxy. The extra-galactic component is assumed to be isotropic.

The image resulting from the Maximum Likelihood Ratio program is based on likelihood ratio tests at user defined grid points in a skyfield containing the object of interest. At each grid point (x_{sky}, y_{sky}) we determine the Maximum Likelihood under two hypotheses: 1) a description of the data in terms of the diffuse background models only (\mathcal{H}_0) and 2) a description in terms of the diffuse background models and a point source at the (x_{sky}, y_{sky}) position (\mathcal{H}_1). Under the \mathcal{H}_1 hypothesis the number of counts (μ) expected in a measured sky pixel (i, j) is given by :

$$\mu_{ij} = \sigma \cdot PSF_{ij} + \alpha^{HI} \cdot M_{ij}^{HI} + \alpha^{CO} \cdot M_{ij}^{CO} + \alpha^{Iso} \cdot M_{ij}^{Iso} \quad (9.1)$$

where M^{HI} , M^{CO} and M^{Iso} represent the convolved diffuse galactic and extra-galactic models.

Because our mosaic of observations is composed of viewing periods with pointing directions concentrated in a narrow band at low galactic latitudes (see Table 9.1) the α^{Iso} scale factors are poorly constrained in the optimization process due to the dominating galactic components. So, we keep them *fixed* at values derived

from a study of the extra-galactic γ -ray emission using a much larger database containing all EGRET Cycle I,II and III observations (Sreekumar et al. 1998).

By optimizing the Likelihood under \mathcal{H}_1 with respect to its free scale parameters, σ , α^{HI} , α^{CO} we can derive the flux and flux uncertainty from σ and its error for a putative source at position (x_{sky}, y_{sky}) . From optimizations under \mathcal{H}_1 and \mathcal{H}_0 we can determine the Likelihood ratio λ defined as $-2 \ln(\mathcal{L}_{\mathcal{H}_0} / \mathcal{L}_{\mathcal{H}_1})$. This quantity is distributed as a χ^2 for 1 degree of freedom for a known source position and yields the source detection significance.

The MLR map for energies > 100 MeV (Fig. 9.1) confirms the detection of the EGRET source 2EG J0220+4228/ 3EG J0222+4253 (Thompson et al. 1995; Hartman et al. 1999) at a $\gtrsim 10\sigma$ significance level for 1 degree of freedom, i.e. the source position is known. The \mathcal{H}_1 and \mathcal{H}_0 hypotheses include also the contributions from well-established γ -ray sources (Hartman et al. 1999) within a 30° radius around our target in order to describe the γ -ray sky near our target optimally. The binned event matrix for this integral energy window is a combination of the matrices for the differential energy windows above 100 MeV, each with a different Earth zenith cut angle. The > 100 MeV exposure matrix is in this case a power-law weighted composition (index -2.1) of the differential exposure matrices. This forms a consistent event/exposure set with respect to the applied selection criteria.

We compared the derived optimum scale factors for the Galactic diffuse emission components with the findings from more detailed studies on this diffuse emission (Strong & Mattox 1996, Hunter et al. 1997) and found that our values are in all cases consistent with the published results.

It is evident from Fig. 9.1 that the high-energy γ -ray source is positionally consistent with both PSR J0218+4232 and 3C 66A (located at $(l,b) = (140.143, -16.767)$). The total excess contains 225 ± 27 counts. We analyzed this excess also in the differential energy windows: 100-300 MeV, 300-1000 MeV and 1-10 GeV. In each window the source was seen: 100-300 MeV $\gtrsim 7.0\sigma$ detection significance and 138 ± 24 counts, 300-1000 MeV $\gtrsim 7.0\sigma$ and 57 ± 12 counts and finally 1-10 GeV $\gtrsim 6.5\sigma$ and 22 ± 6 counts. The location confidence contours for the excesses in the 3 broad energy windows are shown in Fig. 9.2. This figure shows that 3C 66A is the evident counterpart for the 1-10 GeV window (consistent with the third EGRET catalogue results (Hartman et al. 1999), whereas PSR J0218+4232 is the most likely counterpart for the 100-300 MeV window. Between 300 and 1000 MeV both sources contribute to the excess.

For energies below 100 MeV we see indications for an excess, but the EGRET sensitivity is becoming too low and the spatial

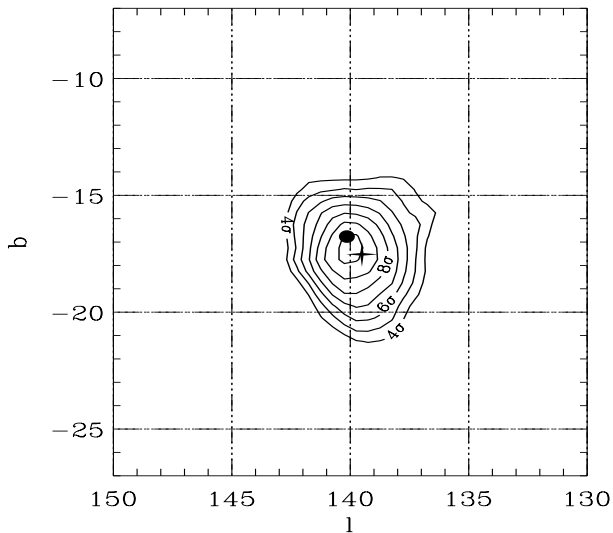


Fig. 9.1. MLR map for energies > 100 MeV of a sky region centered on the EGRET source 2EG J0220+4228 / 3EG J0222+4253, combining data from the 5 observations listed in Table 9.1. The position of PSR J0218+42 is indicated by a star symbol and of 3C 66A by a bullet. The contours start a 4σ detection significance level (1 d.o.f.) with steps of 1σ .

response too wide to draw firm conclusions. We estimated a 2σ flux upper limit for the spectrum of PSR J0218+4232 (see Sect. 9.8).

9.4. Long-term time variability

Earlier studies of γ -ray emission from spin-down powered pulsars showed that they are *steady* γ -ray emitters (see e.g. the review by Thompson et al. 1997). On the contrary, most Active Galactic Nuclei appeared to be highly variable at γ -ray energies (see e.g. Mukherjee et al. 1997). Therefore, we investigated whether there is (absence of) evidence for time variability of 2EG J0220+4228 / 3EG J0222+4253, particularly for the 100-300 MeV and 1-10 GeV bands, in which PSR J0218+4232 and 3C 66A appear to be the most likely counterparts, respectively.

Using integration intervals of typically 2 or 3 weeks, the results are shown in Fig. 9.3. The 100-300 MeV flux measurements are fully consistent with being constant, as expected for γ -ray emission from spin-down powered pulsars. The 1-10 GeV flux points show indications for variability and deviate at a $\sim 2\sigma$ level (93%) from being constant. According to the variability criteria defined by McLaughlin et al. (1996) the 1-10 GeV variability index V of 1.33 points to a variable nature of the 1-10 GeV emission. This type of variability is indeed reminiscent of the behaviour observed frequently for the γ -ray emission from AGN. The above supports the conclusion from the spatial analysis, namely, that 2EG J0220+4228 / 3EG J0222+4253 is multiple: above 1 GeV the BL Lac 3C 66A is the obvious counterpart, whereas below 300 MeV PSR J0218+4232 is the most likely counterpart.

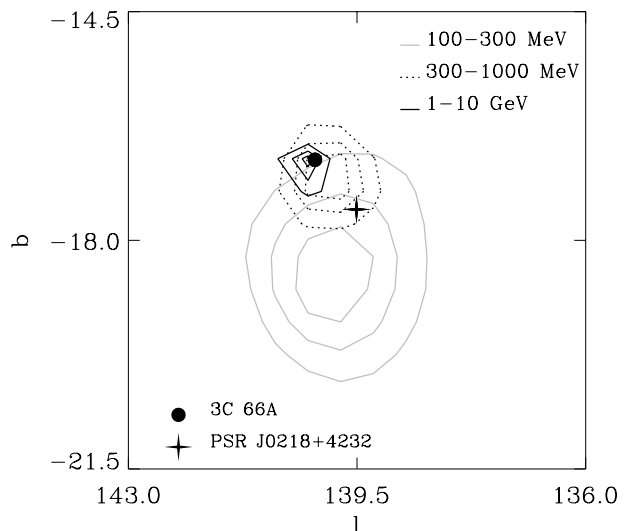


Fig. 9.2. MLR map showing 1, 2 and 3σ location confidence contours of the γ -ray source 2EG J0220+4228 / 3EG J0222+4253 for 3 different energy windows. The shift of the excess towards the pulsar position for decreasing energies is evident. Between 100 and 300 MeV 3C 66A is located outside the 3σ contour, whereas between 1 and 10 GeV this is the case for PSR J0218+4232.

9.5. Timing analysis

In the timing analysis similar event selections have been applied as in the spatial analysis, except we ignored the specific TASC (Thompson et al. 1993) flags of the event triggers in the event selection process. Especially the selection on the TASC zero cross overflow bit (set to 1 if less than 6.5 MeV is deposited in the TASC), which is only effective for the lower energy γ -ray photons (< 150 MeV), is not taken into account. We verified this selection by a timing analysis of the Crab pulsar (combining many Cycle 0 – VI VP's) which showed that ignoring the TASC flags gives a significant improvement of the timing signal, particularly for energies below 100 MeV, with respect to the case in which we demand a TASC energy deposit of at least 6.5 MeV measured by one of its 2 PHA's.

An additional difference in the selection procedure with the spatial analysis, where the spatial information of all events is used, is that we now have to specify an event extraction radius around the pulsar position. Contrary to what is commonly used in the timing analysis of EGRET data, namely, selecting events within an energy dependent extraction radius r_{ext} of $5^{.85} \cdot (E/100 \text{ MeV})^{-0.534}$ containing approximately 67% of the counts from a point-source, with E the measured γ -ray energy, we optimized in each narrow energy window (e.g. 100-150 MeV) the signal-to-noise ratio S/N as a function of extraction radius taking into account the modelled (2d) spatial distribution of the optimized diffuse models and neighbouring sources as obtained in the spatial analysis (see e.g. the thesis of Fierro 1995 p.49-50). This method provides the optimal extraction radius for a given energy window and a given sky-background structure. The values obtained from this study for the narrow energy windows between 100 and 1000 MeV are listed in Table 9.2.

From our timing observations of PSR J0218+4232 at radio wavelengths we obtained one single accurate ephemeris (rms er-

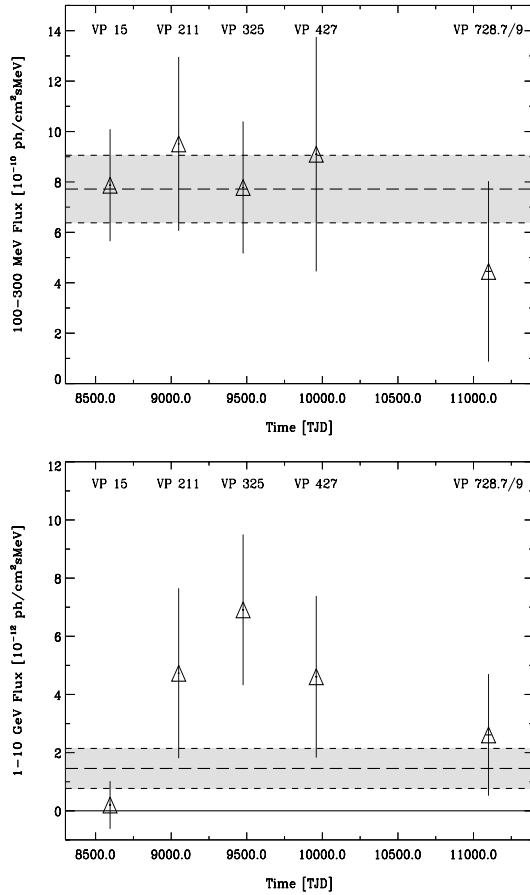


Fig. 9.3. Long-term time variability of the γ -ray source 2EG J0220+4228/3EG J0222+4253 in different energy windows: 100-300 MeV (top) and 1-10 GeV (bottom). The integration time for each data point is typically 2 or 3 weeks. The 100-300 MeV flux points do not show time variability, while the 1-10 GeV data points deviate at the $\sim 2\sigma$ level from being constant (variability index $V = 1.33$). Error bars are 1σ ; the shaded regions indicate the weighted mean $\pm 1\sigma$.

ror $85\mu s$), which is listed in Table 9.3. The validity interval of this ephemeris covers almost 5 years and in view of the stable rotation behaviour observed for millisecond pulsars its validity should extend far beyond the indicated range.

Phase folding the barycentered arrival times, taking into account the binary nature of the system, of the selected events with measured energies between 100-1000 MeV from all observations listed in Table 9.1 yields a 3.5σ modulation significance applying a Z_4^2 test (Buccheri et al. 1983) on the *unbinned* sample of pulse phases. An H-test (de Jager et al. 1989) in which the internal optimization of the number of harmonics is taken into account in the significance estimate yields a 3.2σ modulation significance at an optimum number of harmonics of 4. The 100-1000 MeV pulse profile is shown with 10 bins in Fig. 9.4 with superposed its Kernel Density Estimator (KDE; de Jager et al. 1986) with the $\pm 1\sigma$ uncertainty interval. This KDE approaches the genuine underlying pulse profile (convolved with the instrumental time resolution) for an infinite number of events. The pulse profile shows one prominent narrow emission feature between phases ~ 0.6

Table 9.2. Event extraction radius as a function of energy window

Energy window (MeV)	Extraction radius ($^\circ$)	Enclosed source fraction
100- 150	3.5	0.53
150- 300	2.6	0.56
300- 500	1.8	0.56
500-1000	1.2	0.56

Table 9.3. Ephemeris of PSR J0218+4232

Parameter	Value [†]
Right Ascension (J2000)	$02^{\text{h}} 18^{\text{m}} 6^{\text{s}}.350$
Declination (J2000)	$42^\circ 32' 17''.44$
Epoch validity start/end (MJD)	49092 – 50900
Frequency	$430.4610674213 \text{ Hz}$
Frequency derivative	$-1.4342 \times 10^{-14} \text{ Hz s}^{-1}$
Epoch of the period (MJD)	49996.000000023
Orbital period	175292.3020 s
$a \cdot \sin i$	1.98444 (lt-s)
Eccentricity	0
Longitude of periastron	0
Time of ascending node (MJD)	49996.637640

[†] The last significant digit is given

and ~ 0.7 following a broad less prominent pulse with maximum at phase ~ 0.2 . The phase separation of ~ 0.45 is remarkably similar to the value of ~ 0.47 observed at soft/medium energy X-rays by the ROSAT HRI (Kuiper et al. 1998) and BeppoSAX MECS (Mineo et al. 2000; detailed comparisons will be presented below).

We also produced phase distributions in broader differential energy intervals. The pulse profiles for 100-300 MeV and 300-1000 MeV both showed consistently the same narrow and broad pulses (Z_4^2 probabilities 2.5σ and 1.9σ , respectively). For 30-100 MeV and 1-10 GeV no hints for pulsation were found.

9.6. Pulse phase resolved spatial analysis

The pulse profile shown in Fig. 9.4 reaches a significance of $\sim 3.5\sigma$, indicating that the probability is low, only $4.7 \cdot 10^{-4}$, that this deviation from a flat distribution is caused by a random fluctuation. Given the importance of the discovery of high-energy γ -ray emission from a millisecond pulsar, we investigated further whether there is additional support in our data to claim this detection. As explained above, for the timing analysis the events were selected within an extraction radius around the position of PSR J0218+4232 using only $\sim 56\%$ of the events of a point source. In order to verify whether the source events outside the extraction radius ($\sim 44\%$) exhibit the same timing signature, we produced a pulse profile using all source events by performing a pulse phase resolved spatial analysis for energies between 100 and 1000 MeV.

The procedure is the following: Construct a pulse profile by repeating the spatial analysis for events selected in different pulse phase intervals. Contrary to the phase folding we need to select the events in relatively broad phase intervals to have sufficient statis-

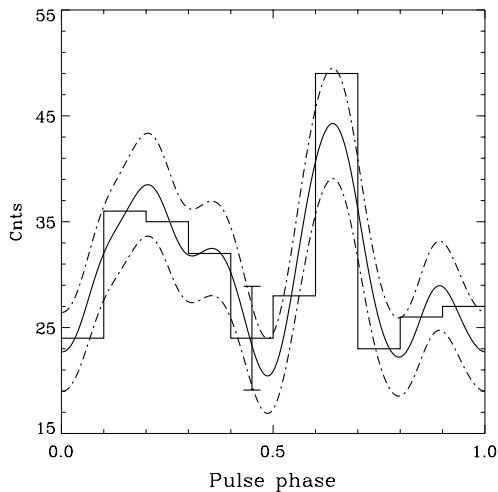


Fig. 9.4. High-energy (100-1000 MeV) γ -ray pulse profile of PSR J0218+4232 combining data from 5 separate viewing periods. The modulation significance is $\sim 3.5\sigma$ applying a Z_4^2 test. Background counts, e.g. from diffuse sky emission and possibly nearby sources, are included. The solid and broken lines indicate the Kernel Density Estimator (see text) with the $\pm 1\sigma$ uncertainty interval. A typical 1σ error bar is shown.

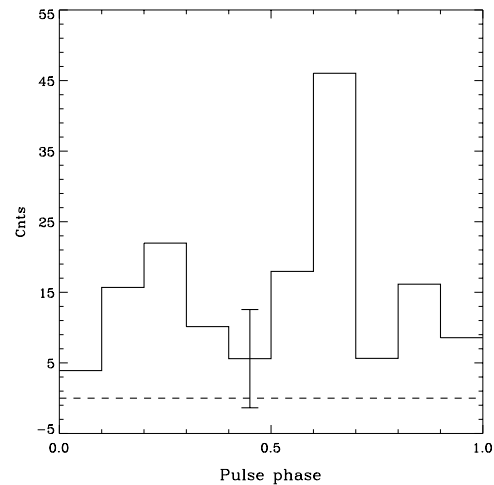


Fig. 9.5. High-energy (100-1000 MeV) γ -ray pulse profile of PSR J0218+4232 resulting from the pulse phase resolved spatial analysis. All background contributions are modelled out, including that of the nearby BL Lac 3C 66A. The profile is similar in shape to the profile from the timing analysis (Fig. 9.4). The number of counts in this profile is a factor of ~ 1.8 higher than the excess counts in Fig. 9.4, as expected for a genuine pulsar signal. A typical 1σ error bar is given.

tics to do the spatial analysis: We selected 10 phase bins of width 0.1.

In order to estimate first the contribution of 3C 66A, which is obviously independent of the pulsar phase, to the total high-energy γ -ray excess in the 100-1000 MeV energy band we have fitted this excess for the full [0,1] phase range in terms of point-sources at the positions of PSR J0218+4232 and 3C 66A. This yielded the following decomposition: the number of counts assigned to PSR J0218+4232 and 3C 66A are 151 ± 52 and 42 ± 51 , respectively. The insignificant 3C 66A contribution, coming from events with energies > 300 MeV, is nevertheless taken into account as a small correction in the pulse phase resolved spatial analysis (4.2 counts are assigned to 3C 66A for each 0.1 wide phase bin). Fitting then the measured 100-1000 MeV spatial event matrices for each pulse phase slice in terms of a PSR J0218+4232 model with a *free* scale factor atop the galactic diffuse models (both with *free* scale factors), the (fixed) isotropic extragalactic component and all (fixed) nearby-source models including 3C 66A, we obtain the *total* number of counts correlating with a point-source at the PSR J0218+4232 position for each phase slice.

The resulting 10 bin pulse profile is shown in Fig. 9.5. The total number of source counts in this light curve is 153 (the background level $\equiv 0$). Comparing Fig. 9.5 with the profile obtained from the timing analysis (Fig. 9.4), it is evident that the shape is statistically identical. For the phase folding we had selected only $\sim 56\%$ of the events for a real source (cf. Table 9.2). Scaling from the number of 153 source counts measured in Fig. 9.5, to be consistent, the number of pulsar excess counts in Fig. 9.4 should be ~ 86 , i.e. the background level should be at ~ 22 . It is evident from this comparison that the two profiles are fully consistent in shape as well as in number of counts in the timing signature. Thus, the pulsed signal is *also* present outside the dataspace confined by the used extraction radius, as expected for a real signal, i.e. the

timing and spatial signatures are consistent with the detection of PSR J0218+4232.

A more well-known display of the same conclusion are “ON”-“OFF” maps, or “pulsed”-“unpulsed” maps. Guided by the shape of the 100-1000 MeV pulse profile in a 20 bin representation (see Fig. 9.7e) we tentatively defined a “pulsed” phase interval as the combination of the phase ranges 0.05-0.40 and 0.55-0.70 and an “unpulsed” interval as its complement. We then produced MLR maps selecting the events now also on their phase location in either of the 2 pulse phase windows for the 100-300, 300-1000 and 100-1000 MeV energy ranges. The results are shown in Fig. 9.6. It is evident that the 100-300 MeV signal is confined within the “pulsed” interval, strengthening the conclusion that PSR J0218+4232 is the counterpart of 2EG J0220+4228 for energies between 100 and 300 MeV. In the 300-1000 MeV “unpulsed” MLR map $\sim 4\sigma$ residual emission is visible which can be explained by emission from 3C 66A and pulsed emission from PSR J0218+4232 emitted outside the defined “pulsed” interval (e.g. possible contribution from a weak pulse near phase 0.9 in Figs. 9.4 or 9.5). The overall picture for energies below 1000 MeV points to a very dominant PSR J0218+4232 and a minor 3C 66A contribution.

9.7. Multi-wavelengths profile comparisons

9.7.1. Comparison with radio profiles

The ephemeris of PSR J0218+4232 given in Table 9.3, and used for our γ -ray analysis, has been determined using Jodrell Bank observations at 610 MHz. The corresponding radio profile is shown in Fig. 9.7a (see also Stairs et al. 1999). It is remarkable that the pulsar is practically never “off”; three pulses seem to cover the entire phase range from 0 to 1.

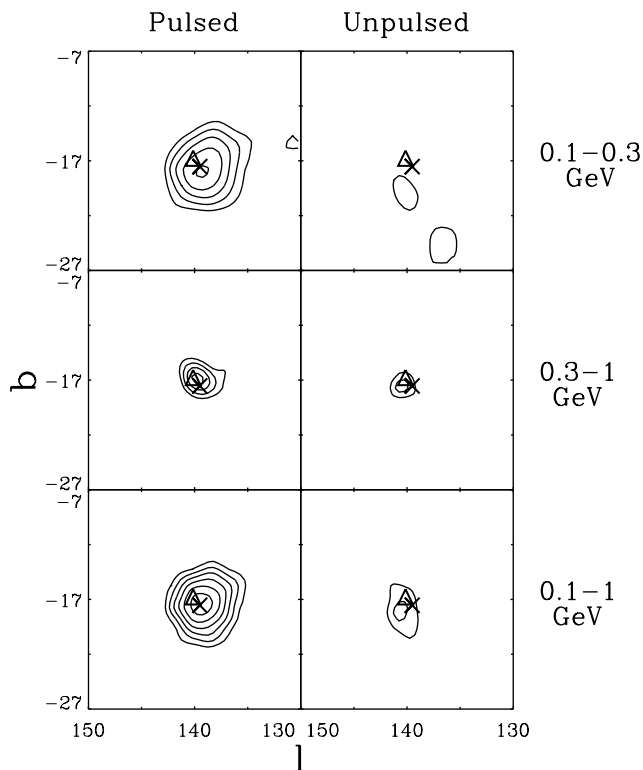


Fig. 9.6. Pulse phase resolved MLR maps of the sky region containing PSR J0218+4232 in 3 different energy windows: 0.1-0.3 GeV, upper panels; 0.3-1 GeV, middle panels; 0.1-1 GeV, lower panels. Left, “pulsed” maps (phases: 0.05 – 0.40 & 0.55 – 0.70); right, “unpulsed” maps (0.40 – 0.55 & 0.70 – 1.05). The contours start at a 3σ significance level in steps of 1σ for 1 degree of freedom. PSR J0218+4232 is marked by a \times and 3C 66A by a Δ symbol. The emission in the 100-300 MeV window is confined to the “pulsed” interval. For the 300-1000 MeV window the “unpulsed” interval shows $\sim 4\sigma$ residual emission. This can be explained by emission from 3C 66A in combination with pulsed emission from PSR J0218+4232 not accounted for in the definition of the “pulsed” window.

Because the fiducial point in the 610 MHz radio profile defining the anchor point in the template used in the fitting process of the time of arrival of the radio pulses is known, its geocentric arrival time specified by the “Epoch of the period” in Table 9.3 can be translated to solar system barycentric arrival time. This timestamp is subsequently converted to a phase zero taking into account the binary nature of the system. This phase zero value, corresponding to the fiducial point, is finally subtracted from the γ -event phases, obtained by the same folding procedure, to align these with the radio profile. Thus, we can compare the 100-1000 MeV pulse profile in absolute phase with the 610 MHz radio profile. The aligned γ -ray pulse profile is shown in Fig. 9.7e, now in 20 bins to allow a more detailed comparison. The bin width of $\sim 115\mu s$ is comparable to the CGRO absolute timing accuracy of better than $100\mu s$. Also shown is the same KDE profile as shown in the 10 bin pulse profile in Fig. 9.4, to aid the comparison of the two γ -ray histograms, given the low counting statistics. In order

to guide the eye, the pulsar phases of the three maxima in the 610 MHz radio profile are indicated by vertical lines.

In Fig. 9.7b is also indicated the 1410 MHz radio profile (Kramer et al. 2000) which has been aligned by cross-correlation with the 610 MHz profile (phase uncertainty ~ 0.01 in alignment). It is clear from this figure that the 2 emission features in the γ -ray pulse profile coincide within the absolute timing uncertainties with 2 of the 3 pulses in the 610 MHz radio profile. Comparing the 610 and 1410 MHz radio profiles it is notable that one of these “radio/ γ -ray” pulses (at phase 0.62) coincides with a dip in the 1410 MHz profile, followed and preceded by smaller pulses. Also between the two main emission features a shoulder is visible in the 1410 MHz profile which is absent in the 610 MHz one.

9.7.2. Comparison with X-ray profiles

We reported earlier significant detections of pulsed X-ray emission from PSR J0218+4232 analysing ROSAT HRI data (4.8σ modulation significance in the 0.1-2.4 keV energy range; Kuiper et al. 1998) and BeppoSAX MECS data (6.8σ , 1.6-10 keV energies; Mineo et al. 2000). In the BeppoSAX MECS analysis we used the same ephemeris of Table 9.3 as in the present work. In the ROSAT HRI analysis, however, we used for the phase folding the extrapolated timing parameters from Navarro (1995). Given the availability of the new ephemeris which is valid over a nearly 5 year period and covers the ROSAT HRI observation, we decided for consistency reasons to reanalyze the 100 ks ROSAT HRI data. In addition, application of improved maximum likelihood algorithms in the spatial analysis to determine the centroid of emission in the X-ray map allowed for a better determination of the optimal extraction radius ($8''$). The result is shown in Fig. 9.7c. The modulation significance has increased to 6σ (Z_2^2 test), particularly the prominence of the second weaker pulse near phase 0.6 has improved in comparison with the result shown in Kuiper et al. (1998).

The new ROSAT HRI profile can be compared with the BeppoSAX MECS profile (Fig. 9.7d; Mineo et al. 2000), which just overlaps in energy window. The alignment of the profiles was done by cross correlation, like in Mineo et al. (2000), since the uncertainties in the ROSAT and BeppoSAX absolute timing are too large to allow an absolute comparison. The identical peak separations of ~ 0.47 and the consistent difference in the spectra of the two peaks (Mineo et al. 2000), make us confident that the alignment is accurate.

The next step is the alignment of the X-ray profiles with the absolute timing of the γ -ray and radio profiles. We cross correlated the most significant X-ray profile (from BeppoSAX MECS) with the EGRET profile, and applied the phase shift which corresponds to the highest probability in the correlation analysis to the aligned ROSAT HRI and BeppoSAX MECS profiles. These aligned profiles are shown in Fig. 9.7. in which the BeppoSAX MECS and EGRET profiles are both displayed in 20 bins. It is obvious that all three high-energy profiles exhibit two pulses with the same phase separation of about 0.47. Fine structure in the gamma-ray profile, like the local maximum at phase ~ 0.9 , is not significant, even though the strong radio pulse at phase ~ 0.9 makes that phase “special”.

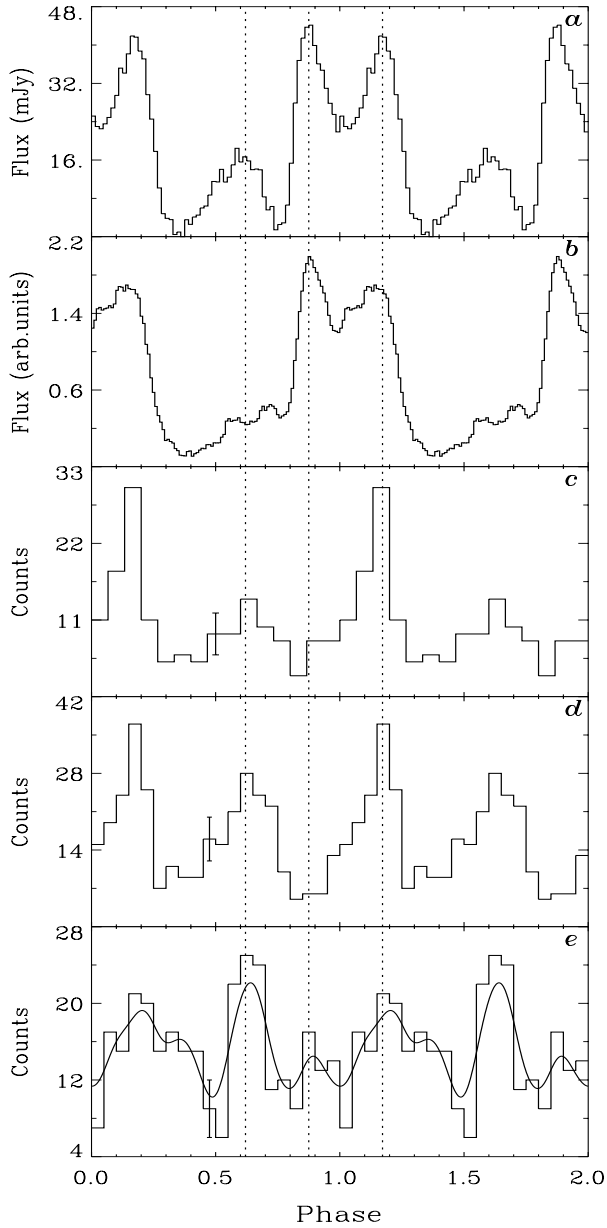


Fig. 9.7. Multi-wavelength pulse profiles of PSR J0218+4232. Radio pulse profile at 610 MHz and 1410 MHz are shown in panels *a* and *b* respectively. *c*) reanalyzed ROSAT HRI 0.1-2.4 keV pulse profile, *d*) BeppoSAX MECS 1.6-10 keV pulse profile and *e*) 100-1000 MeV EGRET pulse profile. Indicated as dotted lines are the positions of the 3 pulses in the 610 MHz radio profile. The X-ray profiles are aligned at their highest correlation value with the EGRET (absolute) 100-1000 MeV pulse profile. Typical $\pm 1\sigma$ error bars are indicated in the X and γ -ray profiles.

9.8. Multi-wavelength spectrum

The X-ray spectrum of the pulsed emission from PSR J0218+4232 between 1.6 and 10 keV is the hardest measured so far for any (millisecond) radio pulsar. The best power-law fit to the BeppoSAX MECS pulsed spectrum has an index -0.61 ± 0.32 . The spectrum becomes somewhat softer (index -0.94 ± 0.22) when

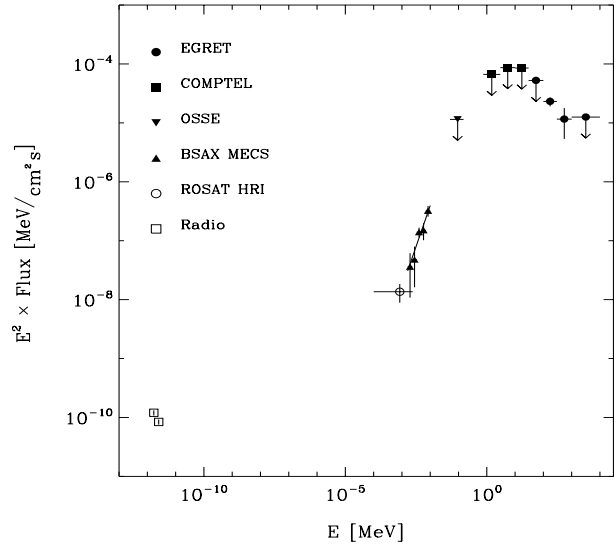


Fig. 9.8. Multi-wavelength spectrum of the pulsed emission from PSR J0218+4232. The high-energy spectrum is characterized by a rapid rise at X-rays, followed by a flattening in the MeV-regime and a decline at high-energy γ -rays. Maximum luminosity is reached in the MeV domain, however, the peak flux is just below COMPTEL's current sensitivity level. The EGRET, COMPTEL and OSSE upper limits are 2σ . Error bars: $\pm 1\sigma$.

a 27% DC component is included (Mineo et al. 2000). This DC component is visible in the ROSAT data (Kuiper et al. 1998) and in the BeppoSAX data up to 4 keV. Above 4 keV there is no sign of a DC component.

In the EGRET γ -ray data above 100 MeV, the signal seen from PSR J0218+4232 is also consistent with being 100% pulsed. However, the detailed structure of the pulse profile is not clear, i.e., is there a phase interval in which the γ -ray signal is clearly off, or how wide are the wings of the pulses? Possibly, the pulsed γ -ray signal extends over the total phase range with only one or two very narrow dips, just like in the radio profile. Therefore, it is difficult to determine a background region in the γ -ray pulse profile for the construction of a pulsed spectrum. We decided to determine the γ -ray spectrum using again the spatial maximum likelihood analysis, estimating the number of source counts (and then flux) on top of the diffuse background models and all relevant nearby sources, for the following energy intervals: 30-100 MeV, 100-300 MeV, 300-1000 MeV, 1-10 GeV. The resulting flux values and upper limits are given in Table 9.4 for PSR J0218+4232 and the simultaneously derived values for 3C 66A in Table 9.5 (power-law photon index ~ -1.5). Table 9.4 also lists the upper limits derived for the simultaneous COMPTEL observations and the OSSE observation during VP 728.7/9 (see Table 9.1). The COMPTEL 2σ -upper limits are derived in a spatial analysis analogous to the EGRET approach. The OSSE 2σ -upper limits are estimated from the statistically flat phase histograms according to the description presented in Ulmer et al. (1991) assuming a duty cycle of 0.5.

In Fig. 9.8 we have collected all available data for a total spectrum from radio up to high-energy γ -rays in the format $E^2 \times flux$, showing the observed power per logarithmic energy interval. The very high luminosity at γ -ray energies between 100 MeV and 1

Table 9.4. CGRO flux estimates for PSR J0218+4232

Energy Range [MeV]	Instrument	Flux / 2σ upper limit [ph / cm ² s MeV]	
0.050	0.073	OSSE	$< 5.29 \cdot 10^{-3}$
0.073	0.103	OSSE	$< 1.97 \cdot 10^{-3}$
0.103	0.151	OSSE	$< 0.87 \cdot 10^{-3}$
0.050	0.151	OSSE	$< 1.16 \cdot 10^{-3}$
0.75	3	COMPTEL	$< 2.87 \cdot 10^{-5}$
3	10	COMPTEL	$< 2.80 \cdot 10^{-6}$
10	30	COMPTEL	$< 2.76 \cdot 10^{-7}$
30	100	EGRET	$< 1.75 \cdot 10^{-8}$
100	300	EGRET	$(7.71 \pm 1.34) \cdot 10^{-10}$
300	1000	EGRET	$(3.86 \pm 2.08) \cdot 10^{-11}$
1000	10000	EGRET	$< 1.25 \cdot 10^{-12}$

Table 9.5. CGRO EGRET time averaged flux estimates for 3C 66A

Energy Range [MeV]	Flux / 2σ upper limit [ph / cm ² s MeV]	
300	1000	$(4.24 \pm 2.11) \cdot 10^{-11}$
1000	10000	$(3.38 \pm 1.08) \cdot 10^{-12}$

GeV is striking and a large fraction of the total spin-down luminosity L_{sd} will be emitted in high-energy γ -rays. This fraction η_{obs} can be estimated as follows:

$$\eta_{obs} = L_{\gamma} / L_{sd} = \frac{1.64 \cdot 10^{34} \cdot (\Delta\Omega / 1 \text{ sr}) \cdot (d / 5.7 \text{ kpc})^2}{2.36 \cdot 10^{35} \cdot (I / 10^{45} \text{ gcm}^2)}$$

with $\Delta\Omega$ the γ -ray beam size, d the distance to the pulsar and I the moment of inertia of the neutron star. Assuming $\Delta\Omega = 1$ sr, $d = 5.7$ kpc and $I = 10^{45}$ gcm² we obtain an efficiency of $\sim 7\%$ for PSR J0218+4232. Over the 100-1000 MeV range the γ -ray spectrum is soft and consistent with a photon power-law index of ~ -2.6 . The extrapolation of the very hard spectrum between 0.1 and 10 keV is just in agreement with the OSSE upper limit(s). Fig. 9.8 suggests that the maximum luminosity is reached in the COMPTEL MeV range just below the COMPTEL upper limits.

9.9. Summary and discussion

In this study we performed detailed spatial and timing analyses on PSR J0218+4232 using the high-energy γ -ray data from CGRO EGRET and found that we have good circumstantial evidence for the first detection of pulsed high-energy γ -rays from a *Class II* ms-pulsar, PSR J0218+4232, namely:

- 1- The spatial distribution is consistent with the pulsar being detected: Between 100 and 300 MeV the EGRET source position is consistent with that of PSR J0218+4232 with the total signal concentrated in 2 pulses. The 100-300 MeV flux does not show time variability at a 2/3 weeks time scale, indicative for a steady γ -ray emitter like spin-down powered pulsars. Above 1 GeV the nearby (angular separation $\sim 1^\circ$) BL Lac,

3C 66A, is the evident counterpart for the γ -ray excess. For energies between 300 MeV and 1 GeV the pulsar and the BL Lac contribute to the excess.

- 2- Timing analysis (phase folding, using the timing parameters measured at radio wavelengths) in the 100-1000 MeV energy interval, selecting roughly 56% of the source photons, yields a double-peaked pulse profile with a $\sim 3.5\sigma$ modulation significance. The same pulsed signature is also present in the data outside the extraction radius used in the timing analysis, containing the remaining $\sim 44\%$ of the source photons.
- 3- The phase separation of ~ 0.45 of the two γ -ray pulses is similar to that measured between the two pulses at X-rays; a comparison in absolute time with the 610 MHz radio-profile shows alignment of the γ -ray pulses with two of the three radio pulses.

EGRET detected six pulsars with overwhelming statistical significance (Crab, Vela, Geminga, PSR B1706-44, PSR B1951+32 and PSR B1055-52; see e.g. the review by Thompson et al. 1997). Compared to these six, the modulation significance of PSR J0218+4232 falls only in the 3-4 σ range, similar to the significance of the weak timing signals found with EGRET from PSR B0656+14 (Ramanamurthy et al. 1996) and PSR B1046-58 (Kaspi et al. 2000). The additional circumstantial evidence for the detection of PSR J0218+4232, particularly the similarity of the double-peaked X-ray and γ -ray pulse profile shapes, and the fact that the X-ray spectrum measured for PSR J0218+4232 below 10 keV is the hardest measured for any pulsar (Mineo et al. 2000) increases the likelihood of the detection. Nevertheless, confirmation of the detections of PSR B0656+14, PSR B1046-58 and PSR J0218+4232 by future high-energy γ -ray missions like the Italian AGILE and NASA's GLAST is important.

The nearby 3C 66A obviously complicated the analyses, but its contribution to the γ -ray excess in the skymaps has consistently been taken into account. The events detected from this BL Lac have no systematic effect on the double-peaked timing signature assigned to PSR J0218+4232 in the timing analysis. However, our results show that earlier publications on the spectrum of 3C 66A (e.g. Dingus et al. 1996; Mukherjee et al. 1997; Lin et al. 1999) should be revised, the time averaged spectrum is significantly harder than published earlier.

In Kuiper et al. (1998) and Mineo et al. (2000) the similarity of the double-peaked X-ray pulse profile of PSR J0218+4232 with that of the Crab pulsar was noted and discussed. It is now striking that the observed 100-1000 MeV pulse profile of PSR J0218+4232 shows one narrow ($\sim 250\mu\text{s}$) pulse preceded ~ 0.45 in phase by a broader pulse, again a morphology very similar to that of the Crab pulsar γ -ray profile. The latter exhibits two distinct pulses at ~ 0.4 phase separation at X-ray and γ -ray energies, with the X-ray and γ -ray pulses being aligned in absolute phase. Unfortunately, we cannot align the X-ray and γ -ray profiles of PSR J0218+4232 in absolute phase, but the similar phase separation suggests that the pulses are also aligned (see Fig. 9.7).

We noted in the Introduction that the surface magnetic field strengths of ms pulsars are 3 to 4 orders of magnitude weaker than that of normal radio pulsars. This makes the boundary condition for the production of γ -rays near the neutron star surface for ms pulsars much less favourable than for normal radio pulsars. It is, however, remarkable that the Crab pulsar and the members of the *Class II* ms pulsars have in common that the magnetic field strengths near the light cylinders B_{lc} are comparable (in the range

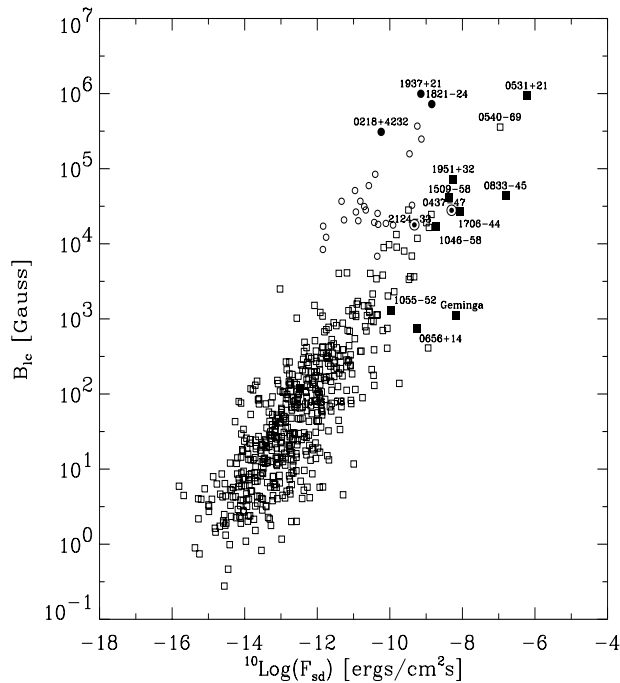


Fig. 9.9. Magnetic field strength near the light cylinder B_{1c} versus pulsar spin-down flux F_{sd} for the sample of normal radio pulsars (\square) and ms pulsars (\circ). The eight (see text) normal pulsars detected above 1 MeV are indicated by a filled square symbol; *Class I* ms pulsars by an encircled filled circle; *Class II* by a filled circle.

$(3 - 10) \times 10^5$ Gauß). In fact, ranking all known radio pulsars by B_{1c} , the three *Class II* ms pulsars rank number 1, 3 and 6, and Crab ranks number 2 (see also the discussion in Saito et al. 1997; Kuiper et al. 1998 and Takahashi et al. 1999).

This is illustrated in Fig. 9.9, showing a scatter plot for all radio pulsars of B_{1c} versus the spin-down flux, $F_{sd} = \dot{E}/(4\pi d^2)$, with \dot{E} the total rotational energy loss rate and d the distance. The three *Class II* ms pulsars are clearly located at the extreme of the B_{1c} distribution. The two *Class I* ms pulsars possess significantly lower, more average values for ms pulsars. Also indicated are the 8 normal pulsars detected by EGRET in high-energy gamma-rays, as well as PSR B1509-58, detected by COMPTEL up to about 30 MeV (Kuiper et al. 1999b). As has been noted in earlier papers, F_{sd} is a good indicator for the probability to detect hard X-ray and high-energy gamma-ray emission from normal radio pulsars. The only normal pulsar near the top of the F_{sd} distribution, not seen by EGRET is PSR B0540-69. This LMC pulsar is detected, however, at X-rays up to ~ 50 keV (Ulmer et al. 1999). In order for ms pulsars to be seen with a hard X-ray spectrum (*Class II*), or even at high-energy gamma-rays (PSR J0218+4232) a high value for B_{1c} seems to be required, in addition to a high F_{sd} . This suggests that B_{1c} is a key parameter for models explaining the production of high-energy emission in the magnetospheres of ms pulsars.

Given in addition the similarities with the Crab of the high-energy pulse profiles (X-rays and also γ -rays for PSR J0218+4232) this suggests that the pulsed high-energy non-thermal emission from the *Class II* ms pulsars and the Crab pulsar have a similar origin in the pulsar magnetosphere, quite likely in a vacuum gap near the light cylinder. We know from radio observa-

tions, however, that the Crab has an orthogonal alignment, while PSR J0218+4232 is a nearly aligned rotator (Navarro et al. 1995, Stairs et al. 1999). Unfortunately, a parameter which is also important in this discussion on the geometry, the impact angle, has only been determined with large uncertainties, and therefore the line-of-sight information for PSR J0218+4232 is unconstrained (Stairs et al. 1999).

If indeed, X-ray emission and γ -ray emission from *Class II* ms pulsars has to be produced in a vacuum gap near the light cylinder, the vacuum gap has to be very short in order to have *narrow* and *aligned* pulses at X-rays and γ -rays, given the very strong curvature of the magnetic field lines in ms-pulsar magnetospheres. In addition, the potential drop has to be very high over this short length to accelerate the particles to the energies required for high-energy gamma-ray production. It is obvious that continuous acceleration of particles and production of X-rays and γ -rays from the surface of the neutron star along the curved magnetic field lines till the light cylinder radius (for PSR J0218+4232 only 111 km) will not render the *narrow* and *aligned* pulses at X-rays and γ -rays.

The Crab pulsar has also its two X-ray and γ -ray pulses aligned in absolute phase with two of the three radio pulses, leading to a consistent picture in which the high-energy pulses and the aligned radio pulses are produced in the same zones in the magnetosphere (see e.g. Romani & Yadigaroglu 1995). The apparent alignment of the γ -ray pulses of PSR J0218+4232 with two of three pulses measured at 610 MHz suggests also that some of the radio pulses are produced in the same zones in the magnetosphere as the γ -ray pulses. However, we would first like to see a better radio estimate of the viewing angle for the PSR J0218+4232 system, and a confirmation of the absolute alignment using new and better observations at X-ray energies, before making further speculations on the geometry.

Theoretical models attempting to explain the high-energy electro-magnetic radiation from spin-down powered pulsars are divided in two main categories distinguished by the production sites of the radiation in the pulsar magnetospheres. The first class of models, polar cap (PC) models, rely on the acceleration of charged particles along the open field lines near the magnetic pole(s) followed by cascade processes given rise to high-energy electro-magnetic radiation (see e.g. Daugherty & Harding 1994, 1996). In the second class of models, outergap models (OG), the acceleration of charged particles and subsequent generation of high-energy radiation takes place in vacuum gaps near the pulsar light cylinder (see e.g. Cheng et al. 1986a,b and Ho 1989). Unfortunately, for the case of ms pulsars no detailed self-consistent model calculations exist for either class of models, allowing predictions for different observational aspects, e.g. pulse phase resolved spectra, pulse shapes, efficiencies. In most cases only one aspect of the emergent high-energy radiation is addressed.

The PC model elaborated by a Polish group (Bulik, Dyks & Rudak), for example, only focusses on the emergent high-energy electro-magnetic spectrum from ms pulsars from X-rays up to high-energy γ -rays, while the pulse shape is ignored. This group predicts a dominating Synchrotron component over the entire X-ray/soft γ -ray band (0.1 keV - 1 MeV) with a spectral photon index of -1.5 (Dyks & Rudak 1999). This does not agree with the much harder photon indices of $\gtrsim -1$ observed for PSR J0218+4232, PSR B1937+21 and PSR B1821-24. The predicted γ -ray spectrum, dominated by curvature radiation, peaks between 10 GeV and 100 GeV and even an inverse Compton scattering

component is predicted at TeV energies (Bulik & Rudak 1999; Bulik et al. 2000). The maximum in the observed spectrum of PSR J0218+4232 (νF_ν or $E^2 F$ representation) is located in the 1–100 MeV range, also in contradiction with their model prediction (see Fig. 9.8). Their γ -ray flux prediction for PSR J0218+4232 is even more than a factor of 10 below the expected GLAST sensitivity level, thus not at all detectable by the less sensitive EGRET telescope for which we present the results.

The polar cap cascade model of Zhang & Harding (2000) including now also, compared to earlier versions, inverse Compton scattering of higher generation cascade pairs provides predictions for both the X-ray and γ -ray luminosities of spin-down powered pulsars, including ms pulsars. In the soft/medium energy X-ray band the model predicts a thermal origin of the spectral features of the pulsed emission from ms pulsars. This is inconsistent with the observed non-thermal (very) hard pulsed spectra of the 3 *Class* II ms pulsars. However, for the *Class* I ms pulsars this could be in agreement with the observed spectral properties.

Zhang and Harding also predict that ms pulsars usually have a considerable high-energy γ -ray luminosity, but due to their weak magnetic field strengths, resulting in quite high photon escape energies, the emergent γ -spectrum is very hard. The latter is not in agreement with the observed soft high-energy (photon Power-law index of ~ -2.6 for energies between 100 MeV and 1 GeV) γ -ray spectrum of PSR J0218+4232.

Thus, so far the PC scenario based models appear to be unsuccessful in explaining the observed X-ray and γ -ray properties of the *Class* II ms pulsars.

An outergap model aiming at predicting pulsed and unpulsed γ -ray emission from ms pulsars was presented by Wei et al. (1996). This model predicts a spectral photon index of -2 for the pulsed emission from a ms pulsar for the energy range of ~ 10 keV to ~ 500 MeV, in contradiction with the spectrum we show in Fig. 9.8 for PSR J0218+4232. The model predicts also a harder unpulsed component with a spectral photon index of -1.5 , dominating the pulsed component above ~ 500 MeV. We have not detected this component for PSR J0218+4232 at energies above 100 MeV.

Concerning the energetics of the γ -ray emission of PSR J0218+4232 it is interesting to compare the observed γ -ray efficiency η_{obs} (fraction of the total spin-down luminosity) of ~ 0.07 with theoretically derived efficiencies. For the PC model of Zhang & Harding (2000) the efficiency scales as $\eta_{\text{PC}} \propto p \cdot \tau^{0.5}$ with p the pulse period and τ the characteristic age of the pulsar. Expressed in the Crab pulsar efficiency η_{Crab} we find for PSR J0218+4232 that $\eta_{0218} \sim 45 \times \eta_{\text{Crab}}$, which translates to an efficiency of $\eta_{0218} \sim 0.05$ substituting the measured Crab γ -ray efficiency of about 0.001. The thick OG model of Zhang & Cheng (1998) yields the following expression for the γ -ray efficiency: $\eta_{\text{OG}} \propto p^2 \cdot \tau^{6/7}$. This translates to $\eta_{0218} \sim 300 \times \eta_{\text{Crab}}$, which means that $\eta_{0218} \sim 0.33$. Thus, within the framework of both PC and OG models the expected γ -ray conversion efficiency is very high, approximately in accordance with the measured efficiency of about 0.1. However, it should be noted that both models predict an even higher efficiency for e.g. PSR J0437-4715, a *Class* I ms pulsar. This pulsar is very nearby but has not been detected as a γ -ray source/pulsar (Fierro et al. 1995).

The circumstantial evidence presented in this paper for the detection of pulsed high-energy γ -rays from ms pulsar PSR J0218+4232 opens a new window in the study of the magnetospheric properties of spin-down powered pulsars. It is unfortu-

nate that we cannot repeat this observation with EGRET anymore. Therefore, deep searches for high-energy γ -ray emission from the *Class* II ms pulsars with future more sensitive gamma-ray missions like GLAST and AGILE are very important. But also earlier sensitive observations at the harder X-rays above 10 keV are very important to bridge the observational gap. Particularly the ESA mission INTEGRAL might be able to extend the hard spectra measured below 10 keV to as high as a few MeV.

Acknowledgements. This work is supported by the Netherlands Organisation for Scientific Research (NWO). We thank Michael Kramer for providing the 1400 MHz radio profile of PSR J0218+4232 obtained with the Effelsberg radio telescope.

References

- Becker W., Trümper J., 1993, Nat 365, 528
 Becker W., Trümper J., 1999, A&A 341, 803
 Bhattacharya D., Srinivasan G., 1991, JA&A 12, 17
 Buccheri R., Bennett K., Bignami G., et al., 1983, A&A 128, 245
 Bulik T., Rudak B., 1999, Astrophysical Letters and communications 38, 37
 Bulik T., Rudak B., Dyks J., 2000, MNRAS, submitted
 Cheng K.S., Ho C., Ruderman M., 1986a, ApJ 300, 500
 Cheng K.S., Ho C., Ruderman M., 1986b, ApJ 300, 522
 Daugherty J.K., Harding A.K., 1994, ApJ 429, 325
 Daugherty J.K., Harding A.K., 1996, ApJ 458, 278
 de Jager O.C., Swanepoel J.W.H., Raubenheimer B.C., 1986, A&A 170, 187
 de Jager O.C., Swanepoel J.W.H., Raubenheimer B.C., 1989, A&A 221, 180
 de Vries C.P., 1994, In: Crabtree D.R., Hanisch R.J., Barnes J. (eds.) ASP Conf. Series 61, 399
 Dingus B.L., Bertsch D.L., Digel S.W., et al., 1996, ApJ 467, 589
 Dyks J., Rudak B., 1999, Astrophysical Letters and communications 38, 41
 Esposito J.A., Bertsch D.L., Chen A.W., et al., 1999, ApJS 123, 203
 Fierro J.M., 1995, PhD. Thesis, Stanford University
 Fierro J.M., Arzoumanian Z., Bailes M., et al., 1995, ApJ 447, 807
 Hartman R.C., Bertsch D.L., Bloom S.D., et al., 1999, ApJS 123, 79
 Ho C., 1989, ApJ 342, 396
 Hunter S.D., Bertsch D.L., Catelli J.R., et al., 1997, ApJ 481, 205
 Johnson W.N., Kinzer R.L., Kurfess J.D., et al., 1993, ApJS 86, 693
 Kaspi V., Lackey J.R., Mattox J., et al., 2000, ApJ 528, 445
 Kawai N., Saito Y., 1999, Astrophysical Letters and communications 38, 1
 van Kerkwijk M.H., 1997, Proc. IAU Coll. 160, 489
 Kramer M., Lange C., Lorimer D.R., et al., ApJ accepted, 2000
 Kuiper L., Hermsen W., Verbunt F., et al., 1998, A&A 336, 545
 Kuiper L., Hermsen W., Verbunt F., et al., 1999a, Astrophysical Letters and communications 38, 13
 Kuiper L., Hermsen W., Krijger J.M., et al., 1999b, A&A 351, 119
 Lin Y.C., Bertsch D.L., Bloom S.D., et al., 1999, ApJ 525, 191
 Lamb R.C., Macomb D.J., 1997, ApJ 488, 872
 McLaughlin M.A., Mattox J.R., Cordes J.M., et al., 1996, ApJ 473, 763
 Mineo T., Cusumano G., Kuiper L., et al., 2000, A&A 355, 1053
 Mukherjee R., Bertsch D.L., Bloom S.D., et al., 1997, ApJ 490, 116

Navarro J., de Bruyn A.G., Frail D.A., Kulkarni S.R., Lyne A.G.,
1995, ApJ 455, L55
Ramanamurthy P.V., Fichtel C.E., Kniffen D.A., et al., 1996, ApJ
458, 755
Romani R., Yadigaroglu I.A., 1995, ApJ 438, 314
Saito Y., Kawai N., Kamae T., et al., 1997, ApJ 477, L37
Schönfelder V., Aarts H., Bennett K., et al., 1993, ApJS 86, 657
Sreekumar P., Bertsch D.L., Dingus B.L., et al., 1998, ApJ 494,
523
Stairs I.H., Thorsett S.E., Camilo F., 1999, ApJS 123, 627
Strong A.W., Mattox J.R., 1996, A&A 308, L21
Sturmer S.J., Dermer C.D., 1994, A&A 281, L101
Takahashi M., Shibata S., Gunji S., et al., 1999, Astron. Nachr.
320, 340
Taylor J.H., Cordes J.M., 1993, ApJ 411, 674
Thompson D.J., Bertsch D.L., Fichtel C.E., et al., 1993, ApJS 86,
629
Thompson D.J., Bertsch D.L., Dingus B.L., et al., 1995, ApJS
101, 259
Thompson D.J., Harding, A.K., Hermsen, W., et al., 1997, Proc.
4th Compton Symp., eds. C.D. Dermer, M.S. Strickman, J.D.
Kurfess, AIP Conf. Proc. 410, 39
Ulmer M.P., Purcell W.R., Wheaton W.A., et al., 1991, ApJ 369,
485
Ulmer M.P., Park S., Finley J.P., et al., 1999, Astrophysical Letters
and communications 38, 29
Verbunt F., Kuiper L., Belloni T., et al., 1996, A&A 311, L9
Wei D.M., Cheng K.S., Lu T., 1996, ApJ 468, 207
Zhang L., Cheng K.S., 1998, MNRAS 294, 177
Zhang B., Harding A., 2000, ApJ submitted

Chapter 10

Populair-wetenschappelijke samenvatting: Hoog-energetische straling van pulsars

10.1. Wat is hoog-energetische straling en hoe detecteer je dit?

In het alledaagse leven speelt de waarneming van objecten en gebeurtenissen middels onze ogen een cruciale rol. Onze ogen zijn gevoelig voor licht, een vorm van elektro-magnetische straling (een golf verschijnsel), met golflengten in het zogenaamde visuele gedeelte van het spectrum. Hoewel dit venster zeer beperkt is, kunnen we toch kleur ontwaren. Verschil in kleur betekent niets anders dan verschil in golflengte van het geregistreerde licht. Een goed voorbeeld van een kleurschakering (spectrum), die we kunnen waarnemen (middels de kegelvormige cellen op ons netvlies), is een regenboog, waarbij het zonlicht is uiteengerafeld in zijn samenstellende golflengte (kleur) componenten. Buiten dit visuele venster kunnen we de directe omgeving niet waarnemen met onze ogen, hoewel we ons bevinden temidden van enorme stromen electro-magnetische straling in de vorm van radio-golven (denk aan het radio-verkeer, tele-communicatie, telefonie, radar etc.) en micro-golven (bijv. een magnetron). Zichtbaar licht en radiogolven zijn vormen van eenzelfde verschijnsel. Het verschil zit gelegen in de golflengte van de straling. Men spreekt van radiostraling indien de golflengte van de straling groter is dan ~ 1 millimeter, terwijl zichtbaar licht veel kleinere golflengten heeft ruwweg tussen $5 \cdot 10^{-7}$ en 10^{-6} meter (een 1 met 6 decimalen achter de komma). Elektro-magnetische straling plant zich voort met de lichtsnelheid, een universele constante met een waarde van 300 000 km/s in vacuüm (de afstand aarde-maan in een tel). De energie, die de straling met zich meedraagt, is omgekeerd evenredig aan zijn golflengte. Vaak spreekt men over de frequentie van de straling. Dit is niets anders dan de lichtsnelheid gedeeld door de golflengte van de straling en dus proportioneel aan de energie van de stralingsdeeltjes (ook wel fotonen genoemd). We spreken van hoog-energetische straling indien de golflengte kleiner is dan ruwweg $1 \cdot 10^{-8}$ meter (1 gedeeld door 100 000 000). Dit correspondeert met foton energien groter dan ~ 100 electron-Volt (eV; dit is $\sim 100\times$ meer energetisch dan een lichtdeeltje uit het zichtbare venster welk een karakteristiek energie heeft van ~ 1 eV). Zo spreken we van Röntgen straling, wanneer de fotonen een energie hebben van ~ 0.1 -100 keV. Gamma-straling vertegenwoordigt de meest energetische vorm van elektro-magnetische straling en heeft energien boven de 100 keV. Toch zijn deze vormen van straling ons niet onbekend in het alledaagse leven. De medische wetenschap maakt gebruik van Röntgen straling voor diagnostische doeleinden, daarbij profiterend van het doordringende vermogen van dit type straling (gaat vrijwel ongemoeid door de huid). Ook gamma-straling wordt gebruikt voor medi-

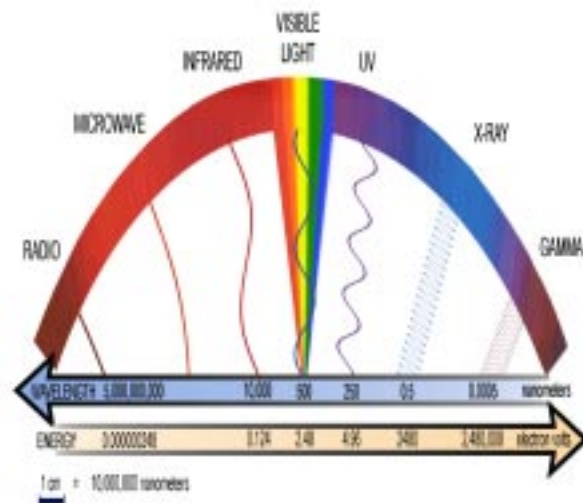


Fig. 10.1. De verschillende vormen van electro-magnetische straling met de daarbij behorende energie en golflengte schaal. De Röntgen en gamma-straling vertegenwoordigen de meest energetische componenten van het electro-magnetische spectrum.

sche doeleinden met name bij de behandeling van kwaadaardige tumoren. Deze straling heeft een zeer doordringend vermogen en kan diep in het lichaam gelegen kankercellen vernietigen. Vers in het geheugen ligt ook nog de ramp met de kernenergie centrale bij Tsjernobyl eind jaren tachtig, waarbij enorme hoeveelheden radio-actieve materiaal de atmosfeer zijn ingeblazen, die gammastraling uitzenden. Met name het radio-actief jodium vormde een gevaar voor het menselijk en dierlijk leven omdat het zich ophoopt in de schildklier, waar het onherstelbare schade aanricht en ongecontroleerde celwoekering teweeg kan brengen. Een overzicht van de verschillende vormen van electro-magnetische straling met de daarbij behorende golflengte en energie schaal wordt getoond in Figuur 10.1.

Het waarnemen van gamma-straling vereist technieken, die sterk verschillen van de telescoop principes, die gebruikt worden bij de langere golflengten (lagere energien), zoals radio-, infrarood-, optische, ultraviolet straling en zachte Röntgen straling (energie kleiner dan ~ 10 keV). Deze straling laat zich goed beschrijven als golfverschijnsel en kan gefocuseerd worden middels lens-en spiegel optiek. De energierijke gamma-straling gedraagt zich meer als (hard) deeltje en dringt vrijwel onghin-

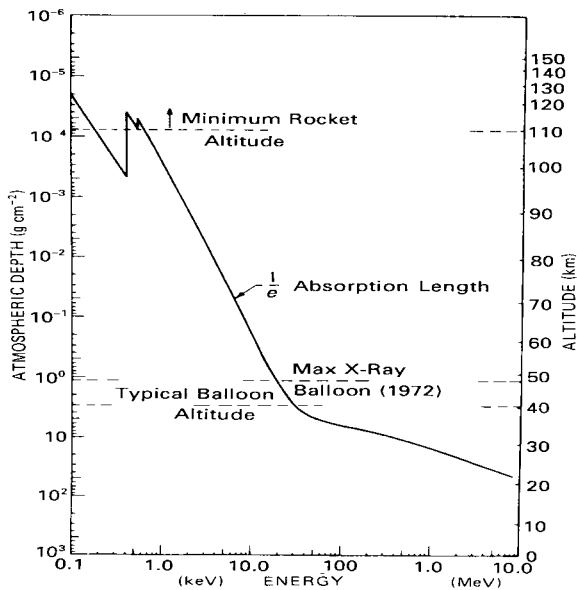


Fig. 10.2. Doorlaatbaarheid van de aardatmosfeer voor hoge-energie straling vanuit de kosmos. De rechter verticale schaal geeft de hoogte aan boven het aardoppervlak. De vette lijn toont de hoogte in de atmosfeer waarbij de inkomende hoge-energie straling verzwakt is tot $\sim 36.8\%$ van de intensiteit buiten de aardatmosfeer.

derd door het detector materiaal heen. Om de vangkans van de gamma-fotonen te vergroten zijn dus grote hoeveelheden detector materiaal nodig, hetgeen de detectie apparatuur groot en zwaar maakt. Ondanks zijn enorm penetrerend vermogen kan *kosmische* gamma-straling het aardoppervlakte (gelukkig) niet bereiken ten gevolge van absorptie in de aardatmosfeer. Een kolom lucht van ~ 10 meter (druk 1 atmosfeer) is voldoende om de intensiteit van gamma-straling te verzwakken tot een ondetecteerbaar niveau. De doorlaatbaarheid van de aardatmosfeer voor kosmische hoge-energie straling wordt getoond in Figuur 10.2 voor energien tussen de 0.1 keV (zachte Röntgen straling) en 10 MeV (midden energie gamma-straling). De vette lijn toont de zogenaamde $1/e$ absorptie lengte in de aardatmosfeer. Deze lijn geeft aan dat de intensiteit van de hoge-energie straling komende vanuit de kosmos gereduceerd is tot $\sim 36.8\%$ van het intensiteit niveau buiten de atmosfeer. Het is dus duidelijk, dat, als je metingen wilt verrichten aan de hoge-energie straling vanuit de kosmos, je de detectie apparatuur boven de aardatmosfeer moet plaatsen middels een raket lancering. Voor energien boven de ~ 20 keV kun je nog wel iets bereiken met ballon vluchten, maar de interpretatie van de (meestal kortdurende) metingen zal verder bemoeilijkt worden doordat de atmosfeer zelf als een sterke hoge-energie achtergrond stralingsbron fungeert. Deze achtergrond straling wordt opgewekt in de atmosfeer, omdat de gasatomen/moleculen in de atmosfeer interageren met de alom aanwezige buitenaardse (energetische) geladen deeltjes (ook wel *kosmische "straling"* genoemd).

Het detectie principe van een gamma-straling detector berust op een van de drie interactie mechanismen van gamma-straling met materie. We onderscheiden 1) het photo-electrisch effect: een gamma-foton ioniseert een atoom (i.e. ontdoet het van een elektron), 2) het Compton effect: een verstrooiing van een gamma-

foton aan een geladen deeltje (meestal een elektron), waarbij zowel de richting als energie van het gamma-foton verandert en tenslotte 3) het paar-vormings effect: een hoog-energetische gamma-foton (energie moet groter dan 1.022 MeV zijn) kan materialiseren tot een electron/positron paar onder invloed van een extern elektrisch veld. Ieder mechanisme heeft zijn eigen energie venster (afhankelijk van het atoomgetal = aantal electronen van het atoom, waarmee in interactie wordt getreden), waarvoor het dominant is ten opzichte van de andere interactie mechanismen. Zo is het photo-electrische effect dominant voor energien tussen de ~ 10 en ~ 100 keV, het Compton effect voor energien tussen de ~ 100 keV en ~ 10 MeV en het paar-vormings effect voor energien groter dan ~ 10 MeV. De dominantie van ieder gamma-straling interactie mechanisme als functie van energie en atoomgetal (Z) van interagerend atoom wordt getoond in Figuur 10.3. Detectie systemen, die de richting en energie van gamma-straling met energien tussen de ~ 100 keV en ~ 10 MeV trachten te meten, maken gebruik van het Compton effect en worden Compton telescopen genoemd. Evenzo, voor energien boven de ~ 10 MeV wordt de materialisatie van gamma-straling gebruikt (bijv. in zogenaamde vonkenkamers) om de eigenschappen van de inkomende gamma-straling te bestuderen (energie en richting kunnen gereconstrueerd worden).

In het voorgaande hebben we het gehad over hoe we gamma-straling kunnen detecteren, echter, hoe gamma-straling geproduceerd wordt is nog niet aan de bod gekomen. We onderscheiden een 4-tal productie mechanismen voor gamma-straling.

- 1- Overgangen tussen energie niveaus binnen een atoomkern, bestaande uit protonen en neutronen, gaan in het algemeen gepaard met de emissie van gamma-straling. Deze straling is mono-chromatisch d.w.z. de straling heeft een wel-gedefinieerde golflengte (kleur) binnen een zeer nauw golflengte bandje (gamma-lijnstraling). Van nature radio-actieve elementen (instabiele atoomkernen) zenden

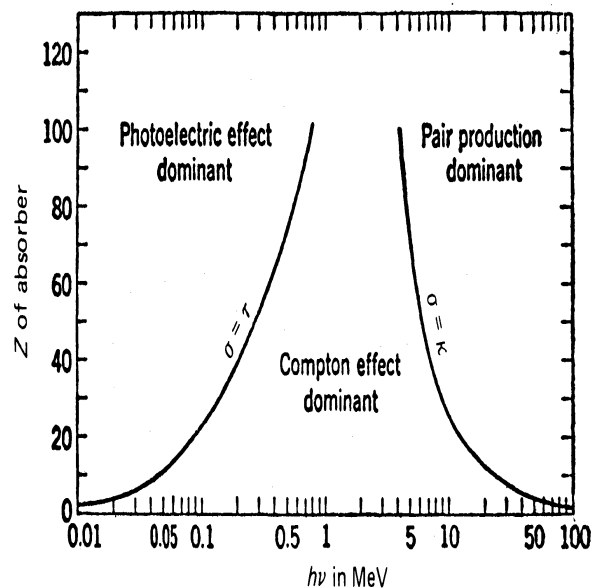


Fig. 10.3. De dominantie van de 3 interactie mechanismen van gamma-straling met materie als functie van gamma-straling energie en het atoomnummer van interagerend materiaal.

een dergelijk type gamma-straling uit (natuurlijke radio-activiteit). Je kunt echter ook radio-activiteit opwekken (induceren) door een atoomkern te beschieten met lichtere deeltjes, veelal protonen of neutronen. Daarbij wordt een instabiele kern gevormd, die vervolgens uiteenvalt in kleinere brokstukken (atoomkernen van lichtere elementen; kernsplijting) veelal onder uitzending van gamma-straling. We spreken dan van geïnduceerde radio-activiteit. Dit mechanisme ligt ten grondslag aan de energie productie in kerncentrales. Het omgekeerde proces, namelijk kernfusie, waarbij uit twee lichte kernen een zwaardere kern wordt gemaakt, gaat ook veelal gepaard met de emissie van gamma-straling. Dit proces ligt ten grondslag aan de werking van een waterstofbom, en is ook verantwoordelijk voor de energie opwekking in het binnenste van sterren.

- 2- Ieder elementair deeltje heeft zijn zogenaamde anti-deeltje. Indien, deze elkaar ontmoeten wordt het massa equivalent van beide deeltjes omgezet in electro-magnetische straling of zogenaamde mesonen. De energie van de electro-magnetische straling ligt in het gamma-energie venster (annihilatie-straling).
- 3- Bij deeltjes interacties bij zeer hoge energie worden in de regel zogenaamde mesonen gevormd, die op hun beurt Π^0 mesonen kunnen vormen, die uiteen vallen in gamma-straling. Dergelijke processen worden bijvoorbeeld in deeltjes versnellers (bijv. het CERN in Geneve, Zwitserland) gegenereerd en vervolgens bestudeerd om de fundamentele krachten in de natuur te onderzoeken.
- 4- Indien een geladen deeltje versneld wordt, gaat het electro-magnetische straling uitzenden. Bij versnellingen tot nabij de lichtsnelheid kunnen gamma-fotonen geproduceerd worden.

10.2. Hoog-energetische straling vanuit de kosmos

De eerste pogingen om kosmische gamma-straling middels satelliet experimenten te detecteren voeren terug totaan het begin van de jaren 60. Zo registreerde de gamma-detector aan boord van de **Explorer-11** tussen April en September 1961 22 (!) kosmische gamma-fotonen met energien groter dan 50 MeV. Begin 1962 heeft een gamma-experiment aan boord van de **OSO 1** (uit de reeks Orbiting Solar Observatories) metingen verricht aan de buitenaardse gamma-straling met energien tussen de 0.5 en 3 MeV. Daaruit kwam een fundamenteel experimenteel probleem naar voren, namelijk de onderschatte intensiteit van de (ongewenste) achtergrond gamma-straling, die gecreëerd werd in de omgeving van de detector door hoog-energetische kosmische stralingsdeeltjes. Deze achtergrondstraling overschaduwde de intrinsiek lage gamma-intensiteiten van kosmische gamma-bronnen, zodat metingen hiervan in hoge mate bemoeilijkt worden. De **OSO 3** met aan boord o.a. een gamma-experiment gevoelig voor gamma-straling met energien groter dan 50 MeV registreerde midden 1967 621 gamma-fotonen, waarvan de ruimtelijke verdeling geconcentreerd was langs het melkwegvlak. Dit wees op een galactische (uit de melkweg) oorsprong d.w.z. dat de gamma-straling opgewekt wordt in het sterrenstelsel waar de zon (met zijn zonnestelsel) deel van uitmaakt.

Ondertussen doemde geheel onverwachts een nieuw verschijnsel op aan het hemel firmament, namelijk dat van de "gamma-ray bursts". Dit zijn plotselinge kortstondige uitbarstingen van gamma-straling van kosmische oorsprong, die werden ontdekt in 1969-1970 met de militaire (Amerikaanse) **Vela-5A/B**

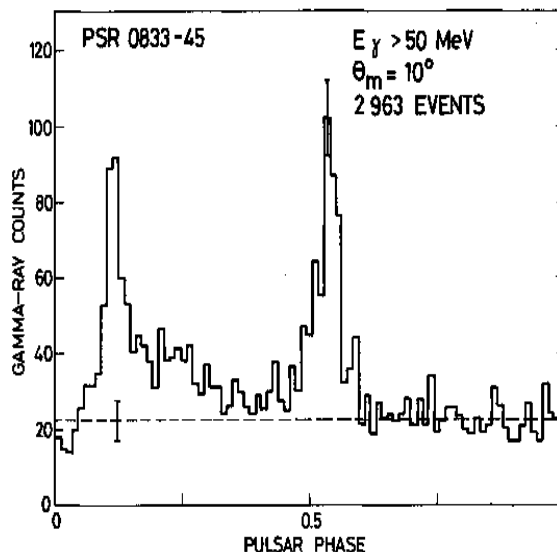


Fig. 10.4. COS-B gamma-lichtkromme van de Vela pulsar (PSR B0833-45) voor de period 20 Oct. - 28 Nov. 1975.

satellieten. Dit netwerk van satellieten moest toezien op de naleving van een verdrag tussen de supermachten, die kernproeven in de atmosfeer verbood. Heden ten dage (na bijna 30 jaar mysterie) weten we dat dit verschijnsel een extra-galactische (buiten ons melkwegstelsel) oorsprong heeft en dat het één van de meest energetische processen in de kosmos vertegenwoordigt. Later, begin jaren 70, werd gamma-lijnstraling ontdekt in de data van een gamma-experiment aan boord van de **OSO 7** in een zonnevlam, die op 4 Aug. 1972 plaatsvond.

Een enorme sprong voorwaarts werd gemaakt met de geheel aan gamma-astronomie gewijde experimenten aan boord van de Amerikaanse **SAS-2** (November 1972 - Juni 1973) en Europese **COS-B** (Augustus 1975 - April 1982). De vonkenkamer aan boord van **SAS-2** (gevoelig voor gamma-fotonen met energieën tussen 35 MeV en 1 GeV) registreerde ~ 8000 kosmische gamma-fotonen. De geproduceerde hemelkaart toonde een aantal (discrete) gamma-bronnen bovenop een diffuse gloed van gamma-straling gegenereerd in het melkwegvlak. Dit beeld werd bevestigd en de kaart sterk verbeterd (meer dan 210 000 kosmische gamma-fotonen werden geregistreerd) middels metingen met de vonkenkamer aan boord van de **COS-B** satelliet (gevoelig voor gamma-fotonen met energieën tussen 30 MeV en 5 GeV). Twee van de ~ 30 gamma-bronnen konden ondubbelzinnig geïdentificeerd worden met bekende hemelobjecten. Eén gamma-bron viel niet alleen ruimtelijk samen met de Vela pulsar, maar vertoonde ook een karakteristiek tijdssignaal ("lichtkromme") bij een frequentie, die reeds eerder gevonden was bij metingen in het radio-venster aan de Vela pulsar (zie Figuur 10.4 voor een **COS-B** lichtkromme van de Vela pulsar voor een observatie, die plaatsvond van 20 Okt. - 28 Nov. 1975). Hetzelfde gold voor een gamma-bron, die samenviel met de Crab pulsar.

Een andere belangrijke ontdekking werd gemaakt met de gamma-spectrometer aan boord van de **HEAO-3** satelliet in de midden jaren 80. Vanuit het binnen gebied van onze melkweg werd gamma-lijnstraling ontdekt met een energie van 1.809 MeV,

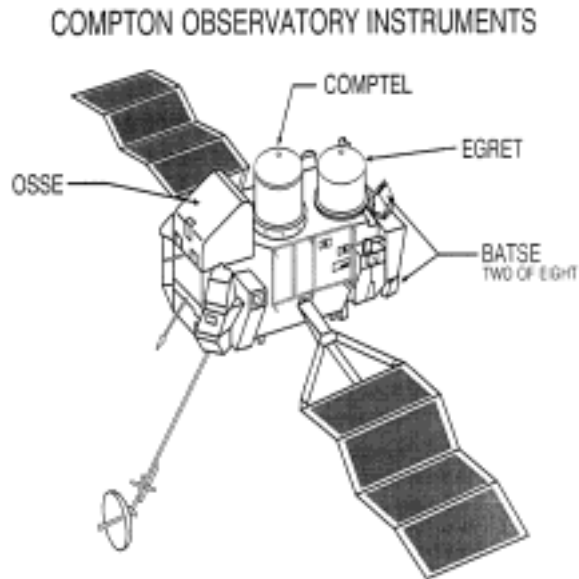


Fig. 10.5. Het Compton Gamma-Ray Observatory.

die karakteristiek is voor het verval van ^{26}Al . Deze ontdekking opende een nieuw venster voor het onderzoek aan de zogenaamde nucleosynthese, de vorming van elementen, in de kosmos.

Het was duidelijk dat in het gamma-venster een enorm potentieel aan astrofysische gegevens voorhanden lag. Vandaar dat in de jaren 80 een gamma-missie werd voorbereid, die het gamma-onderzoek een grote stap voorwaarts moest brengen. Dit leidde uiteindelijk tot de bouw van het Gamma-Ray Observatory, één van de vier grote observatoria onder supervisie van NASA. Het Compton Gamma-Ray Observatory (CGRO; zie Fig. 10.5), gelanceerd op 5 Apr. 1991, met aan boord 4 complementaire gamma-experimenten, die tezamen het gamma-venster van ruwweg 20 keV tot 30 GeV bestrijken, heeft zowel de kwaliteit als kwantiteit van de gamma-ray data enorm verbeterd. Deze satelliet, geheel gewijd aan gamma-astronomie, met een gewicht van 17 ton en afmetingen van $7.5\text{m} \times 5.5\text{m} \times 4.5\text{m}$ is de zwaarste civiele satelliet, die tot nu toe is gelanceerd. De 4 CGRO experimenten zijn:

- 1- BATSE, bestaande uit 8 detectoren op iedere hoek van het CGRO platform, speurt de hemel af naar kortstondige plotselinge uitbarstingen van gamma-straling in het 20 keV - 1 MeV venster.
- 2- OSSE, bestaande uit 4 onafhankelijke detectoren, is evenals BATSE een niet-afbeeldend detector systeem, gevoelig voor gamma-straling met energien tussen de 50 keV en 10 MeV.
- 3- COMPTEL, een afbeeldende Compton telescoop, die waarnemingen verricht in het onontgonnen midden-energie gamma-venster van 0.75 tot 30 MeV.
- 4- EGRET maakt gebruik van een vonkenkamer en brengt de meest energetische gamma-component in kaart (30 MeV - 30 GeV).

De doelstelling was om met dit instrumentarium de (zeer) energetische kosmische processen, die vaak ten grondslag liggen aan de productie van gamma-straling, in detail te onderzoeken. De astrofysische scenario's waarin dit gebeurt lopen ver uiteen: zowel

compacte objecten, zoals neutronensterren of stellaire zwarte gaten en de kernen van actieve melkwegstelsels, als het ijle interstellaire (de ruimte tussen de sterren) medium zijn bronnen van gamma-straling.

In dit proefschrift heb ik me gefocuseerd op de eigenschappen van pulsars in het hoge-energie venster. Wat zijn dit nu voor objecten? Het gangbare model voor een pulsar is dat van een snel draaiende (rotatie perioden tussen de 1.5 milliseconde en 10 seconde) neutronenster met een extreem sterk magnetisch veld, dat geheld is ten opzichte van de draaiingsas. Straling, opgewekt in de magnetosfeer van dergelijke systemen, zal voor een verre waarnemer, die kijkt onder een willekeurige hoek, een gepulst karakter vertonen (vandaar de benaming pulsar; voor een meer aards analoog, denk aan de bundels van een vuurtoren). Een neutronenster is een eind-evolutie produkt van relatieve zware sterren (met massa's groter dan $\sim 8\times$ die van de zon) en heeft een massa, die ongeveer gelijk is aan die van de zon. Echter, de materie is samengeperst in een bolvormig volume met een straal van ~ 10 km (vandaar de naam compact object)! De combinatie van een snelle rotatie en een sterk magneetveld wekt in de magnetosfeer enorme elektrische velden op (vergelijk een fiets dynamo), waardoor geladen deeltjes tot enorme snelheden versneld kunnen worden. Deze versnelde deeltjes zenden hoog-energetische staling uit in de vorm van Röntgen - en gamma-straling.

Ik heb voor dit onderzoek met name de data van CGRO COMPTEL geanalyseerd en in mindere mate de data van CGRO EGRET (eerste gedeelte van dit proefschrift). Ook zijn gegevens geanalyseerd, die verkregen werden met de instrumenten gevoelig voor Röntgen straling aan boord van ROSAT (Duits/Engels/Amerikaanse Röntgen Satelliet) en BeppoSAX (een Italiaans/Nederlandse onderneming), in het bijzonder voor een gedetailleerd onderzoek aan de hoge-energie emissie van milliseconde pulsar PSR J0218+4232 (tweede gedeelte van dit proefschrift).

10.3. Overzicht van dit proefschrift

Dit proefschrift bestaat uit 2 afzonderlijke gedeelten, waarin wetenschappelijke resultaten worden gepresenteerd, voorafgegaan door een Engelstalige inleiding (Hoofdstuk 1). In het eerste gedeelte (Hoofdstukken 2 – 5) bespreek ik voor 4 verschillende pulsars de (hoge-energie) resultaten, die verkregen zijn na analyse van COMPTEL/EGRET data.

In Hoofdstuk 2 wordt de zoektocht naar gamma-straling van de bron "Geminga" in het 0.75 - 30 MeV energie venster beschreven gebruikmakend van de COMPTEL gegevens. Geminga is ontdekt als hoge-energie gamma-bron (energien groter dan 50 MeV) in de data van de SAS-2 satelliet. De aard van Geminga is lange tijd een mysterie geweest, maar de ontdekking van pulsaties bij Röntgen energien in ROSAT data en de daarop volgende ontdekking van hoge-energie gamma-ray pulsaties in EGRET data maakten duidelijk dat we te doen hebben met een pulsar, die geen (noemenswaardige) radio-straling uitzendt. De COMPTEL waarnemingen, die bij deze zoektocht gebruikt zijn, zijn verspreid over de eerste 3.5 jaar van CGRO missie. We hebben Geminga niet significant kunnen detecteren in het midden gamma-energie venster.

Hoofdstuk 3 gaat over de midden gamma-energie eigenschappen van pulsar PSR B1951+32, ontdekt als hoge-energie gamma-pulsar in EGRET data. In dit geval meten we een zwak gamma-signaal in de COMPTEL data.

PSR B1509-58 komt aan bod in Hoofdstuk 4, waar we de detectie rapporteren van gepulste gamma-straling tot tenminste 10 MeV in de COMPTEL data. In tegenstelling tot beneden de 1 MeV, waar zowel BATSE als OSSE gepulste emissie detecteren, is het gepulste signaal boven de 10 MeV niet meer van betekenis en is niet te herkennen in EGRET data.

Tenslotte wordt het eerste gedeelte afgesloten (Hoofdstuk 5) met een uitvoerige beschrijving van de hoge-energie straling van de Crab pulsar (PSR B0531+21), zoals waargenomen door COMPTEL, waarbij nagenoeg alle beschikbare data gebruikt worden. Deze resultaten zijn geplaatst in een veel breder kader, van zachte Röntgen tot harde gamma-straling, door ook de analyse resultaten van andere hoge-energie instrumenten erbij te betrekken. We vinden onder andere, dat de puls vorm sterk energie afhankelijk is, en dat de gepulste emissie samengesteld is uit tenminste 3 verschillende spectrale componenten, elk met een eigen puls-fase afhankelijkheid.

Het tweede gedeelte van dit proefschrift is geheel gewijd aan de hoge-energie straling, van zachte Röntgen tot harde gamma-straling, van milliseconde pulsar PSR J0218+4232. Zo wordt in Hoofdstuk 6 de detectie gemeld van een zachte Röntgen bron ter plekke van PSR J0218+4232 gebruikmakend van ROSAT "High Resolution Imager" (HRI) data. In een veel langer durende vervolg waarneming met de ROSAT HRI wordt tenslotte ook een gepulst Röntgen signaal gedetecteerd (Hoofdstuk 7). De energie verdeling van de gepulste Röntgen straling is vervolgens onderzocht gebruikmakend van BeppoSAX metingen en de bevindingen zijn te vinden in Hoofdstuk 8. Tot slot wordt in Hoofdstuk 9 de (zeer) waarschijnlijke detectie gerapporteerd van gepulste hoge-energie (100-1000 MeV) gamma-straling van PSR J0218+4232 in EGRET data. Dit betekent de *eerste* detectie van een milliseconde pulsar in het hoge-energie gamma venster.

10.4. Wetenschappelijke bijdrage van dit onderzoek en vooruitzichten

In het pre-CGRO tijdperk waren er slechts 2 pulsars bekend, die hoge-energie gamma-straling (energien groter dan ~ 30 MeV) produceerden, namelijk de Vela en Crab pulsar. De Crab pulsar vertoonde gepulste emissie van zachte Röntgen tot hoge-energie gamma-straling, in tegenstelling tot de Vela pulsar, waarvan alleen hoge-energie gamma-straling werd waargenomen. Data van het Compton Gamma-Ray Observatory hebben het aantal gamma-ray pulsars bijna doen verviervoudigen met name in het EGRET energie venster (boven de 30 MeV). In het onontgonnen midden gamma-energie gebied heeft COMPTEL (0.75-30 MeV) met hoge significantie van 3 pulsars, te weten, de Crab pulsar, PSR B1509-58 en de Vela pulsar, gepulste straling waargenomen. Voor PSR B1951+32 is een zwak gamma-signaal gevonden. De detecties betekenen een verviervoudiging van het aantal gamma-pulsars in het midden gamma-energie gebied! De resultaten voor de Crab pulsar, PSR B1509-58 en PSR B1951+32 worden (voor het eerst) in detail gepresenteerd in dit proefschrift (voor de Vela pulsar is de analyse, gebruikmakend van alle beschikbare COMPTEL data, in voorbereiding).

Het bepalen van de emissie karakteristieken van gamma-ray pulsars over een zo breed mogelijk energie venster kan licht werpen op de productie mechanismen en productie plaatsen van de hoge-energie straling in de magnetosfeer van een pulsar. We kunnen zo de evolutie van pulsars beter begrijpen, omdat het energie verlies vanuit de magnetosfeer in de vorm van pulsar wind

(een continue uitstroom van geladen deeltjes vanuit het "open" magnetische veld gebied van een pulsar) en hoge-energie electromagnetische straling bepalend is voor het rotatie-energie verlies van pulsars.

Het onderzoek aan de hoge-energie stralingseigenschappen van milliseconde pulsars, met name PSR J0218+4232, kan hierbij een belangrijke rol spelen. Immers, hoewel de sterkte van het magneetveld en de afmeting van de magnetosfeer van deze objecten veel kleiner is dan die van normale pulsars (dus veel ongunstigere rand condities voor versnellingsprocessen, die hoge-energie straling opwekken), wordt er toch bij 3 van dergelijke systemen, te weten PSR B1821-24, PSR J0218+4232 en PSR B1937+21, hoge-energie straling uit de magnetosfeer waargenomen. De hoge-energie karakteristieken van PSR J0218+4232 worden voor het eerst in detail besproken in Hoofdstukken 6-9 van dit proefschrift, van ontdekking als zachte Röntgen bron tot (zeer) waarschijnlijke hoge-energie gamma bron.

Reeds uitgevoerde waarnemingen met het Chandra X-Ray Observatory, toekomstige (goedgekeurde) waarnemingen met de Rossi X-ray timing Explorer en mogelijke waarnemingen met de instrumenten aan boord van INTEGRAL (ESA gamma-ray missie; gevoelig in het X-ray/gamma-ray energie venster van 10 keV - 10 MeV; verwachte lancering in 2002) van deze bron zullen het hoge-energie beeld verder complementeren, met name in het harde Röntgen/zachte gamma gebied. Van de op stapel staande hoge-energie gamma-missies GLAST (NASA missie; gevoelig in het gamma-energie venster van 10 MeV - 100 GeV, $\sim 50\times$ gevoeliger dan EGRET; verwachte lancering in 2005) en AGILE (Italian Space Agency missie; gevoelig in het gamma-energie venster van 30 MeV - 50 GeV, gevoeligheid vergelijkbaar met EGRET; verwachte lancering in 2002) mag verwacht worden dat het gepulste karakter van de hoge-energie gamma-straling van PSR J0218+4232 bevestigd wordt en verder in detail kan worden onderzocht. Dit zal mogelijk leiden tot een beter begrip van pulsar magnetosferen. Helaas zijn er de komende 10-15 jaar geen gamma-missies gedefinieerd, die gevoelig zijn in het midden gamma-energie venster ($\sim 1-30$ MeV), zodat de COMPTEL database gedurende de nabije toekomst de enige informatiebron vormt voor het onderzoek aan pulsars in het midden gamma-energie venster.

Curriculum vitae

Op 2 april 1960 ben ik geboren in Zaandam, waar ik ook mijn jeugd heb doorgebracht. De lagere school is doorlopen aan de Hugo de Groot school van 1966 tot 1972. Het middelbare onderwijs is gevolgd van 1972 tot 1978 op de gymnasium afdeling van het Zaanlands Lyceum te Zaandam, waar ik met goed gevolg het eindexamen Gymnasium-B heb afgelegd.

Gedurende mijn jeugd tijd werd al duidelijk dat ik grote interesse had in alles wat met sterrenkunde en ruimtevaart te maken had. Een logisch gevolg hiervan was de keuze om natuur- en sterrenkunde te gaan studeren en dit werd gedaan aan de gemeentelijke universiteit van Amsterdam. Het kandidaatsexamen in de natuur- en sterrenkunde heb ik behaald op 14 februari 1982. Het doctoraal examen werd cum laude behaald op 31 augustus 1987, met als hoofdvak sterrenkunde en als bijvakken capita selecta uit de natuurkunde en capita selecta uit de wiskunde. Zowel het klein- als groot onderzoek, vereist voor dit examen, heb ik uitgevoerd onder begeleiding van Prof. Dr. J. van Paradijs. Het betrof data analyse van optische waarnemingen aan de Röntgen dubbelster SMC X-1 (klein-onderzoek) en theoretische berekeningen aan de lichtkromme van de Röntgen dubbelster LMC X-3 (groot-onderzoek).

Na mijn doctoraal studie ben ik in oktober 1987 begonnen bij het Laboratorium voor Ruimteonderzoek Leiden (ROL) als wetenschappelijk programmeur binnen het COMPTEL project onder supervisie van Dr. W. Hermsen. COMPTEL is een van de 4 instrumenten aan boord van het Compton Gamma-Ray Observatory (CGRO), dat werd gelanceerd in april 1991. Het COMPTEL project wordt uitgevoerd door een internationaal consortium bestaande uit het Max-Planck Institut für extraterrestrische Physik (Garching; Duitsland), de Stichting Ruimte Onderzoek Nederland SRON (Utrecht), de University of New Hampshire (Durham; VS) en de Astrophysics Division van ESA (Noordwijk). In het begin hadden mijn werkzaamheden voornamelijk betrekking op het schrijven van calibratie software, maar het werd langzamerhand duidelijk, dat promotie onderzoek in het verschiet zou liggen. Gekozen werd uiteindelijk voor een onderzoek aan pulsars, die een goede kans maakten om gedetecteerd te worden in het COMPTEL energie venster. De onderzoeks resultaten voor vier van dergelijke pulsars worden gepresenteerd in het eerste gedeelte van dit proefschrift.

Gedurende het onderzoek heeft er een integratie plaatsgevonden tussen SRON-Leiden (voormalig ROL) en SRON-Utrecht, hetgeen een verhuizing van werkplek naar Utrecht inhield. Daar kwamen we in contact met Prof. Dr. F. Verbunt van het Sterrenkundig Instituut Utrecht, die ons betrok bij zijn onderzoek aan de Röntgen emissie van de milli-seconde pulsar PSR J0218+4232. Vervolgonderzoek aan dit object met instrumenten aan boord van de Röntgen satellieten ROSAT en BeppoSAX, en met de gamma instrumenten aan boord van CGRO heeft geleid tot de detectie van gepulste Röntgen straling en zeer waarschijnlijk ook van gepulste hoog-energetische gamma-straling. Deze onderzoeksresultaten zijn te vinden in het tweede gedeelte van dit proefschrift.

Tijdens mijn onderzoek heb ik vele COMPTEL vergaderingen bijgewoond, beurtelings plaatsvindend in een van de deelnemende instituten. Hier werd de stand van zaken betreffende COMPTEL data verwerkings software, analyse resultaten en dergelijke in detail besproken. Ook heb ik vele symposia en workshops bezocht. Zeker vermeldenswaardig zijn de twee NATO advanced study institutes betreffende "Timing Neutron Stars" (April 1988 in Çeşme, Turkije) en "The many faces of Neutron Stars" (Oct. 1996 in Lipari, Italië), het 3^{de} en 4^{de} COMPTON Symposium (Juni 1995 in München, Duitsland; April 1997 in Williamsburg, VS), de 3^{de} en 4^{de} INTEGRAL Workshop (Sept. 1998 in Taormina, Italy; Sept. 2000 in Alicante, Spanje) en tenslotte het IAU Colloquium 177 "Pulsar Astronomy – 2000 and beyond" (Sept. 1999 in Bonn, Duitsland).

Naast het doen van onderzoek heb ik gedurende 3 semesters het werkcollege "Stralings processen in de astrofysica" verzorgd in Leiden. Dit jaar heb ik het practicum gedeelte geleid van het vak "Grondslagen van de Observatieve Sterrenkunde" in Utrecht.

Na mijn promotie blijf ik werkzaam bij de hoge-energie afdeling van SRON.